



HAL
open science

Contribution of Cryo-Holography in electron microscopy for the study of biological materials

Elio Karim

► **To cite this version:**

Elio Karim. Contribution of Cryo-Holography in electron microscopy for the study of biological materials. Biotechnology. Université Paul Sabatier - Toulouse III, 2023. English. NNT : 2023TOU30347 . tel-04593062

HAL Id: tel-04593062

<https://theses.hal.science/tel-04593062>

Submitted on 29 May 2024

HAL is a multi-disciplinary open access archive for the deposit and dissemination of scientific research documents, whether they are published or not. The documents may come from teaching and research institutions in France or abroad, or from public or private research centers.

L'archive ouverte pluridisciplinaire **HAL**, est destinée au dépôt et à la diffusion de documents scientifiques de niveau recherche, publiés ou non, émanant des établissements d'enseignement et de recherche français ou étrangers, des laboratoires publics ou privés.



THÈSE

**En vue de l'obtention du
DOCTORAT DE L'UNIVERSITÉ DE TOULOUSE**
Délivré par l'Université Toulouse 3 - Paul Sabatier

Présentée et soutenue par

Elio KARIM

Le 15 décembre 2023

**Apport de la Cryo-Holographie en microscopie électronique pour
l'étude des matériaux biologiques**

Ecole doctorale : **SDM - SCIENCES DE LA MATIERE - Toulouse**

Spécialité : **Chimie-Biologie-Santé**

Unité de recherche :

CEMES - Centre d'Elaboration de Matériaux et d'Etudes Structurales

Thèse dirigée par

Etienne SNOECK et Pierre-Emmanuel GLEIZES

Jury

M. Angus KIRKLAND, Rapporteur

M. Daniel LÉVY, Rapporteur

Mme Anne-Marie GUÉ, Examinatrice

M. Sergio MARCO GARRIDO, Examineur

M. Etienne SNOECK, Directeur de thèse

M. Pierre-Emmanuel GLEIZES, Co-directeur de thèse



THÈSE

En vue de l'obtention du

DOCTORAT DE L'UNIVERSITÉ DE TOULOUSE

Délivré par l'Université Toulouse 3 - Paul Sabatier

Présentée et soutenue par

Elio KARIM

15 December 2023

Developing (Cryogenic) Electron Holography for the Study of Biological Materials

Ecole doctorale : SDM - SCIENCES DE LA MATIERE - Toulouse

Spécialité : Chimie-Biologie-Santé

Unités de recherche

**CEMES - Centre d'Elaboration de Matériaux et d'Etudes
Structurales**

CBI - Centre de Biologie Intégrative - Sous-unité MCD
Directeurs de Thèse

Etienne SNOECK et Pierre-Emmanuel GLEIZES

Jury

M. Angus KIRKLAND, Rapporteur

M. Daniel LÉVY, Rapporteur

Mme Anne-Marie GUÉ, Examinatrice

M. Sergio MARCO GARRIDO, Examineur

M. Etienne SNOECK, Directeur de thèse

M. Pierre-Emmanuel GLEIZES, Co-directeur de thèse






Acknowledgments

I would like first to express my sincere appreciation to the jury members for accepting to evaluate my thesis and participate in the jury. It was an honor meeting accomplished people, some of I already knew which, for me, is a great motivation in my future career. I would like to thank, from the bottom of my heart, my precious family, starting with my parents (Nicolas and Joyce) who accompanied me throughout my life and helped me come to France and settle, providing me with moral and financial support, especially in the first year and a half when I did not have any income. Nothing would have been the same without you guys. Thanks to my two brothers, Christian and Etian, for your constant support and kindness. I am so lucky to have you as my brothers. Thank you to my families in Qatar (Rudy and co.) and Australia (Peggy and co.) for always staying in contact and being there on my thesis day. Thanks to my family in Germany (Robert and all) for helping me come to France and inviting me on many occasions to visit. Of course, thanks to my grandparents as well, whom I love dearly.

Thanks to all my friends who were here during these three years, and I sincerely hope I will not forget anyone (I apologize in advance). Thank you, Alex, for all these amazing hiking trips we went on, which made me discover a new hobby. Congratulations on getting married to the great Marianne! Thank you to my great 'French' friend Rami Younes, who stayed close even with all the misunderstandings that happened between us. Thanks to Chadi and Razan (congrats for the baby girl), Wassim, Roy, Ali, Anna, the Lebanese gang that was always close to me. Thank you to Farid, a great friend who also gave me the contact for the Lebanese food people for the thesis pot. Thank you to the people I knew outside of the lab and with whom I shared many memories, Davy! Thanks also to the people who came temporarily to Toulouse, Carlos, Jorge, Georges Khoury, Marlene, Elia. Thank you to my friends in all the other parts of the country, Anthony, Carolle, Dana, Karim, and all the others.

Thank you to Kedar and Estefania for helping organize my thesis and for these three years in the CEMES laboratory. Thanks to all the CEMES people, too, PhDs, post-docs who were always welcoming and nice, Kilian, Julien, Anaïs, Marine, Simon, Benoît, Liz, Eloïse, Leifeng, Loïc, Min Anh, Benjamin, Bumsu, Salomé, Quentin (with whom I learned a bit of skiing), Martin, Younes, and all the others. A big thanks to the Indian community I got to know in Toulouse with Sruthi, Akshay, Vishnu, Sanjay, and especially the kind-hearted Megha, the girl who became very close to me even though she came a few months before my thesis to the CEMES.

Thank you to all my great friends who are still in Lebanon: Mario, Maya, Ralph, Rami Al Alam, Ranine, and the duo Carolle N. and Mary, but also all my other friends. Thanks also to the friends I met at the CBI, although I did not spend much time there: Maxime (and Emeline, whom I met because of you), Julie, Sarah, Paolo, Anaïs A., Hussein, Sophie, and Sofiane, and thank you for the great desserts you did for my thesis!! Thank you to both my CEMES and CBI teams, which were honestly filled with talented and amazing people that helped me throughout my thesis struggles and experiments. You guys created a great work environment for me that was very interactive. Thanks also to all the people outside of my teams (Cécile, Vanessa, Stephanie, Ramteen...) who taught me a lot and were patient with me.



Finally, I would like to thank my two amazing directors, Etienne and Pierre-Emmanuel, who took great care of me, were always here if I had any questions or was struggling with something. I was very lucky to have very responsive and understanding people to help me through these three years. I also want to thank the region Occitanie and Université de Toulouse for providing the funding and therefore this opportunity. I am very thankful for everyone, and I hope I did not leave anyone out. It has been an amazing journey, and I hope one day to look at this manuscript and be proud of what I did and where it got me, and with whom I did it.

Thank you all for everything!



ABBREVIATIONS LIST


| | |
|--|--|
| 2D: Two-dimensional | LEEPS: Low-Energy Electron Point Source |
| 3D: Three-dimensional | LoG: Laplacian of Gaussian |
| 4D: Four-dimensional | MTF: Modulation Transfer Function |
| aa: amino acid | MAADF: Medium Angle Annular Dark Field |
| ACTF: Amplitude Contrast Transfer Function | MIP: Mean Inner Potential |
| ADF: Annular Dark Field | NMR: Nuclear Magnetic Resonance |
| AF: Assembly Factors | NOE: Nuclear Overhauser Effect |
| BSE: Backscattered Electrons | PCTF: Phase Contrast Transfer Function |
| BF-TEM: Bright Field TEM | PDB: Protein Data Bank |
| CCD: Charge Coupled Devices | PP: Phase Plate |
| CMOS: Complementary metal-oxide-semiconductor | RNA: Ribonucleic Acid |
| Cryo-EM: Cryogenic Electron Microscopy | rRNA: ribosomal RNA |
| Cryo-ET: Cryogenic Electron Tomography | ROI: Region of Interest |
| CTF: Contrast Transfer Function | SE: Secondary Electrons |
| DDD: Direct (electron) Detection Device | SEM: Scanning Electron Microscopy |
| DF: Dark Field | SGD: Stochastic Gradient Descent |
| DNA: Deoxyribonucleic Acid | SH: Sample Holder |
| DQE: Detective Quantum Efficiency | SNR: Signal to Noise Ratio |
| e-PIE: Extended-Ptychographical Iterative Engine | SPA: Single Particle Analysis |
| FEG: Field Emission Gun | STA: Sub-Tomogram Averaging |
| FFT: Fast Fourier Transform | STEM: Scanning Transmission Electron Microscopy |
| FIB: Focused Ion Beam | TEM: Transmission Electron Microscopy |
| FOV: Field of View | TMP: Tape Measure Protein |
| FRWR: Full-Resolution Wave Reconstruction | TMV: Tobacco Mosaic Virus |
| FSC: Fourier Shell Correlation | VPP: Volta Phase Plate |
| FT: Fourier Transform | WTF: Wave Transfer Function |
| GIF: Gatan © Imaging Filter | ZPP: Zernike Phase Plate |
| GUI: Graphical User Interface | |
| HAADF: High Angle Annular Dark Field | |
| IDP: Intrinsically Disordered Protein | |
| iDPC: integrated Differential Phase Contrast (STEM) | |
| KLH: Keyhole limpet hemocyanin | |
| LAADF: Low Angle Annular Dark Field | |
| LB: Lysogeny Broth | |

Summary

| | |
|---|-----------|
| ABBREVIATIONS LIST..... | V |
| GENERAL INTRODUCTION AND THESIS MOTIVATION | 1 |
| CHAPTER 1: TRANSMISSION ELECTRON MICROSCOPY..... | 4 |
| 1.1 ELECTRONS AS PARTICLES AND WAVES | 4 |
| 1.2 ELECTRONS AND MATER INTERACTIONS..... | 5 |
| 1.3 THE TRANSMISSION ELECTRON MICROSCOPE | 6 |
| 1.3.1 General principles | 6 |
| 1.3.2 The I2TEM microscope | 9 |
| 1.3.3 The Talos Arctica microscope | 11 |
| 1.3.4 Image formation in TEM | 12 |
| 1.3.5 The wave description | 12 |
| CHAPTER 2: ELECTRON HOLOGRAPHY: A SOLUTION FOR THE OBSERVATION OF BIOLOGICAL SPECIMENS ? | 16 |
| 2.1 THE STRUCTURE OF BIOLOGICAL MACROMOLECULES..... | 16 |
| 2.1.1 A brief description of the T4, T5 and T7 bacteriophages.... | 18 |
| 2.1.2 The T4 bacteriophage tail | 19 |
| 2.2 SOLVING THE STRUCTURE OF MACROMOLECULES | 19 |
| 2.2.1 X-ray crystallography..... | 20 |
| 2.2.2 Nuclear magnetic resonance | 20 |
| 2.2.3 Visualizing macromolecules and viruses by electron microscopy with negative staining | 21 |
| 2.2.4 Cryo-electron microscopy | 22 |
| 2.3 SINGLE PARTICLE ANALYSIS | 24 |
| 2.4 CRYOGENIC ELECTRON TOMOGRAPHY AND SUB-TOMOGRAM AVERAGING | 25 |
| 2.5 THE PHASE PROBLEM..... | 28 |
| 2.5.1 Amplitude objects vs phase objects | 28 |
| 2.5.2 How X-ray crystallography solved the phase problem..... | 30 |
| 2.6 USING ELECTRON HOLOGRAPHY TO DIRECTLY MEASURE THE PHASE OF THE EXIT WAVE..... | 31 |

| | | |
|-------------------|---|-----------|
| 2.6.1 | The history of electron holography..... | 31 |
| 2.6.2 | Obtaining phase images by off-axis holography | 31 |
| 2.6.3 | Focal series in-line holography as an alternative phase retrieval technique | 35 |
| 2.6.4 | Hybrid holography: getting the best of two in-line and off-axis methods..... | 38 |
| 2.6.5 | Ptychography: Another phase retrieval method in development..... | 38 |
| 2.7 | SAMPLE PREPARATION AND TEM GRIDS | 39 |
| 2.7.1 | T4 bacteriophage culture and purification methods..... | 39 |
| 2.7.2 | TEM Grids..... | 40 |
| 2.7.3 | Room temperature TEM grids preparation..... | 41 |
| 2.7.4 | Cryogenic sample preparation..... | 42 |
| CHAPTER 3: | OFF-AXIS ELECTRON HOLOGRAPHY ON BACTERIOPHAGES..... | 44 |
| 3.1 | INTRODUCTION | 44 |
| 3.1.1 | The aims of off-axis development..... | 44 |
| 3.1.2 | Off-axis holography software developments | 45 |
| 3.2 | CONVENTIONAL OFF-AXIS ELECTRON HOLOGRAPHY | 46 |
| 3.2.1 | Challenges for biological off-axis electron holography | 46 |
| 3.2.2 | Testing off-axis holography on negatively stained bacteriophages..... | 50 |
| 3.2.3 | Off-axis holography of unstained bacteriophages | 52 |
| 3.2.4 | From a CMOS OneView camera to a K3 direct detector | 57 |
| 3.3 | CRYOGENIC OFF-AXIS HOLOGRAPHY | 64 |
| 3.3.1 | Towards cryogenic off-axis holography | 64 |
| 3.3.2 | The challenges of cryogenic microscopy on the I2TEM | 65 |
| 3.3.3 | Dose limitation | 66 |
| 3.3.4 | Off-axis cryo-holography of T4 and T5 bacteriophages..... | 68 |
| 3.3.5 | The phase noise problem | 72 |
| 3.3.6 | Conclusion..... | 74 |
| 3.4 | THE PERSPECTIVES OF THIS PROJECT | 75 |
| 3.4.1 | First attempt of off-axis holography on cell sections | 75 |
| 3.4.2 | Long distance beam interference..... | 76 |

| | |
|---|------------|
| CHAPTER 4: IN-LINE ELECTRON HOLOGRAPHY ON BACTERIOPHAGES | 77 |
| 4.1 INTRODUCTION | 77 |
| 4.1.1 Adapting in-line holography to biological samples | 77 |
| 4.2 CONVENTIONAL IN-LINE HOLOGRAPHY | 78 |
| 4.2.1 Negative stain in-line holography | 78 |
| 4.2.2 Unstained sample in-line holography | 80 |
| 4.3 CRYOGENIC IN-LINE HOLOGRAPHY..... | 81 |
| 4.3.1 T4 and T5 bacteriophages cryo-in-line experiments | 81 |
| 4.3.2 Testing cryogenic in-line holography for individual particle imaging of pre-40S ribosome particles | 89 |
| CHAPTER 5: ALTERNATIVE PHASE IMAGING TECHNIQUES: HYBRID ELECTRON HOLOGRAPHY AND ELECTRON PTYCHOGRAPHY | 91 |
| 5.1 HYBRID ELECTRON HOLOGRAPHY | 91 |
| 5.1.1 The advantages and limitations of combining off-axis and in-line electron holography | 91 |
| 5.1.2 Experimental procedure | 92 |
| 5.1.3 Combining off-axis and in-line holography: first test on the T4 bacteriophage..... | 93 |
| 5.1.4 Perspectives | 96 |
| 5.2 OTHER TEM METHODS FOR THE STUDY OF BIOLOGICAL SAMPLES: ADF-STEM AND ELECTRON PTYCHOGRAPHY | 97 |
| 5.2.1 Introduction | 97 |
| 5.2.2 STEM imaging of the T4 bacteriophage | 97 |
| 5.2.3 4D-STEM ptychography of the T4 bacteriophage | 99 |
| CHAPTER 6: CONCLUSIONS AND THE FUTURE OF ELECTRON HOLOGRAPHY | 101 |
| 6.1 OFF-AXIS ELECTRON HOLOGRAPHY..... | 101 |
| 6.2 FOCAL-SERIES IN-LINE ELECTRON HOLOGRAPHY | 103 |
| 6.3 HYBRID ELECTRON HOLOGRAPHY | 104 |
| 6.4 ELECTRON PTYCHOGRAPHY ON THE T4 BACTERIOPHAGE..... | 104 |
| 6.5 THE FUTURE OF ELECTRON HOLOGRAPHY | 105 |
| ANNEX: SUMMARY TABLES..... | 109 |



| | |
|---|------------|
| ANNEX CHAPTER: SPA OF DOUBLE MUTANT PRE-40S PARTICLES FOR THE STUDY OF THE MATURATION PROCESS..... | 111 |
| 7.1 INTRODUCTION | 111 |
| 7.1.1 Understanding the 40S subunit maturation process..... | 111 |
| 7.1.2 Single particle analysis (SPA) | 112 |
| 7.2 SPA ANALYSIS OF THE PRE-40S PARTICLE | 116 |
| 7.2.1 SPA analysis of the full pre-40S particle | 116 |
| 7.2.2 Resolution enhancement of the Pre-40S head..... | 120 |
| 7.2.3 Analysis and Discussion | 127 |
| RESUMÉ ÉTENDU DE LA THÈSE..... | 131 |
| BIBLIOGRAPHY..... | 155 |
| SHORT ABSTRACT | 174 |

GENERAL INTRODUCTION AND THESIS MOTIVATION


The context and general aim of this thesis

The exploration of biological structures is governed by a range of imaging techniques that vary according to the scale of the target and the desired level of detail. Light microscopy enables the observation of large structures with a resolution limited by diffraction to around 200 nm in the wavelength range of visible light [1]. To go beyond this limit, super-resolution microscopy was recently developed including several different fluorescence techniques [2].

When investigating sub-cellular structures or exploring molecular events, light-based methodologies rely on the utilization of fluorescent molecules. Therefore, fluorescence and single-molecule techniques enable the visualization of the fluorescently labeled molecules linked to our target, rather than the target itself. Structural biology has facilitated the direct observation of biological macromolecules. It is mainly centered around three major techniques: electron microscopy, X-ray crystallography, and nuclear magnetic resonance (NMR), which enable access to the high resolution 3D structures of various macromolecules.

The 3D structure determination of biological macromolecules has long been the focus of research and improvement. It enables nowadays to achieve routine resolutions below 5 Å. Accessing such information helped push many fields, from the most basic understanding of macromolecule functions to therapeutic drug discovery and protein engineering [3,4]. These constant efforts over the years led to several Nobel prizes both in physics and chemistry with the early discovery of X-ray diffraction by crystals by Max von Laue [5] and the studies on the 3D structure of globular proteins by Max Ferdinand Perutz and John Cowdery Kendrew [6] among others. The most recent Nobel prize (in chemistry) in this field was awarded to Richard Henderson, Jacques Dubochet, and Joachim Frank in 2017 [7] for developing cryo-electron microscopy (cryo-EM), a major technique for macromolecule structure determination. In the wake of this Nobel Prize, electron microscopy became a standard practice for studying biological specimens and macromolecules. In this context, I performed my PhD thesis in the two CEMES and CBI laboratories in Toulouse using electron microscopy for the study of biological materials.

The CEMES group has a very good expertise in electron holography and the CBI one is expert in cryo-EM. Recently, Dr. C. Gatel et al. at CEMES have pushed forward the off-axis electron holography method [8] to achieve a phase sensitivity of 2 milliradians on the dedicated I2TEM microscope. This allows to detect very low phase shifts, like those produced by materials made of atoms with small atomic numbers (Z), including biological samples. The phase sensitivity has even been improved recently by the installation of a new direct electron detector (*results to be published*). This progress was made possible thanks to the development of a unique 300 keV electron microscope dedicated to electron holography, the I2TEM, equipped with a biprism set-up. From there came the idea of combining the CEMES and CBI expertise to explore the capabilities of off-axis electron holography to study biological specimens. Our goal was to develop alternative EM ways to study unstained samples at room temperature, but



also in cryogenic conditions, at low electron doses. The use of off-axis electron holography to study biological materials was mostly studied in a thesis dating from 1999 done by Alex Harscher [9].

The uniqueness of this work, which had never been done using the current state-of-the-art microscopes, together with the prospect of a new direct electron detector on the I2TEM at the CEMES sparked this thesis. The subject of the thesis was also extended to include in-line holography, taking advantage of the recent installation of a fully automated Talos Arctica cryo-EM at the CBI, and then hybrid electron holography. These two benefited from the help of Dr. Bumsu Park, postdoc at CEMES and specialist in in-line holography analysis. Compared to off-axis electron holography, in-line holography has the ability to be performed on any electron microscope with standard optics, like the Talos Arctica, but at the cost of complex image analysis.

The current electron microscopy methods used in biology enable high resolutions. Our objective was therefore to improve upon their drawbacks, which will be discussed later in chapter 2. We focused on optimizing both the in-line and off-axis holography methods and taking advantage of the enhanced signal-to-noise ratio and contrast provided potentially by these two techniques.

As test samples, we used the T4 and T5 bacteriophages. These samples are well described and easy to produce. T5 was prepared and purified by Dr. Amélie Leforestier in her LPS laboratory at the University of Saclay.

As part of this thesis, we had a few collaborations with other groups. The main one was with Sara Bals's team in the EMAT laboratory in Belgium, where we corresponded with her and Adrian Pedraza Tardajos. They helped us improve the off-axis holography results by providing us with clean graphene on quantifoil TEM grids as TEM support for the biological samples.

The manuscript layout

We therefore focus in this manuscript on two major electron holography techniques: off-axis electron holography and focal series in-line holography. The manuscript is divided into two bibliographical chapters and three chapters describing the results:

- Chapter 1 discusses the theories and basics of electron microscopy that are essential to understanding advanced EM principles like those regarding the electron wave, the phase and amplitude information transfer, and the electron microscope itself.
- Chapter 2 focuses mostly on biology and describes the composition of biological macromolecules, cryo-EM, and electron holography principles. The last part of this chapter gives details of the sample preparation protocols used during this thesis.
- The results part of this manuscript begins with chapters 3 and 4, about the off-axis holography and in-line holography experiments respectively. They are the main chapters of this thesis. Both are divided into the introduction of each method; the room temperature experiments and then the cryogenic temperature experiments. Details on the performances and the limitations and drawbacks of the two techniques are discussed.
- Chapter 5 discusses other (S)TEM methods used for biological sample imaging. First, we present the enhanced capabilities of hybrid holography, which combines off-axis and in-line holography to get better information on a larger spatial frequency spectrum. A paragraph is then focused on the ptychography results obtained by an Oxford group with our T4 bacteriophages.

- A general conclusion compares and discusses the holography methods used in this thesis with the current capabilities of the known electron microscopy methods used in biology.
- An additional chapter is included in the annex. It presents a classic cryogenic electron microscopy analysis that I performed as a side project. It concerns the determination of the structure of yeast pre-40S ribosomal particles by single particle analysis.

This thesis was highly exploratory from the start, and a lot of time was devoted to improving all aspects of the experiments, from sample preparation and TEM grid selection to the image acquisition protocol.



CHAPTER 1: TRANSMISSION ELECTRON MICROSCOPY

1.1 ELECTRONS AS PARTICLES AND WAVES

Electrons were first discovered by J.J. Tomson in 1897 [10]. They are negatively charged particles that orbit around the atom core. Those particles also behave as waves. This property of being particles and wave is called the wave-particle duality [11]. Louis De Broglie was the first to introduce this concept and proposed the well-known equation that links the particle momentum, p , to its wavelength λ [12]:

$$\lambda = \frac{h}{p} \quad (1.1)$$

The wave behavior of fast electrons has been demonstrated by Davisson and Germer, who showed in 1927 that the electron beam is diffracted when it passes through a nickel crystal [13]. This wave-particle duality was further confirmed by the double slit experiment with electrons by Claus Jonson in 1961 [14]. The wave property of the electrons therefore captured the interest of scientists.

In any imaging techniques the optimal spatial resolution, which is defined by the minimum distance between two points that can be imaged separately, is directly related to the beam wavelength. It is determined by the Rayleigh criterion which links the resolution of the instrument to the wavelength of the used radiation and the numerical aperture of the instrument.

$$R = \frac{0,61\lambda}{NA} \quad (1.2)$$

with λ the wavelength of light and NA the numerical aperture [15].

The maximum lateral resolution that can be obtained with classic bright-field light microscopy is ~ 200 nm due to the wavelength limit of the visible light. Using interference and structured illumination techniques, light microscopy can achieve up to ~ 100 nm (lateral resolution). In addition to that, scientists found a way around it with super-resolution light microscopy which, in turn, could achieve down to ~ 30 nm [15,16]. More recently, Reinhardt et al. were able to achieve angstrom resolutions with fluorescence [17]. However, because fast electrons (i.e., accelerated over ~ 50 kV) have much shorter wavelength than photons, electron microscopy is able to directly and routinely image structure with a much higher resolution than light microscopy.

Wavelength of accelerated electrons depends on the accelerating voltage. The energy of an accelerated electron is $eV = \frac{1}{2}mv^2$, with e the charge of an electron and V the accelerating voltage, its wavelength can then be calculated [18]:

$$\lambda = \frac{h}{\sqrt{2meV}} = \sqrt{\frac{150}{V(\text{volts})}} (\text{\AA}) \quad (1.3)$$

The table below reports the wavelengths for various accelerating voltage:

| | | | | | |
|---------------|--------|--------|--------|--------|--------|
| V | 100 kV | 120 kV | 200 kV | 300 kV | 1.5 MV |
| λ (Å) | 0,038 | 0,035 | 0,027 | 0,022 | 0,01 |

In addition to spatial resolution, electron penetration goes up with higher acceleration voltages which means that thicker specimens can be studied when increasing the electron beam energy, but with a drawback that the higher the electron energy, the higher the irradiation damage on sensitive materials [19]. The most commonly used voltages in TEM nowadays are in between 80 kV and 300 kV giving us up to atomic resolution with acceptable equipment costs [19].

1.2 ELECTRONS AND MATTER INTERACTIONS

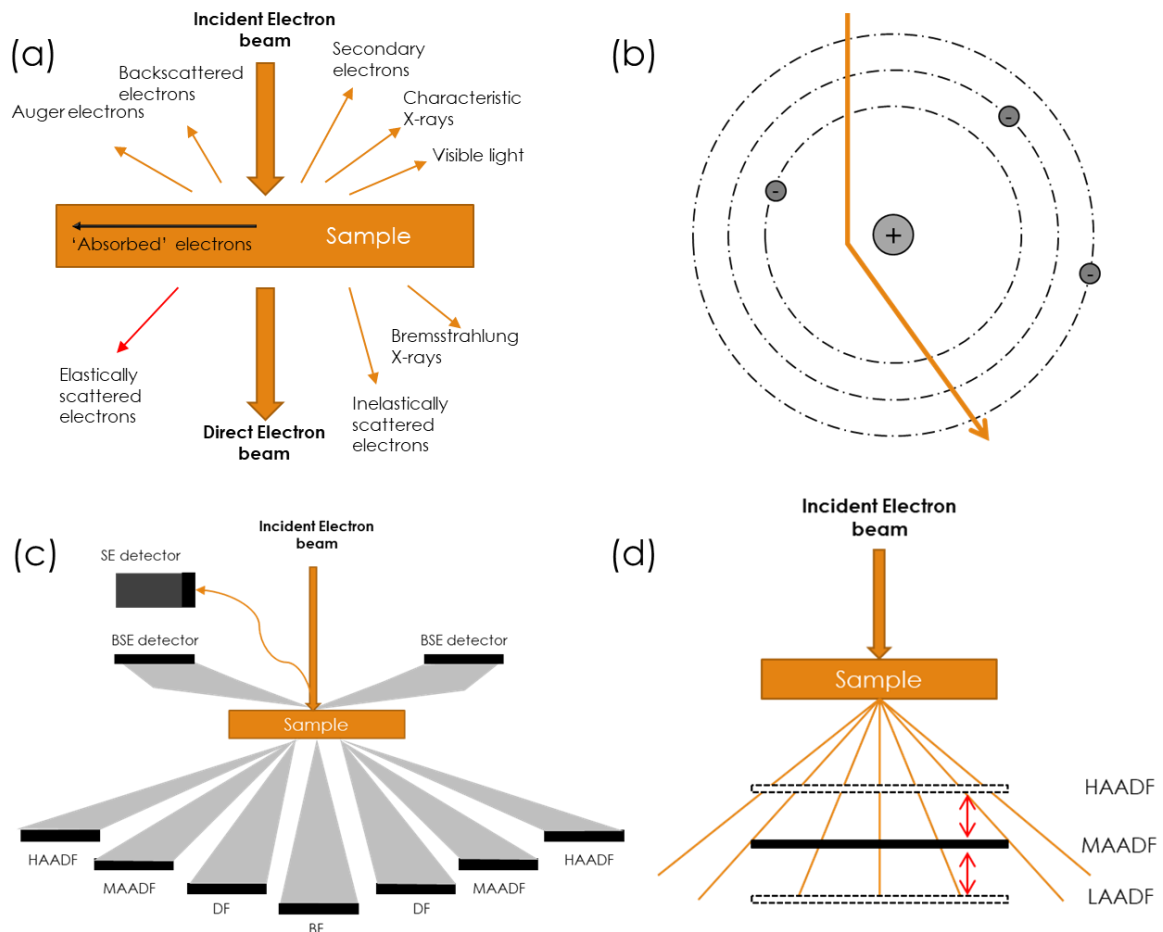
Fast electrons are an ionizing radiation which can transfer part of its energy to the sample atoms when interacting with them. This interaction causes the release of several types of secondary radiations as shown in figure 1.1a. Some of these emitted radiations are exploited in electron microscopy to get information about the sample the electron beam interacted with. Backscattered electrons (BSE) and secondary electrons (SE) are collected in scanning electron microscopy (SEM), inelastically scattered electrons are collected in electron energy loss spectroscopy (EELS), and elastically scattered electrons are used in bright field (BF) TEM as well as scanning transmission electron microscopy (STEM). STEM technique can provide different types of images using annular detectors detecting electrons scattered at different angles (figure 1.1c): high angle, medium angle and low angles electrons (HAADF, MAADF and LAADF respectively) [20].

In TEM and STEM the very large majority of electrons are elastically scattered by the atom nucleus, which is positively charged, without energy loss as represented in figure 1.1b. These electrons as well as the unscattered ones who traveled along the central axis of the incident beam ends up to create a bright field (BF) image. In these BF images inelastically scattered electrons create noise which reduces the signal to noise ratio (SNR). The location of the different detectors in STEM can be seen in figure 1.1c. By decreasing the sample-detector distance (camera length), we can collect higher angles scattered electrons and inversely as shown in the figure 1.1d [21].

Electron-matter interactions in TEM can also induce large damage effects of important concern, especially for irradiation sensitive materials like organic and biological samples. Many types of beam damage may occur in parallel: sample heating, electrostatic charging, ionizing damage (radiolysis), atom displacement damage, sputtering and hydrocarbon contamination. These various damages are dependent of the different types of electrons scattering occurring for each electron interaction [22]. The higher acceleration voltage of the electron beam, the higher the electron beam damages of the sample [23]. In addition, this damage is stronger

when using a highly bright focused probe, like in STEM where the beam can be focused to a diameter as small as to 0.1 nm when using an aberration corrector [24].

Biological samples are composed of atoms with low atomic numbers (C, H, N, O, S, P), which makes them more sensitive to the electron beam. In our experience with frozen samples of thicknesses between 100 and 200 nm, detail of 4 nm starts degrading beyond $\sim 75 \text{ e}^-/\text{\AA}^2$ (see §3.3.2). This dose is very low when compared to the high doses around 10^5 and $10^6 \text{ e}^-/\text{\AA}^2$ used when studying inorganic materials [25]. Negative staining solutions containing heavy atoms (U, Gd, W...) are used to enhance the TEM contrast of biological materials and have the secondary benefit of protecting them from electron damages [26].



1.3 THE TRANSMISSION ELECTRON MICROSCOPE

1.3.1 General principles

Transmission electron microscopy allows to create images of samples using accelerated electrons. The electrons are extracted from a source (either by heating or by cold field

emission) then accelerated by an electrostatic potential, generally between 80 and 300 kV. The fast electron beam then passes through a set of *electromagnetic lenses* and *apertures* allowing to shape it and focus it on the object. In a TEM, the sample is located within the *objective lens* which creates the first image of the sample. This image is further magnified by a set of lenses (intermediate lenses and projectors) down to the detector.

The image formation process starting from the source and ending on the detector is summed up in these five steps:

- 1) The extraction and then acceleration of the electrons from the source.
- 2) The formation of a parallel electron beam in TEM.
- 3) The interaction of the electron beam with the sample.
- 4) The formation of the first image of the specimen in the image plane of the objective lens (together with the formation of its diffraction pattern in the back focal plane of the objective lens – see figure 1.4).
- 5) The magnification then projection of the image on the detector plane

Therefore, the main basic parts of TEM microscopes are:

- The electron gun including the source and the accelerating part
- The condenser lenses
- The objective lens
- The magnification and projector lenses
- The detector

In the following, we will focus on three important components for our study: The *electron gun*, the *objective lens* and the *camera detector*. For a broader and more detailed description of all the different components of an electron microscope, please refer to the book “Transmission Electron Microscopy; Part 1: Basics” by D.B. Williams and C.B. Carter [23].

The Electron gun

Electron sources are tips from which electrons are extracted before being accelerated. There are three types of electrons sources that differ from each other in the way electrons are extracted.

1. First, the thermo-ionic sources are tungsten filaments or lanthanum hexaboride (LaB₆) monocrystals from which electrons are extracted by heating the tip to give electrons enough energy to overpass their work function [23]. The tungsten filaments are mainly used for conventional imaging like the TEM experiments we performed for this thesis on negative stain samples. On the other hand, LaB₆ sources are sharper thermo-ionic sources. Furthermore, electrons are extracted from LaB₆ at lower temperature than those for tungsten filaments (1400-2000 K for LaB₆ versus 2700 K for tungsten) and have a longer lifetime [27]. The Jeol 2100 TEM we used at the CBI laboratory is equipped with LaB₆ source for higher resolution studies like cryo-electron tomography or cryo-EM grid check-ups. The thermo-ionic sources are the least coherent electron sources [28].

-
2. Secondly, Schottky field emission sources (Schottky FEG) also called thermal FEG are guns which require heating the tip between 1600 and 1800 K and the application of an electrostatic potential to extract electrons. One example is the tungsten tip (<100 nm) which is covered by a thin layer of ZrO. The latter helps reducing the required energy (the work function) to extract electrons. They have a longer lifetime than thermo-ionic sources and provide more coherent beam. The electron beam is smaller and brighter than thermo-ionic sources i.e. a higher current density compared to the one of thermo-ionic sources, which makes them more suitable for high resolution experiments [29]. On the other hand, FEGs require very high vacuum in the order of 10^{-7} Pa and higher which is challenging to achieve in a TEM column [30].
 3. Lastly, cold field emission guns (cold FEG) are guns operated at around 300 K (no heating required). Electrons are extracted exclusively by applying an electrical potential difference. It consists on a very thin tungsten tip with a virtual source, which is the area where electron leave the gun, of 4 nm only compared to 28 nm for a Schottky [31]. They offer the highest emission current density as well as being the brightest source of electrons. It is worth to note that graphene-nickel cold FEG are also showing a lot of potential for TEM applications due to their usability in poor vacuum conditions which is permitted by a very low work function value. Graphene sources are also chemically inert, very bright, and very thin at the edge [32].

The objective lens

The objective lens is the most important lens in the electron microscope which creates the first magnified image of the sample. Its optical qualities (aberrations) determine the final image resolution. As other lenses, the objective lens is an electromagnetic lens that creates a strong magnetic field that permits to bend the electron beam passing through it as glass lenses make it for photonic beams. This lens is made up of a copper coil in the center of which is located a cylindrical yoke of soft magnetic material, the pole piece. The converging effect can be tuned by controlling the electrical current sent through the copper coils. Current changes modify the strength on the magnetic field in the pole piece gap and change the focusing of the lens. Different types of objective lenses exist and the one we use in the off-axis holography experiment is an immersion lens in which the sample is placed within a twin lens system. In this type of lenses, the small pole-piece gap allows to create a homogenous and high magnetic field and therefore to reach a high spatial resolution of the whole microscope. The drawback is that this small gap it reduces the possible sample holder tilt angles [23] and makes more difficult to perform in-situ and tomography experiments.

The detectors:

A 2D TEM image is a projection along the z axis of the interaction the electron beam experienced with the 3D real object, at the detector level. Digital cameras are detectors consisting in an array of electron sensitive pixels that count incident electrons. There are three main classes of camera detectors: classic charge coupled devices (CCD), complementary metal-oxide-semiconductor (CMOS) CCDs, and direct electron detector devices (DDD). One important parameter of these detectors is the pixel dwell time which is the time needed for a pixel to detect a new electron after having detected a first one. Others like the DQE and the MTF are explained below.

CCDs are the oldest digital cameras that appeared in the 1980s and have gradually replaced the photographic films in TEM [33]. CCD camera consists on scintillator which transforms the detected electrons into photons, coupled through fiber optic to the sensor [34] (figure 1.2a).

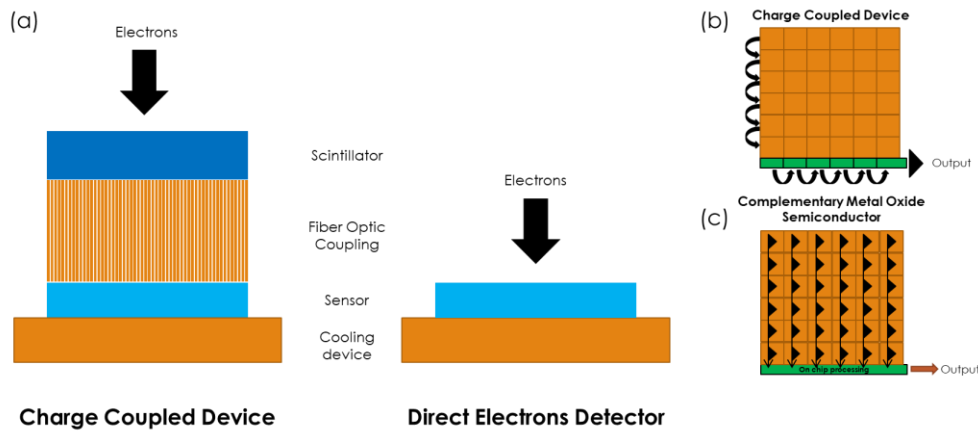


Figure 1.2 Different camera technologies based on (a) the electron pathway and (b) the sensor technology. (a) Comparison of the CCD camera equipped with a scintillator to convert electrons to photons to DDD that detects the electrons directly with its electron-resistant sensor. (b) Comparison of the classic CCD sensor technology to the more efficient and faster CMOS technology.

More recently, CMOS CCD cameras were developed (figure 1.2b). They have a similar structure as CCD cameras but differ at the charge to voltage conversion step, which is done pixel by pixel in CMOS and allows higher readout speeds [35]. A disadvantage of both the CCD and CMOS cameras is the errors induced by the electron to photon conversion. In other words, the so-called detective quantum efficiency (DQE) of a CCD is less than 1 which means that not all the electrons are converted into photons, the DQE being better on a CMOS camera than a classic CCD one [35].

Recently to overpass this issue, direct electron detectors (DDD cameras) started hitting the market. The difference with the previously described cameras is that the DDD sensor is sufficiently thinned for electrons to pass through without damaging it. It can thus be directly exposed to the electron beam and can count all the incident electrons. In addition, because the scintillator and optical fibers are no longer needed (figure 1.2a), the associated noise disappears, and images are of higher signal to noise ratio (SNR). DDDs are equipped with a CMOS type sensor with fast sampling rates. Being way faster than CCD cameras, DDDs allow to record movies (multiple-frames images), which allow to correct specimen drift, contrary to single frame images [36]. Compared to CCDs, DDDs possess a high DQE as well as a higher Modulation Transfer Function (MTF). The MTF is the detector's sampling ability as a function of the spatial frequencies [37,38]. This makes them much more performant for low dose experiments.

Another characteristic of the DDD cameras is the availability of two main electron detection modes: the linear and the counting modes. The linear mode consists on integrating the electron detection events during the exposure time at a specific frame rate. The counting mode on the other hand detects individual electron events at specific pixels and digitalizes each event separately. For low dose experiments, like what mainly done in this study, the counting mode offers better contrast and better SNR [39,40].

1.3.2 The I2TEM microscope

In this thesis, the main off-axis holography experiments were performed at the CEMES laboratory, on the I2TEM (*Interferometry and In-situ Transmission Electron Microscope*) which is schematized in figure 1.3. This microscope based on a HF3300 column was built by

Hitachi High Technology (HHT) in a close collaboration with the CEMES group. It is mainly used for in-situ experiments and off-axis holography.

The electrons are emitted by a cold FEG and is operated at 300 kV acceleration voltage. This microscope is equipped with a triple condenser lenses system named C1, C2 and C3. The currents in C2 and C3 are set to align the beam and the electron dose is modified by spreading or concentrating the beam using the C1 current. The objective lens is a high-resolution twin lens with a pole piece gap of 11 mm. A spherical aberration corrector (CEOS) located below the objective corrects for its aberrations [41]. The imaging lenses are composed by three intermediate lenses (I1, I2, I3) and two projector lenses (P1, P2). These two lenses groups contribute to the image magnification before the camera (or the fluorescent screen).

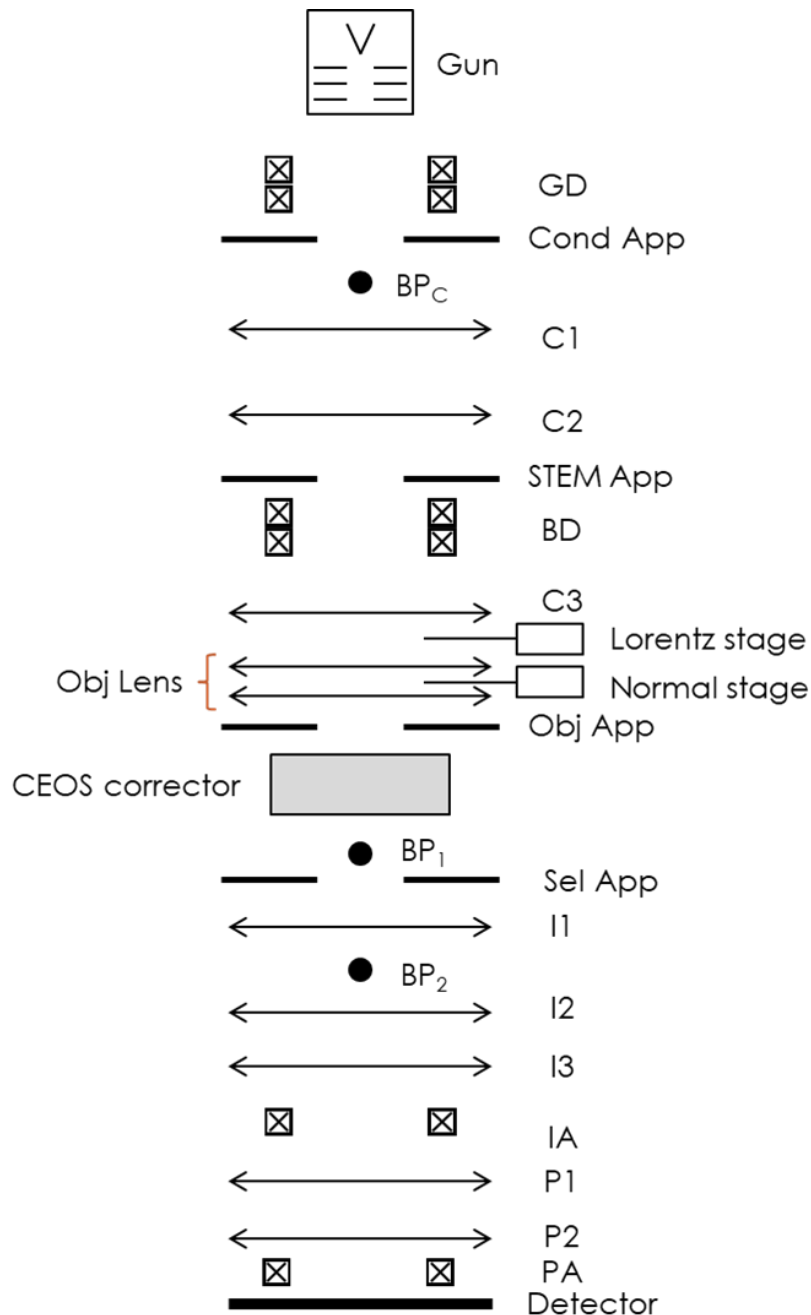


Figure 1.3 Schematic representation of the I2TEM microscope. GD: Gun deflectors, C: Condenser lens, BP: Biprism, BD: Beam Deflectors, App: Aperture, Sel App: Selective aperture, I: Intermediate lens, P: Projector lens, IA: Intermediate Alignment, PA: Projector Alignments.

The initial experiments were conducted on a 4096 x 4096 pixels One View CMOS camera. The later experiments were conducted on a 5760 x 4092 pixels K3 DDD camera acquired at the end of 2022.

In addition to those main components, the I2TEM contains 3 biprisms, two of which, BP1 and BP2 are used for off-axis electron holography (figure 1.3). These biprisms will be discussed in further details in part 2.6.1.

The I2TEM, as shown in figure 1.3, possess two goniometers to insert sample stages at different levels: the so-called “Lorentz goniometer” located above the objective lens allows to obtain large view images of samples studied in a field free environment while the “normal goniometer” allow high resolution imaging of samples placed within the pole piece of the objective lens.

This configuration enables the following 3 different imaging modes:

1. **Normal mode:** the sample is set inside the objective lens as shown in figure 1.3. This mode takes full advantage of the objective lens with a current around 12 A and permits to reach the best resolution of the TEM (0.05 nm).
2. **Lorentz mode:** this mode requires inserting the sample above the objective lens as shown in figure 1.3. The sample is then outside the magnetic field of the objective lens. In this mode, the focus is obtained by modifying the objective lens current used here as “Lorentz lens”. Lorentz mode is used for two purposes:
 - It allows studying magnetic samples in a field free environment and therefore without saturating them.
 - The field of view in this mode is much broader than what can be reached in low magnification mode when the objective lens current is lowered. It is essential for the study of samples of more than 100 nm in size.

The Lorentz mode was used for the off-axis holography and hybrid holography experiments in this thesis.

3. **TL11 mode:** the sample is inserted in the normal stage like in the normal mode, but the objective lens is turned off to set the sample in a field free environment. The focus is adjusted using the first transfer lens TL11 of the Cs corrector (figure 1.3). The TL11 lens is weaker than the objective lens therefore the spatial resolution of the TL11 mode is lower. *(The main advantage of the TL11 is that the objective lens can be used to apply small magnetic fields on samples to study in-situ magnetic domain motion and magnetic switching).*

1.3.3 The Talos Arctica microscope

The cryo-EM and cryo in-line experiments were conducted on a Talos Arctica from FEI at the CBI laboratory. This microscope is equipped with a FEG gun and operated at 200 kV. Most of the experiments were done using a 3840 x 3712 pixels K2 camera. The microscope was later equipped with a K3 direct electron camera. It is equipped with a sample autoloader that can accommodate up to 12 grids as well as a liquid nitrogen auto-filling system enabling fully automated acquisition over several days while at around -175°C. An additional advantage with this microscope is the piezoelectric stage, offering a high stability compared to a mechanical stage like on the I2TEM.

1.3.4 Image formation in TEM

The most important lens for the image formation is the objective lens (figure 1.4). Located below the sample in a conventional TEM, it focuses the electron beam that has interacted with the sample, in its back focal plane where a diffraction pattern of the sample is formed and creates a magnified image of the sample in its image plane [42]. The aberrations of the objective lens (mainly the spherical aberration, C_s) are the main parameters that degrade the resolution of the final TEM image. Most of the objective lens aberrations can be corrected using aberration correctors which are complex multipolar optical systems developed in the early 2000s'.

The imaging part of the electron microscope (intermediate and projector lenses) magnify the first image and propagate it down to the detector. Note that this imaging part can be set to transfer the back focal plane of the objective to obtain the diffraction pattern of the sample on the detector.

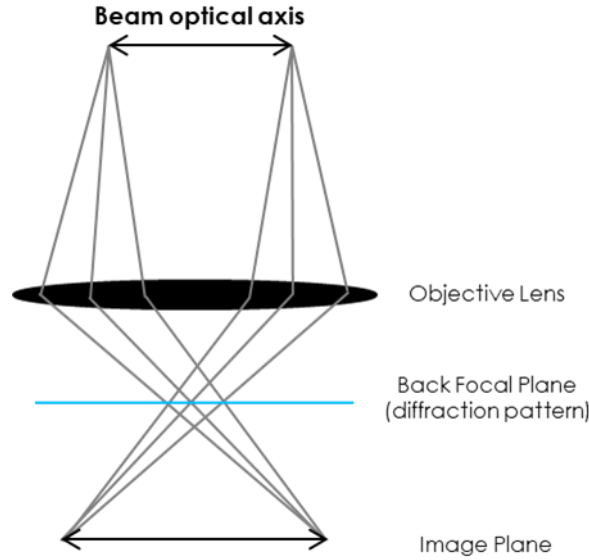


Figure 1.4 Ray diagram of the electron beam passing by the objective lens.

1.3.5 The wave description

Considering the incident electron beam as an electronic plane wave $\psi_0(\mathbf{r}) = e^{i\vec{k}\cdot\vec{r}}$ illuminating an object. This wave interacts with the sample and is modified in amplitude and phase. After interaction, the exit-wave can be expressed in real space \vec{r} (x, y, z) by the object electron wave equation [23]:

$$\psi_{obj}(\vec{r}) = a(\vec{r}) \times e^{i(\vec{k}\cdot\vec{r} + \varphi(\vec{r}))} \quad (1.4)$$

with a being the exit wave amplitude, and φ the exit wave phase shift induced by the interaction of the electron with the sample.

In the approximation where the electron beam is supposed to weakly interact with the object, which is the case for thin biological sample, the equation becomes:

$$\psi_{obj}(\vec{r}) = (1 + i\varphi(\vec{r})) \times e^{i\vec{k}\cdot\vec{r}}$$

In this weak phase approximation, the object only induces a small phase shift of the incident beam and multiple diffractions within the sample are excluded. The phase shift only depends on two parameters, the sample thickness z and the atomic potential [43].

The phase shift of the electron beam at the exit plane (x,y) of the sample is given by:

$$\varphi(x, y) = C_E V_p(x, y) \quad (1.5)$$

with:

$$V_p(x, y) = \int V(x, y, z) dz \quad (1.6)$$

with C_E the interaction constant defined by the electron energy and V_p the projected atomic potential integrated along the z axis. The local potential $V(x, y, z)$ depends on the sample atomic composition and the atomic density.

The exit-wave is focused by the objective lens in its back focal plane where it creates a diffraction pattern. This diffraction pattern can be described by the mean of Fourier optics according to Abbe theory described by L. Reimer [44] being the Fourier Transform (FT) of the exit-wave [43]:

$$Diff_{ideal}(q) = FT(\psi_{obj}(r)) \quad (1.7)$$

The aberrations of the microscope are taken in consideration by multiplying the Fourier transform $FT(\psi_{obj}(r))$ by the wave transfer function “WTF”:

$$WTF = B(q) \times e^{-i\chi(q)} \quad (1.8)$$

where $B(q)$ representing the aperture diaphragm on the beam path and $\chi(q)$ describing the wave aberration due to the lenses. $\chi(q)$ depends mainly on the wavelength, the spherical aberration, and the defocus [23].

The diffraction pattern can then be expressed as:

$$Diff_{ideal}(q) = FT(\psi_{obj}(r)) \times WTF. \quad (1.9)$$

An image of this object-wave is formed in the image plane of the objective lens and is expressed as the inverse Fourier Transform (FT^{-1}) of the diffraction image (figure 1.4). The beam is then propagated by the intermediate and projectors lenses of the microscope down to the detector with possible few additional distortions that could easily be corrected.

The WTF function acts on the object wave both on its amplitude and phase. It can be expressed as the sum of the amplitude contrast transfer function (ACTF) and the phase contrast transfer function (PCTF) and is written as follow:

$$WTF = ACTF + i PCTF. \quad (1.10)$$

ACTF and PCTF represent the transmission of the amplitude information and the phase information respectively.

They can be expressed as function of $\chi(q)$ [45]:

$$PCTF = -\sin(\chi(q)) \quad (1.11)$$

$$ACTF = \cos(\chi(q)) \quad (1.12)$$

Depending of the values of $\sin(\chi)$ and $\cos(\chi)$ the transfer of the phase to the final image is enhanced or lowered (figure 1.5).

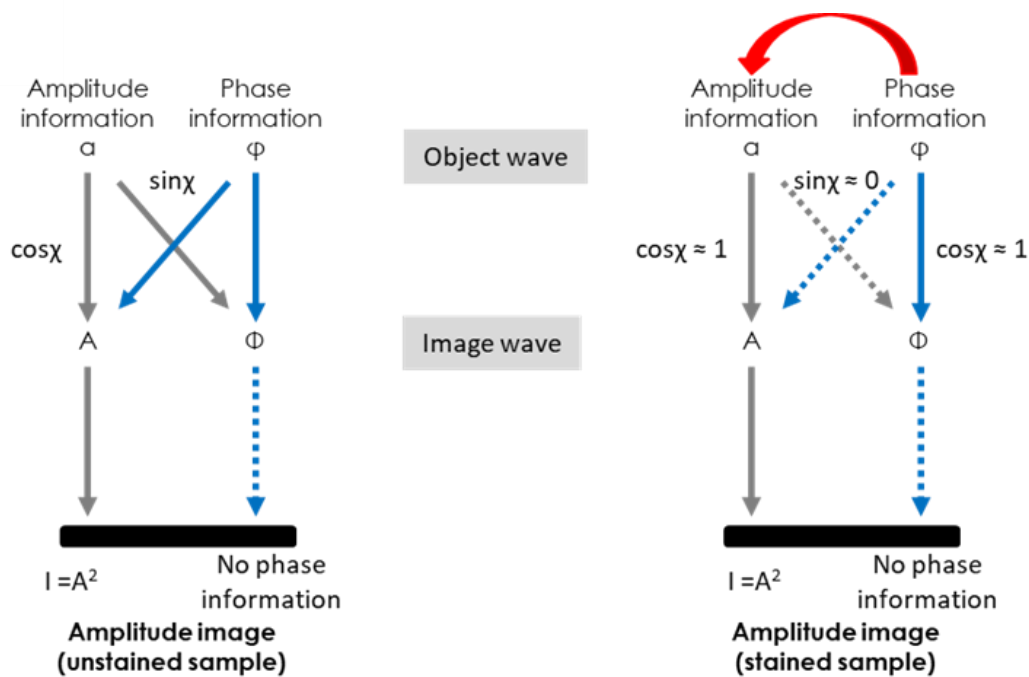


Figure 1.5 Amplitude and phase transfer information for unstained (left) and stained (right) samples, from the object wave to the image wave, and finally to the detector. Full lines mean that the information is transferred and the opposite is true for dashed lines.

In the case of an unstained low Z sample in conventional TEM (figure 1.5 left), the amplitude information “ a ” is transferred from the image wave to the object wave “ A ” with a slight loss of information. The same happens with the phase information as shown in the figure 1.5. Only the amplitude of the wave (its intensity) is detected. To obtain more phase contrast, we can defocus which will enhance the transfer of phase to amplitude ($\sin \chi \approx 1$) and diminish the transfer of amplitude ($\cos \chi \approx 0$). On the detector it will result in a contrast due to the phase shift [43].

Another option is to stain our sample (figure 1.5 right). The staining molecules will transfer the phase contrast to amplitude contrast by scattering the wave [43]. In this case, $\cos \chi \approx 1$ and $\sin \chi \approx 0$. No amplitude contrast is lost and the resulting amplitude is greatly enhanced. Defocusing on top of staining enable more phase transfer giving a higher resolution [46].

Phase plates

An alternative to enhance the phase contrast by defocusing is the use of phase plates (PP) to create an additional phase shift to the electron beam that pass through the sample. In this mode, the sample is imaged in-focus. PPs give better contrast than defocusing but limits the resolution to $\sim 3 \text{ \AA}$ due to spherical aberrations [47]. To put it simply, PPs convert phase contrast to amplitude contrast [48]. They are divided into four groups: thin film phase plates, like the Zernike phase plate (ZPP), electrostatic phase plates like the Börsch PP, beam-induced phase plates like the HFPP, and other concepts [49]. However, many problems limit the use of PPs like a short lifespan, fringe artifacts, the need for manual alignment, and electrostatic charging. Those problems were solved by the Volta phase plate (VPP), successor of the ZPP, consisting on a $\sim 10 \text{ nm}$ thin continuous amorphous carbon constantly heated at around 200°C to prevent charging. However, the phase shift increases during the experiment due to the constant electron beam interaction with the same carbon area of the PP [47]. This requires

changing the illuminated area of the phase plate every ~ 25 images. The highest resolution achieved in SPA using a VPP is 3.2 \AA on hemoglobin [50].

Another promising phase plate design is the laser phase plate (LPP), consisting on a continuous-wave laser beam [51]. This PP allows a very long lifetime without charging. It is currently under development and has not been yet commercialized. Other techniques are also present but not yet tested with electron like the diffractive phase plates [48].

Alternatively, image contrast may also be improved by recovering the phase-shift of the exit wave. This can be done by electron holography that permits to collect both the amplitude and the phase of the exit wave. This will be discussed in greater details in the next chapters.



CHAPTER 2: ELECTRON HOLOGRAPHY: A SOLUTION FOR THE OBSERVATION OF BIOLOGICAL SPECIMENS ?

2.1 THE STRUCTURE OF BIOLOGICAL MACROMOLECULES

While cell biology studies cells and their organelles from the nanometric to micrometric scale, structural biology aims to resolve the structure of macromolecules at high-resolution. Bridging these two scales of observation is one of the major challenges in modern biology and electron microscopy can accommodate these two scales. While initially reserved to X-ray crystallography and nuclear magnetic resonance (NMR), high-resolution studies are now possible by cryo-electron microscopy (cryo-EM). Pioneers of these techniques, namely Jacques Dubochet, Joachim Franck and Richard Henderson, were awarded the Nobel prize in chemistry in 2017 [52].

Electron microscopy enabled the first direct observation of the samples unlike the other two techniques which deliver either a diffraction pattern or a spectroscopy profile that need to be analyzed. Observing biological specimens under the electron microscope has unraveled the intracellular organization at the nanometer scale, revealed the structure of viruses and brought a direct way to look at molecular interactions. With cryo-EM, it is now possible to solve the structure of macromolecules at maximum resolutions that can reach up to 1.4 Å.

Large polymer biological macromolecules include nucleic acids (DNA, RNA) and proteins. The structure of RNA and DNA presents similarities. They are made of a chain of nucleotides formed by a phosphate, a sugar and a base that is specific for each kind of nucleotide [53]. RNA differs from DNA by the presence of an additional hydroxyl group on the sugar and one of the four possible bases. Nucleotides are linked to each other through the binding of the phosphate group of one nucleotide to the 3'-OH group in the sugar of the adjacent one. The end of the chain with a free phosphate is called the 5' end, while the other end with a sugar molecule is called the 3' end. DNA and RNA can be simple or double stranded and adopt an helicoidal fold [54]. The whole molecule can form intricate 3D structures through both intramolecular interaction and intermolecular association with other nucleic acid chains or proteins.

Proteins on the other side are composed of a succession of amino acids. An amino acid is a molecule with a conserved core and a variable radical "R", also called side chain, as shown in the top left of figure 2.1a. The central carbon is called the carbon alpha. There are

20 different amino acids, in other terms 20 different side chains [55]. A protein is defined by its sequence, i.e. the ordered list of amino-acids in the peptide chain. This sequence is called the primary structure of the protein (figure 2.1a). Along this chain, groups of amino acids can form specific folds, namely alpha-helices or beta-strands, which define secondary structures. The 3D structure of the whole molecule is called the tertiary structure (figure 2.1a). Each part of the complete sequence will have a specific 3D structure with different degrees of mobility. Some proteins assemble into multimers, which defines the quaternary structure. For example, the protein in figure 2.1a forms a dimer. Some cell components like ribosomes result from the assembly of proteins and RNAs (see chapter 5).

An example of protein structure at high resolution is shown in figure 2.1b with the apoferritin (PDB: 7A6A). It was solved by cryo-EM and single particle analysis at 1.25 Å resolution [56]. This protein is characterized by an octahedral symmetry. Once the electron density map is obtained (figure 2.1b), the primary sequence of the protein can be fitted into the map. The fitted sequence is shown in figure 2.1c with its secondary structures, in this case a large number of alpha-helices. An in-depth look into the protein enables to see its sequence with the atomic placements. The higher the resolution of the map, the more accurate the fit with the molecular model. This allows to visualize for example the molecular interactions like the hydrogen bonds in the cyan dotted lines in figure 2.1d between the atoms of the proteins, or with the water molecules (red spheres). It also shows the positioning of the side chains relative to each other or to the protein backbone (figure 2.1e).

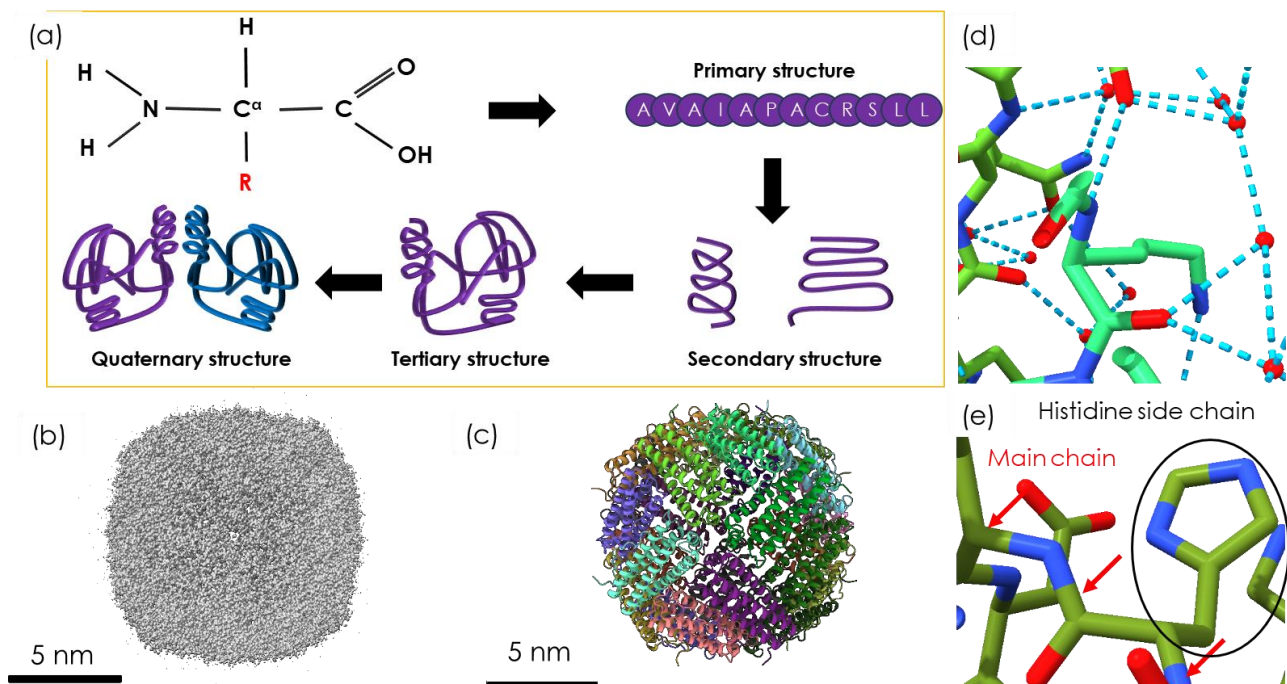


Figure 2.1 (a) Single amino acid molecule followed by the primary (sequence), secondary (3D domains), tertiary (sequence of 3D features) and quaternary (combination of many tertiary structures) structures. (b) Atomic resolution electron density map of the apoferritin (pdb: 7A6A). (c) Protein sequence after fitting in the map shown in (b). The tertiary structure is shown. (d) A zoom into the apoferritin sequence (c) showing the hydrogen links inside the structure and also with water molecules (red spheres). In the molecule represents oxygen, blue nitrogen and green carbon. (e) An example from the structure in (c) showing a histidine side chain (black circle) and the main sequence of the protein (red arrows).

2.1.1 A brief description of the T4, T5 and T7 bacteriophages

In the work presented in this manuscript, we used bacteriophages as our model samples. Bacteriophages, or phages for short, are viruses that infect bacteria. Most have double-stranded DNAs and operate by injecting their genetic material (DNA or RNA) inside the bacteria. They are the most represented entity on earth with an estimated 10^{31} bacteriophages on the planet [57]. In medicine, an increasing interest is developing for using the bacteriophages to cure bacteria-resistant infections for humans with many successful cases already [58–60].

The T4 bacteriophage belongs to the *Myoviridae* family and infects *Escherichia coli*. It consists of an 80 by 100 nm icosahedral head, called capsid, containing double-stranded DNA and formed by 155 hexameric units called capsomers, linked to a 140 nm contractile rigid tail on which long fibers are attached [61]. The tail shows periodic lines when observed in 2D. These lines correspond to proteins arranged along an helicoidal path around the tail axis with 4 nm between each ‘ring’ as well as a 17.2° rotation of the protein ring between two of them [62]. Opposite to the head on the tail is the baseplate. The T4 tail is non-flexible, but it contracts to eject DNA during infection [63]. This is visible on the negative stained preparation shown in figure 2.2a and b.

The T5 phage has a similar overall structure, but belongs to the *Siphoviridae* family. Its icosahedral capsid is made of 120 hexamers and 11 pentamers and is linked to a 160 nm tail. Unlike in T4, this tail is flexible and non-contractile [64]. Images of T5 phages before and after DNA injection (figure 2.2c and d) show the modification of the internal structure of the tail after the expulsion of the tape protein (TMP) that is usually filling the tail [65]. The T4 and T5 virions in the figure 2.2 were stained with the same solution of uranium acetate. Because of the charge differences due to the different protein composition of the capsids, T4 is negatively stained (darker surrounding), while T5 is positively stained (lighter surrounding). Lastly, the T7 bacteriophage (results not shown) belongs yet to another family, the *Podoviridae*. Its icosahedral capsid is composed of 415 copies of a unique protein, gp10 [66]. It is linked to a 23 nm-long tail, which is too short to perforate a bacteria membrane. Nevertheless, it forms a perforating tube by polymerizing proteins contained in the capsid [67].

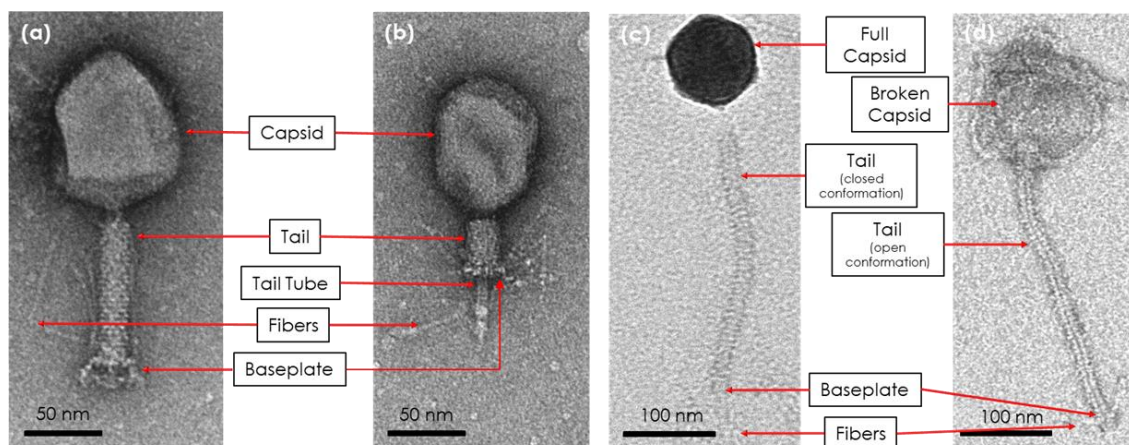


Figure 2.2 (a) Negatively stained T4 bacteriophage in its normal configuration. (b) Negatively stained T4 in its contracted (post-DNA injection) state where the tail tube become visible. (c) Positively stained T5 in its normal state. (d) Stained broken T5 bacteriophage showing the post-DNA injection conformation of the tail.

2.1.2 The T4 bacteriophage tail

In our experiments, we aim at resolving the T4 bacteriophage tail (figure 2.3a) and the resolution indicators we are looking at.

As discussed in 2.1.1, the T4 phage, depicted in figure 2.3a, is formed by a 100 nm × 85 nm capsid, also called the capsid, and a 110 nm long and 20 nm in diameter tail sheath ending with the feet or baseplate. Inside the tail sheath is a smaller tube called the tail tube. It serves as a channel for DNA injection inside the bacterial host [68]. Not shown in figure 2.3a are the tail fibers that help the phage to recognize the host bacteria [63]. The tail sheath is composed of repeats of a hexamer of the gp18 protein [69]. The surface electrostatic potential is represented in figure 2.3b and c. Each gp18 protein contains a negatively charged surface (red) as well as a slightly positively charged surface (blue). The lumen of the tail tube on the other hand is highly negatively charged, which helps ejecting the DNA by repulsing the latter negative charges [68]. We considered the 4 nm periodic pattern formed by the gp18 rings on the tail as a good target for the resolution of our holography experiments. In addition, the 17.2° rotation of each ring creates helices that we also aimed to evidence. Last, we sought to image these rings at room temperature, despite the risk of electron beam damage on unstained samples with the prospect of visualizing more details in cryogenic conditions.

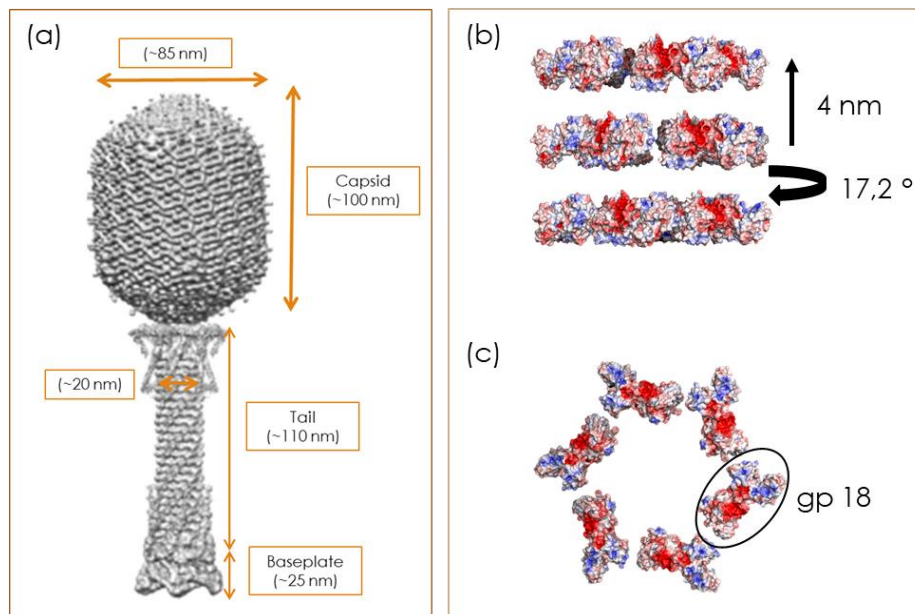


Figure 2.3 (a) 3D structure of the T4 bacteriophage obtained by cryo-EM, from Leiman et al. [69] (b) Stack of three hexamers of the gp18 protein that compose the tail sheath. (b) and (c) show the surface potential, computed on chimeraX, of the hexamer. Blue and red areas are respectively positively and negatively charged.

2.2 SOLVING THE STRUCTURE OF MACROMOLECULES

Solving the structures of small biological molecules constituted a long and challenging journey for the biologists. Nowadays, three main techniques made their mark in the study of macromolecules: X-ray crystallography, NMR and cryo-EM.

2.2.1 X-ray crystallography

In 1912, Max von Laue and Paul Ewald conducted some experiments to prove the existence of space lattices in crystals as well as proving the wave nature of light. This led to the birth of X-ray crystallography and X-ray spectroscopy [70]. In 1926, James Sumner obtained the first crystal of a protein, the jack bean urease, an enzyme [71]. Following this discovery, John Kendrew and Max Perutz solved the first two structures of crystallized biological molecules: myoglobin in 1958, a protein present in the muscle cells with a role in oxygen storage [72], and hemoglobin in 1960, the protein responsible for oxygen transport in red blood cells [73]. X-ray crystallography work by Rosalind Franklin brought also a major contribution to the discovery of the DNA double helix by James Watson and Francis Crick in 1953 [54]. Since then, X-ray crystallography has been the major technique in determining the 3D structure of biological macromolecules, giving birth to structural biology. Currently, X-ray crystallography has led to the highest number of published structures in the protein data bank (PDB) with more than 179 000 structures in total [october 2023 [74]].

X-rays were chosen for their wavelength between 0.1 and 10 nm, way smaller than that of visible light (380 to 700 nm) [75]. This smaller wavelength provides access to higher resolution information compared to light microscopy as discussed in part 1.1.1. X-ray crystallography consists in sending X-rays onto a crystal and recording the diffraction spots on a 2D detector, and repeating the process for different orientations of the crystal. This technique enables high resolution structures below 3 Å resolution, while being versatile and reliable. The current record of resolution we are aware of is 0.48 Å with a small protein named crambin acquired at the PETRA II synchrotron [76]. On the other hand, X-ray crystallography requires a highly concentrated sample and is a time-consuming technique [70]. Furthermore, X-ray crystallography is exclusive to crystallizable protein. This requires to find the perfect crystallization conditions, and to obtain diffracting crystals, assuming that the sample can be crystallized which is still challenging. An extension of X-ray crystallography named X-rays free electron laser (XFEL) uses powerful sources to image very small crystals, with the aim of imaging proteins without the need of crystallizing them [77].

2.2.2 Nuclear magnetic resonance

Thirty-three years after the development of X-ray crystallography, Felix Bloch and Edward Purcell discovered nuclear magnetic resonance (NMR) by the end of world war II [70]. NMR was first used in material sciences on the study of fluids in rocks and other applications, until W. C. Dickinson on one hand [78], and W. G. Proctor and F. C. Yu on the other [79], discovered independently the chemical shift effect. This signal detected by NMR is specific for each atom pair covalent bond. Jardetzky later introduced NMR to biology by studying amino acid or proteins and biological solution NMR [70]. One of the biggest developments in NMR that benefited the structural biology community was the discovery of the nuclear overhauser effect (NOE) in 1953 by A.W. Overhauser [80]. To put it simply, it is the signal detected due to an interaction between protons (nuclei) that are less than 6 Å far from each other in space [81]. Other effects are also used for 3D structure interpretation like the residual dipole coupling. NMR quickly became a strong technique in structural biology. To this day, more than 14000 structure deposited on the PDB have been resolved by NMR [november 2023 [74]]. Samples (solution or solid) are placed in a strong magnetic field that stimulates the nuclei of specific atoms by adding radio frequency pulses across a broad frequency range for each atom. This puts these atoms in an excited state and causes the

simulated atoms nuclei to resonate at specific frequencies till they return to their ground state [82]. The interesting part is that these resonances can be transmitted through covalent bonds, but also through space for short distances which will inform on the amino-acid sequence and the 3D structure respectively. However, only atoms with odd atomic numbers resonate [70]. This includes hydrogen ^1H , carbon ^{13}C , which provides a wealth of data in biological molecules. NMR has many advantages like giving precise quantitative analysis, needing minimal sample preparation, and being a highly automatable and reproducible technique. It is the only technique in structural biology that can easily detect hydrogen atoms. It is also possible to study dynamics phenomena up to the order of 10^{-12} seconds [83,84]. However, on top of not being sensitive to all the atoms, NMR remains limited to small proteins, although this is improving. It is currently possible to use NMR for proteins less than 100 kDa in weight, especially with the recent availability of high field super-conducting magnets in addition to more developed acquisition protocols [85]. One challenge was to suppress the water signal of the solution for biological NMR, which has been solved. One way is to exchange hydrogen atoms ^1H with deuterium ^2H , and the other being the suppression of the water signal by specific pulsed sequences such as the "Watergate" sequence [86].

2.2.3 Visualizing macromolecules and viruses by electron microscopy with negative staining

The Transmission Electron Microscopy (TEM) story started with Ernst Ruska designing and building the first electron microscope that was achieved in 1932 [70]. At that time, it was clear for most of the biologists that putting a sample under an electron beam within a TEM would destroy it. Unlike crystallography and NMR, TEM indeed requires high vacuum (see §1.1.3), which leads to the dehydration of biological samples. The sample is also exposed to irradiation damages by the incident electrons (see §1.1.2.b). Furthermore, biological specimens produce a low amplitude contrast due to the small atomic numbers of the atoms they are made of. That did not stop scientists like H. Ruska or E. Pfankush and G. A. Kausche who observed and published in 1940 two separate papers showing micrographs of unstained bacteriophages by TEM [87,88] (*the English version of them were published in 2011* [89,90]). To enhance contrast, researchers thought of using heavy metal solutions to decorate the samples. While initially used to directly contrast the sample (positive staining), especially ultrathin sections of resin embedded cells or tissues, contrasting solutions were then successfully used to stain isolated viruses and macromolecules by "negative staining". With this protocol, published in 1959 by Brenner and Horne [91], the heavy metal ions outline the sample rather than directly staining it. This method yields much contrasted images of the objects than positive staining when applied to small isolated objects, like macromolecular complexes or viruses. In addition to bringing contrast, staining molecules protects the sample from electron beam damages. However, and although negative staining can be used to reconstruct 3D structures at low resolution, the contrasting solutions are not inert and can interact with the sample. Some of them are acidic and other are neutral, some can be cationic and some anionic. The most commonly used contrasting agent is uranyl acetate, which has an acidic pH between 3 and 4 and is cationic [26]. Last but not least, stained samples are not protected from dehydration. Due to these limitations, as well as the size of the staining molecules, spatial resolution is limited to 10-20 Å when reconstructing by single particle analysis [92], which is insufficient for a high-resolution view of macromolecular structures. Nevertheless, negative staining is still today an essential and straightforward technique for visualizing isolated particles, but also checking purity, concentration and heterogeneity of a macromolecule sample.

2.2.4 Cryo-electron microscopy

Despite the resolution limitation of negative staining, De Rosier and Klug published the first 3D reconstruction of the tail of the T4 bacteriophage by single helical Fourier technique in 1966, proving that TEM was suitable to reconstruct biological samples structures [93]. Yet, dehydration of the samples, staining molecules sizes and interactions with the contrasting agent remained major obstacles to high-resolution studies. The first major step towards cryo-EM was the demonstration by Taylor and Glaeser that samples frozen in liquid nitrogen were protected from dehydration, and to some extent also protected from radiative damage produced by the electron beam [94]. However, this requires that the samples to be frozen in amorphous ice, both to preserve the morphology of the sample and to avoid diffraction of the electron beam by ice crystals. The technique was not easy to perform until the development of the plunge freezing technique by Dubochet and his colleagues using the “French guillotine”, which enabled easy sample vitrification in amorphous ice [95]. Dubochet compared the different states of ice while explaining how to obtain each state of ice, as summarized in the figure 2.4 (left). In plunge-freezing, amorphous ice is obtained by ultrafast cooling in liquid ethane. Heating of the frozen sample causes a state transition of the vitreous ice, in other terms its crystallization leading first to cubic ice, and then to hexagonal ice depending on the energy provided. Crystallization of vitrified ice is irreversible. Slow freezing of water yields hexagonal crystal ice. The right part of figure 2.4 shows the different states of ice with their corresponding diffraction patterns, as shown by Dubochet et al. [95]. In a cryo-EM experiment, the sample is maintained at -175 °C thanks to a specific holder equipped with a liquid nitrogen tank.

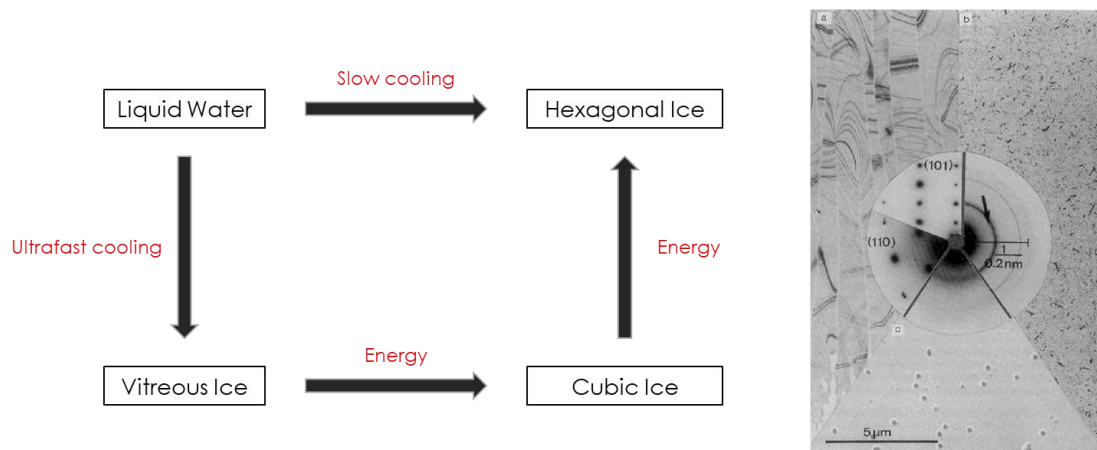


Figure 2.4 (Left) Figure showing the major ice states met in cryo-EM and the conditions to go from one to another. (Right) Electron micrographs of the different ice states with their diffraction patterns obtained from Dubochet et al. [95]. (a) is hexagonal ice, (b) is cubic ice and (c) is vitreous ice. Two diffraction patterns are shown for the hexagonal ice and correspond to two different atomic axes of observation.

The first structure of a protein solved at atomic resolution by cryo-EM was that of bacteriorhodopsin, but this was achieved by using electron diffraction [96]. Methods were developed based on tomography principles to reconstruct the 3D structure of macromolecules by direct imaging by cryo-EM. These methods, called single-particle analysis (SPA), are based on the recording of a very high number of images (10,000 to 1,000,000) of the considered macromolecule, ideally presenting along random orientations (see §2.3). Joachim Frank and his colleagues used for the first time single particle analysis method to determine the structure of the ribosome complex of the bacteria *Escherichia Coli* at 25 Å resolution [97]. It was not until 1997 that microscopists were able to go below the 10 Å resolution barrier. The first quasi-

atomic structure was obtained in 2010, at the start the “big boom” of cryo-EM, with a 3.5 Å resolution structure of the human adenovirus structure [98]. In the following years, cryo-EM witnessed a revolution with the direct electron detectors (or DDDs, for direct detection devices), which were a game changer with respect to the CCD cameras (see §1.1.3) along with different hardware improvements [99]. Due to the vulnerability of frozen biological samples to irradiation (see §1.1.2.a), it is mandatory to work in low-dose conditions, more specifically between 20 and 40 $e^-/\text{Å}^2$ for proteins [100], and up to $\sim 70 e^-/\text{Å}^2$ for more resistant specimens like bacteriophages. EM experiments at such low doses result in very low SNR images that is significantly improved by DDDs compared to CCD cameras. In addition, the improvement of stage stability and the introduction of low-temperature grid autoloading devices in 200-300 keV TEMs permitting multiple days acquisitions of data and enabling acquisition of a higher number of images and thus, much more particles, lead to a much better final resolution. On the software side, single particle analysis was boosted by programs for 3D reconstruction based on Bayesian statistics like Relion and cryoSPARC [101,102], and their implementation on GPUs. These programs as well as the single particle procedure will be discussed in part 2.3 and 7.1.2.

Following the cryo-EM revolution with the new hardware and software, the maximum attainable resolution went below 2 Å, and 3 to 5 Å resolution structures became very common. Yip et al. were able to determine in 2020 the structure of the apoferritin’s structure at 1.25 Å resolution using single particle analysis [56]. Nakane et al. also managed at the same time to achieve 1.22 Å resolution on the same protein [103]. The fact that apoferritin is symmetrical helps achieving such a high resolution as each symmetrical unit (4 units in this case) is treated as a single particle.

The structure of membrane proteins is more challenging to resolve as these proteins require stabilization in membrane-like environments. Some purification techniques have been developed based on the use of mild detergents molecules or amphipols, which mimic the phospholipids composing the cell membrane [104–106]. High-resolution structures of membrane proteins were solved, the best resolution being 1.7 Å with the $\beta 3$ -GABA_A receptor protein [107].

To date, more than 17 500 structures deposited on the PDB have been resolved by cryo-EM [october 2023 [74]]. Since 2016, more structures resolved by cryo-EM are being published each year than structures resolved by NMR (figure 2.5), with cryo-EM structures outnumbering NMR in the PDB. Cryo-EM may become the most used technique in structural biology in a few years after surpassing X-ray crystallography in the number of released structures.

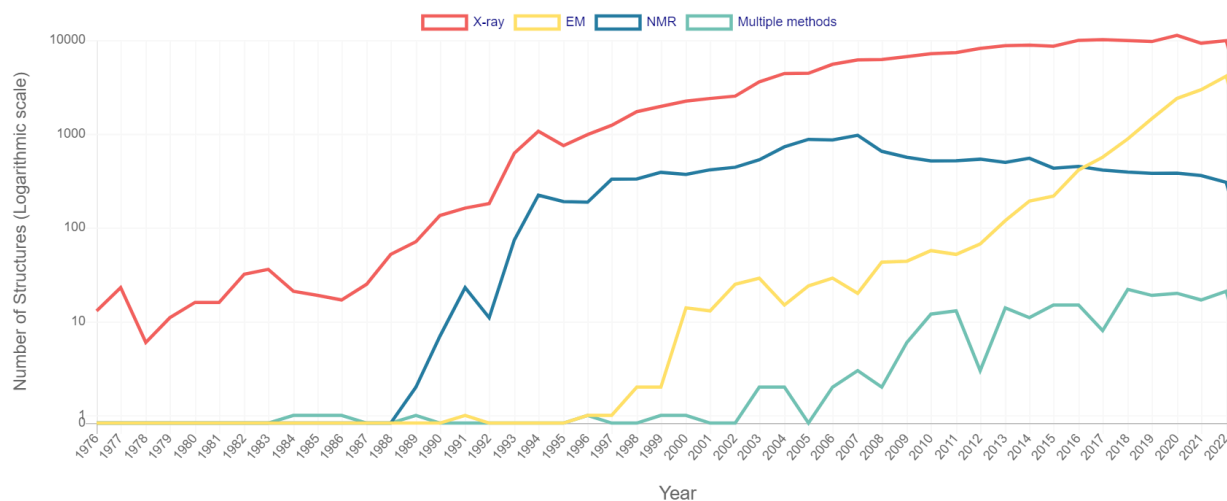


Figure 2.5 The number of total structure deposited on the PDB by method from 1976 to 2022 [74].

2.3 SINGLE PARTICLE ANALYSIS

Single particle analysis (SPA) takes advantage that a solution of macromolecules frozen in vitreous ice shows 2D projections along random orientations. These projections can then be back-projected to reconstruct the electron density map of the atoms composing the macromolecule in 3 dimensions. SPA is followed by fitting the known peptide or nucleotide chains forming the macromolecule into the map to reveal the position of the various atoms. Fitting these molecular chains into the cryo-EM density maps can be more or less precise depending on the resolution of the 3D map.

First, thousands of micrographs are obtained after a few hours, even days, of automated acquisitions. The particles are picked, first using a reference free auto-picking algorithm (Relion 3 and forward), by specifying the minimum and maximum diameters of our particles [108]. This is done instead of the long manual picking that was required in earlier versions of Relion. In our example in figure 2.6, done on the Talos Arctica at the CBI, we started with over one million pre-40S ribosomal particles. A first 2D classification is then run. This classification helps to remove any contamination or bad signal and to keep the good classes. Then, these 2D classes are used as ‘2D templates’ to run a new auto-picking. 2D classification is then performed again. This process can be iterated till the 2D classes are satisfactory. In our example in figure 2.6, we ended with 26 2D classes.

The next steps then consist in reconstructing the 3D volume, or even several volumes (3D classification), either by using the published structure of a similar macromolecule as a 3D reference or by generating a *de novo* 3D model. The obtained 3D classes can be individually refined and further analysis can be applied. One of the 3 classes we obtained is shown in figure 2.6 with an internal view (left) and an external view (right). Because of its high flexibility, the head (upper part) is not visible in the internal view leading to a poor resolution with loss of details inside the structure.

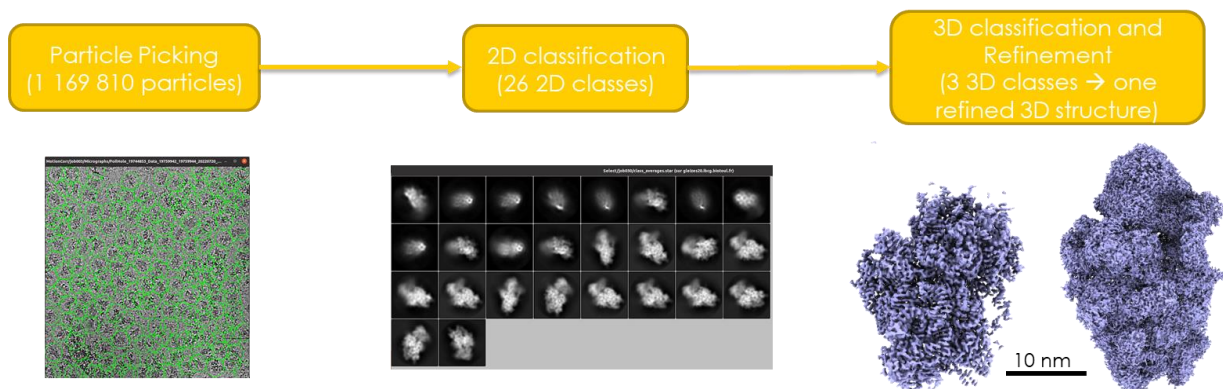


Figure 2.6 Main SPA steps on pre-40S ribosomal particles. The particle picking image shows a micrograph example where all the ‘particles’ are surrounded by green circles. The 2D classification shows all the obtained orientations with more particles oriented along the (x, y) plane of the micrograph. The 3D classification shows an example of a reconstructed volume with, on the left an inside view of the details (lower contour level) and on the right the view of the outside (higher contour level).

SPA takes advantage of the large number of particles that contribute to the 3D reconstruction, which leads to signal averaging and noise reduction. Particle images are classified according to their orientation and the relative projection angles of these views are determined to perform 3D reconstruction. Historically, it was first done using cross-correlation [109]. This approach was not practical as the orientations determination needed to

be done by eye. This challenge was overcome by new tools to determine automatically the orientations developed by Martin van Heel and Joachim Franck in the early eighties [110]. A major step forward was then accomplished with the development of software like Relion [111] and cryoSPARC [101], which regroup all the necessary algorithm for the whole SPA workflow and are based on Bayesian statistics. These statistics consist in optimizing a target function based on prior information and the experimental data with minimal help other than the input information (parameters; e.g. the number of classes needed in a 3D classification) [102]. Compared to older methods, Bayesian statistics excel in orientation assessment and class averaging.

Achieving high resolution depends on many factors including SNR, flexibility of the structure, randomness of the orientations, and symmetry of the structure. Sufficient SNR is achieved by the averaging of a very high number of particle images. This is classically done by extracting images of particles from multiple fields of view, and classifying them according to their orientation, forming a 2D class. The number of particle images required to achieve high resolution is independent of their size [112]. Hence, although bigger particles offer more contrast, more particles are needed to sample all orientations.

A problem with SPA is the few preferred orientations in which the particles lay on the grid or when some particles orientations are missing in the images. It is believed to happen at the air-water interface when proteins are adsorbed right after blotting the excess of liquid on the grid to form a very thin layer of the solution at the surface of the grid [113]. A known example is the influenza hemagglutinin trimer protein described by Y. Z. Tan et al., that exhibits a highly preferred orientation [114]. Several solutions exist to solve this issue but none is universal for all proteins. Some protein domains showing structural flexibility are often poorly resolved, since the various conformations observed in individual particles do not align in the average 3D reconstruction. The result in the 3D reconstruction is a decreased resolution of this part. Advanced classification methods, like ‘multibody refinement’ in Relion [115] or 3DVA in cryoSPARC [116] allow to distinguish distinct conformations by analyzing the domains flexibilities. Continuous flexibility represents a highly challenging problem, but recent software based on deep neural networks now tackle this problem and can help study these flexibilities, like cryoDRGN [117,118] and 3DFlex that is included in cryoSPARC [119].

The presence of symmetry in the particle favors the resolution as the particle can be divided into symmetrical units, giving the algorithm more particles to average. With rapid advancements in analysis software, which will likely continue to improve with AI, we believe cryo-EM will expand even further.

2.4 CRYOGENIC ELECTRON TOMOGRAPHY AND SUB-TOMOGRAM AVERAGING

SPA analysis enables high resolution 3D volume reconstruction, but is based on the averaging of multiple identical objects, which is possible for molecules or viruses. This is not suitable for big and unique samples like cell slices and samples that exhibit a preferable orientation. Along this line, SPA cannot be used to study organelles and viruses in the cellular context. To observe the 3D structure of unique objects by electron microscopy, it is possible to use electron tomography. This technique consists in acquiring TEM images of the sample at multiple tilt angles then aligning and back-projecting these 2D images to reconstruct the volume image. When performed at low temperature on a frozen sample, it is called cryo-electron tomography (Cryo-ET). Some alternatives to cryo-ET exist for samples exhibiting

preferred-orientations, like the use of deformed ultrathin/lacey grids for example [120], or by introducing a hydrophilic self-assembled monolayer on top of holey carbon grid [121].

For cryo-ET, thin sections ($<0.5 \mu\text{m}$) and thin part of cells may be plunge frozen in liquid ethane. Vitrification of thicker samples like cells may require high pressure-freezing, which must then be followed by cryo-sectioning (ultrathin sectioning at very low temperature) to produce 50-200 nm sections [122] or by cryo-FIB milling, which creates an ultrathin "lamella" out of a frozen cell [123]. High pressure freezing was first introduced by Moor and Riehle in 1968 [124]. It consists in freezing the sample under 2000 bars to lower the temperature of ice crystal nucleation and thereby favor formation of vitreous ice [125].

Even though cryo-ET provides lower resolution than SPA, one can reach up to 3 nm, which is enough to answer many biological questions [126]. Despite all the advantages of cryo-ET, there are still many problems to solve. Even though it can be applied on thick samples, it is still limited to samples up to $\sim 500 \text{ nm}$ thick which means that it is not possible to image full-size micro-organisms like bacteria and archaea [126]. Another problem is the requirement of acquiring each tilt image at lower dose compared to SPA, since the same area is imaged at multiple angles implying that the total dose must be fractionated by the number of images. This reduces the SNR [127] and may affect the final resolution. On top of the low dose per image, tilt angles are limited to $\sim 60^\circ$ due to increasing length of the electron path through the sample (figure 2.7) and the shadowing by the stage that occur at higher tilts [128]. This leads to incomplete information, also known as the missing wedge as some projections of the sample volume cannot be recorded. Finally, sample drift, mainly due to beam induced motion and stage instabilities may occur during image recording. This is easily corrected by aligning the frames of each image and then aligning the images taken at different tilts [127].

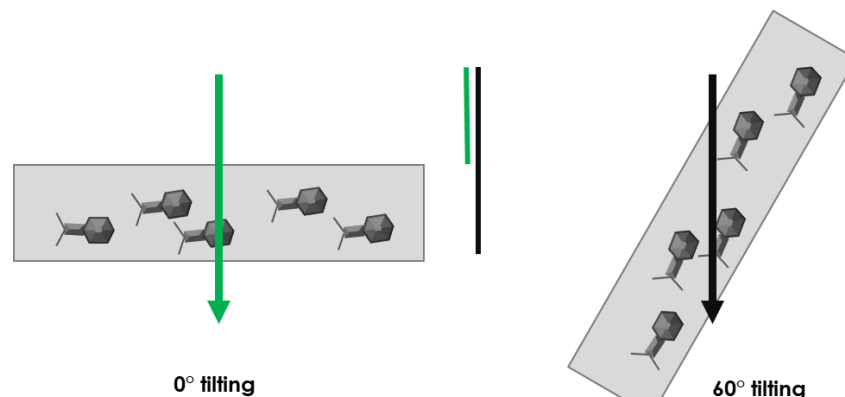


Figure 2.7 Illustration of the tilt effect on the electron perceived thickness. The more we tilt, the more matter does the electron goes through.

Furthermore, it is possible to reconstruct the 3D structures of small objects like ribosomes by averaging the 3D particles. It is called sub-tomogram averaging (STA), which is the equivalent of SPA for tomography. The difference with SPA is the fact that the averaged particles are 3D volumes that were reconstructed by analyzing the tomogram [127].

The general workflow of STA is represented in the figure 2.8a. This figure was made using images provided on www.blog.delmic.com [129]. First, the tomogram is acquired by tilting (1). Each particle is randomly oriented. All particles are reconstructed individually (2) to obtain the 3D particles. Then, each one is extracted before aligning the 3D volumes, called sub-tomograms (3). They are finally averaged to obtain the final 3D volume. Two examples are shown in figure 2.8b and c, obtained by Erdmann et al. [130]. The LSU is at 23.6 Å resolution (EMD-11048) while the SSU is at 25.03 Å resolution (EMD-11044).

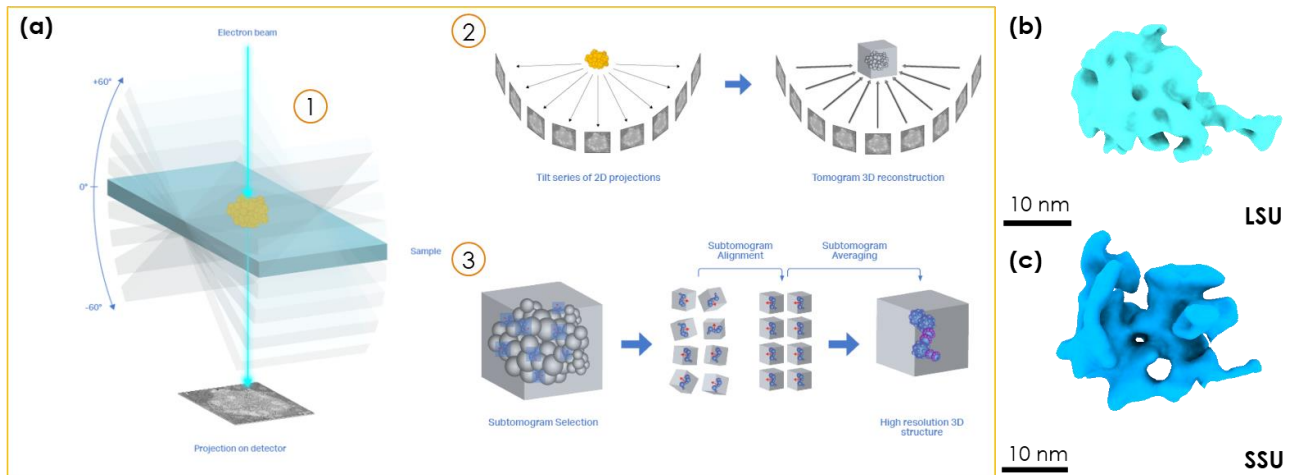


Figure 2.8 (a) Sub-tomogram averaging workflow [129]. (b) LSU sub-tomogram averaged structure [EMDB: EMD-11048]. (c) SSU sub-tomogram averaged structure [EMDB: EMD-11044].

Recently, structures below 1 nm were resolved by cryo-ET and STA [131–133]. Another way of achieving sub-nanometers resolutions is combining STA and SPA [134]. In addition to classic tomography, cryo-STEM tomography [135] as well as through-focal tilt series experiments [136] were demonstrated on thick specimens, to try to fill classic cryo-tomography struggles due to sample thickness in case of cells for examples. Those methods are not well developed yet and more work is needed.

STA has been used to study intracellular processes involving large complexes like ribosomes [130] or the nuclear pore complex [137]. An example from Erdmann et al. [130] is shown in figure 2.8. They studied the intracellular organization of the synthesis of the large (LSU) and small (SSU) ribosomal subunits in the nucleus of the unicellular algae *Chlamydomonas reinhardtii* cells [130].

The nucleolus, the part of the cell nucleus where these multimolecular complexes are assembled, is shown in figure 2.9a. Nascent pre-ribosomes in the nucleolus appear as particles (white arrow), and some are floating alone in the nucleoplasm (black arrows). Particles were identified and extracted from the tomographic reconstruction (tomogram) based on the comparison of their shape with the known structures of pre-ribosomes that are used as templates. Sub-tomogram averaging was then performed with the extracted particles (figure 2.9b). The two ribosomal particles thus obtained are shown in figure 2.9c. These data (1) reveal the structure of precursor ribosomal particles in this alga, and (2) show the peripheral distribution of LSU and SSU in the nucleolus (figure 2.9d), with distinct probability density function (PDF) at the nucleolar surface (figure 2.9e).

This analysis illustrates the capabilities of cryo-ET for identifying and localizing macromolecules inside the cell.

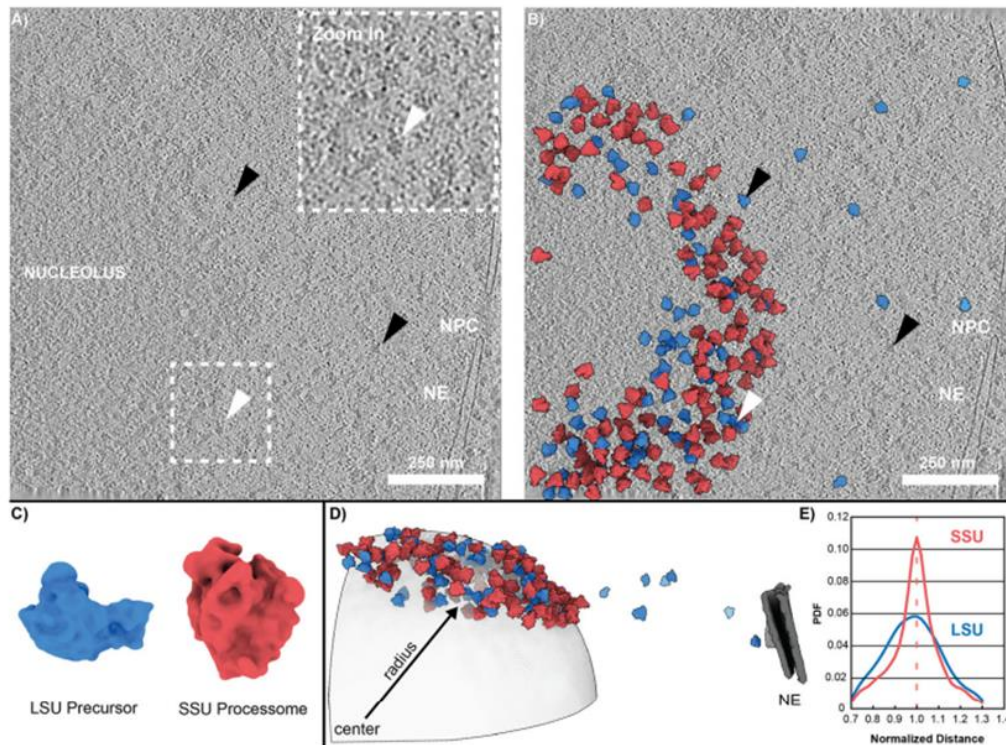


Figure 2.9 (a) Electron micrograph showing the different particles inside of the cytoplasm. Large particles can be identified inside the nucleolus (white arrows), whereas some can be seen floating in the nucleoplasm (black arrow). (b) Reference-free template matching LSU and SSU. (c) Individual LSU and SSU 3D particles. (d) 3D distribution of the LSU and SSU along a sphere. (e) Probability density function (PDF) distribution of the SSU and LSU particles. NPC: Nuclear Pore Complex; NE: Nuclear envelope.

2.5 THE PHASE PROBLEM

Having presented the current methods used to study biological macromolecules at high resolution, we now look at a major issue concerning the observation of such samples: the phase problem.

2.5.1 Amplitude objects vs phase objects

If we analyze the elastically scattered electron waves, we will come upon two cases. The first one is when the object is composed of high atomic number atoms. In this case, the object is an “amplitude object”. As shown in figure 2.10a, the amplitude object reduces the amplitude marked with the green line in the exit wave (below) compared to the incident wave (above). Additionally, the phase of the wave is also shifted by the object, which is shown by the blue arrow.

The second one is an object composed of low atomic number atoms. In contrast with the amplitude object, the phase object in figure 2.10b reduces very lightly the amplitude of the electron wave. In this case, the object is called a “phase object” [43]. Biological objects still produce a phase shift (below) compared to the incident wave (below), although phase-shifts are small. For example, the oxygen atom produces a phase shift around $2\pi/50$ rad, while an

elementary charge produces a phase shift of $2\pi/100$ rad [45]. The current microscopes allow, in theory, to measure small phase shifts, like those induced by biological objects.

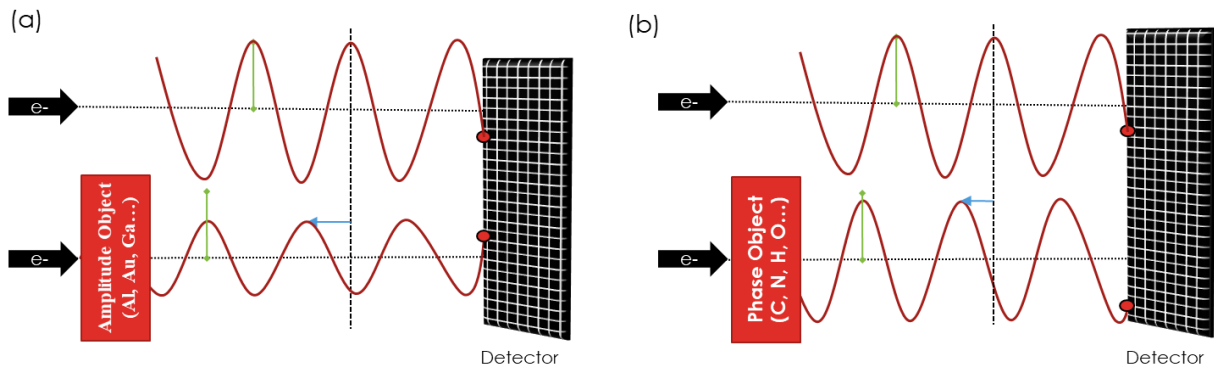


Figure 2.10 Comparison between a reference electron wave passing through vacuum and another one passing through an amplitude object (left) or through a phase object (right). The reference wave's amplitude is shown by the green line and the phase shift relative to the reference wave is shown with the blue arrow.

A concrete example is given in figure 2.11, with 10 nm gold beads in (a) and (c) and the T4 bacteriophage in (b) and (d). All the micrographs were acquired on a CCD camera mounted on a high contrast Jeol 1400 with a tungsten thermoionic filament operated at 80 kV. Both images in figures 2.11 c,d were acquired at focus. We observe that the gold beads are clearly and easily contrasted whereas the bacteriophage has a low SNR and contrast, in addition to the impossibility to see any structural detail. On higher acceleration voltage microscopes, the contrast is even lower, which is aggravated at low electron doses.

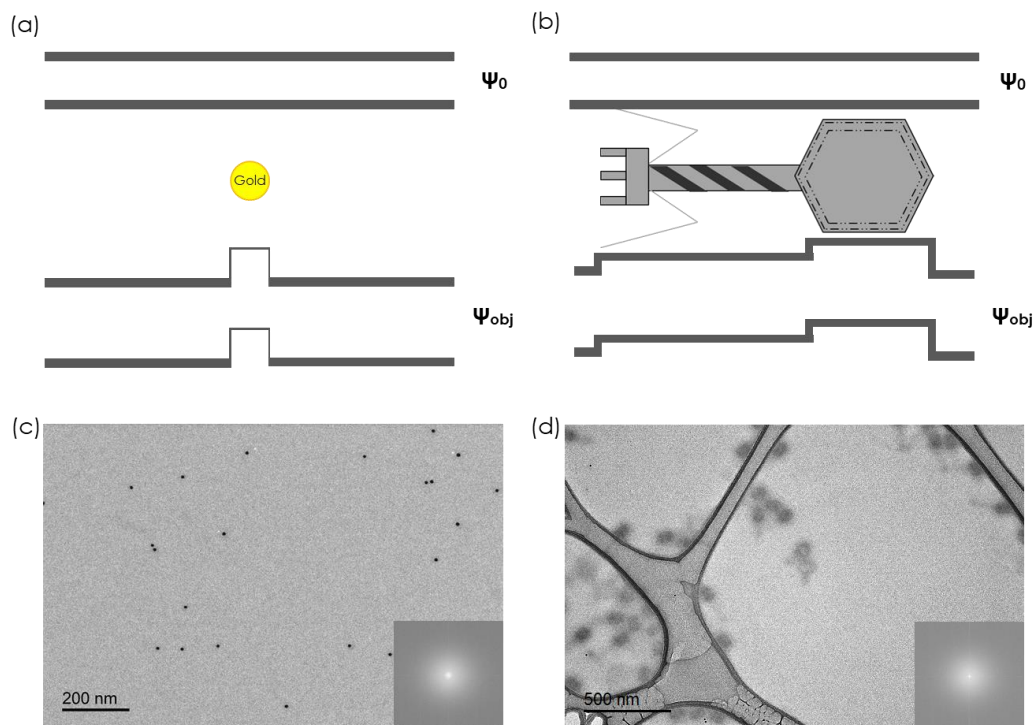


Figure 2.11 The modification of the electron beam wavefront when passing by (a) an amplitude object (gold bead) or (b) a phase object (bacteriophage). The line's thickness in (a) and (b) represents the amplitude and the shift of the line corresponds to the phase shift. (c) An electron micrograph of gold beads on carbon at focus as shown by the FFT (down right corner). (d) An electron micrograph of T4 bacteriophages on ultrathin carbon (Ted Pella) at focus as shown by the FFT (down right corner).

2.5.2 How X-ray crystallography solved the phase problem

X-ray crystallography is based on the X-rays diffusion within the sample. The peaks of electron density in the sample unit cell tells us about the 3D position of the atoms in it. This smallest repetitive motif in the periodic crystal, affect the phase shift of the X-rays but this information is lost when we only collect the intensity of the diffraction peaks [138].

One method to retrieve the phase shift of each diffracted beam is the use of calculations based on basic assumptions enabling the phase extraction, like the similarity with another protein of known structure. This method only works for very small molecules, and for proteins where the resolution of the data is at least 1.2 Å [139]. Molecular replacement is the most used phasing method. It consists in using a similar structure to obtain the phases from the known structure. However, the obtained model and the reference model must be at least 25% identical in sequence and adopt a similar tertiary structure [139]. Another well-known method is isomorphous replacement. This method is beneficial for big structures like proteins where the resolution of the diffraction patterns is usually limited to 2-3 Å [138]. It consists in putting the protein crystals in heavy-atoms solutions like CuSO₄ to replace some light atoms by heavy ones. This leads to a change in the intensities of the diffractions and allows the phase calculation. In addition to the previous two phasing methods, anomalous scattering is also used. It is based on wavelength dependent scattering of some atoms like sulfur which can be found in some amino acids [139]. A recent promising method is the use of high-performance deep learning programs like Alpha fold 2 [140] and RoseTTAFold [141] to predict the sequences of proteins and use these predictions similarly to molecular replacement [142]. A drawback is the fact that it only generates one model, given a specific sequence, therefore neglecting the sample heterogeneity [143].

The most used methods for biological samples, as well as their general principles are summarized in the following table:

| Phasing Method | Principle |
|-------------------------|--|
| Direct method | Calculations based on molecular assumptions |
| Molecular replacement | Availability of a structurally similar structure |
| Deep learning model | Modeling the 3D structure using deep learning |
| Isomorphous replacement | Replacing sample atoms with heavy atoms |
| Anomalous scattering | Detecting wavelength sensitive scatterings due to specific atoms |

For cryo-EM, a different approach was adopted with either the SPA or tomography which relied on multiple orientations of 2D images to reconstruct the whole 3D structure. In the following section, we present an electron microscopy phase retrieval technique, electron holography. As well as gaining contrast, our method enables the retrieval of many information regarding our sample charge, magnetic properties if any, and sample thickness among others.

2.6 USING ELECTRON HOLOGRAPHY TO DIRECTLY MEASURE THE PHASE OF THE EXIT WAVE

2.6.1 The history of electron holography

Electron holography was proposed in 1947 by Denis Gabor, a renowned scientist who participated in the development of electromagnetic lenses [144]. Electron microscopes were facing a big challenge due to lenses aberrations at the time which severely limited the achievable resolution [18]. Gabor's idea was to retrieve the full information of the amplitude and the phase of the electron waves condensing at the detector and to compensate for all optical aberrations. The first experimental holography in-line setup he developed consisted of a point source, an objective lens that converges the beam to the specimen, and a detector plane [145]. The beams having diffused by the sample interact with the direct beam creating interference fringes: the hologram. Gabor separated the imaging process into a two-part: the hologram formation and reconstruction step to reconstruct the image of the object [18]. The first few experiments were conducted using light, but light sources at the time were not coherent enough to conduct such experiments. The wave coherence, temporal and spatial describe respectively the correlation between waves at different moments in time and the correlation between waves at different points in space. Temporal coherence is dependent on the source energy spread while spatial coherence depends on the effective source size [146]. Less energy spread and a smaller effective source size means more coherence. Electron holography relies on electron waves interference. Therefore, high beam coherence is necessary to obtain interference fringes of high contrast.

Early electron holography experiments were conducted with electrons by T. Hibi in Japan who came up with the conclusion that the thermoionic electron sources did not provide enough coherent electron wave for electron holography [18]. In light optic, the first big improvement was the apparition of lasers, which provide highly coherent photon beams. A new holography setup was used, called "off-axis" [147] where the sample is not in the central axis of the beam, but shifted apart. The beam part going through the object (object beam) is separated from the reference beam unlike in-line in the initial Gabor's setup. In TEM the development of (cold) field electron guns ((c)FEG) providing coherent electron beams opened the path to electron holography which was mainly driven by A. Tonomura and his colleagues. Following many experiments, they succeeded in 1978 to obtain reproducible results using a FEG at 70 kV acceleration voltage [148]. Later, H. Lichte participated greatly in the development of electron holography [149]. From here onward, electron holography developed and thrived in the material sciences, but not much in biology.

2.6.2 Obtaining phase images by off-axis holography

Off-axis holography was firstly used in optical microscopy by dividing the laser beam into a reference and an object beam using beam splitters [150]. Its application in electron microscopy became possible after the development of a beam splitter for electron microscopes. It is the electrostatic biprism, invented by G. Mollenstedt and H. Duker in 1955 [151]. This biprism is a thin conducting filament that is electrostatically polarized and that bends the electrons that passes on each side of it and therefore make them overlap [148]. They

later succeeded in recording the first electron hologram using such a biprism [18]. Nowadays, electrostatic biprisms are made of a metal-coated glass wire with a diameter less than 1 μm [148].

The interference of two electron waves is similar to that of light. It produces interference fringes revealed in a TEM hologram as alternating dark and white fringes. This is shown in figure 2.12 where the two parts of the beam interfere to give rise to what is commonly called the “hologram” or interference pattern that could be recorded on a detector. Interferences occur when two coherent waves interact, thus filtering inelastically scattered electrons [152]. The position of the fringes at each point of the hologram depends on the relative phase of the two waves at these positions. It can be constructive (resulting in white fringes) or destructive (dark fringes). Considering one of the waves as reference wave of a constant phase, the hologram allows retrieving the amplitude and phase carried by the object-wave that has interacted with the sample. For this interference to happen, a specific setup and alignment is required. As already discussed, the electron wave has to be as coherent as possible and extracted from a coherent electron source.

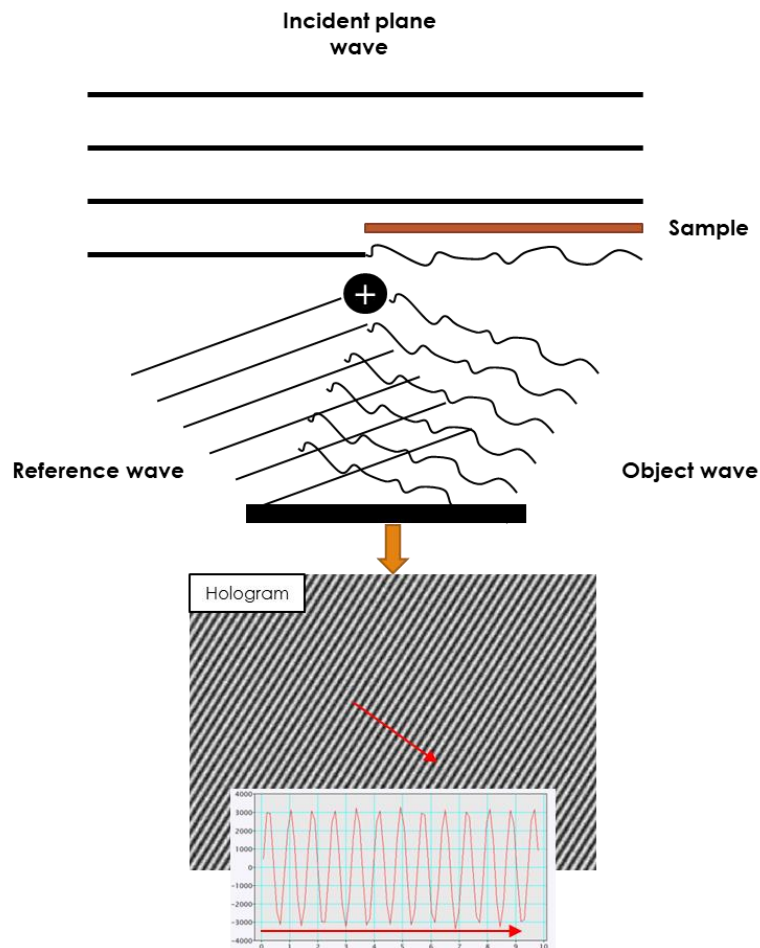


Figure 2.12 Representation of the biprism-induced interference between the unmodified reference beam and the object beam. The interference pattern is represented in the figure below showing alternating black and white fringes. A profile represented by the red arrow is shown below the image showing the wave nature of the interference fringes.

To enhance the coherence, the incident electron beam is shaped elliptically instead of round with the long axis of the elliptical beam perpendicular to the biprism wire. The sample is displaced off the central axis of the microscope as shown in figure 2.13b instead of being in

the center as shown in figure 2.13a. In these figures, the part of the beam that does not pass through the sample is colored in light blue, and the one passing through the sample in dark blue. The ideal situation is when the reference beam passes only through vacuum or, when there is no vacuum area available, close to the sample through the clean thin support nearby. The two parts of the beam then arrive to the biprism which deflects them perpendicularly to its axis. The interference pattern is then recorded at the detector position. After image acquisition, the hologram is analyzed to reconstruct both the so-called amplitude and phase images. To correct for phase changes induced by the projector lenses and phase variations due to the pixelated detectors a second “reference” hologram is recorded with two reference beams interfering in the vacuum [153].

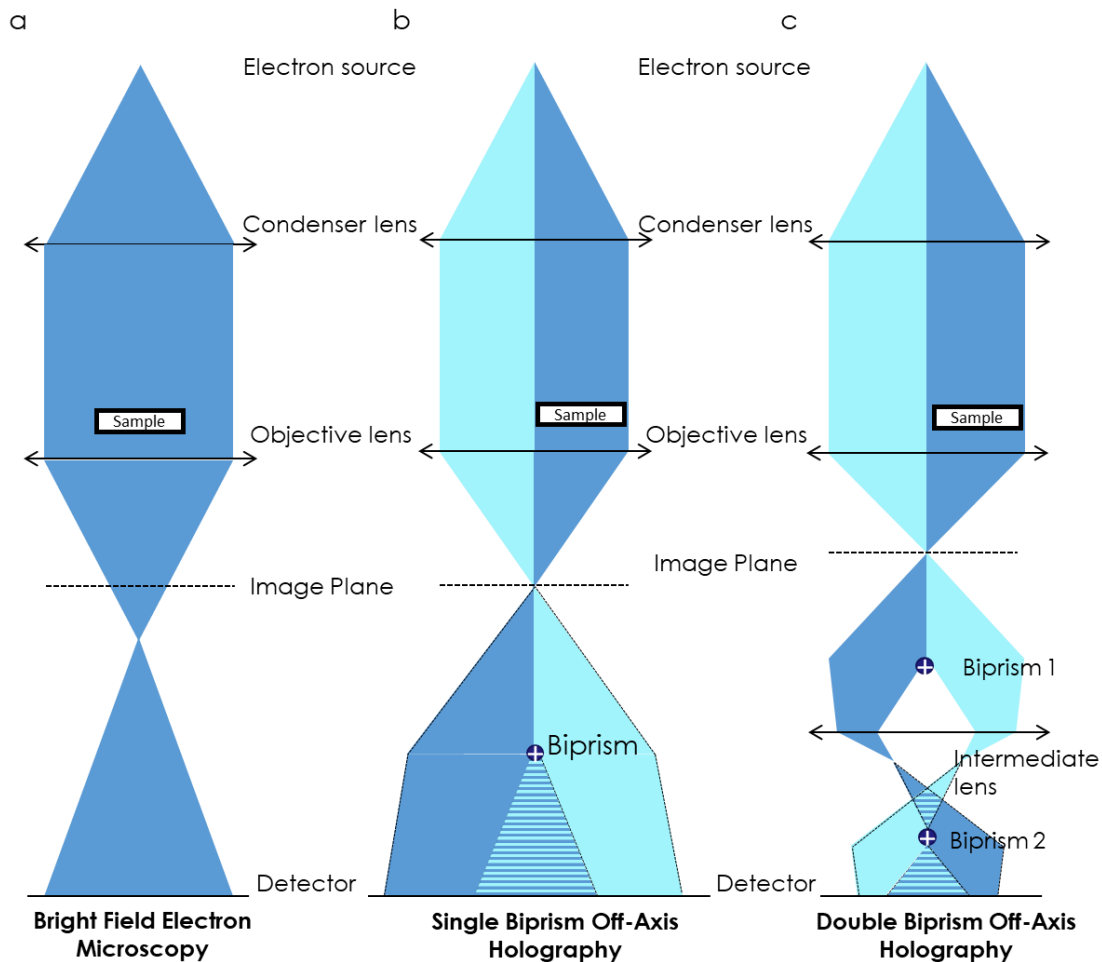


Figure 2.13 Electron beam path in a bright field setup in an electron microscope. (b) Electron beam path in a single biprism setup with the interference area below the biprism shown by the dark and light blue stripes. (c) Electron beam path in a double biprism setup. The final hologram is acquired at the detector plane.

In our studies on the I2TEM microscope, we use a more complex two biprisms setup shown in figure 2.13c. This system offers many advantages. First, we can control independently the fringe spacing and the width of interference also referred to as field of view (FOV) [154]. Second, the Fresnel fringes due to the biprism that is observed on the hologram borders are eliminated. In the two biprisms configuration, the first one, called biprism 1 (BP1) is located between the image plane of the objective lens and the first intermediate lens, I1 and the second one called biprism 2 (BP2) between the first, I1 and the second I2 intermediate lens. An important parameter is to set the I1 current so BP1 image is in the image plane on the detector.

The reconstruction processes of the amplitude and phase images from a hologram are shown in figure 2.14. First, we acquire the object hologram followed by the reference hologram taken in complete vacuum. We then perform a Fourier Transform (FT) of the object hologram. In this FT, we use a mask to select one of the two side band reflections that contain the phase and amplitude information. The size of the mask limits the resolution i.e. the bigger the mask, the better spatial resolution but also the higher the noise within the reconstructed images. The masked area in the FT is then inverse Fourier transformed to obtain a complex image from which the amplitude image and the phase image are mathematically calculated [155]. Figure 2.14 shows an amplitude and phase image of a 10 nm gold bead on a 3 nm thick carbon support.

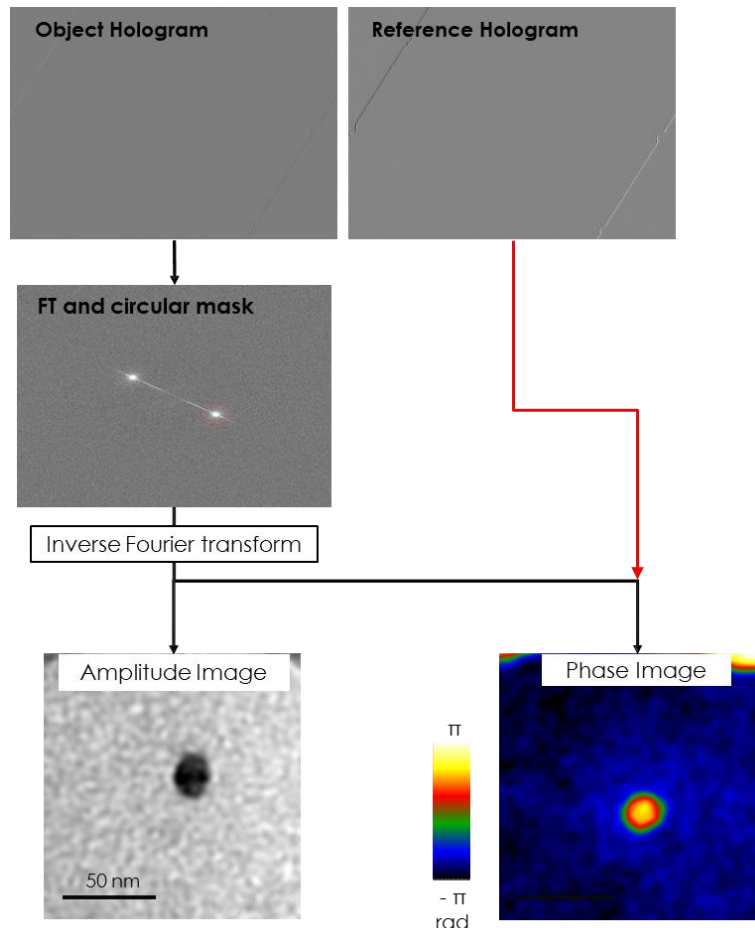


Figure 2.14 Off-axis hologram analysis workflow of a 10 nm gold bead using the qHolo code in Digital Micrograph. Two holograms are acquired, one of our objects and another of the vacuum. The reconstruction process consists first on applying a circular mask on one of the side bands of the FT of the object hologram, followed of an inverse FT and an extraction of the amplitude and phase images. Corrections are made on the phase image using the vacuum hologram.

Since the first hologram, off-axis holography has thrived in material science for example to measure individual charges [156], to study magnetic materials [157,158], to measure strain [159] and other applications. However, the application of electron holography, especially in off-axis to biological samples has been very limited. As the goal is to investigate unstained samples (see chapter 3 for a more detailed discussion), the biological samples to be studied will be very sensitive to the electron beam. The first attempt to use electron holography to study biological objects was carried out by Kawasaki et al. on the ferritin protein (apoferritin + iron) which is constituted of a protein shell containing a Fe_2O_3 core [43]. At that time, experiments were made at very low acceleration voltage of 45 kV for the ferritin. The main

advantage for using ferritin as test sample is the reasonable contrast obtained due to the iron core of high Z number. The phase shift for the protein shell was measured to be 0.26 rad. Since then, and including the ferritin paper, we count around 12 papers in which off-axis holography was used to study biological materials like T5 bacteriophages [43] or collagen fibers [152].

For many reasons, electron holography experiments were conducted in cryogenic conditions once. First, because the vitreous ice is very sensitive to the electron beam with bubbles forming at electron doses above $45 \text{ e}^-/\text{\AA}^2$ [43]. Second, the (ice) water molecules in which the object is embedded can contribute significantly to the measured total phase shift (charging of ice, ice thickness variation...) making it difficult to extract the phase shift only due to the studied object. Those are the challenges that we aim to overcome in our work in cryogenic conditions.

2.6.3 Focal series in-line holography as an alternative phase retrieval technique

Off-axis holography is one among other electron holography techniques. One is the low-energy electron point source (LEEPS) microscopy. It is similar to Gabor's in-line holography but without the use of lenses at all [160]. In biology, LEEPS was used to study the Tobacco Mosaic Virus (TMV) achieving 0.95 nm resolution [161]. This method is not limited by the lens aberrations (no lens!), but only by the electron beam damage effects on biological specimens. We are aware of twenty electron holography methods developed on electron microscopes that can be divided on two groups based on the sample location relative to the microscope axis [145]. The in-line group corresponds to all the interference methods where the sample is placed in the central axis of the microscope. Currently, a very popular acquisition scheme is the through focal method. This in-line technique has been used for years because it is easy to perform [145]. To acquire a focal-series, we start from the most under-focused (or over-focused) value and acquire a series of images from negative to positive (or inversely) by varying the defocus ending with the last image with the same value of defocus but with an opposite sign. The defocus step between images is chosen based on the expected resolution and the microscope parameters (magnification, contrast...). The defocuses can be a linear, quadratic or cubic sequence. The non-linear sequences are preferred by allowing a better sampling of the frequency spectrum [162]. In fact, the image contrast varies more significantly when at small defocuses whereas it varies less at higher ones. The values of the defocuses will follow this equation [162]:

$$|\Delta f_n| = \Delta f |(n - n_{ref})^p| \quad (2.1)$$

with Δf_n the defocus focus value for the n^{th} image of the focal serie; p the linearity of the focal series with a value of 1 for a linear progression of the defocus and superior to 1 for a non-linear progression (2 for quadratic and 3 for cubic series); n_{ref} is the number of the central (in-focus) image.

The beam path is shown in figure 2.15a with the sample in the center of the beam. The example shown in figure 2.15b consist of three images: $n^{\circ}0$ ($-1 \mu\text{m}$), $n^{\circ}1$ (focus), and $n^{\circ}2$ ($+1 \mu\text{m}$) from under-focused to over-focused respectively, $n_{ref} = 1$, and $\Delta f = 1 \mu\text{m}$.

During acquisition is best to maintain the same position between images by marking visible references on the image and limit the drift between images. This drift will be corrected (either manually or by image analysis methods like cross-correlation) when analyzing the focal series for the amplitude and phase image reconstruction.

The image reconstruction processes use different types of algorithms specific for focal series datasets. For the latter, many algorithms specific for focal series datasets exist. A few examples include the maximum a-posteriori developed by A. Kirkland [163], or custom scripts like pyFSrec [164]. In our case, we used the so-called Full-Resolution Wave Reconstruction (FRWR) iterative algorithm developed by Christoph Koch [165]. The advantage of this code is its ability to recover a large spectrum of frequencies. Low frequencies are collected more efficiently at high defocuses whereas high frequencies are collected at low defocuses [162]. The general workflow is presented in figure 2.15b. It follows the online tutorial provides by C. Koch [166].

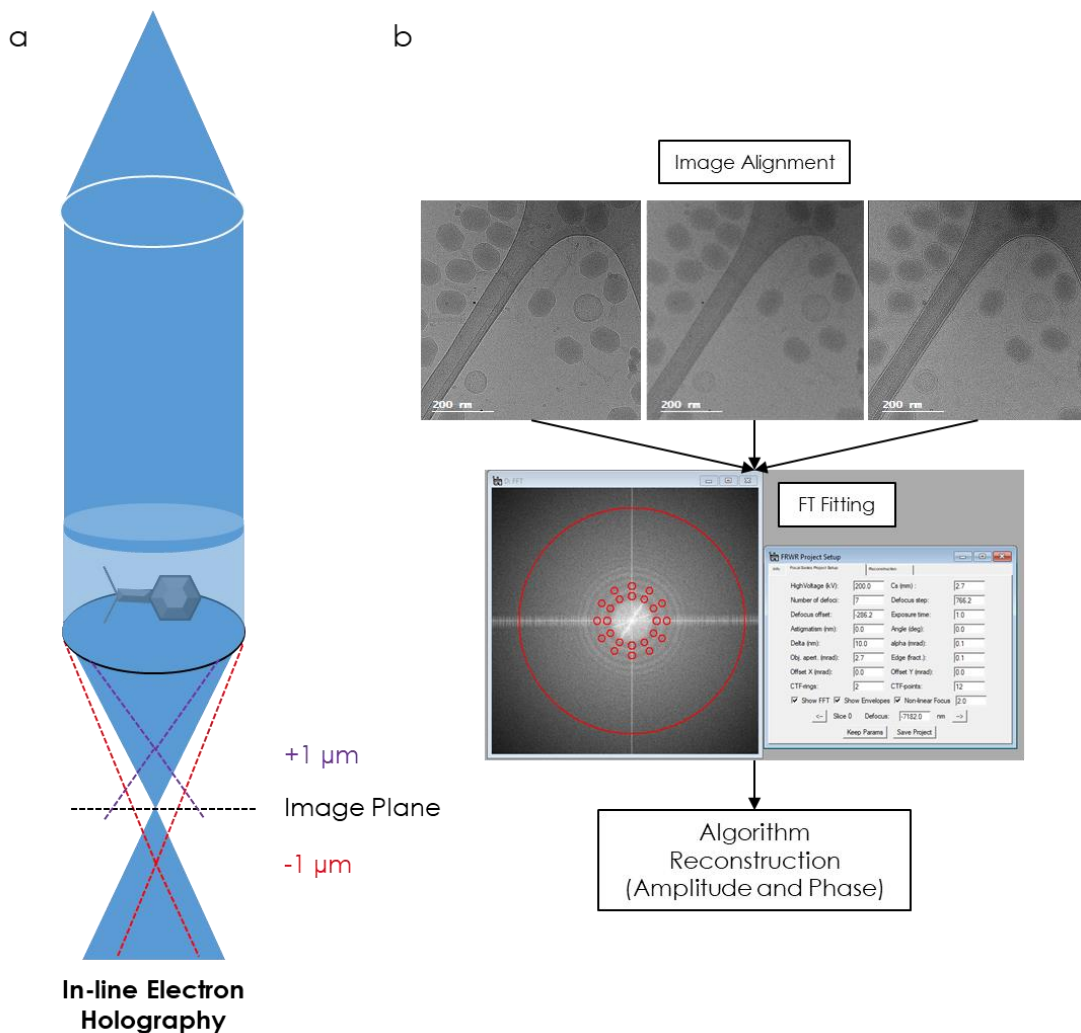


Figure 2.15 In-line holography focal series reconstruction workflow. (a) Electron beam path of a bacteriophage showing a simple example of a focal series consisting of three images at $-1 \mu\text{m}$ (red dashed lines), focus (full blue) and $+1 \mu\text{m}$ (violet dashed lines). (b) A simplified example showing 3 images (under-focused, focused and over-focused) in cryo-EM. After basic alignments, the parameters for the in-line algorithms are determined using the FFT of each image. Finally, the amplitude and phase images are extracted by an iterative algorithm, in our case FRWR.

Before the phase reconstruction process, the series is transformed into an image stack for pre-alignment. The purpose of this starting step is to make the reconstruction easier for the algorithm with the least drift between the stack frames. The “large” drifts between frames are corrected manually while the smaller one can be corrected automatically by image analysis. The next step consists on recalling the FRWR graphical user interface (GUI) which displays the FFT of the current frame of the stack. Using the GUI, we input parameters of the TEM experiments (mainly the acceleration voltage, the spherical aberration (Cs)) and determine manually the exact defocuses and the defocus step in addition of other parameters shown in figure 2.15b (second step). Before running the reconstruction, the defocus-related rotation and the magnification changes between frames have to be corrected to completely align all frames.

After aligning the images, the brightness across all frames has to be normalized. A common region of interest (ROI) is then selected, extracted and reconstructed. Finally, the iterative algorithm is run to reconstruct the amplitude and the phase images of the selected ROI.

Compared to off-axis holography, there is neither need for a biprism for interference, nor a vacuum area next to the sample. Even though the focal-series method is effective and can be carried out on any microscope, some limitations have to be considered. The current FRWR algorithm is effective at analyzing a large range of frequencies but it is not so efficient for the low frequencies analysis as those can rapidly change with experimental parameters [167]. It is yet to be studied if this method remains relevant for the study of biological samples and to compare its results with simulations or others imaging techniques like off-axis holography. In-line reconstruction is also slower (non-linear equations), and requires multiple exposures for the different defocuses values thereby increasing the total electron dose the sample is exposed to [76].

Previous in-line electron holography experiments on biological materials were carried out at room temperature and at low electron energy to limit radiation damage [149]. Nevertheless, low energy electrons induce more electrostatic charging and lower SNR. Stevens et al. [168] worked on filamentous phages prepared on TEM grids by freezing the grids in liquid ethane then sublimating the ice [169]. In addition, they used perforated grids and were able to obtain phages hanging across the slits over the vacuum. With this method, they were able to obtain clear phase images of these phages due to the absence of the additional phase shift by the support.

Other preparation methods were also applied. Longchamp et al. used electro-spray deposition followed by low-energy in-line electron holography acquisition using a lens-less setup [170]. They succeeded to obtain phase images of the cytochrome C, the BSA and the hemoglobin proteins all imaged with resolutions around 8 Å. In-line holography experiments carried out at room temperature never succeeded to get resolutions below that value. A few experiments were done at cryogenic temperatures and the first phase reconstruction obtained at low temperature was done by Matsumoto and his colleagues in 1995 on frozen DNA [171]. More recently, Cheung et al. reconstructed phase images using a 20 kV modified STEM microscope [169]. With this instrument, they succeeded in reconstructing the earthworm erythrocyruorin protein, the TMV, and the T4 bacteriophages studied at a very low dose of $0.2 \text{ e}^-/\text{Å}^2$. However, their microscope is limited to resolutions not surpassing 2 nm. Other tests were done using single defocused micrograph with promising results [171–173].

2.6.4 Hybrid holography: getting the best of two in-line and off-axis methods

The idea of combining different electron holography method was first explored in 1996 by Morin et al [174] to observe organic materials by combining off-axis holography with LEEPS technique (called ‘projection electron microscopy’ in their article). Back then, they were able to achieve a 7 nm resolution. A lot has changed since then, with the development of better microscopes and software. This inspired Keskinbora et al. to experiment the combination of off-axis holography with in-line holography (focal series) on iron-filled carbon nano-onion samples [175]. The spatial resolution of the off-axis method alone was 0.97 nm and that of in-line and hybrid holography 0.4 nm.

Hybrid holography is possible as off-axis and in-line images can be acquired on the same microscope by first taking a focal series, then moving the biprisms inside of the field of view to acquire the off-axis hologram of the same area. It then requires the TEM to be equipped with biprisms. The reconstruction of the amplitude and the phase images of the in-line experiment is done using as starting image for the iterative process, those reconstructed from the off-axis data [175]. This method allows to combine the “good” performances of the in-line holography for the reconstruction of high frequencies with the “good” performances of the off-axis holography for the reconstruction of low frequencies [175]. The resulting hybrid method is therefore more effective in covering the whole frequency spectrum. Many challenges however arise from acquiring many datasets. The most important one is the increase of the total electron dose the sample received when cumulating the exposure times for the two methods, which then require to reduce the dose for both off-axis and in-line experiments and therefore the SNR of both experiments. Keskinbora et al. proposed a solution by acquiring small-defocus images in in-line to collect the highest frequencies before the high defocuses [175]. This will allow the retrieval of those high frequencies first, given that they will be the first lost due to beam damage. C. Koch proposes to reduce the number of defocused images acquired for the in-line to three as it is still possible to reconstruct the phase with three images only [162]. Intriguingly, to our knowledge, hybrid electron holography was never tested on cryo-vitrified samples, probably due to the dose limitation and possibly the absence of powerful cryo-compatible biprism equipped microscopes.

2.6.5 Ptychography: Another phase retrieval method in development

Many other phase extraction techniques exist and some of them were successfully used on biological object. Defocused 4D-STEM ptychography analysis is one of the most promising after recent developments in low-dose acquisitions [176,177]. Like electron holography, ptychography experiments is divided into an acquisition step and a post-experiment reconstruction process. The development of this technique was mainly driven by Peter Nellist and Angus Kirkland’s teams in Oxford. 4D-STEM consists on acquiring, on a pixelated detector, diffraction patterns obtained by scanning a convergent electron probe onto the sample. At each (x, y) probe position on the sample a 2D (k_x, k_y) diffraction pattern constituted of discs (like in CBED) is obtained in the Fourier space [178]. The whole dataset is then analyzed using an iterative algorithm named e-PIE for extended-Ptychographical Iterative Engine [179]. “Ptychography” designates the analysis procedure through this iterative algorithm to extract the amplitude and phase information.

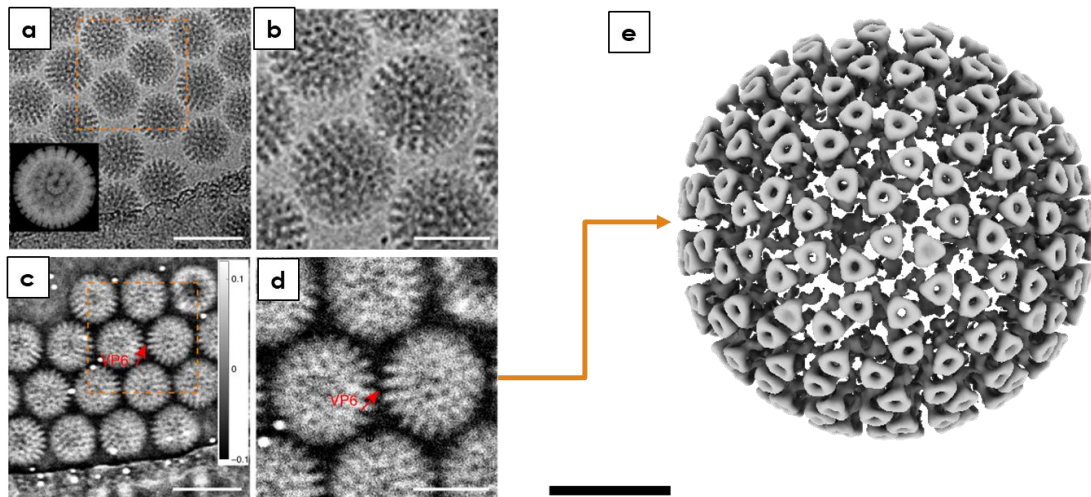


Figure 2.16 Electron ptychography of the rotavirus DLP. (a) BF cryo-TEM image of the rotavirus DLPs. A model is shown in the bottom left and correspond to the PDB structure “3KZ4”. (b) Zoom into the ROI of (a). (c) Phase image obtained by electron ptychography of the same rotavirus DLPs. The phase scale is in radians. (d) Zoom into the ROI defined in figure c. The VP6 spike protein is shown by the red arrow. (e) 3D reconstruction of the rotavirus DLP at 18.6 Å resolution. (a-b-c-d) are all from L.Zhou et al. [180]. (e) is from X.Pei et al. [181]. The scale bars in (a) and (c) are 100nm, and are 50 nm in (b) and (d). The scale bar in (e) is 20 nm.

The latest 4D STEM ptychography breakthrough was the successful reconstruction of phase images of ice embedded rotavirus double layered particles (DLP), as well as HIV-1 virus-like particles at very low doses from 22.8 to 5.7 $e^-/\text{Å}^2$ collecting information to around 8.6 nm [180]. The rotavirus cryo-TEM BF image, acquired at 35 $e^-/\text{Å}^2$, is shown in figure 2.16a with the reference model in the bottom left (PDB: 3KZ4). A zoom into the squared region is shown in figure 2.16b. In comparison, the phase image in figure 2.16c shows an enhanced contrast compared to the BF image with a well visible VP6. A zoom of the squared region is shown in figure 2.16d. The figures 2.16a, b, c, and d are all taken from L. Zhou et al. to show a concrete example of the ptychography results [180]. The authors were also able to apply the technique to a large field of view on adenovirus infected cells in this same article.

Recently this year, the authors succeeded in reconstructing the 3D structure of the rotavirus DLP. They resolved 3 structures using 3 different beam convergence semi angles. The best of the 3 was obtained at 18.6 Å resolution and is shown in figure 2.16e (EMDB: 35917) [181]

2.7 SAMPLE PREPARATION AND TEM GRIDS

2.7.1 T4 bacteriophage culture and purification methods

The T4 bacteriophage was cultivated and purified at the CBI. The initial T4 solution was kindly provided by Pierre Genevaux (LMGM-CBI).

5 mL of *Escherichia coli* MC4100 bacteria (*E. coli*) was first incubated in lysogeny broth (LB) medium overnight at 37°C with 180 round per minute (rpm) shaking. After 5 to 6 hours, the culture was diluted twice (2 flasks with 5 mL media) and incubated overnight in the same conditions. The next morning, the culture was then diluted 10 times and incubated at 37°C

with 180 rpm shaking for 30 minutes before adding the T4 bacteriophage solution. In our case, we added 450 μ L as the solution was too old. The mix was incubated for 3.5-4.5 hours in the same conditions. Intact and lysed *E. coli* were eliminated by low speed centrifugation at 5000g for 20 minutes at 4°C. The supernatant containing the bacteriophages was then transferred to a new tube and ultra-centrifuged at 35000g for 40 minutes at 4°C under vacuum to pellet the bacteriophages. The supernatant was discarded and the bacteriophage pellet was resuspended in 10 mL of buffer solution containing 10 mM HEPES buffer at pH 7.0 and without additional salts. If needed, the phage suspension can be further centrifuged on a sucrose cushion as explained by Payne et al. [182] to further reduce contaminations, but did not use this as the solution was clean in our case. The phage solutions were stored at 4°C. T4 is stable at least one year at 4°C and over 1 month at 30°C in presence of 10 mM of Mg ions [183]. In general, bacteriophages are stable at pH between 5 and 8, but some are stable down to pH 3 [184].

The T5 and T7 phage solutions were prepared and purified by our collaborator Dr. Amélie Leforestier at the LPS laboratory in Paris-Saclay university. These two bacteriophages are suspended in 100 mM NaCl, 10 mM Tris-HCl, pH 7.6, 1 mM CaCl₂ and 1 mM MgCl₂ and were stored at 4°C.

2.7.2 TEM Grids

Sample preparation requires the use of TEM grids. A large variety of grids can be used and they differ based on the shape, the number of squares, support films and other parameters. In the following table, we summarized the type of grids we used, for which TEM method, its main characteristics, and the main advantage:

| Support type and thickness | Grid type and size | Technique of use | Advantage |
|---|----------------------------|-----------------------------|-----------------------------|
| 10 nm continuous carbon | Copper 300 mech | Conventional TEM | Cheap |
| 2-3 nm ultrathin carbon with lacey | Copper 400 mech | Electron holography | Very clean support |
| Lacey carbon | Copper 300 mech | Cryo-EM and Cryo-holography | Big lacey holes |
| Holey carbon with a 0.35-1 nm continuous graphene | Gold 300 mech (Quantifoil) | Electron holography | Clean and very thin support |

The quantifoil with graphene grids were prepared and cleaned by Sara Bals' team at the EMAT laboratory at Antwerp university in Belgium, who previously developed efficient cleaning techniques for the graphene [185]. This collaboration started after testing commercial graphene which was not sufficiently clean even after having tried to clean it by acetone baths without success. All the other grids were commercial ones.

2.7.3 Room temperature TEM grids preparation

Unstained sample preparation

The unstained TEM grids were prepared as shown in figure 2.17, steps 1 to 5.

- Before the sample deposition on the TEM grid, 4 μL of T4, T5 or T7 solutions were mixed with 1 μL of 10 nm Au beads (BBInternational) pre-diluted 20 times (step 1), as gold beads are used as fiducial markers for drift correction.
- The TEM grid is hydrophilized by glow discharge for 30 seconds with a 10 mA negative air plasma in case of a carbon grid or an ultrathin carbon film on lacey grid (step 2). Graphene grids (from Sara Bals' group) were placed under an electrostatically charged plastic ruler. Another alternative to the ruler method is to use graphene oxide that is naturally hydrophilic but 1.5 or 2 times thicker than classic graphene [186].
- We then dropcast 4 μL of the phage-gold beads solution on the grid and let it rest for 2 minutes (step 3).
- The grid was blotted with a Whatman paper to remove the excess of liquid (step 4). It was then left to dry for a few minutes and stored at room temperature in grid boxes.

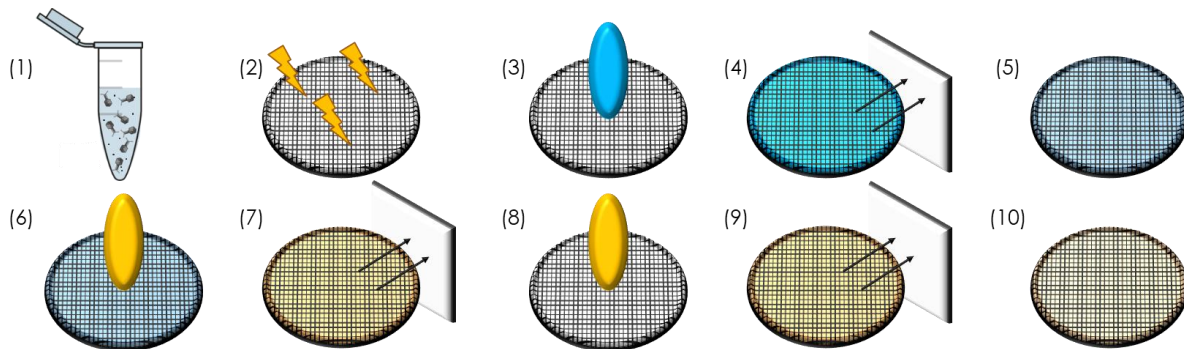


Figure 2.17 Sample deposition on TEM grids protocol. 1 through 5 constitute the unstained sample preparation and 1 to 10 the staining sample preparation. In negative staining we do not use gold beads.

Stained sample preparation

For staining, we followed all the steps in figure 2.17 except that we did not use gold beads. After steps 1 to 3, grids were blotted but not completely dried (step 4). Then, we immediately deposited half of the total volume of staining solution (step 6), namely 4 μL of 1% uranium acetate ($\text{AcU} - \text{C}_4\text{H}_6\text{O}_6\text{U}$). This was followed by an immediate blot (step 7) and another deposition of 4 μL of uranium acetate (step 8). After 1 minute, we blotted the grid to remove all the remaining liquid (step 9). It is then left for a few minutes to dry and stored at room temperature in grid boxes (step 10).

As shown in figure 2.18, unstained T4 (a) and T5 (b) bacteriophages appear as low contrast particles. Figure 2.18c shows nice negatively stained T4 virions, including two examples of contracted tails. In figure 2.18d, T5 phages appear positively stained due to the contrasting agent entering capsid, and the removal of the remaining stain by the blotting. Both preparations were stained with the same solution.

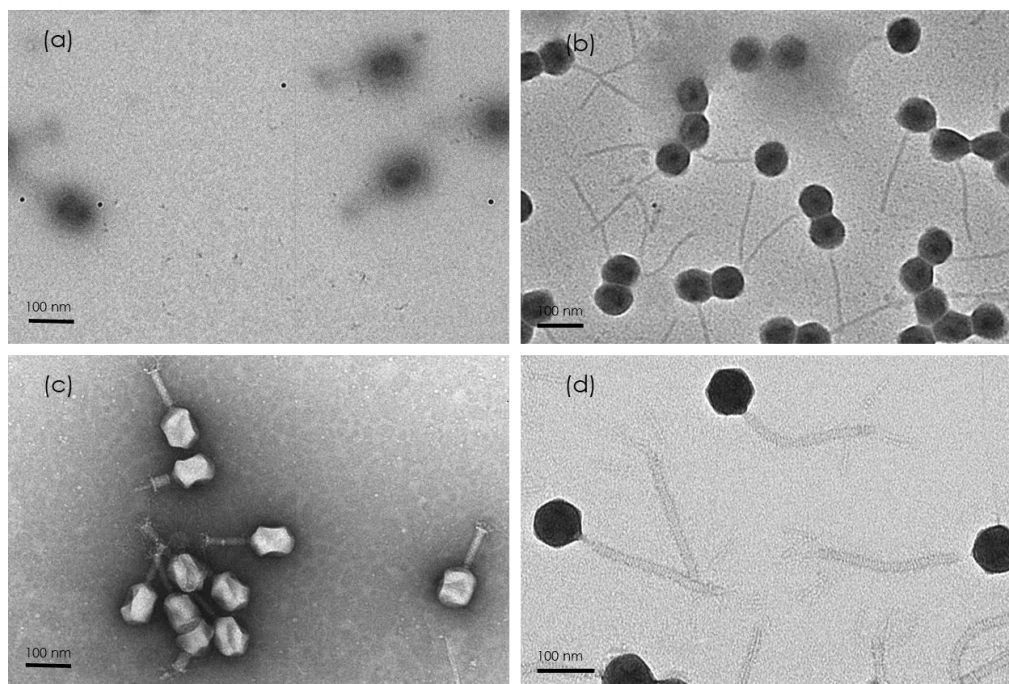


Figure 2.18 (a) Unstained T4 bacteriophages with 10 nm gold beads. (b) Unstained T5 bacteriophages with 10 nm beads. (c) Negatively stained T4 bacteriophages. (d) Positively stained T5 bacteriophages. All the images were acquired on a Jeol 1400 equipped with a tungsten source and operating at 80 kV.

2.7.4 Cryogenic sample preparation

Cryogenic sample preparation requires that the samples stay below -170°C from sample vitrification till TEM imaging of the grid.

For sample vitrification, two well-known automated cryo-EM plunge freezers are mostly used, FEI's Vitrobot and Leica's EM GP. At the CBI, we use the Leica EM GP. The principle, shown in the figure 2.19, is the same for the two equipment. The grid is first fixed to tweezers before depositing $3\ \mu\text{L}$ of the sample solution. Then the tweezers are attached at the end of the plunger (figure 2.19a). The Leica EM GP includes a chamber where the temperature is maintained at 25°C with 95% humidity. The chamber is lowered to be placed around the grid (not shown) and the grid is blotted under controlled temperature and humidity conditions before being dropped at a high speed into liquid ethane (figure 2.19b) cooled by liquid nitrogen (figure 2.19c). The vitrified grid is then transferred into the grid box inside a metallic cup containing liquid nitrogen and then stored in a liquid nitrogen container. Unlike liquid nitrogen which rapidly evaporates in contact of a warmer object, liquid ethane can absorb about 100°C heat without significant evaporation, which makes it a more efficient cryogenic liquid [187].

We usually choose to add gold beads for cryogenic off-axis holography with $1\ \mu\text{L}$ to $4\ \mu\text{L}$ of phage solution, and not to for classic cryo-EM. In our case, we used lacey grids although better alternatives exist like the Quantifoil® grids. Lacey grids were glow-discharged using negatively charged air plasma with a 25 mA current for 30 seconds before dropcasting $3\ \mu\text{L}$ of the solution. The sample was then vitrified and stored in liquid nitrogen.

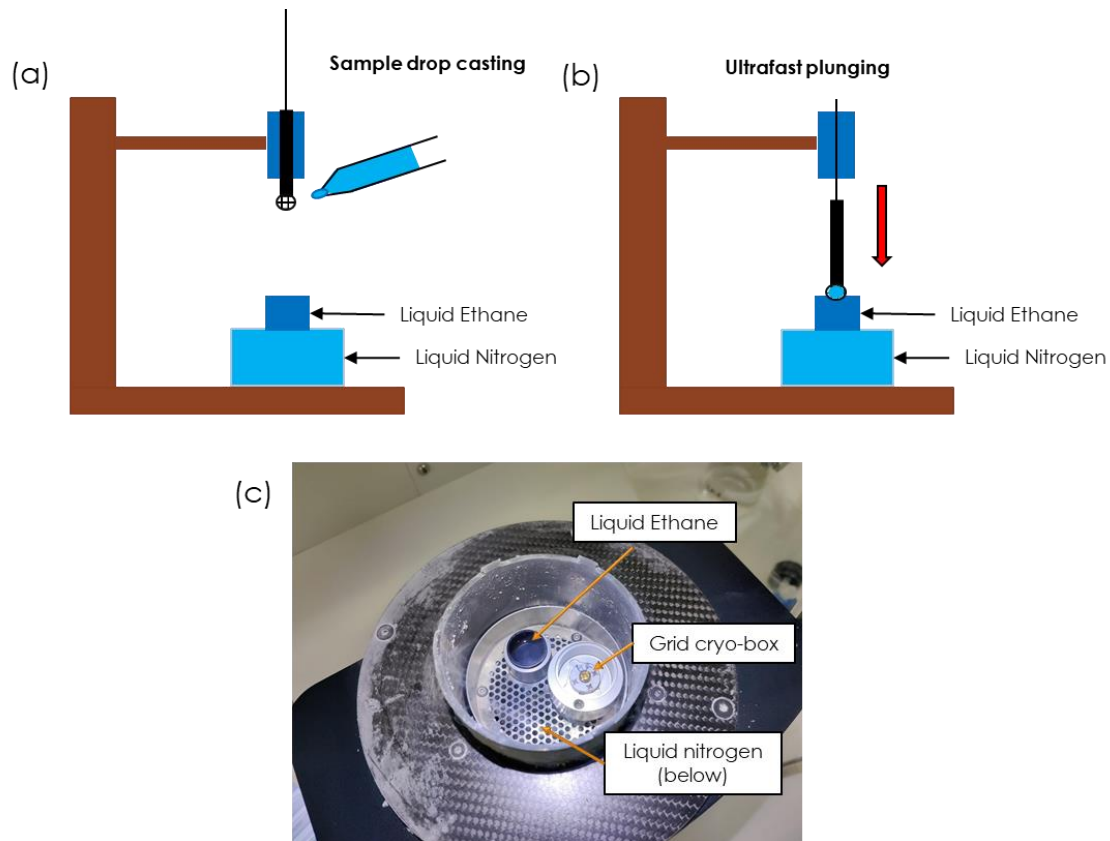


Figure 2.19 (a-b) Representation of the sample vitrification using the “ French guillotine” concept developed by Jacques Dubochet. The solution is placed on the grid which is fixed to the plunging machine. (b) The grid is plunged into the small liquid ethane reservoir for quick freezing of the water. (c) Picture of the Leica EMGP configuration where the liquid ethane is above the liquid nitrogen storage. The cryobox is inside a metallic cup that is filled with liquid nitrogen.

Alternative techniques for sample deposition as well as sample vitrification exist nowadays. For sample deposition, two other methods than the one we described earlier exist: droplet-based methods and scribing based methods [188]. The droplet-based method consists on depositing micrometer-sized droplets on the grids instead of millimeters as in normal deposition using a pipette, and letting them spread on the grid. Several droplet-based methods exist like the electrostatic spray for example [189]. The scribing-based method consists in “writing” on the grid by hovering a mobile part at 10 μm from the glow discharged grid which will absorb the solution [188]. Two devices using this method were developed. One of them, the Cryowriter can deposit around 20 nL of solution [190].

For the sample vitrification methods, an alternative to plunge-freezing is the jet vitrification. Instead of plunging the grid in liquid ethane, the pre-clipped grid is placed between two jets of the cryogen (liquid ethane) that is targeting the center of the grid, before plunging it a liquid nitrogen bath [191].



CHAPTER 3: OFF-AXIS ELECTRON HOLOGRAPHY ON BACTERIOPHAGES

3.1 INTRODUCTION

3.1.1 The aims of off-axis development

Even though TEM is able to achieve medium (10-20 Å) to high (2-5 Å) resolutions on biological samples using the current imaging techniques, many limitations and challenges still remain with the current EM methods. As discussed in chapter 2, these challenges mostly result from the low Z contrast of biological materials, which requires the use of staining solutions that may induce sample modification, and the difficulty of performing SPA on small or flexible proteins in cryogenic TEM. Herein, we aim at evaluating an interferometric TEM technique that does not require the crystallization of the sample or any other complex and time-consuming sample preparation method: electron holography, with its two main variations, off-axis and focal series in-line. This chapter focuses on off-axis electron holography.

The goal of this PhD work is to evaluate the performance of electron holography for the study of biological specimens at medium as well as at high resolutions, and at room temperature and under cryogenic conditions, to determine whether off-axis holography can be a competitive alternative technique for single molecule analysis. For this purpose, dedicated microscopes like the I2TEM at CEMES for off-axis holography were used.

While the main high-resolution imaging techniques of biological samples (NMR, X-ray crystallography and cryo-EM SPA) are averaging the information from multiple particles [170], electron holography should be able to achieve high SNR phase contrast imaging and thus image individual proteins without the need of averaging a high number of particles. Currently, intrinsically disordered regions of proteins like membrane receptors, or disordered proteins (IDP) that cryo-EM fails to analyze [192], can only be studied by NMR [193] and/or modelled by deep learning algorithms like “alphafold2”, which can also determine the accuracy of the prediction using a metric provided by the program [194].

Unlike NMR and cryo-EM, off-axis electron holography, with its capability to detect small phase shift of the exit electron wave should be able to visualize both small and large proteins. Although most of the previous experiments using holography were performed on viruses, few tests using the off-axis method were done on smaller proteins like collagen fibrils and ferritin [43]. In this thesis, we mainly used the T4 and T5 bacteriophages as proof-of-concept samples. The advantage for using such samples is their high resistance to electron

irradiation, compared to smaller proteins that require TEM studies with doses below $40 \text{ e}^-/\text{\AA}^2$, and their easy production and purification procedures. The dimensions of these bacteriophages are usually between 100 and 200 nm. In our case, we tried targeting resolutions enabling to visualize the 4 nm periodical structures in the tail of these bacteriophages. We performed off-axis holography both at room temperature for sample checking and experiments adjustment, and at cryogenic temperature for higher resolution studies. We also performed preliminary tests of off-axis holography on cells, that will be briefly discussed at the end of this chapter.

3.1.2 Off-axis holography software developments

Off-axis holography acquisitions on the I2TEM required the development and optimization of programs for stable and automated acquisitions. All the software developments were developed in the CEMES by Dr. Christophe Gatel and presented in the following paragraphs.

Drift correction: Like in other direct imaging technique, sample drift is a major problem as acquisitions can last few tens of seconds, blurring the image. To avoid having to acquire multiple frames and aligning them in post-processing, a real-time continuous drift correction process was developed by Dr. Christophe Gatel in the context of the thesis of Dr. Julien Dupuy [195]. For this procedure, two drift calibrations of the stage are carried out for the software to be able to move the stage and compensate the drift with an accuracy of 0.13 nm in the x axis and 0.25 nm in the y axis.

π -shifting: A so called “ π -shifting” technique was developed by C. Gatel as well [8] that greatly enhances the final contrast of the fringes. It consists on imposing a π -shift of the interference fringes during exposure in the middle of the acquisition time, by tuning the current of the gun tilt or the beam tilt deflectors of the I2TEM and subtracting the two stacks of holograms acquired before and after the “ π -shifting” of the fringes [196]. This process allows removing the autocorrelation part (central band at $k = 0$ of the FFT of the hologram) and therefore drastically enhances the fringe contrast and the phase sensitivity of the experiment.

Lenses-BD: Finally, a major program integrated in Digital Micrograph[®] is “Lenses-BD”. This last code also developed by C. Gatel make up for the lack of automation in the I2TEM by enabling to save two sets of parameters, in our case a low magnification and low dose set of parameters we named “*search mode*”, and a high magnification and higher dose set of parameters named “*record mode*”. These two modes are shown in figure 3.1b and 3.1c. In “*search mode*”, we can visualize the field of view (FOV) where the beam overlap and interference occur. In the “*record mode*”, only the FOV is acquired. For the analysis of the holograms, we use a commercialized program also developed by C. Gatel called “qHolo” [8].

All the previous experimental parameters being optimized, the only notable difficulty is to limit the total electron dose the sample is exposed to, keeping sufficient SNR to detect small phase shifts. This requires adjusting the focus, calibrating the fringes movement and sample drift corrections away from the sample, before launching the acquisition while exposing the sample with the electron beam, all performed in the “*record mode*” as shown in figure 3.1a. This has to be done manually as no automation exists for the sequence: image adjustment - sample motion - final acquisition.

These procedures are crucial for electron holography studies of biological samples, which require low-dose TEM configuration. Indeed, reducing the electron dose also reduces

the fringe contrast, and automation is therefore essential to optimize with efficiency the electron hologram acquisition on very low contrast samples.

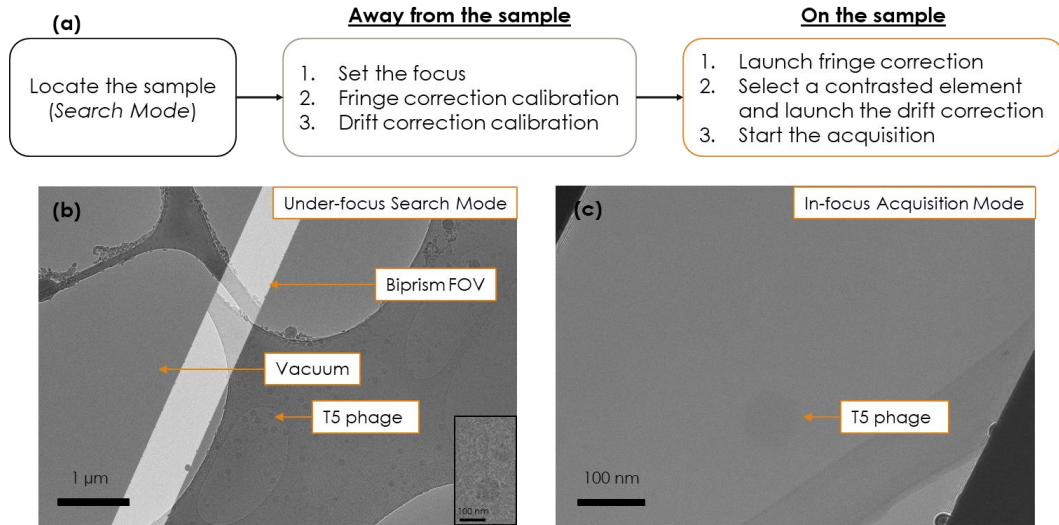


Figure 3.1 (a) Low-dose workflow for biological samples imaging using the Lenses-BD code. (b) "Search mode" image of a cryogenic sample. The bright area is the hologram FOV. A T5 phage is shown in the right bottom corner. The search mode is under-focused to allow the visualization of the samples and low magnification to have a broader FOV and a more spread electron beam to minimize the electron dose. (c) "record mode" image in-focus with a very low contrasted T5 phage.

3.2 CONVENTIONAL OFF-AXIS ELECTRON HOLOGRAPHY

3.2.1 Challenges for biological off-axis electron holography

In ideal conditions of samples insensitive to beam damage and with a perfect detector, off-axis holography has the ability of detecting phase shifts beyond $2\pi/1000$ [197] with an electron dose sufficient to get high signal. Quantitatively, the phase detection limit φ_{lim} depends on the detector parameters, the electron dose, the fringe contrast, and the mask used for the Fourier reconstruction. It is defined by the following formula:

$$\Delta\varphi_{lim} = MTF(q) \times \sqrt{\left(\frac{2\alpha}{DQE(q) \times N_0 V_0^2}\right)}$$

with 'q' the spatial frequency. It then depends on the camera modulation transfer function (MTF) and DQE, the electron dose, defined by N_0 that is the average number of electrons per pixel, V_0 that is the fringe contrast, and α the ratio of the area inside the sideband mask versus the total area of the Fourier space [40].

As mentioned earlier, increasing indefinitely the dose is not an option for biological samples. The only way to enhance phase detection is to optimize fringe contrast. We therefore had explored and tested different microscope conditions to determine the limits imposed by the sensitivity of the biological materials to the electron beam.

Sample preparation:

Performing off-axis holography to study biological samples requires a reproducible sample preparation procedure and clean TEM grid supports which have to be as thin as possible to reduce additional phase shift from it.

a) *TEM grids:*

We have performed electron holography experiments on different types of grids. As discussed previously, off-axis holography requires a clean substrate that is as thin as possible. We first tested commercial single and double layered graphene supports, then commercial ultrathin carbon, and finally handmade graphene.

Commercial graphene layer (Ted Pella[®]): Graphene is a pure material only made of 2D carbon layers, a single atomic layer being 0.34 nm thick [198]. It causes very low inelastic scattering and a single layer is transparent to electrons at 300 kV [199]. Moreover, graphene is highly conductive and stable under the electron beam. Charges dissipation is crucial for beam-sensitive samples as it enhance their resistance to beam charging effects [198]. However, one of the major problems with graphene is its contamination, either during preparation, or when stored at atmospheric pressure. Cleaning this material has been a major challenge for graphene growers [200]. Different methods are used [185,201–203], but none completely solves the problem. Indeed, we observed spots on commercial graphene, as we can see in the empty grid in figure 3.2a. These spots are distributed all over the graphene support on the TEM grid.

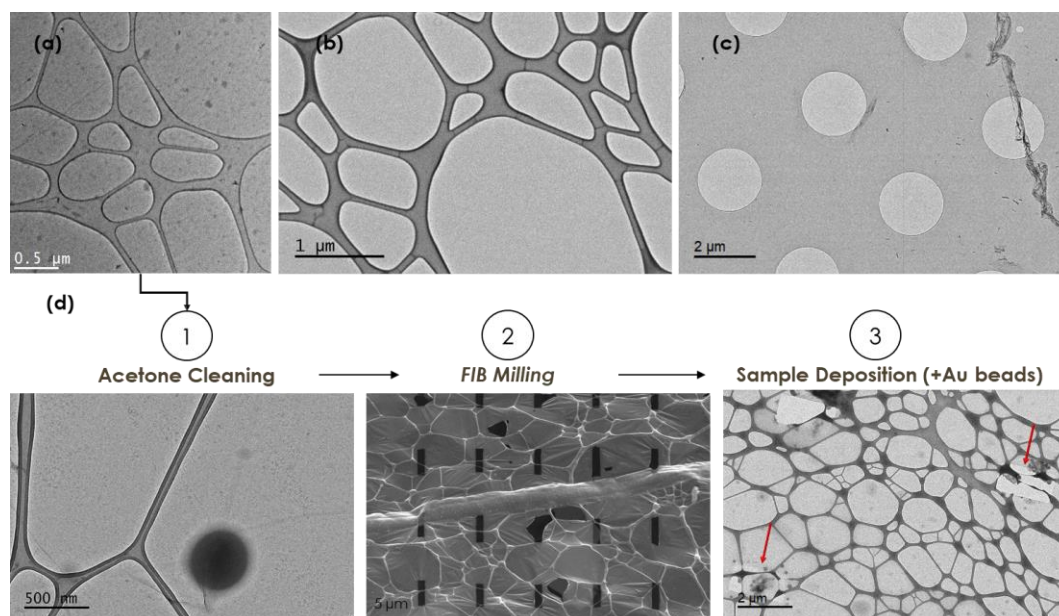


Figure 3.2 The various supports used in this study: (a) commercial graphene, (b) ultrathin carbon, and (c) quantifoil graphene grids. (d) Cleaning procedure used for the commercial graphene grid. The red arrows in step 3 are pointing at the rectangular holes shown in step 2.

To solve the graphene contamination problem, we tried a cleaning process using acetone and ethanol. Acetone is widely used by graphene growers for contamination removal [204]. In our case, we tried a simpler procedure with the help of Sebastien Pinaud in the CEMES cleanroom to avoid contamination. Graphene grids were submerged in acetone for 15 minutes and this operation was repeated once with clean acetone. The grid was then plunged in 70% ethanol for 10 minutes to remove the remaining acetone on the grid. Lastly, the grid was blotted and left a few minutes to dry. Figure 3.2d (step 1) shows that acetone cleaning improves the graphene cleanness, although contaminations and some solvent remain.

Beside contamination, lacey grids also suffer the lack of empty areas allowing overlapping of the sample beam with a reference beam passing through vacuum. To achieve this, we used focused ion beam (FIB) on the FEI Helios Nanolab 600i to mill patterns of rectangular vacuum areas using gallium ion beam across square on the grid as shown in figure 3.2d (step 2). After dropcasting the sample, we observed the accumulation of contaminants across the drilled holes due to the water surface tension when blotting as shown in the step 3 in figure 3.2d. Therefore, we gave up exploring this path.

Commercial ultrathin carbon layer (Ted Pella®): Since commercial graphene always contains contaminations, we tried the ultrathin carbon support, which is thicker (2-3 nm) but much cleaner as shown in figure 3.2b. Its disadvantages besides the increased thickness compared to graphene, is that it is held by a lacey support. This lacey can be abundant in some areas and overlap with our sample when imaging in off-axis holography.

Graphene support on Quantifoil®: We started a collaboration with the group of Prof. Sara Bals from the EMAT laboratory in Antwerp, Belgium. Her team is expert in high resolution (S)TEM tomography experiments and particularly carried out on nanoparticles. To perform these quantitative 3D experiments, they have developed a procedure to grow thin graphene layers as very low contrast support [185]. They have the knowledge and the equipment to produce very clean graphene layers deposited on quantifoil holey carbon grids before being vacuum-sealed. These graphene support grids were stored in a low vacuum ($\sim 10^{-2}$ hPa) desiccator as soon as they were received. As shown in figure 3.2c, the graphene in the carbon holes is continuous and much cleaner compared to the commercial one. Nevertheless, hydrophilization of graphene has to be done differently as it is easily destroyed by classic air plasma charging [202]. This was smartly solved with the help of Abner Velazco-Torrejon by holding an electrostatically charged plastic ruler or sheet above the grid until blotting was applied.

Graphene oxide layer: Another choice for very thin support could be the use of graphene oxide which is a good alternative for stained and vitrified samples due to its electron transparency and high hydrophilicity [186]. Graphene oxide is however thicker than graphene and commercial supports are between 0.8 and 1.2 nm thick. These grids were not used in this manuscript work.

In conclusion, we mainly worked with the quantifoil graphene from Sara Bals' group and occasionally with ultrathin carbon. As previously stated, graphene was preferred as it is thinner and also because of the overlap of lacey with our objects with ultrathin carbon grids in off-axis holography.

b) *Phage purification procedures:*

The second challenge was the sample solution preparation. During the first year of this thesis, we purified T4 phages by adding chloroform to the phage-lysed bacteria mixture as shown in the figure 3.3 (up). In addition to releasing phages that are still inside the bacteria, chloroform also releases all their protein and DNA content causing a lot of contamination in the solution. Furthermore, chloroform if not completely eliminated can cause bubbles under the electron beam. Following the chloroform purification, phages were transferred in a HEPES or Tris-HCl buffer containing salts (Ca^{2+} , Mg^{2+} , Na^+ , Cl^-). Those salts often crystallized across most of the grid. To solve these problems, the purification procedure was modified (figure 3.3 down) and followed the concentration by centrifugation process presented by Kutter et al. [184].

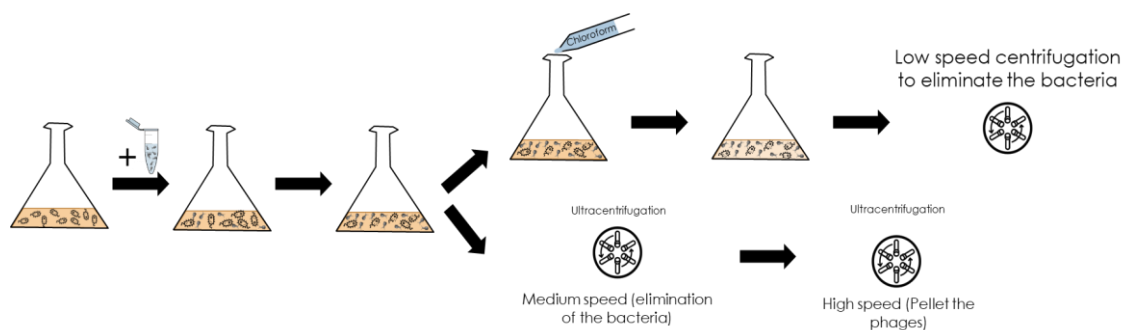


Figure 3.3 The two T4 purification methods. *E. Coli*, the host bacteria of the T4 was cultivated in lysogen broth (LB). Phages were then added, leading to infection and bacterial lysis. (Up) Chloroform was then added to destroy all *E. coli* and bacterial debris were removed by low speed centrifugation. (Down) Full and lysed bacteria were eliminated by medium speed centrifugation. Phages were then pelleted by ultracentrifugation and resuspended in a clean buffer.

In this protocol, the phage pellet was resuspended in a 10 mM HEPES without salts at pH 7.0. The disadvantage of such low salt and buffer concentrations is the aggregation of phages when left still for many days. Based on publications and our experience, we now use a higher buffer concentration like 20-50 mM HEPES to prevent aggregation, and a slightly higher pH around 7.2. Our T4 phage solutions were stable at 4°C for several months without much loss in phage concentration.

Experiment optimization for off-axis holography

Achieving 4 nm resolution is a hard task when developing a new “invasive” diffractive technique as many factors may affect the quality of the results (images). First, the choice of the sample, its purification, and the grid supports are important parameters to select before optimizing the TEM experiments. The different options we have been looking at are presented in table 3.1.

Concerning the purification methods, we established that the 2-steps ultracentrifugation is a much better alternative. We also determined that a thinner but clean support, here the holey carbon graphene provided by Prof. Sara Bals’s group in Belgium, was the best option. Among our samples, the T4 bacteriophage was the preferred one for its thicker and rigid tail, which was easier to image, especially on unstained preparation at room temperature (see below).

| Purification method | Chloroform extraction | 2-steps ultracentrifugation | |
|---------------------|-----------------------|-----------------------------|---------------------------------|
| TEM grid support | Commercial Graphene | Ultrathin Carbon | Holey Carbon graphene (S. Bals) |
| Sample | T4 phage | T5 phage | T7 phage |

Table 3.1 Different sample-related parameters that were tested (independently) and optimized for off-axis holography on unstained samples. T7 bacteriophages tests are not shown in this manuscript as we mainly worked with the T4 and T5.

The microscope parameters were less straightforward to optimize. The different parameters and options we have studied are presented in table 3.2. As discussed above, we determined early on that the Lorentz mode was more suitable to observe bacteriophages of a few hundred nanometers long. We also tested high and low electron doses with different dose rates combined to various fringe spacing. As our goal was to achieve high resolution, we tested both room temperature and cryogenic temperatures. Last, we had the opportunity in the last year of this thesis, to perform experiments using a K3 direct detector from Gatan, which allowed us to compare its higher capabilities relative to a 4k-4k pixels CMOS OneView camera.

| I2TEM mode | Normal Mode | Lorentz Mode |
|-------------------------|--|--|
| Electron Dose | High : 80-450 e ⁻ /Å ² | Low : 15-80 e ⁻ /Å ² |
| Acquisition time | Short : t < 20 s | Long : t > 20 s |
| Inter-fringe | 0,6-0,9 nm | 0,9-1,2 nm |
| Temperature | Room temperature | Cryogenic temperature |
| Camera | OneView CCD | K3 DDD |

Table 3.2 Different microscope-related parameters that were tested (independently) and optimized for off-axis holography on unstained samples.

In this chapter, we first present our tests concerning the most relevant parameters and their effects on the overall results, evidencing the current capabilities of off-axis electron holography. Our target for this analysis was to achieve a spatial resolution of 4 nm, and to optimize the phase sensitivity (i.e. the phase image SNR) required to observe details of this resolution.

3.2.2 Testing off-axis holography on negatively stained bacteriophages

Before observing unstained samples, we tested several parameters of the microscope using negatively-stained T4, like the FOV in the ‘normal mode’. We also measured the contrast we could achieve under a 300 kV accelerated beam and determined the optimal acquisition parameters to obtain a phase image of high SNR. To make these first experiments easier we performed them on high contrasted samples.

The first off-axis holography test on negatively stained T4 phages was performed in normal mode (figure 3.4) and in Lorentz mode (data not shown) on samples deposited on classic carbon support and commercial graphene respectively. This experiment was conducted in the “high-resolution mode” with the OneView camera without the π -shifting process and with a 2 second exposure per hologram. As the stain offered enough contrast at low electron dose, such short exposure time was sufficient.

The results of this experiment are shown in figure 3.4. In this example, the original holograms were recorded with the sample slightly under-focused, as shown in the magnified “zoom” on which the fringes are weakly visible due to the very short exposure time. The FT of the hologram shows a central band and the two side bands. These side bands contain the amplitude and phase information of the object exit-wave. The FOV is a narrow band, 155 nm long and 70 nm wide. The imaging of the full 220 nm long phage thus required taking several images to cover the whole structure.

On the phase image in figure 3.4, we note a fairly high contrast on the capsid itself. The tail is not visible in the amplitude image, but appears in the phase image. No detail is highlighted in the original hologram even though the whole phage is somewhat visible. This is due to the contrasting agents and the slight defocus used to record the hologram. The presence of the staining molecules explains the grainy signal compared to an image without staining (see the next part) resulting in a very noisy phase image. The phase profile of the capsid indicates a phase shift of 1.5 radians with a phase sensitivity, which is measured as the standard deviation of the phase signal in a flat empty area, is around 0.65 radians, a high value that is 43% of the maximum phase shift induced by the T4 capsid. In these experimental conditions, the T4 tail rings can be observed mainly because of the staining background. This background is however noisy due to these molecules and the use of a carbon grid which is thicker than ultrathin carbon or graphene.

These preliminary experiments on negatively stained samples indicate that electron holography experiments have to be carried out in Lorentz mode to have a sufficiently large FOV and that staining has to be avoided. In fact, even if it produces high amplitude contrast, it also results in very noisy phase images.

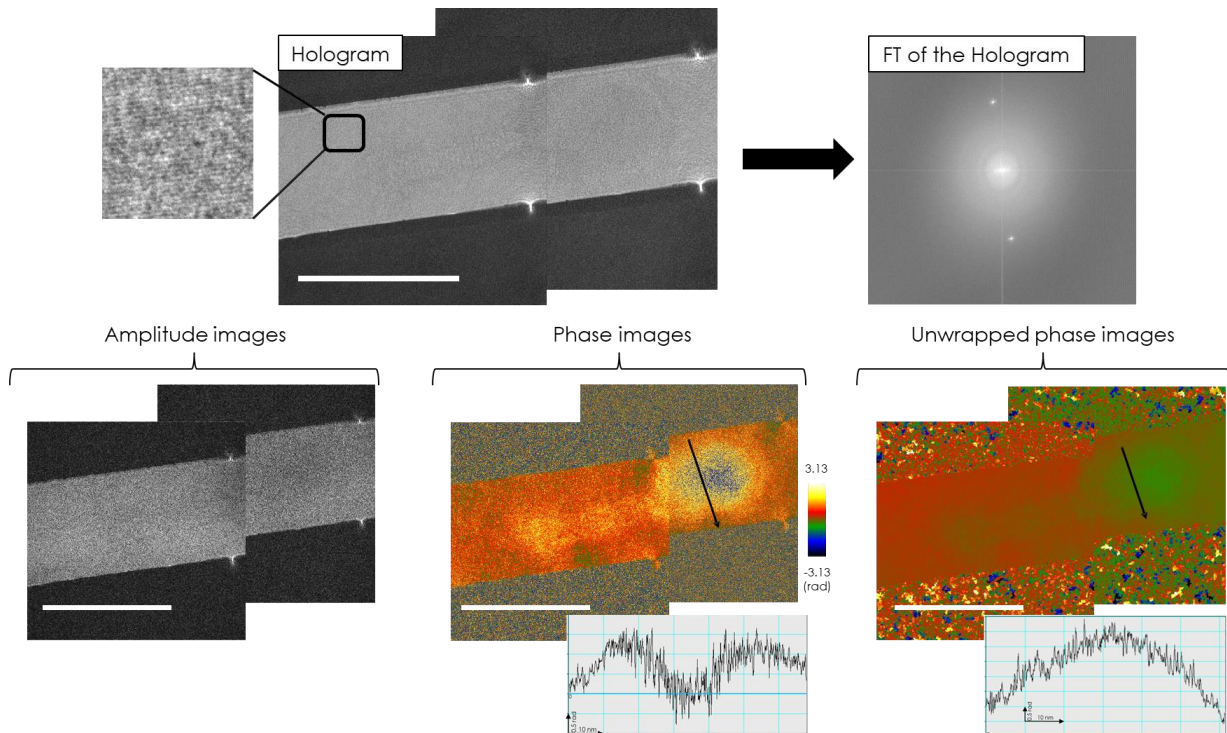


Figure 3.4 Off-axis electron holography of a negatively stained T4 bacteriophage in high resolution mode. The raw holograms are shown in the top left with a zoom on the interference fringes. A FT of one hologram is shown in the central band and the two sidebands. The amplitude images, phase images and unwrapped image are shown with the phase profile measured across the capsid. The x axis represents the 'x' coordinate along the profile in nm and the y axis the phase shift in radians. The scale bar is 100 nm.

3.2.3 Off-axis holography of unstained bacteriophages

Off-axis holography on the T4 bacteriophage

Room temperature off-axis holography experiments were repeated on unstained bacteriophages and our efforts were pushed to improve the resolution and the phase sensitivity. As in all imaging techniques, a compromise has to be found between spatial resolution and phase sensitivity. We aimed to observe details of about 4 nm on the unstained samples, which is far from the ultimate resolution of the I2TEM, achievable in high-resolution electron holography (0.5 nm).

The spatial resolution is set by the fringe spacing of the hologram. We generally adjust the fringe spacing in order to have 3 to 4 fringes within the wished resolution depending on the size of the selected numerical mask used afterwards for the Fourier analysis of the hologram [43]. Spatial resolution is also affected by radiation damage in addition to the phase sensitivity degradation (see the equation of the phase error in 3.2.1). Therefore, the dose has to be carefully controlled as well. To correct for sample drift during exposure, we add in the phage solution 10 nm diameter gold beads, which give high contrast dots used to correct for sample drift even at low doses.

We performed the first off-axis electron holography experiments on unstained samples at high electron dose to minimize phase noise and maximize fringe contrast, while ignoring the beam damage. For these experiments, the phages were purified with the chloroform extraction method. The T4 phages were deposited on ultrathin carbon grids from Ted Pella[®]. As first tests, images were acquired with 4 minutes exposure time, accounting for a dose around $10^3 \text{ e}^-/\text{\AA}^2$, a high dose expected to damage biological material.

First tests were performed on samples deposited on commercial graphene supports (results not shown). In these experiments, we noticed thickness changes in the graphene as well as contamination. Furthermore, after improving the image contrast by calculating the isophase map of the phase image, we could only see the T4 overall shape (capsid, tail and baseplate).

We then changed the grid support and used ultrathin carbon from Ted Pella[®]. These supports are very clean and stable. Nevertheless, the abundant lacey, as pointed above, was often overlapping with the phages when performing the interferometric experiments, a limitation that added to its increased thickness compared to a single graphene layer. In spite of these issues, we were able to obtain a significant improvement in the phase images.

Figure 3.5 shows an example of the resulting phase image displaying a very flat background with only few contaminations. The exposure time of the hologram was 4 minutes long. The different parts of the T4 are easily recognizable as we can easily describe the specimen morphology, but without details of the tail structure. The phase sensitivity in this experiment is 0.04 rad. We observe a slightly smaller maximum phase shift of 1.6 radians for the capsid (figure 3.5) compared to the previous experiment.

Using ultrathin carbon grids enabled us to evidence that the grid support cleanness was not the only source of contamination (non-sample related signals), but that contamination also came from the sample solution which was not pure enough.

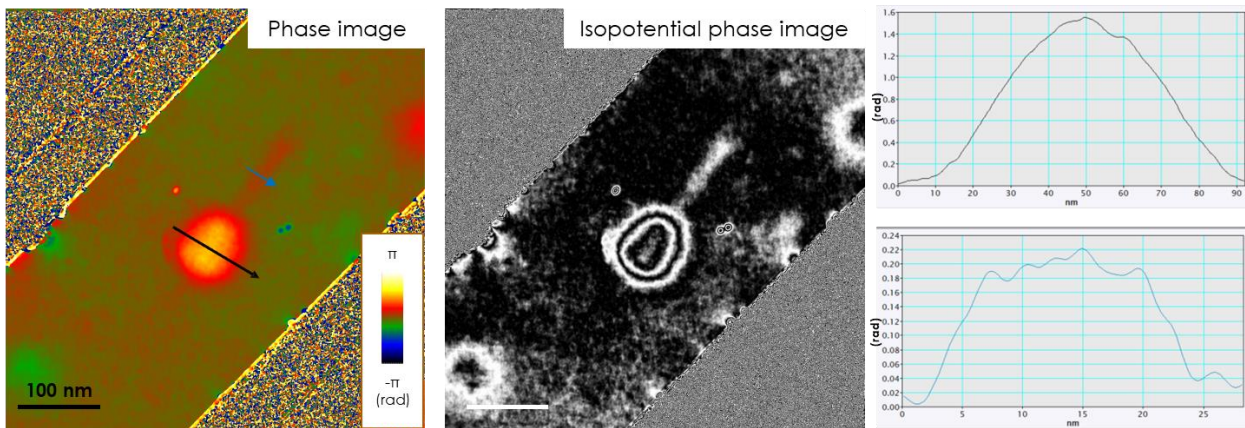


Figure 3.5 Off-axis holography of the T4 bacteriophage on ultrathin carbon using a CMOS camera. This hologram was taken at a lower magnification compared to other CMOS camera results. The phase image shown a flat, relatively clean support (phase sensitivity = 0.04 rad). The isophase phase image (cosine [$9 \times$ phase]) is shown with the more contrasted phage and the visible baseplate. The phase profiles shown on the right correspond to the arrow on the phase image with the same color. The x axis represents the 'x' coordinate along the profile in nm and the y axis the phase shift in radians.

After testing the commercial ultrathin carbon grids, we reproduced the experiments using the quantifoil grids covered by a continuous graphene layer generously provided by Sara Bals's group at EMAT (figure 3.2). These supports appeared extremely thin, stable, and clean. Using the One View CMOS camera, we were able to obtain highly contrasted holograms as the one in figure 3.6. In this experiment, the exposure time is reduced from 4 minutes (previous experiments) to 50 seconds with a total electron dose of $387 \text{ e}^-/\text{\AA}^2$ achieving a fringe contrast of 24% with a fringe spacing of 0.86 nm leading to 1.7 nm resolution with the selected numerical mask.

The electron doses we used in similar experiments were in general between 250 and $350 \text{ e}^-/\text{\AA}^2$. While this dose is still high and may affect structural details like the tail ring, it allows to obtain phase images with sufficient resolution and sensitivity while keeping the general morphology of the phage undamaged. In the image presented in figure 3.6, the phage is laying on clean graphene with its capsid touching the edge of a carbon hole. This can be seen in the amplitude image but without much information as the contrast is too low. The very uniform phase image in the continuous graphene support indicates a clean and flat surface with a mean close to zero. The bright spot right next to the phage is the phase-shift of a 10 nm gold bead used for the image drift control. The phase sensitivity in the phase image is 0.06 rad.

The different parts of the virus (capsid, tail and baseplate) are clearly visible. The capsid and tail profile exhibit more important phase signal compared to the previous experiments done with a considerably higher dose, with maximums of 2.4 rad and 0.25 rad respectively. However, we could not clearly visualize the tail rings, which is likely to be damaged at this dose. The isophase phase image allows a better visualization of the tail without revealing further details. The baseplate in this image is much more contrasted than in the raw phase image, but with noise making a part of it blurred.

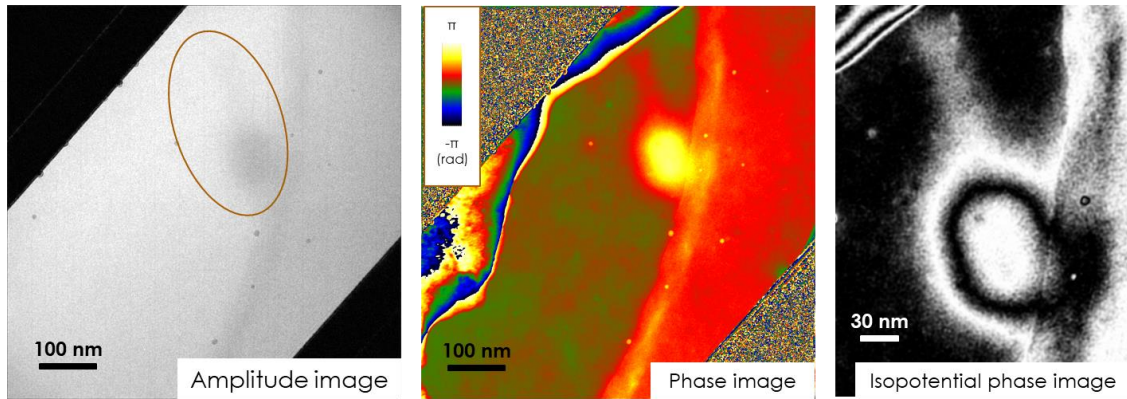


Figure 3.6 Off-axis holography of the T4 bacteriophage on holey carbon graphene using a CMOS camera. The fringe spacing is 0.86 nm. The amplitude image shows the position of the phage (circle). The phase image shows the well contrasted bacteriophage with its capsid touching the carbon. The isophase is shown ($\cos [-4 \times \text{phase}]$) with a closer look into the tail and baseplate.

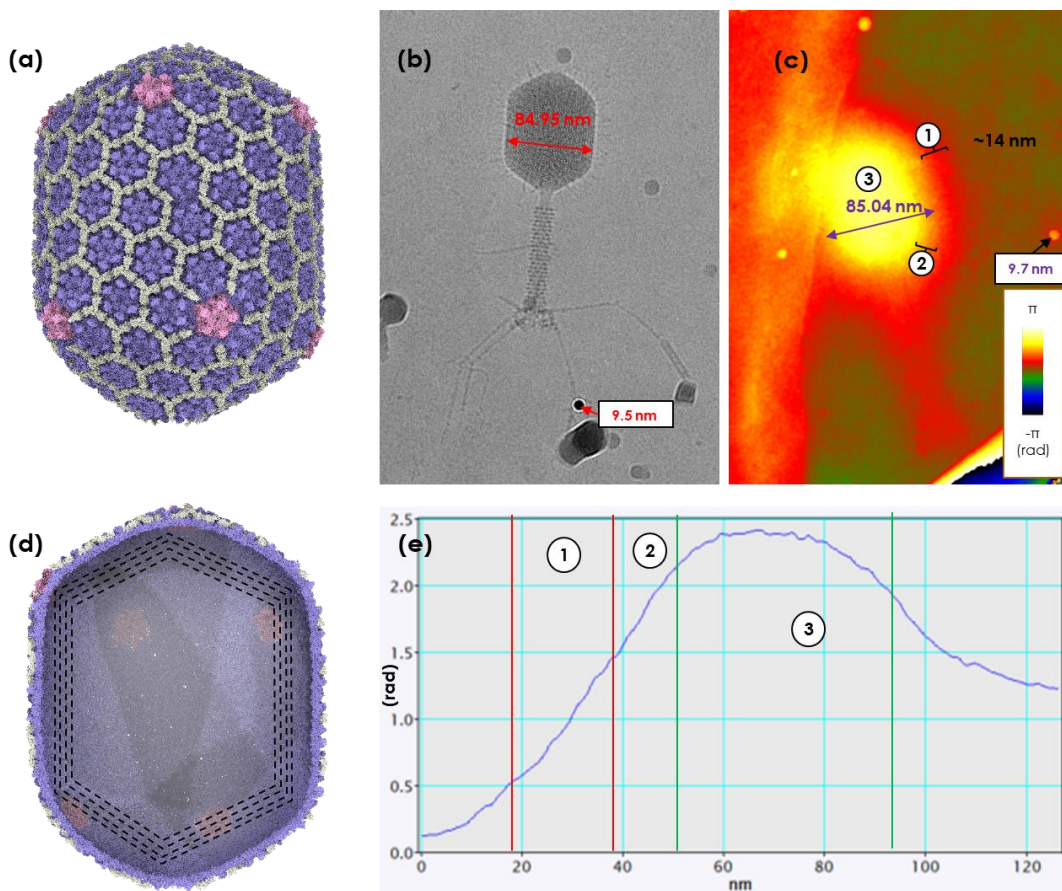


Figure 3.7 In-depth analysis of the T4 phase image of figure 3.6. (a) and (d) show the 3D structures of the outside and inside of the empty capsid respectively (pdb: 7VS5). (b) Cropped cryo-EM image of a T4 taken on a Talos Arctica. (c) Crop of the phase image shown in figure 3.6. The capsid signal is divided into 3 parts or phase domains based on the phase color. (e) Phase profile of the T4 capsid with the 3 phase domains as shown in (c).

If we look further into details of the phase structure of the T4, we can visually divide the T4 capsid into 3 distinct regions (figure 3.7c), each represented with a different color (i.e. different phase shifts) indicating the good sensitivity of the phase image (for imaging the capsid). Knowing the dimensions of the T4 capsid, which we measured in cryo-EM by

obtaining defocused BF images of the T4 on the Talos Arctica (figure 3.7 b), we can infer the different parts of the phage.

We assume that area “3” in figure 3.7c corresponds to the interior of the capsid, as shown in figure 3.7d. It contains the signal due to the phage capsid as well as the DNA as shown in the external and internal view of the full capsid presented in figure 3.7a and 3.7d respectively. The DNA is stacked close to the border of the capsid by a packaging machine to a near-crystalline density [61]. The capsid also contains many proteins encoded by 289 genes [57]. Area “2” would correspond to the phage capsid edges (figure 3.7 d), and area “1” could correspond to the capsid surface ‘decoration’ proteins called the highly immunogenic capsid protein (Hoc), the “hair” around the capsid visible on figure 3.7b [61]. A structure of three out of the four domain is present in the PDB under 6SHS and shows that one domain is ~ 3.6 nm [205], meaning that 4 domains should be around 14 nm. However, we demonstrated later that area 1 refers to the electrostatic charges of the capsid (see figure 3.16). However, it is extremely complex to measure the charge due to the variable mean inner potential (MIP) resulting from thickness and composition variability, the MIP being the volume averaged electrostatic potential. The three areas of the capsid phase signal are shown in the phase profile in figure 3.7e.

These first experiments showed the importance of having a clean sample to perform holography and avoid contamination in the reference area. Therefore, we improved the purification process by using ultracentrifugation as described above in figure 3.3. This led to an improvement of the cleanness of the solution compared to the chloroform process, especially by eliminating residual bacterial proteins resulting from cell lysis.

One of the most interesting results with this cleaner solution was the observation of a retracted virus as shown in figure 3.8. The tail and the baseplate changes upon DNA ejection compared to the non-contracted phage [206], as shown in figure 3.8a. The fringe spacing in the hologram was 0.85 nm and the experiment was carried out with a total electron dose of $505 \text{ e}^-/\text{\AA}^2$. The phase shift of the capsid is about 2.5 rad, similar to what was measured in other T4 capsids containing DNA. The phase profile of the tail shows a phase shift of 0.8 radian, higher than previous measurements, while the internal tail tube phase shift is less than 0.5 rad. We therefore conclude that this phage still contains its DNA and that the conformational change of the retracted tail was triggered without DNA injection. We assume it is due to sample preparation or purification. On the other hand, the tail tube signal is subject to a high noise (sensitivity = 0.13 rad) as we can see in the figure 3.8 (bottom right).

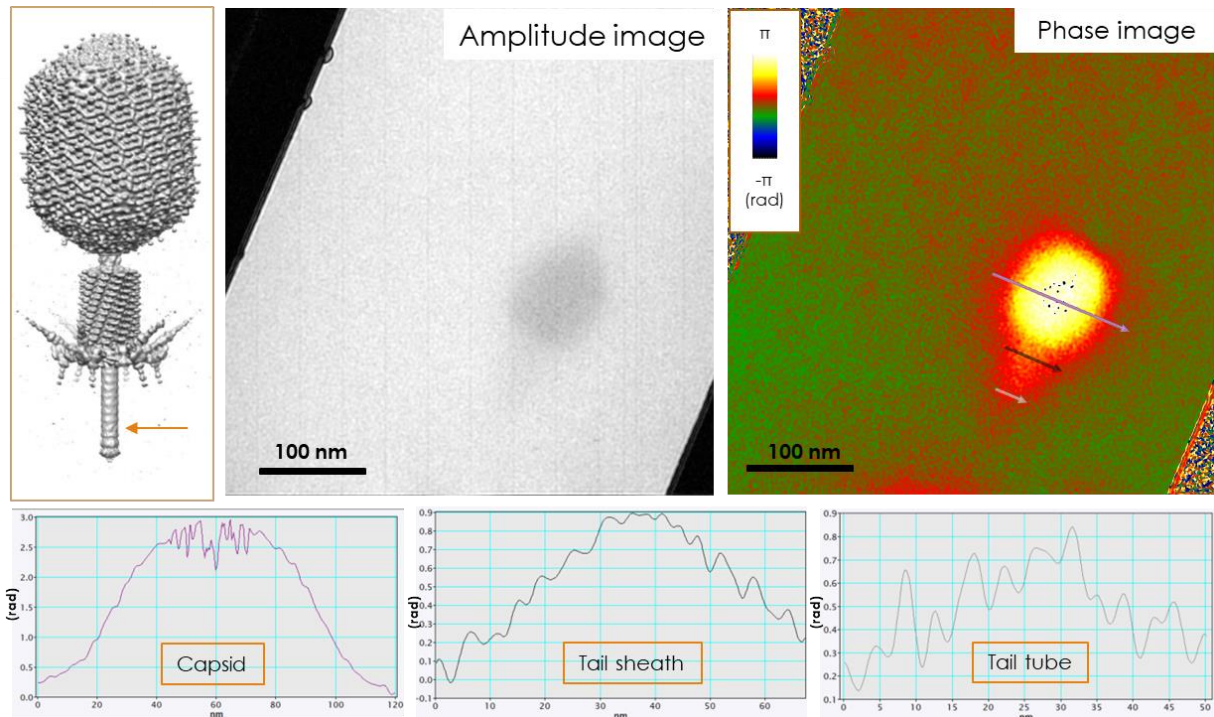


Figure 3.8 Off-axis holography of a retracted T4 bacteriophage. The retracted T4 3D structure is shown in the top left, from Leiman et al. [69]. The tail tube, which is in the center of the tail sheath is shown by the yellow arrow. The amplitude image shows the capsid as well as the short tail. The phase image reveals more clearly the retracted phase. The phase profiles of the capsid (purple profile), the tail (black profile), and the tail tube (red profile) are shown at the bottom from left to right. The 'y' axis is in rad and the 'x' axis in nm.

Incidentally, we observed an additional way of enhancing the phase contrast of our object. It was luckily obtained exposing the grid to a heating source (i.e. a simple lamp bulb) for 4 to 5 minutes. In this electron holography experiment performed on this “exposed” sample, the electron beam exposure time was 1 minute with π -shifting and sample drift correction. The total electron dose is $193.6 \text{ e}^-/\text{\AA}^2$.

The heat source induced some carbon or other contamination deposition on the phage as shown in the amplitude image of figure 3.9. The unwrapped (linearized) capsid phase profile in figure 3.9 (bottom left) shows a 3.5 rad phase shift compare to the 2-2.5 rad obtained previously. Meanwhile, the tail signal is very noisy as the phase sensitivity is 0.09 rad (figure 3.9 bottom right). This contrast enhancement, in a situation where we have a good sensitivity, could be interesting when observing the general morphology of a specimen without staining as it helps preserving the sample regardless of dehydration at room temperature. In the shown example, the capsid is sharp compared to the more rounded capsid in the previous experiments.

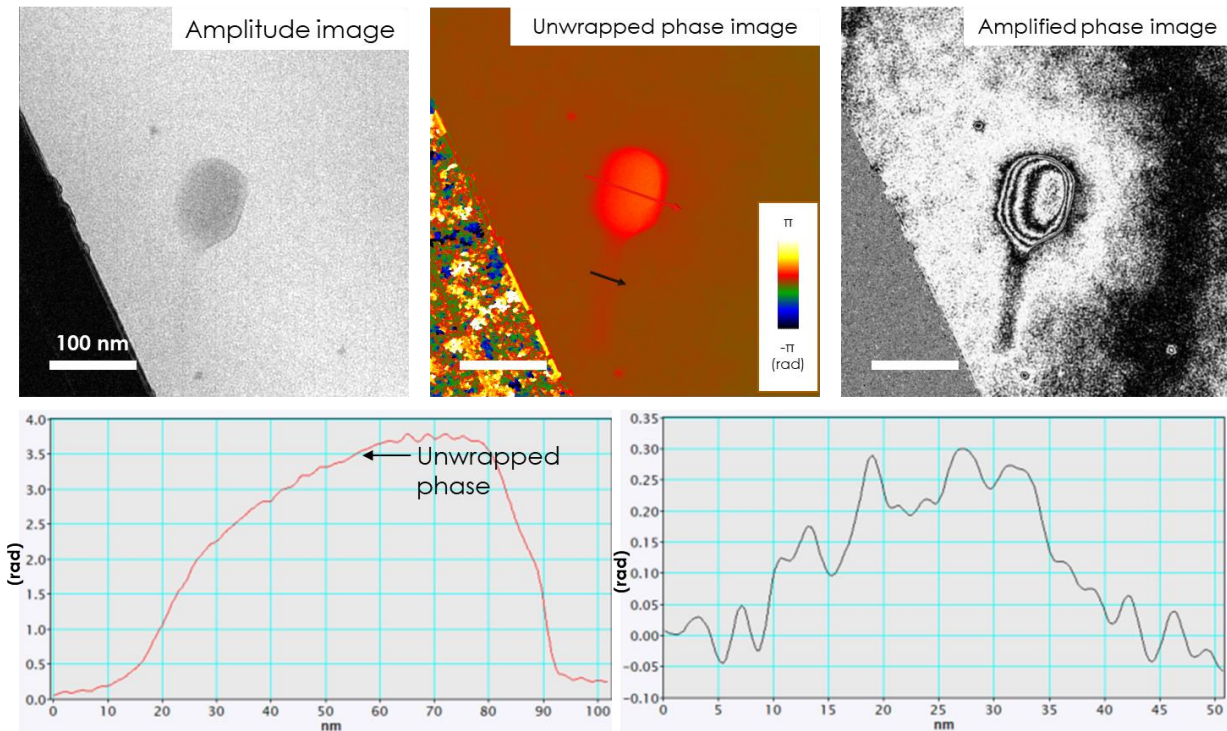


Figure 3.9 Off-axis holography of a contrast enhanced T4 phage. The amplitude image shows a darkened capsid. In the unwrapped phase image, we can see a high induced phase shift and a clear and very well defined tail. The isophase of the phase image shows that the tail rings are not visible. The capsid phase profile (bottom left) and the tail phase profile (bottom right) of the unwrapped (linearized) phase are shown. The 'y' axis is in rad and the 'x' axis in nm. The phase sensitivity is 0.09 rad.

3.2.4 From a CMOS OneView camera to a K3 direct detector

Despite the improvements we described previously, the resolution and phase sensitivity remained insufficient at electron doses below $100 \text{ e}^-/\text{\AA}^2$ to get 4 nm details, due to a too low fringe contrast. We had however the chance to acquire during the last year of this PhD a K3 DDD from Gatan[®]. It took nevertheless more than 5 months for the K3 to be installed and it was finally functional only in November 2022, few months before the end of this PhD.

Using this new direct detector camera, the fringe contrast in vacuum improved by 3 to 4 times. We could then reduce the fringe spacing, meaning getting a better spatial resolution while keeping a high fringe contrast above 30%. Furthermore, the contrast of the hologram is sufficient at very low doses to correct for the stage drift, which was previously not possible with the OneView camera.

In off-axis holography, FT of holograms acquired with a OneView camera display a large central band (figure 3.10a) as well as more extended side bands. On the contrary, due to a reduced low frequencies noise on the K3 camera, the central spot in the FT of holograms is much smaller (figure 3.10b), which permits to choose larger numerical masks for the side band selection without adding noise from the central band [8].

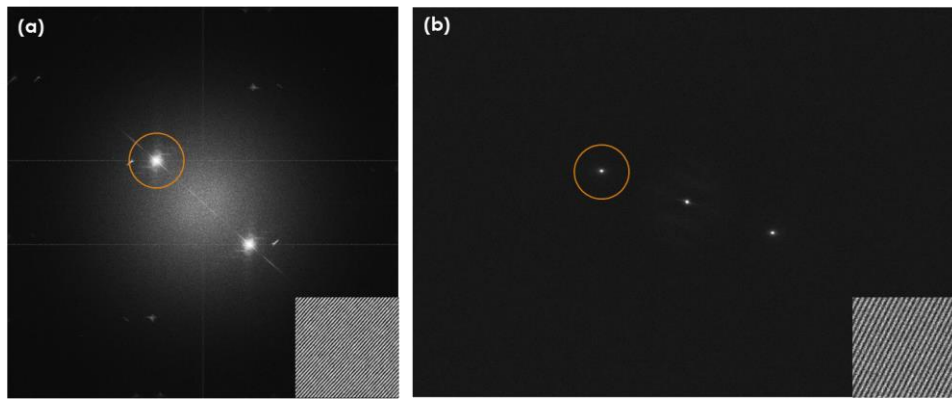


Figure 3.10 Comparison of the FT of a hologram taken with (a) the one view CMOS and (b) the K3 DDD. The fringes of each FT hologram are shown in the bottom right corner but differ in the experimental parameters. A numerical circular mask used for amplitude and phase extraction is shown on a side band in both images.

High electron dose protocol

We first compared this new K3 camera with the OneView camera, by studying unstained T4 bacteriophages at "high" electron doses ranging from 150 to 450 $e^-/\text{\AA}^2$. An example is shown in figure 3.11 with a T4 virion deposited on an ultrathin carbon support grid. The fringe spacing in the hologram was 0.57 nm and the total electron dose 213.73 $e^-/\text{\AA}^2$. It is lower than the dose of 387 $e^-/\text{\AA}^2$ used for the experiment in figure 3.6, although remaining high for a non-protected biological object.

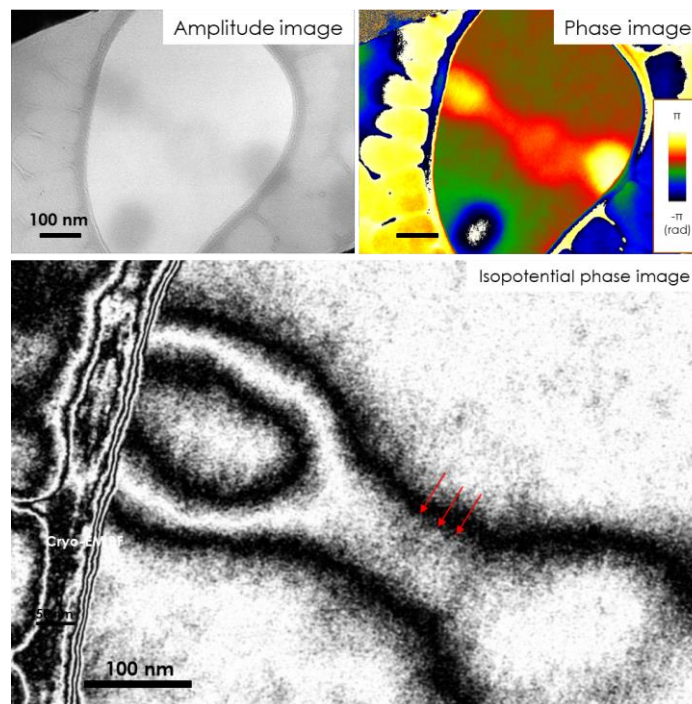


Figure 3.11 Off-axis holography of the T4 bacteriophage on ultrathin carbon using the K3 direct electron detector. The amplitude image shows the capsids of three phages in the FOV. The phase image shows the three phages, two of which appears to be attached to a contamination. The isophase ($\cos [6 \times \text{phase}]$) phage image shows the T4 with its tail. A periodic signal similar to tail rings is pointed at by the red arrows.

The amplitude image in figure 3.11 shows 3 phages. Two phages are evidenced in the phase image with a flat support below them, as well as a third phage of opposite phase sign indicating that it comes from the other side of the biprism (ghost image). In the isophase of

the phase signal, a periodic signal appears in the phage tail. Three of them, which are the most visible are pointed at by the red arrows. Although this looks like tail rings, the noise and high electron dose makes it impossible to determine the nature of this signal that is not visible in the raw phase image.

In general, a clear improvement in the phase sensitivity and better phase images were obtained when using the K3. We also noticed a two times improvement in the fringe contrast with this camera as well as a noticeable reduction in the noise. With both detectors, the maximum phase shift measured at the capsid was the same, varying between 2 and 2.5 rad.

High dose off-axis holography experiment on T5 bacteriophages

We aimed at reproducing the conventional off-axis holography experiments we performed on the T4 bacteriophage with T5 virions. We therefore initiated a collaboration with Dr. Amélie Leforestier at the “Laboratoire de Physique des Solides” (LPS) in Paris-Saclay University who has long been working on these phages. The T5 samples she provided us were suspended in a Tris-HCl buffer with salts. In our observations, T5 virions were mixed with 10 nm gold beads and dropcasted on a graphene grid. The results are reported in figure 3.12. The fringe spacing in the hologram was 0.54 nm and the total electron dose in this test experiment was $142.5 \text{ e}^-/\text{\AA}^2$. The T5 bacteriophage differs from T4 by the smaller diameter and longer length of the tail. The T5 tail is 12 nm in diameter [64], to be compared with 20 nm of the T4 tail sheath. T5 tails are less visible in amplitude and phase images, even with a very small fringe spacing combined with a numerical mask leading to 1.08 nm resolution. Contrary to what we observed in the T4 phages, we measured a similar phase shift in all observed capsids of different isolated T5 phages, with a maximum phase shift of ~ 2.2 rad.

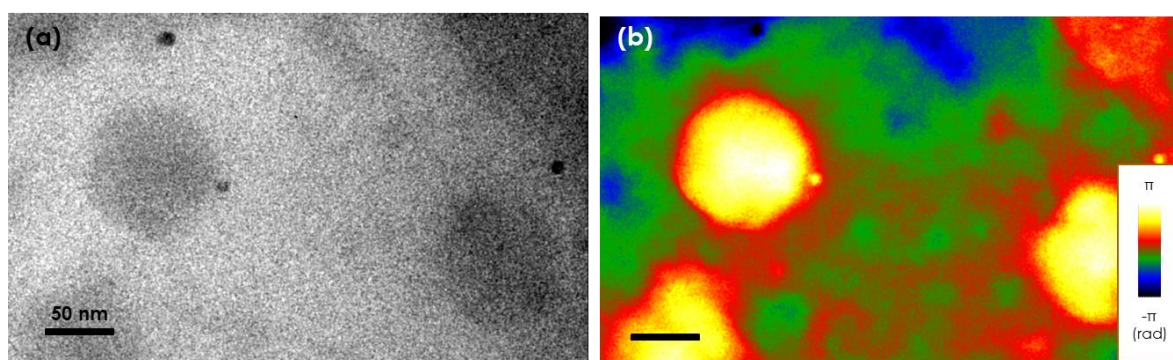


Figure 3.12 Off- axis holography of the T5 bacteriophage on graphene support (Sara Bals) using the K3 direct electron detector. (a) Amplitude image of the hologram. The phages capsids are visible while the tails are not. (b) Phase image of the T5 hologram. We can see very good contrast on the capsid, but with no tail phase signal. The phase sensitivity is 0.09 rad.

The T5 tail in the case of the unstained bacteriophage is however visible in under-focused images in BF (not shown). Due to the storage of the T5 for many months during the K3 installation on the I2TEM, contaminations appeared in our solution which made it difficult to acquire many images. However, imaging clean areas in low dose was successful as shown in the low dose part below.

Low electron dose protocol

To fully test the performances of off-axis holography with the K3 camera, we performed low dose imaging on the T4 bacteriophage. As no low dose automation is available

on the I2TEM microscope, an acquisition procedure workflow, presented in the figure 3.13, has been created:

1. First, the stage is moved to an empty area not far from the sample, and we switch to the ‘*record mode*’ and set the focus (figure 3.13 left).
2. The fringe movement correction parameters are then calibrated as well as the stage drift correction parameters. Regarding the latter, the stage motion is corrected by a feedback loop that detects a movement in a specified square on the live camera image and compensates by moving the sample stage [207]. However, the sample stage movements on the I2TEM correspond to different x and y axis on the camera depending on the sample stage position, which therefore needs calibration.
3. The objective astigmatism is then corrected.
4. We switch to the wide FOV and lower dose in the so-called ‘*search mode*’ to locate the sample (figure 3.13 middle). At that step, another mode, called ‘*minimum dose record mode*’, is selected. In this mode, the dose is reduced to the minimum while allowing gold beads to remain visible. The fringe movement correction is also started. A gold bead or other highly contrasted object is selected so we can launch the drift correction immediately before beginning the acquisition. This step only takes up to 5 seconds. The last operation then consists in adjusting the dose at the target value by setting the original C1 lens value, starting the drift correction and immediately starting the acquisition. This low-dose procedure was used for both room and cryogenic temperatures.

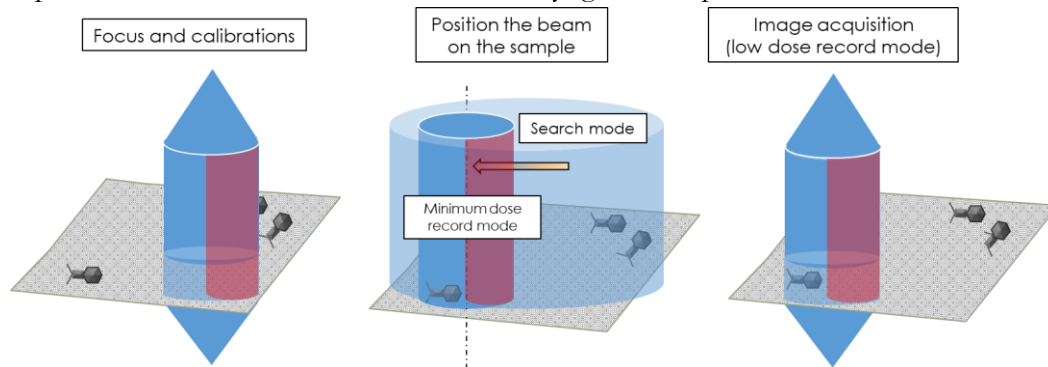


Figure 3.13 Low dose acquisition scheme.

A low dose experiment performed on the T4 bacteriophages on graphene quantifoil at room temperature is presented in figure 3.14. The fringe spacing in the hologram was set to 1.46 nm which in theory is sufficient to visualize the tail rings based on the usual sizes of selected numerical masks in the reconstruction procedure. The total electron dose of $31.2 \text{ e}^-/\text{\AA}^2$ was sufficient to get amplitude and phase images where both the capsid and the tail of the phage are clearly visible. However, at such low dose, the noise is high, leading to lower the phase sensitivity. This makes it difficult to observe high-resolution structures like the tail rings we aimed at visualizing. It also appears that the graphene support around the phage does not have a uniform thickness. Nevertheless, the phase profiles for the capsid and tail (figure 3.14) showed a maximum phase shift of 2.6 rad for the capsid and 0.25 rad for the tail, in agreement with the high dose experiments. The phase sensitivity in this image is 0.08 rad. We also tried acquiring holograms with doses between $45 \text{ e}^-/\text{\AA}^2$ and $65 \text{ e}^-/\text{\AA}^2$ (not shown), which led to phase images with phase sensitivities between 0.1 and 0.15 rad respectively.

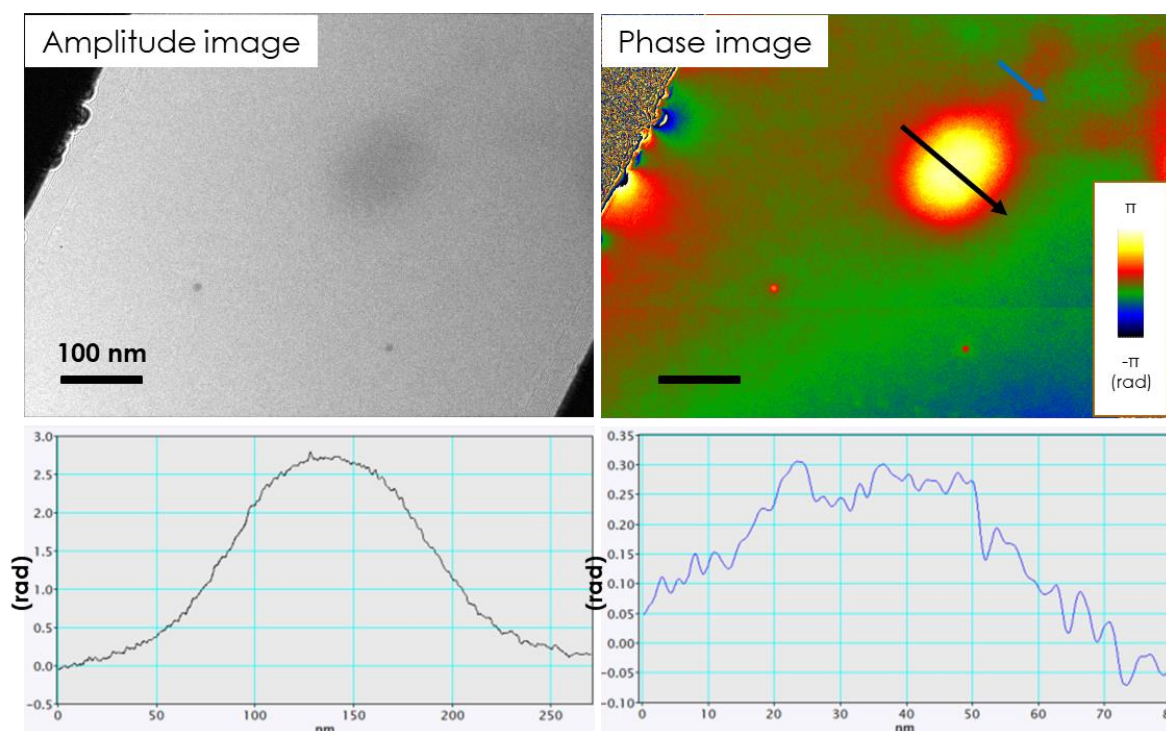


Figure 3.14 Low dose conventional off-axis holography of a T4 bacteriophage on graphene using the K3 camera. *Top:* The amplitude is shown in the top left, and the phase image in the top right. *Bottom:* The phase shift profiles of the capsid (black profile) and tail (blue profiles). The 'y' axis is in rad and the 'x' axis in nm.

To summarize, our off-axis electron holography experiments demonstrate the limitations of this technique when carried out at room temperature. The major limiting parameter is the high electron dose required to obtain phase images, which produces radiative damage, especially at room temperature [22]. This factor is even more critical with respect to our goal of observing unstained specimen, which are less protected compared to stained ones.

Regarding the T5 phage, and to understand the reason behind not seeing its tail in off-axis holography, we conducted off-axis acquisitions in low electron doses regimes, ranging between 50 and 60 $e^-/\text{\AA}^2$. Two examples of phase images of T5 bacteriophages from different holograms are shown in figures 3.15a and 3.15b. Both holograms were acquired on the same grid with a graphene support (from Sara Bals's team). Figure 3.15a shows a phage with a visible tail (black arrow). The phase sensitivity is 0.08 rad, with what looks like contaminations around the phage. The signal of the phage itself is clear. The tail phase shift is 0.25 rad while the capsid phase shift is 2.5 rad (profiles not shown). The tail of the phage in figure 3.15b is also visible (black arrow). The phase sensitivity in this image is 0.06 rad and the support is cleaner (no noise around the phage).

In an attempt to depict the T5 tail rings, we computed the magnified isophase images ($\cos [8 \times \text{phase}]$) that are shown in figures 3.15c and 3.15d. The tails are clearly visible in both. However, the noise in both prevent us from visualizing the rings. The quality of the image is better in 3.15d with less noise which agrees with the lower phase sensitivity. Observing the T5 tail in BF cryo-EM (Talos Arctica) allows visualizing the rings in under-focused images like the one in the figure 3.15e where the rings appear in a however noisy image.

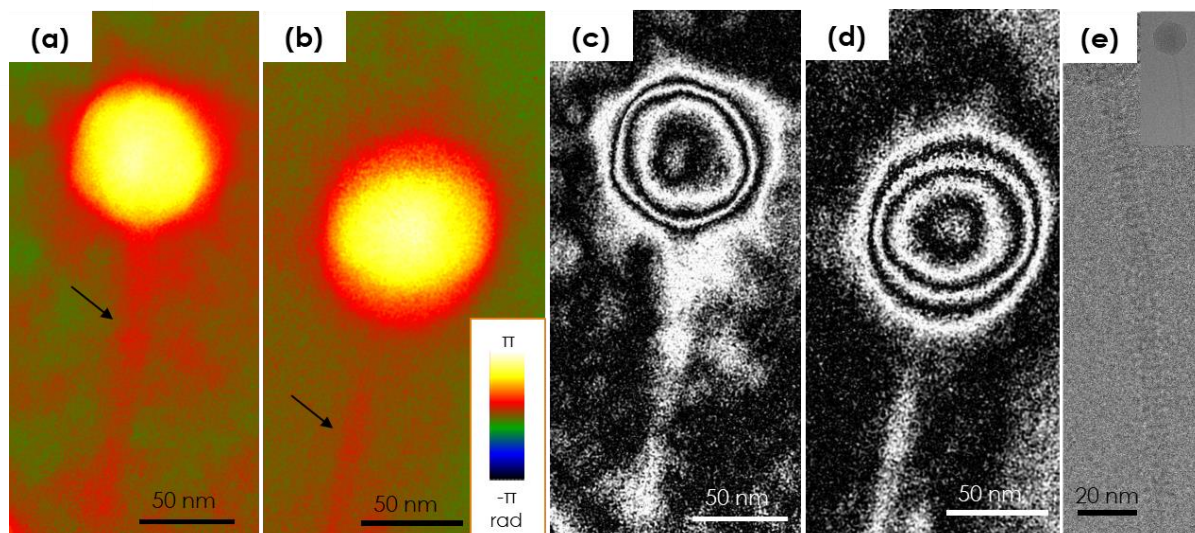


Figure 3.15 Low electron dose off-axis holography of the T5 bacteriophage. (a) Phase image of a T5 bacteriophage with an arrow pointing at the tail. (b) Phase image of a T5 bacteriophage from another hologram with an arrow pointing at the tail. Both (a) and (b) were acquired at $59.7 \text{ e}^-/\text{\AA}^2$. (c) and (d) are the isophase images ($\cos [-8 \times \text{phase}]$) of (a) and (b) respectively. (e) Cryo-EM under-focused image of a T5 bacteriophage's tail (full image in the top right).

Following these low electron dose experiments, it is essential to use low doses less than $80 \text{ e}^-/\text{\AA}^2$ to retain high resolution information while having a good phase sensitivity equal or lower than 0.06 rad (see §3.2.6). A major parameter to achieve such phase sensitivity as best as possible is the quality of the reference beam which should have a constant phase shift, possibly “0” when it passes through a vacuum area as explained in part 2.6.2. Any additional phase shift variation of the reference beam will degrade the final result. In the best conditions in Lorentz mode with a clean solution and thin graphene support, we are currently able to achieve 0.05 radian sensitivity and obtain enough spatial resolution to observe the phage morphology and tail. This is achieved at the cost of a high dose condition i.e. $> 100 \text{ e}^-/\text{\AA}^2$ as low dose results in high phase noise.

In the end, we could not succeed to observe the T4 and T5 tail fibers showing the limits of room temperature off-axis holography sensitivity. Based on our results, off-axis electron holography, at such magnifications, makes it possible to study phages and viruses at room temperature and medium resolutions. This constitutes an improvement over the previously published results with off-axis holography [43], but further improvements are still required to bring a significant gain when compared to current biological imaging techniques.

Evidence of a phase shift dependence on the global charge

In a collaboration with Dr. Amélie Leforestier, we received T5 bacteriophages treated with spermine (spT5), a polyvalent cation. This treatment neutralizes the DNA, normally negatively charged, by entering the T5 capsid [208]. Our original goal was to study the charge effect on the bacteriophage by cryogenic in-line holography. However, we could not thoroughly analyze the in-line holography data because of time-constraints.

The spT5 phages were suspended in the same Tris-HCl buffer as for the non-treated T5 with the only addition of spermine. The non-treated phages were deposited on a graphene support (from Sara Bals' group) whereas the spermine treated ones were deposited on ultrathin carbon (Ted Pella[®]).

The spT5 were imaged by off-axis electron holography on the I2TEM, equipped with the K3 DDD. Three examples are shown in figure 3.16a, two of non-treated T5 phages, labeled ‘normal’ and one of spermine-treated T5 phages, labeled ‘spermine’. Profiles were taken across 4 phages and are displayed in the graph in figure 3.16b. A clear difference arises between the profiles of the non-treated and spermine-treated phages. The former induces a maximum phase shift of 2.5 rad and the latter a phase shift of 1.6 rad.

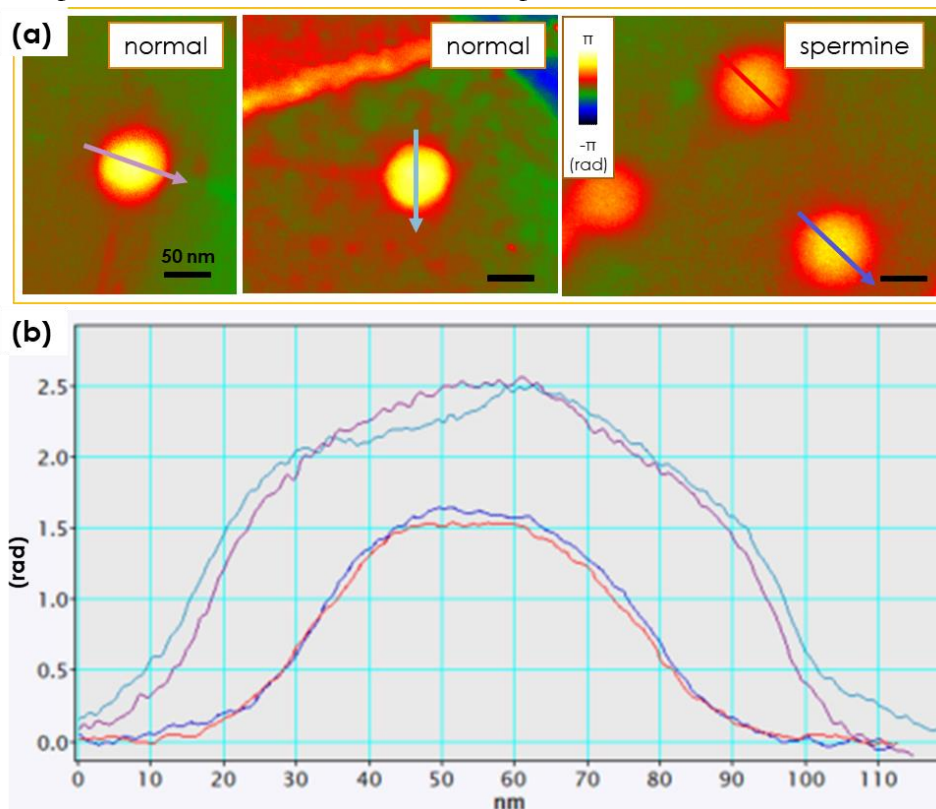


Figure 3.16 Comparison of the capsid phase shift of non-treated and spermine-treated T5 bacteriophages. (a) Images of the 4 phages used in this figure. The first two (left and middle) were taken at a low electron dose ($60 \text{ e}^-/\text{\AA}^2$) whereas the one on the right was taken at a high dose ($188 \text{ e}^-/\text{\AA}^2$). The phase sensitivities from left to right are 0.06, 0.08 and 0.05 rad. The profiles shown by the arrows are displayed in the graph in (b). Each colored profile corresponds to the same color arrow on the images.

This difference is not dependent on the electron dose as we showed in the T4 experiments. Furthermore, the low resolution morphology of the capsid is not altered as already demonstrated at high doses (below $450 \text{ e}^-/\text{\AA}^2$) on the T4 phages. Therefore, as the beam phase shift obtained in off-axis electron holography measures the local electrostatic potential, we argue this phase shift difference measure the DNA neutralization. More experiments are however needed to quantify the loss of charges before and after the DNA neutralization.

This experiment highlighted the potential of off-axis holography in detecting, and probably measuring charge differences between samples submitted to various chemical treatments.

3.3 CRYOGENIC OFF-AXIS HOLOGRAPHY

3.3.1 Towards cryogenic off-axis holography

After conducting experiments on phages at room temperature, off-axis holography experiments were performed in cryogenic conditions. Off-axis holography has rarely been tested in cryogenic condition before and without much success. Several reasons can explain why only two attempts were performed by Harsher in his thesis submitted in 1999 [9], and by Weierstall and Lichte in 1996 [209]:

1. The ice surrounding a sample shifts the phase, lowering the contrast of the hologram fringes, thus increasing the noise.
2. The sample sensitivity to the beam and the beam-induced sample motion [43].
3. The premature state of cryo-EM and the limited hardware and software capabilities that were available at the time, especially regarding detectors.
4. The total absence of cryo-EM dedicated microscopes equipped with biprisms and the absence of automation for low dose acquisition on biprism-equipped microscopes.
5. Furthermore, the big development of cryo-EM in the last 20 years has raised the expectations for developing new techniques and shifted the focus to the now routinely achievable sub-4 angstrom resolutions.

In this thesis, we faced many challenges to develop this “cryo-Holo” experiment. In particular, no cryo-EM experiment has been previously performed on the I2TEM, which was not equipped for this application. For this purpose, we purchased a multi-specimen cryo-Transfer Holder model 910 from Gatan, one of the few compatible with the Hitachi HF3300, together with the model 1905 temperature controller.

To be able to work at low temperatures and low doses, we developed the manual low dose workflow depicted in figure 3.13, and tested the cooling down of the sample holder and the two liquid N₂ traps of the I2TEM, before experimenting on a real sample. Most importantly, the installation of the K3 camera made it possible to go to very low doses while having enough fringe contrast.

The sample holder (SH) as well as the cryogenic station are shown in figure 3.17a before the insertion in the upper Lorentz stage, and after insertion in figure 3.17b. We also acquired for this thesis a cryogenic container to store the vitrified samples at the CEMES, where the experiments are carried out, as well as a secondary vacuum pumping station (figure 3.17c) for the cryo-SH bake-out cycle. The bake-out cycle consisted of heating the nitrogen container of the SH (see in figure 3.17a) at 100°C for 6 hours under secondary vacuum the night before the experiment.

All the mentioned hardware were crucial for the following experiments, together with the software part explained previously in the part 3.1.2.

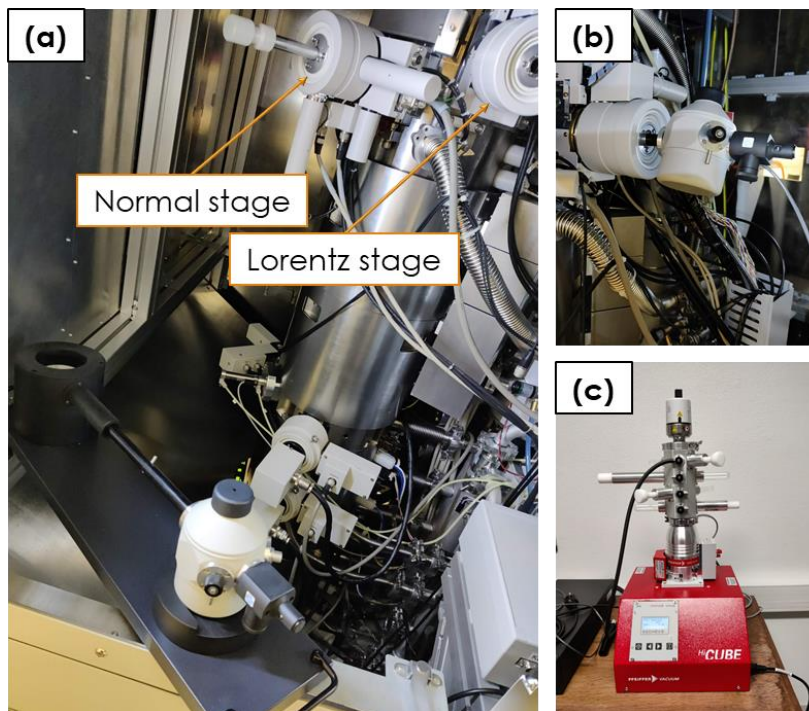


Figure 3.17 (a) Cryogenic sample holder in its station. The station helps cooling the tip and keeps it in liquid nitrogen for sample transfer. (b) Cryogenic sample holder inside the Lorentz upper stage inside the column and outside of the beam (before contact inside the microscope). (c) Turbo pumping station by Fishione capable of secondary vacuum. It was modified to add a Hitachi side entry.

3.3.2 The challenges of cryogenic microscopy on the I2TEM

With all the available hardware and software, we had to solve, bypass or limit some challenges, thus preventing us from working under optimal conditions. Not having any automation on the I2TEM microscope made the low dose experiments challenging. The “lenses-BD” software developed by Christophe Gatel was a great help as explained previously, but not enough on its own to make the whole process fast and easy. The ‘*search mode*’ and ‘*record mode*’ have to be set prior to introducing the sample holder in the beam path. This is done manually before saving all the lenses parameters and transferring them in the ‘lenses-BD’ plugin. The dose is also calculated and set in vacuum. For ‘*search mode*’, the dose is always set to $\sim 0.008 \text{ e}^-/\text{\AA}^2\cdot\text{s}$. The dose and the lens parameters are then set for the ‘*record mode*’ (target dose: $65 \text{ e}^-/\text{\AA}^2$). We insert the sample holder under the beam and search for the sample in ‘*search mode*’. After finding a ROI, 5 minutes of waiting time is required to minimize or even stop the sample holder drift. This is done by staying in ‘*search mode*’ and blanking the beam by closing the gun valve. When ready for acquisition, the gun valve is opened and the position of the stage adjusted before switching to ‘*record mode*’ for acquisition.

Beyond developing automation, the main problem on the I2TEM came from the sample holder itself. In Hitachi microscopes, the tip of the sample holder comes in contact with the goniometer in the so-called “ear” to allow the ‘y’ axis movement. Without this contact, when the SH is not fully inserted, only movements along the ‘x’ axis are possible. In cryo-EM, we noticed an increase in temperature of the SH due to this contact. It went from -175°C when partially inserted (figure 3.18a) to either -162°C or -164°C , with one or two liquid nitrogen traps filled respectively, when fully inserted (figure 3.18b).

A first solution is presented in figure 3.18c where the sample holder, initially in the SAS position at -175°C is inserted inside the beam. We then have 4 to 5 minutes to operate before the temperature reaches -169°C . At this point, we pull the SH to the SAS position and let the temperature decrease. After 8 minutes, the temperature is back to -175°C and we can repeat the cycle. However, this method does not allow to have 5 minutes of resting time after insertion, which is essential to limit the drift. Furthermore, in absence gold particles in the frozen sample, which can often be the case, the drift correction algorithm cannot be used. Therefore, this approach was abandoned. We instead tried to keep the temperature as low as possible by filling the two liquid nitrogen traps which limited the increase of the temperature to -164°C instead of -169°C .

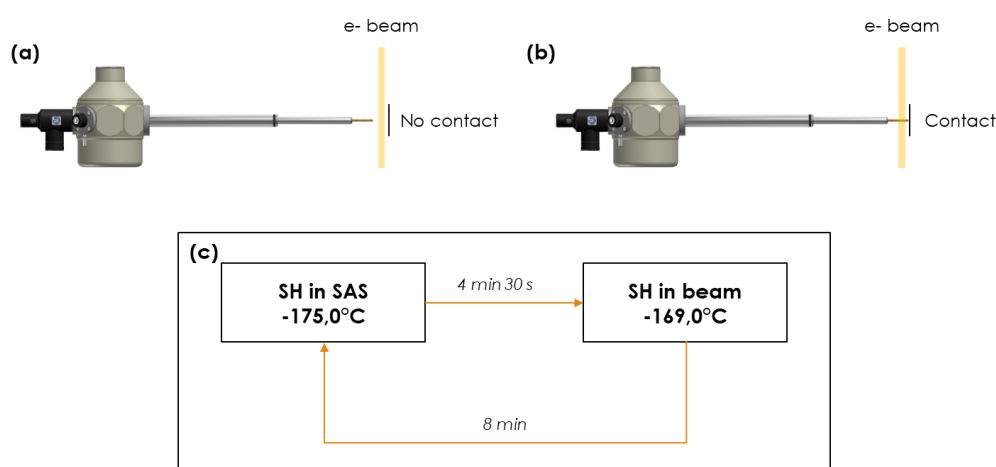


Figure 3.18 (a) Cryo-SH in the 'SAS' position: inside the column and outside the beam path. (b) Cryo-SH in the 'inside' position: Inside the column and inside of the beam path. We have contact with the microscope component. (c) Method to prevent the temperature of increasing above -169°C .

Nobel laureate Prof. J. Dubochet reported that the crystallization of vitreous ice starts when the temperature goes above -163°C [95]. McMillan and Los used X-rays to study ice devitrification. They found a variable crystallization temperature between -133°C and -117°C depending on the warm-up rate [210]. Overall, these published data suggest that temperatures between -164°C and -164.5°C should be safe to prevent ice crystallization. However, we did observe crystallization of the amorphous ice under our experimental conditions, followed by ice sublimation, which often did not allow to perform observations. For example, we were able to conduct an experiment at -162°C , and had only one in 10 squares with crystallized ice. This could be related to the ice thickness or the temperature increase rate. In total, only a few "cryo-Holo" sessions were successful in which we obtained the results presented below.

3.3.3 Dose limitation

As already presented in the previous pages, phages, as all biological samples, are very sensitive to electron irradiation. Our room temperature experiments demonstrate how difficult it is to visualize the 4 nm periodic structure of the phage tail chosen as test. In the following, we aimed at quantifying the maximum dose the phage can support at low temperatures before its structure gets damaged to evaluate the maximum electron dose we can use in our low dose, low temperature acquisitions.

Our experimental method was to analyze in cryogenic conditions on the Jeol 2100 at the CBI, the damage induced by electron irradiation using different electron dose increments. Our main results are presented in figure 3.19. In this experiment, the phages were located in a thin ice region of the grid. Similar experiments were also conducted in areas with thicker ice for comparison (data not shown). In the shown example, we exposed the same area multiple times with an electron dose of $20 \text{ e}^-/\text{\AA}^2$. The images were then aligned using ‘Digital Micrograph’ software. We used the cross-correlation coefficient as an easy and effective way to assess the evolution of the phage damages as a function of the electron dose. The cross-correlation coefficient of image “n” (dose = $n \times 20 \text{ e}^-/\text{\AA}^2$) was measured relative to the first image acquired with a $20 \text{ e}^-/\text{\AA}^2$ dose.

The first row in figure 3.19 represents the analysis of the full image (with the lacy carbon included in the image). The slope of the cross-correlation versus the electron dose plot in figure 3.19a shows two parts. The first part for doses $< 70 \text{ e}^-/\text{\AA}^2$, corresponds to the degradation of high frequency details, as seen in the images shown in figure 3.19 b and 3.19d where tail details disappear above $60 \text{ e}^-/\text{\AA}^2$. At higher doses, the lacy carbon and the capsid structure are damaged and bubbles form in the ice at about $120 \text{ e}^-/\text{\AA}^2$. When we perform the same analysis on the capsid and the tail only, on an area shown in the yellow square in figure 3.19b, we obtained a slightly different cross-correlation curve shown in figure 3.19c. In this case, we observe 3 different behaviors when increasing the dose. The first one corresponds to high frequency damages for doses less than $70 \text{ e}^-/\text{\AA}^2$, followed by a plateau between 80 and $140 \text{ e}^-/\text{\AA}^2$. In this dose range, more specifically around $120 \text{ e}^-/\text{\AA}^2$, we observe low resolution beam damage and bubbling in the capsid. The orange arrow shows the tail rings which disappear for doses between 60 and $80 \text{ e}^-/\text{\AA}^2$, whereas the capsid ‘Hoc’ proteins, that appear like filament around it (yellow arrows), remain visible until $100 \text{ e}^-/\text{\AA}^2$. The third part of the graph corresponds to the low frequency damages and bubbling.

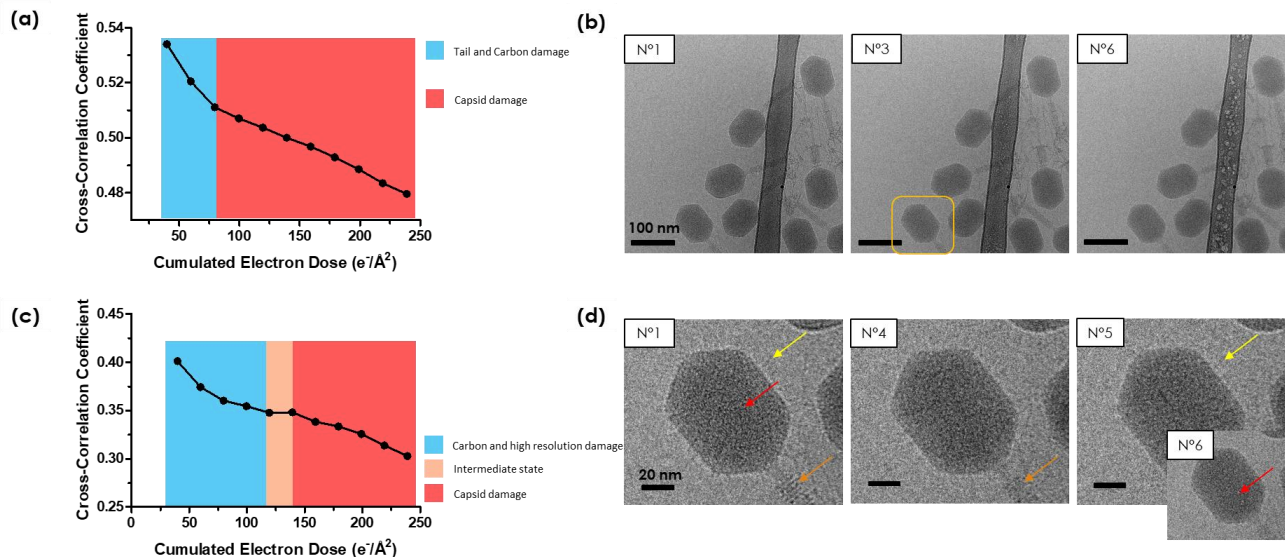


Figure 3.19 Electron dose damage test in cryogenic condition by multiple exposures of the same FOV by increments of $20 \text{ e}^-/\text{\AA}^2$. The images were previously aligned before calculation. (a) Cross-correlation coefficient variation regarding the electron dose for the full image (shown in (b)). (b) Images of the exposures n°1, 3 and 6 corresponding to total electron doses of 20, 60 and $120 \text{ e}^-/\text{\AA}^2$ respectively. (c) Cross-correlation coefficient variation regarding the electron dose for a cropped image (shown in (d)). (d) Crop of the yellow square ROI in (b) showing the tail (orange arrow), capsid decoration protein ‘Hoc’ (yellow arrow), and capsid (red arrow) at the doses for which we lose the corresponding structure’s signal. The images correspond to total electron doses of 20, 80, 100 and $120 \text{ e}^-/\text{\AA}^2$ respectively.

To summarize our experiments, the tail structure is damaged at doses around $70 \text{ e}^-/\text{\AA}^2$ while the phage overall shape remains intact for such doses. Or, this approach is nonetheless not very precise as we are not looking at the object live during exposure. Another way would be to acquire a video of our sample while it is exposed to a constant electron dose. A more quantitative approach would be to study the disappearance evolution of the diffraction reflections corresponding to the tails rings as a function of the dose in the diffraction pattern [211,212].

These results can be compared with the analysis of the evolution of the diffraction pattern of crystallized proteins exposed to electrons. This can be much more quantitative as it makes it possible to follow live the resolution deterioration by looking at the diffraction spots. An example is a study by Glaeser and Taylor on a crystallized enzyme, namely the catalase [213]. In their publication they plotted the intensity decay of different diffracted spots as a function of the dose in electron diffraction experiments carried out at different temperatures. In the cryogenic experiment, they used 100 keV electrons [94]. We interpolated the curve presented in the first figure of Glaeser and Taylor's publication [94] to estimate the maximum dose supported by catalase protein before 4 nm structural details are damaged and compared it with our experimental measurements on T4 bacteriophage. These interpolations of the limit dose give $0.4 \text{ e}^-/\text{\AA}^2$ at room temperature and $2 \text{ e}^-/\text{\AA}^2$ at -120°C (frozen hydrated catalase). These doses are low as the typical values in cryo-EM are around $40 \text{ e}^-/\text{\AA}^2$ [214]. Nonetheless, the current cryo-EM microscopes operate at 200 or 300 kV acceleration voltages making the values we interpolated hard to compare as the electrons interact differently with the samples depending on their energies [19].

3.3.4 Off-axis cryo-holography of T4 and T5 bacteriophages

We first performed off-axis cryo-holography experiments on the T4 bacteriophages. We plunge-frozen T4 solutions deposited on lacey grids at the CBI before transferring them to the CEMES. Electron doses ranging from 30 to $70 \text{ e}^-/\text{\AA}^2$ were used for most acquisitions. High doses around $100 \text{ e}^-/\text{\AA}^2$ were also tested to see the effect of the electron dose on the SNR.

Figure 3.20 shows two low dose experiments obtained by cryogenic off-axis holography on frozen sample. In figures 3.20 a, b and c, the hologram was acquired during 20 seconds with a total dose equal to $47.3 \text{ e}^-/\text{\AA}^2$. The amplitude image in figure 3.20a shows very low contrast and is quite noisy due to the amorphous ice surrounding the object. Conversely, the phase image in figure 3.20b is much more contrasted, with the capsid, the tail and the baseplate visible and well defined even if a large phase heterogeneity appear in the background. The phase sensitivity of this image is 0.16 rad, a value that is much higher than the 0.06 rad sensitivity we target. This high noise makes it impossible to visualize the tail rings of the T4 (and neither the tail fibers). Computing the isophases reveals all the neighboring phages with similar phase shifts (figure 3.20c). It is worth noting that it is difficult to find isolated phages, in other words empty reference areas close by to overlap with our ROI, as phages tend to cluster in cryo-EM (cropped out in this example).

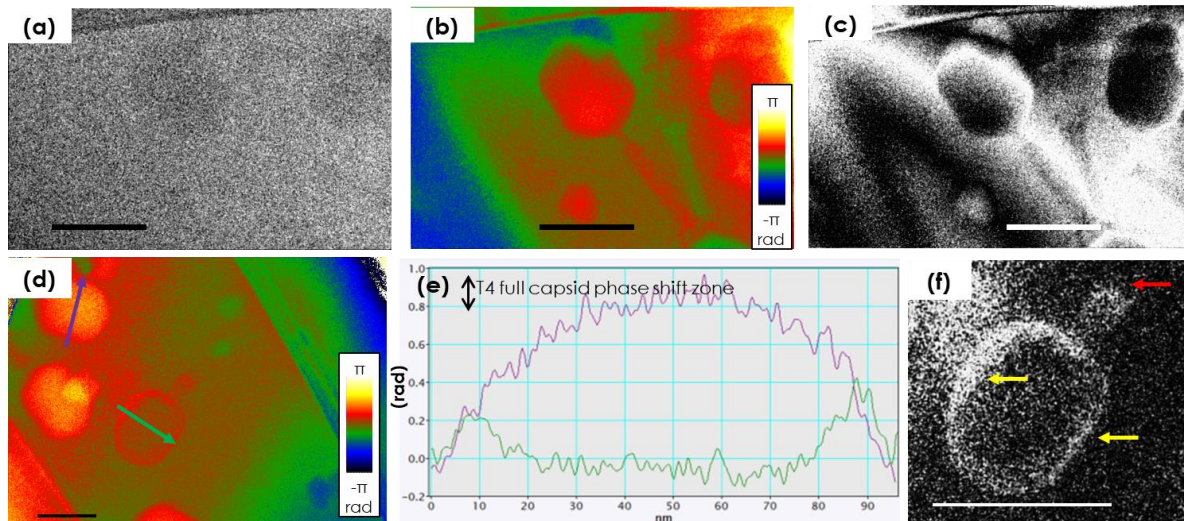


Figure 3.20 Low electron dose cryogenic off-axis electron holography of the T4 bacteriophage. (a-b-c) First hologram analysis. (a) Amplitude image of the first hologram. (b) Phase image of the first hologram. (c) Isophase ($\cos [5 \times \text{phase}]$) image of the phase shown in (b). (d) Phase image of the second hologram. (e) Phase profiles of the empty (green profile and arrow) and full (purple profile and arrow) capsids. The double arrow shows the zone of maximum shift values of full capsids. (f) Isophase image ($\cos [-5 \times \text{phase}]$) of the empty capsid phage in (d) showing the capsid and the tail. The scale bars are all 100 nm.

The second example (figure 3.20d) shows a contracted empty phage. In this experiment, the hologram was acquired over 20 seconds with a total dose of $47.4 \text{ e}^-/\text{\AA}^2$. Even though the background is more homogeneous than in the first example, the phase noise is high with a 0.16 rad phase sensitivity. Nonetheless, we can see in figure 3.20e that the empty capsid has a phase shift around zero compared to the 0.9 rad at maximum for the full capsid, indicating the absence of DNA. For comparison, a full capsid in cryogenic low dose conditions (less than $70 \text{ e}^-/\text{\AA}^2$) induces phase shifts between 0.8 and 1 rad as we determined in figure 3.20e. The phase shift induced by the borders of the capsid in the 2D projection reaches around 0.3 rad as can be seen from the empty capsid phase profile. When computing the isophase of the phase image of the empty phage (figure 3.20f), we can notice two things:

1. The phase signal of the capsid is asymmetric (yellow arrows) probably due to the noise and the contamination signal visible on the left of the capsid in figure 3.20f.
2. The tail tube is not visible (red arrow), which indicates the phase sensitivity is not sufficient.

Given the high level of noise in the phase images at low dose, we performed acquisitions at higher doses. Figure 3.21a shows the phase image obtained from a 20 second hologram with $101 \text{ e}^-/\text{\AA}^2$. Within our expectations, the phase sensitivity improved to 0.08 rad at the cost of the beam damage. This dose destroys the structure of the tail as we observed earlier in part 3.3.2. In figure 3.21a, two much better-defined bacteriophages surrounded by a homogeneous background are evidenced. Not only are the capsid and the tail well distinguished separated by the collar, but the baseplate is also clearly visible in the phase image, with the tip of the tube pointing out of the baseplate on one of them (see phage pointed by the black arrow in figure 3.21a). However, the tail rings are not visible, which is probably due to radiation damage. In this phase image, the capsid maximum phase shift is 0.8 rad which is the value obtained in low dose cryogenic experiments (figure 3.21b - green profile). The phase shift of the tail is 0.3 rad (blue profile). This experiment evidences once again the double phase

noise-electron dose problem as the rings are not distinguishable, in this case most likely due to the electron beam damage, making it difficult to achieve high resolution images.

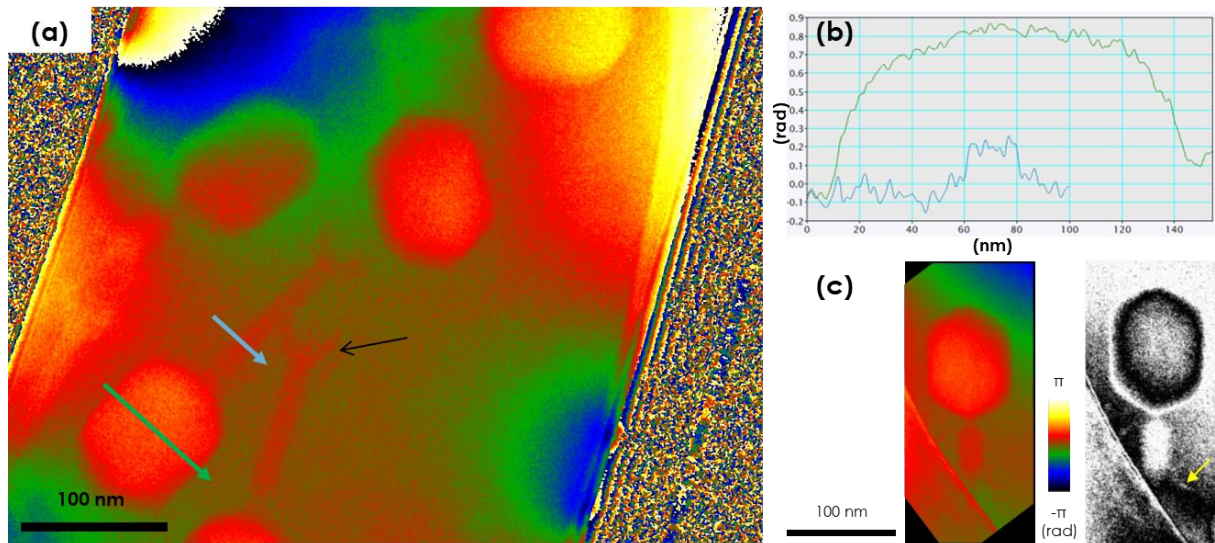


Figure 3.21 High electron dose cryogenic off-axis electron holography of the T4 bacteriophage. (a) Phase shift image of the T4 bacteriophages. (b) Phase profiles of the capsid (green) and tail (blue) of the T4 phage in (a). (c) *Left*: Cropped raw phase image of a contracted T4 phage. *Right*: Isophase ($\cos [5 \times \text{phase}]$) image of the phase. The yellow arrow shows a visible tail fiber.

At these higher electron doses, we could also distinguish details on a contracted phage as shown in figure 3.21c (left). Here, the phase image was obtained from a 20 second hologram with total dose of $99.5 \text{ e}^-/\text{\AA}^2$. The phase sensitivity is 0.08 rad. The phase image shows a T4 bacteriophage with a fully contracted tail. We believe this conformation appears to be a preparation artifact as the phage still contains its DNA. When looking at the isophase image in figure 3.21c (right) we can clearly see the contracted tail sheath. The tail sheath fringes are visible in the isophase image when looking along the left border of the sheath, the right side being noisier. We can also identify one tail fiber (yellow arrow).

To complement the experiment performed on the T4 bacteriophage, we performed observations with T5 virions provided by Dr. Amélie Leforestier. Figure 3.22 shows a phase image extracted from a 20 second hologram with a total electron dose of $51.8 \text{ e}^-/\text{\AA}^2$. The phase sensitivity in this image is 0.08 rad. In this experiment we were able to obtain holograms with a weaker noise than previous holograms acquired in the same dose range. The phase image in figure 3.22a shows a non-homogeneous background signal across the FOV (left to right). In absence of carbon support on these grids, we attribute this variability to differences in the ice thickness. The tails of the T5 phages, which are 12 nm in diameter, are visible. Similar to T4 tails, the tail rings of the T5 phages were not detected, due to insufficient phase sensitivity.

The full capsid is well defined as we can see in figure 3.22b and induces a maximum phase shift of 0.9 rad (figure 3.22d, blue curve). On the other hand, the empty capsid shown in figure 3.22c, that is obtained by analyzing another hologram with a total exposure dose of with $38.8 \text{ e}^-/\text{\AA}^2$, produces a 0.2 rad phase shift at the borders while it is almost zero inside (figure 3.21d, red curve).

The phase shift of the T4 and the T5 capsids are similar due to the fact that they both have similar diameter: 86 nm for the T4 [61] and 90 nm for the T5 [215]. Therefore, the average means inner potential of both capsids do not differ much resulting in a similar phase shift.

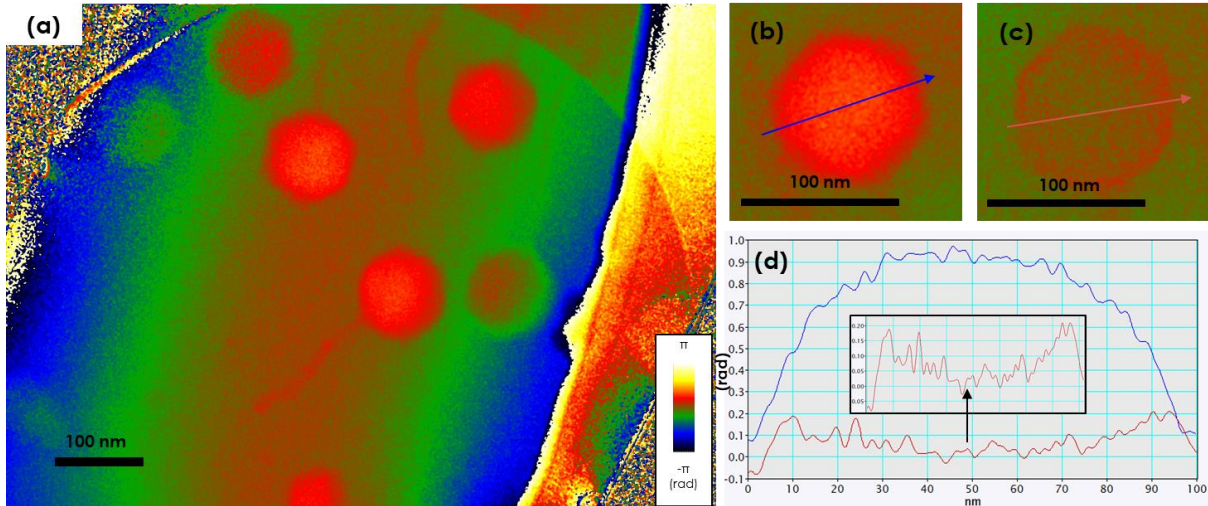


Figure 3.22 Low electron dose cryogenic off-axis electron holography of the T5 bacteriophage. (a) Phase image of T5 bacteriophages. (b) Crop of the phase image in (a) showing a full T5 capsid. (c) Crop of another phase image showing an empty T5 capsid. (d) Phase profiles of the full and empty capsids shown in (b) and (c) respectively. The x axis is in nm and the y axis in rad.

Phase shift decrease upon vitrification

One final observation is the lower phase shift values measured on the capsid in cryo compared to the ones measured at room temperature. This is obtained for both T4 and T5, and for all phase images and is not related to the electron dose as room temperature experiments did not show a dose-shift dependence. We therefore tried to understand the difference between the measured phase shift in both room and cryogenic temperatures.

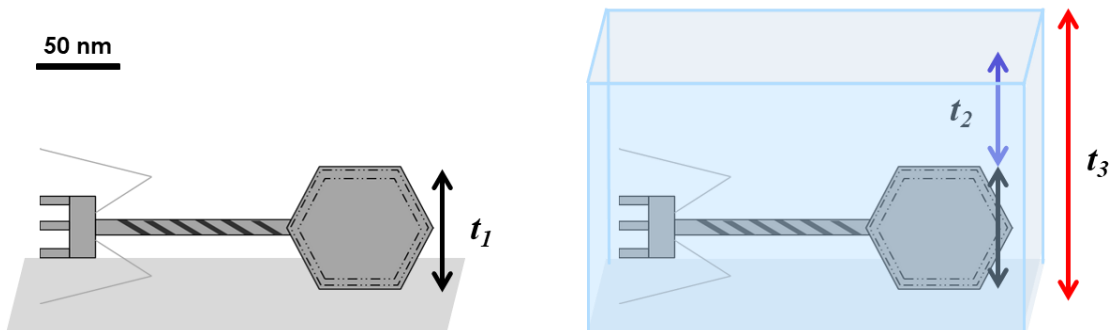


Figure 3.23 Comparison of the electron path through a bacteriophage capsid at room temperature (left) and cryogenic temperature (right). t_1 is the phage capsid thickness, t_2 is the vitreous ice thickness and t_3 the total thickness. In the room temperature figure (left), the total thickness and capsid thickness are the same.

We looked at the phase shift formula, given in equations 1.5 and 1.6:

$$\varphi = C_E \cdot V \cdot t$$

The two conditions were then analyzed.

1. In the case of the room temperature (figure 3.23 left), the phase shift is only due to projected potential V of the capsid (see equation 1.6 for V_p).

With φ_{ref} the phase shift selected in the reference area taken on the graphene or ultrathin carbon close to the sample, in this case negligible, the phase shift measurement due to the capsid compared to the reference is:

$$\begin{aligned}
\varphi_{measured RT} &= \varphi_{capsid} - \varphi_{ref} \\
&= C_E V_{capsid} \cdot t_1 - \varphi_{ref} \\
\varphi_{measured RT} &= C_E V_{capsid} \cdot t_1
\end{aligned}$$

2. In the case of the vitrified bacteriophage (figure 3.23 right), the vitreous ice layer adds additional phase shift. The phase shift of the beam that passes through the capsid and the ice is:

$$\varphi_{measured Cryo} = C_E V_{capsid} \cdot t_1 + C_E V_{ice} \cdot t_2$$

With φ_{ref} the phase shift of the vitreous ice nearby the sample, the measurement of the phase shift is:

$$\varphi_{measured Cryo} = C_E V_{capsid} \cdot t_1 + C_E V_{ice} \cdot t_2 - C_E V_{ice} \cdot t_3$$

as $t_3 = t_1 + t_2$:

$$\varphi_{measured Cryo} = C_E V_{capsid} \cdot t_1 + C_E V_{ice} \cdot (t_2 - t_1 - t_2)$$

$$\varphi_{measured Cryo} = C_E (V_{capsid} - V_{ice}) \cdot t_1$$

Compared to the phase shift measured at room temperature, the one measured at cryo-temperature indicates a MIP potential of the capsid lowered by the ice MIP and explains the phase shift decay observed in cryogenic conditions.

In addition to the previous explanation, the MIP also decreases with decreasing temperature associated to the density increase of the biological material with temperature decrease. This was evidenced by M.N. Yesibolati et al. in a recent publication [216] where they measured by off-axis electron holography combined with liquid phase TEM the MIP of liquid water of about 4.48 eV, higher than the previously measured MIP of vitreous water of 3.5 eV [217]. In our experiment, the electrostatic potential decrease by this effect is mostly due to the vitrification of the solution inside the capsid.

Our analysis on the decrease of the measured phase shift indicates it is mainly due to the vitreous ice formation with a possible contribution from the decrease of MIP resulting of the variation of the biological sample density when lowering the temperature.

3.3.5 The phase noise problem

Our electron holography experiments in cryogenic conditions show that the phase noise is a major problem preventing us from achieving high single image resolution. Equation of part 3.2.1 shows the phase noise is unavoidable in off-axis electron holography and increases with lowering the dose. With increasing the dose, the phase noise decreases to reach values below 0.06 rad for doses above $200 \text{ e}^-/\text{\AA}^2$. As expected, using a direct electron detector like the K3 camera with a better MTF and DQE, improves notably the phase sensitivity compared to a CMOS camera. The K2 camera already gives a noise reduction in the phase of at least two times as demonstrated by Chang et al. [40]. The noise reduction is even better with the K3 due to a better readout speed and SNR [218,219]. This camera upgrade was essential in making low dose cryo-holography possible. However, even this upgrade, along π -shifting and fringe stabilization were not enough to sufficiently reduce the noise in low doses. Noise remain too high for the resolutions we aimed to achieve.

To illustrate the effect of the dose on the phase noise, we calculated the SNR for cryo-EM phase images and plotted them as a function of electron dose (figure 3.24a). The SNR was calculated using the following formula:

$$SNR = \frac{S_{capsid} - B}{N_{std}}$$

with S_{capsid} the maximum signal coming from the capsid, B the background average signal and N_{std} the average noise, that is the standard deviation measured on a flat empty surface.

Looking at the T4 bacteriophage phase images, with the exception of the hologram with the lowest dose, we can see an improvement of the SNR from 7 around $46 \text{ e}^-/\text{\AA}^2$, up to 11.8 for $100 \text{ e}^-/\text{\AA}^2$. This is explained by the noise decrease from around 0.15 to 0.07 rad, as shown in figure 3.24b. Therefore, it is necessary to have doses of at least $100 \text{ e}^-/\text{\AA}^2$ to go below 0.07 rad. We also looked at the T5 data where we evidenced an increase in the SNR from 1.5 around $35 \text{ e}^-/\text{\AA}^2$ to 8 around $20\text{-}70 \text{ e}^-/\text{\AA}^2$, with one exception to the SNR of 12 at $38.8 \text{ e}^-/\text{\AA}^2$. Improvement of the SNR with the dose was correlated as well to a decrease of the noise (figure 3.24b) with the one exception that we just mentioned. The noise went down from around 0.14 rad for a dose of $32 \text{ e}^-/\text{\AA}^2$ to 0.09 rad for the doses of 51.8 and $69.6 \text{ e}^-/\text{\AA}^2$. These low doses did not allow to reach or go below 0.07 rad.

While electron dose is a critical parameter of the SNR, we note that there is not a strict correlation between phase sensitivity and electron dose, as we could obtain a “good” phase sensitivity for the hologram acquired at a dose of $38.8 \text{ e}^-/\text{\AA}^2$. Understanding the reason behind this, is crucial in reducing the noise as increasing the dose alters the sample. One likely explanation is the ice thickness which reduces the fringe contrast and increases the total phase shift we measured. Furthermore, non-homogeneous ice thickness is expected to induce phase shift variations adding additional phase noise. As in cryo-EM, achieving a low and constant ice thickness constitutes a major challenge for cryo-holography. This is classically achieved by improving the fast-freezing conditions, but also by acquiring a low magnification map of the entire grid in order to choose the squares displaying ice of the best quality. This latter option is currently not implemented on the I2TEM. Furthermore, bacteriophages should be ideally vitrified using Quantifoil grids as the vitreous ice thickness will be ideal for such large samples [220].

Figure 3.24c shows that we were able to obtain the best SNR in off-axis room temperature holography experiments using the K3 camera, which gives an SNR two times better than the CMOS camera. Off-axis holography cryogenic experiments yield a significantly lower average SNR. BF-TEM observation of unstained samples yielded even lower SNR values, although replacing the CMOS detector with a DDD detector doubled it. Finally, conventional cryo-EM experiments, using lower doses than what used for BF imaging at room temperature, show a very low SNR of 0.78. It should be noted that the ambient temperature data are based on measurements at high electron doses.

The results of off-axis experiments carried-out at low doses are encouraging with recent improvements in phase sensitivity due to the use of DDD.

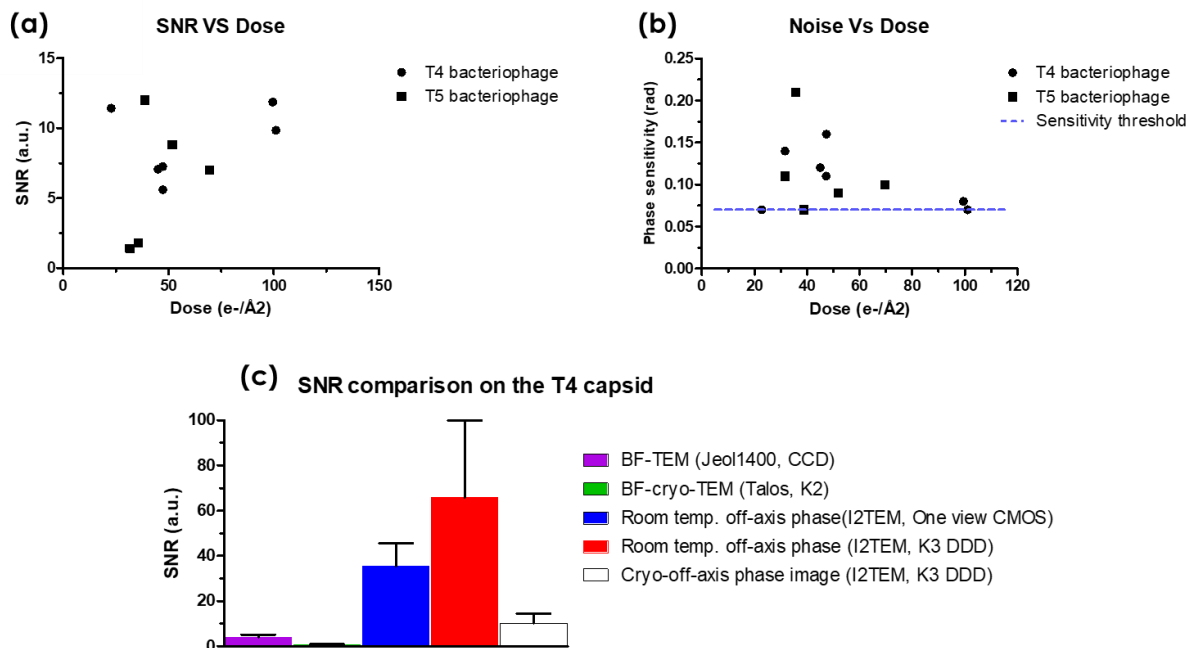


Figure 3.24 (a) SNR of all the obtained phase images of the T4 and T5 samples by cryo-off-axis holography plotted as a function of electron dose. (b) Phase noise in radians of the T4 and T5 phase images obtained by cryo-off-axis holography plotted as a function of electron dose. Our goal is to go below the sensitivity threshold of 0.07 rad. (c) Histogram comparing the best achievable SNR using different TEM techniques: BF TEM on unstained bacteriophages, cryo-EM using a K2 camera, as well as room temperature off-axis holography using either a CMOS or a DDD, and finally off-axis holography in cryogenic conditions using a K3 DDD. Every histogram is the average of three values and the error bar corresponds to the standard deviation.

3.3.6 Conclusion

In this chapter, we showed one of the first cryogenic off-axis holography experiments on biological sample using a K3 DDD and a cold FEG equipped microscope dedicated to electron holography. These experiments show the possibility to acquire holograms at low electron dose and extract phase images with a sensitivity around 0.1 rad.

We however faced major problems. The first one was the technical difficulties linked to the implementation of cryo-electron microscopy on the I2TEM, a microscope that was not designed for this type of application. Hence, the cryogenic stage cannot maintain the temperature at -172°C : it rises to $-164/-162^{\circ}\text{C}$ and favors the crystallization of the amorphous ice. It was therefore difficult to obtain suitable FOVs. Solving this issue may not be trivial as it requires hard-engineering on the holder. Secondly, despite the set-up of several lens modes to perform cryo-EM, low-dose image acquisition remains challenging and automation of the procedure must be improved. Finally, adaptation of the K3 camera to this equipment turned out to be complicated and took several months. This led to a long down-time of the microscope and the DDD could only be used during the last six months of this thesis.

The other major intrinsic issue is the phase noise in cryo-EM images which increases with the ice thickness and inhomogeneities. However, vitreous ice protects the samples to a certain degree. Without it, the bacteriophages would be damaged even at lower electron doses. In addition, ice offers a hydrated environment that conserves the structure of the specimen close to native state. To keep the sample undamaged, we determined that the electron dose must remain below $70\text{ e}^{-}/\text{\AA}^2$ while keeping the phase noise below 0.07 rad to get sufficient phase sensitivity. As discussed above, minimizing the phase noise will require to optimize the

ice thickness and improve the possibility to check ice quality on the whole grid to focus on the most suitable zones.

3.4 THE PERSPECTIVES OF THIS PROJECT

In addition to working on isolated particles like bacteriophages, we also tested off-axis holography on ultra-thin sections of cells embedded in resin (part 3.4.1). The following section presents results achieved using the One View camera by Gatan. In addition, we present a few ideas that were discussed during the thesis and that could open more possibilities for biological samples off-axis holography in the near future. We will talk about the microscope improvements that could be explored (part 3.4.2) as well as sample experiments (part 3.4.3).

3.4.1 First attempt of off-axis holography on cell sections

Beside testing high resolution off-axis electron holography imaging of samples in the 100 nm size range we also tried performing off-axis holography on larger samples using the TL11 mode, which offers a larger FOV than the Lorentz mode. We wanted to expand off-axis holography to cover specimens like cell sections. For these experiments, we used 80 nm sections of resin embedded cells, namely HEK (data not shown) and yeast *Saccharomyces cerevisiae* cells on carbon-formvar grids. The sections were prepared by Vanessa Soldan and Stephanie Balor at the METi platform at CBI. The sections used for off-axis holography were fixed using glutaraldehyde and osmium, and embedded in Epoxy resin, but no further staining was added making the resulting staining very weak. We will thus mention them as unstained in this part for simplicity. An 80 nm sample is very thick for off-axis holography and requires to have vacuum areas next to the sample to avoid overlapping regions of additional thickness. For this purpose, we used the FEI Helios Nanolab 600i, equipped with a gallium focused ion beam (FIB) to mill squares next to the cells and imaged the part of the cell overlapping with the vacuum areas.

An experiment conducted on a yeast cell is presented in figure 3.25. The image was acquired over 30 seconds with π -shifting. The total electron dose is $203.6 \text{ e}^-/\text{\AA}^2$. The unstained yeast is shown in figure 3.25a with its nucleus, the left dark compartment inside the cell, and a vacuole on its right [221]. The off-axis results are shown in 3.25b. The imaged area is in the red square in the TEM image shown in the top left corner of the amplitude one. The FOV is 750 nm in diameter but could be further improved by 100 nm. In both the amplitude (left) and the phase (right), no noticeable cell component is visible. The phase sensitivity in this example is 0.16 rad which is not enough to resolve cell details. This low sensitivity results from the sample thickness. Furthermore, it is difficult to drill a vacuum square for the reference beam at a correct place for a given cell area to be studied.

Unwrapping the phase image makes it easier to see, as shown in figure 3.25c. However, no special feature is recognizable.

We faced many challenges with cell off-axis holography. First, during sample preparation, more specifically milling holes in the resin using FIB, we noticed a charging effect due to the electron beam. We then chose to carbon coat the resin with 15 nm of carbon prior to milling to protect the cells and prevent any beam induced damage and the charging of the resin as was done in FIB-SEM tomography by Trebichalska et al.[222] but this additional layer

increases even more the sample thickness resulting in a large decrease in the contrast of the interference fringes.

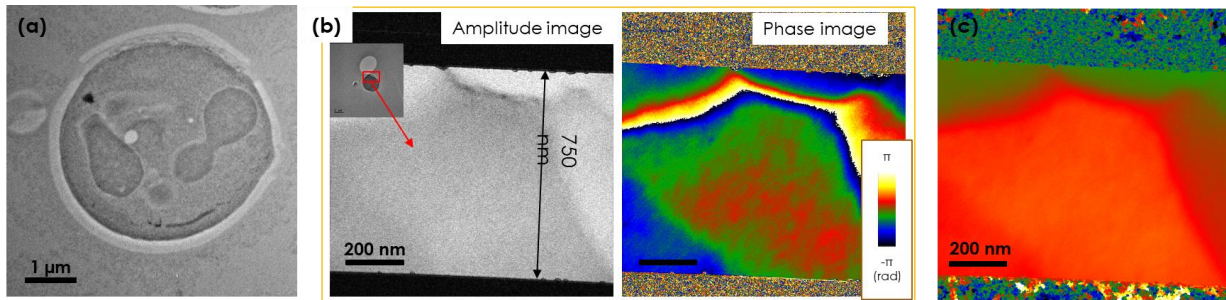


Figure 3.25 Yeast cell off-axis holography. (a) TEM image of an unstained yeast cell taken on a Jeol 1400 operating at 80 kV. (b) Amplitude and phase images obtained by off-axis holography. The original area is shown in the low magnification image in the top left corner of the amplitude image with the area in the red square that is imaged in holography. (c) Unwrapped phase image.

A future perspective is to obtain thinner slices, as it is possible to go down to 50 nm [223], and to add a thinner carbon coating around 4 nm. In addition, as the experiments were conducted with a CMOS camera, it should be carried out again using the K3 that would improve the results like what was obtained on the bacteriophages.

We highlighted across this chapter two major issues when performing off-axis holography on large biological samples. The first is the cleanness of the sample solution. The second, the electron beam sensitivity of our samples. To solve the electron dose problem, covering the sample with a thin layer of carbon, around 2-4 nm maximum could greatly help. The goal is to have a conductive layer on top of our sample that is thin enough and will improve the sample resistance to the electron beam. This idea is inspired, as we said above, by what is already done with cell sections [222]. As long as our total thickness is low enough, the fringe contrast should remain high for sufficiently resolved phase images.

3.4.2 Long distance beam interference

A common struggle with using grids with supports like graphene or carbon is the difficulty to find vacuum areas. Having a reference beam in vacuum improves the phase image. In most holograms, the acquisition was done with the sample-interacting beam overlapping with a beam passing through the support nearby. It is indeed often unavoidable that the reference beam pass through lacey in the case of ultrathin carbon, and classic carbon with the lacey-quantifoil grids which overlaps with our sample.

A solution for these problems is to split the beam in a way to make the reference part overlap with a distant vacuum area compared to the normal overlapping that is one with the area next to the sample. That way we would only need one vacuum area, that can be a broken grid or support. The beam could be split by using the available condenser biprism on the I2TEM. However, this would be a very difficult procedure as to adjust the beam path to have interference fringes.

CHAPTER 4: IN-LINE ELECTRON HOLOGRAPHY ON BACTERIOPHAGES

4.1 INTRODUCTION


4.1.1 Adapting in-line holography to biological samples

Together with Dr. Bumsu Park, a post-doctoral researcher who spent two years in our group at the CEMES laboratory, we tested the through-focal in-line electron holography (in-line holography for short) as an alternative method to obtain high contrast phase images. The experiments were carried out on T4 and T5 bacteriophages at room temperature, but also at cryogenic temperature on the Talos Arctica, which is a fully automated dedicated cryo-EM microscope recently installed at the CBI laboratory fitted with a K2 DDD.

The main advantage of in-line holography experiments is that they can be carried out on any microscope, and various open-source software for image reconstruction are freely available. For image analysis and phase image reconstruction, we used FRWR, which stands for ‘Full-Resolution Wave Reconstruction’, a software that has been developed by Prof. Christoph Koch [165]. Compared to off-axis holography, due to its flexibility and adaptability (see section 2.5.3), in-line holography, in all its forms, has been developed by many groups and is more widely used for studies of organic [164,224] and biological [168,225] materials, although there are only few published results on a high-end cryo-EM microscope. However, we are not aware of the use of the ‘focal-series’ variant of in-line holography on biological objects.

In-line holography issues and limitation

Through-focal in-line holography is a semi-quantitative method [162]. A complementary technique has to be used in parallel to perform quantitative measurements. A possible way is to use a phase image obtained by off-axis electron holography as starting image for the reconstruction, in the so-called hybrid electron holography technique (see §5.1). In our experiments, we obtained simulated images that we compared with the ones generated by the FRWR algorithm. This helped us to validate the obtained amplitude and phase images.



We were also told by Prof. Peter Nellist [private communication QEM2023] about the unreliability of in-line holography reconstruction at the objects borders which is one of the points of attention when analyzing quantitatively the phase image results.

Another difficulty of the in-line workflow is the analysis of the image series itself. The FRWR iterative algorithm indeed requires a powerful CPU and a full analysis takes about 12 hours to a day for a 7 image dataset stack of ~400 Mb as the FRWR code is not GPU optimized. The many trials and errors required for the optimization of the algorithm parameters also contribute to these long times. In addition, the resulting phase image is very sensitive to the initial alignment accuracy of all the images of the series. The only way to verify the image alignment outside detailed visual inspections is to check the output of the reconstruction process at certain “checkpoints” as no live visual is provided during the iterative runs. The algorithm can only generate intermediate phase images that are used to indicate whether the process runs fine or not. The phase image reconstruction therefore requires a good expertise in using the FRWR algorithm.

Additionally, as shared by in-line holography experts, the image reconstruction is a difficult process. The acquisition parameters, for example the defocus step and range, the astigmatism, as well as those used in the reconstruction algorithm (gradient flipping, bandpass filtering...) have a huge importance in the reliability of the final image making self-learning quite difficult. Moreover, there are only few specialists in the world, and even fewer (if any) are working on biological samples. We had the chance to receive one expert in our team, which made this project easier. When all the acquisition parameters are known, the whole process of alignment can be learned and done until the last main difficult step, which is running the data sets in the iterative algorithm.

To be able to obtain the required data sets, the total electron dose the sample can support has to be estimated prior to each experiment and, based on the minimum number of images the focal series requires, the electron dose per image can be fixed and therefore the exposure time for each image. Among others parameters of the microscope to be chosen, the most important are the defocus step and the initial and final defocus values.

For the acquisition, we needed to manually create a workflow as the automation only works for single image per area for a classic cryogenic TEM acquisition. Having done this, we tested many focus step and defocus values in order to define the optimal parameters.

Similar to off-axis experiments, we started the in-line experiments on negative stained T4 bacteriophages studied on a HF2000 operating at 200kV and equipped with a CCD. We then tested the in-line holography on an unstained sample combining the result with off-axis experiment performed at room temperature on the I2TEM (in a so-called “hybrid holography method” (see chapter 5)). Finally, we performed in-line holography experiments in cryogenic conditions, first on a Jeol 2100 equipped with a CCD, and then on the Talos equipped with a DDD camera, which yielded the best in-line phase images.

4.2 CONVENTIONAL IN-LINE HOLOGRAPHY

4.2.1 Negative stain in-line holography

A good way to test the capability and learn about the difficulties of in-line holography is first to perform it on stained objects, as they are more contrasted, and at room temperature

for obvious practical reasons. Our test was conducted on the HF2000 equipped with a cold FEG gun, operating at 200 kV, and a CCD camera. We used a T4 bacteriophage solution that we drop-casted on a commercial graphene support (©Ted Pella) and then stained.

The focal series consists in 9 defocused images from -8 to $+8$ μm defocus with a defocus step of 2 μm (figure 4.1d). The exposure time is 2 seconds per image. Unfortunately, we do not know the exact electron dose as the CCD is an old model (MSC TK1024M) and no information about the gain is available. During the iterative reconstruction, the experimental images are compared to simulations generated by the algorithm from a trial wave function for each defocused image. The difference between the simulation and the experimental amplitude images is used to update the trial wave function before a new iteration [149].

The figure 4 illustrate the method: the first defocused image acquired at -8 μm defocus is shown in figure 4.1a, together with the corresponding simulated one in figure 4.1b. The difference between the -8 μm defocus experimental and simulated images is shown in figure 4.1c.

The phase image resulting of the reconstruction algorithm is reported in fig 4.1e. We can observe two very contrasted and well-defined bacteriophages laying over a background that shows additional bright contrast. These contrasts might result from aggregated proteins, also visible in figure 4.1a and b. Those proteins originate from the bacteria that were cultured with the phages. Preparing the phages using the chloroform method, releases the bacterial proteins found in the solution.

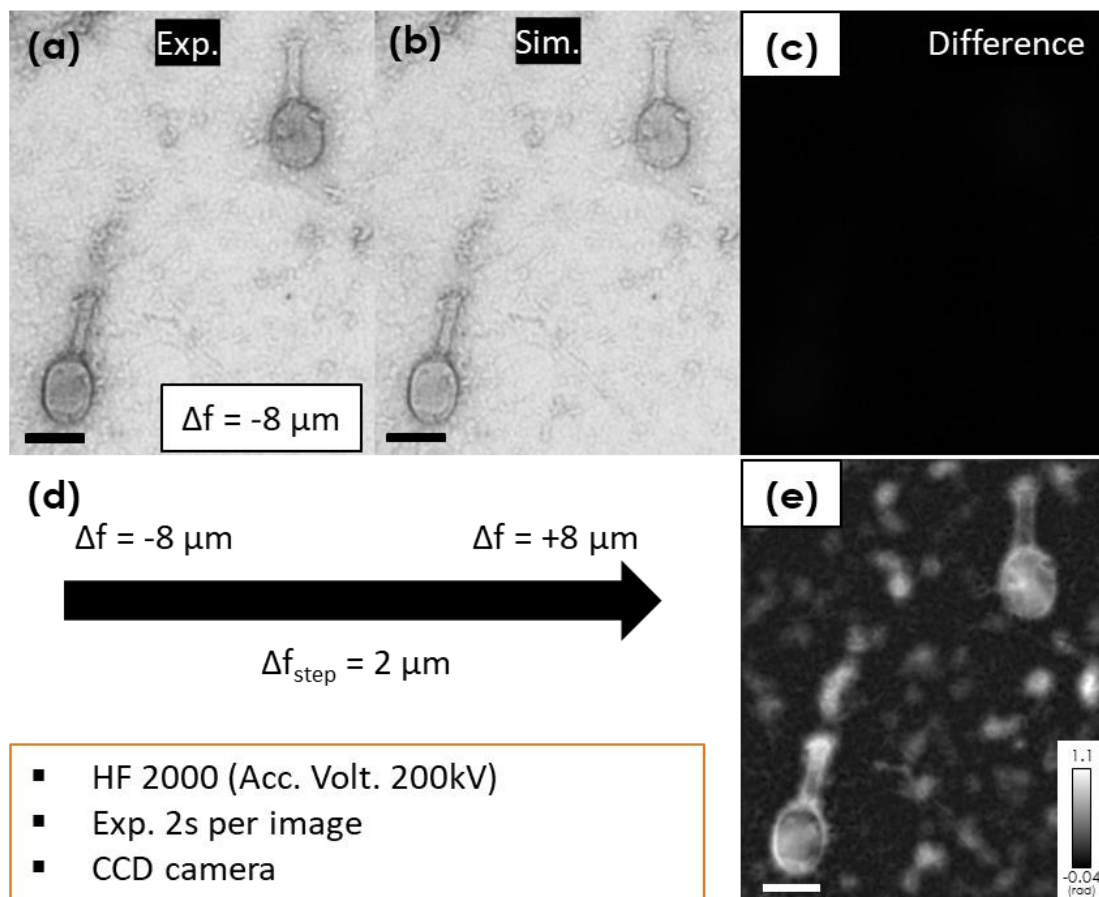


Figure 4.1 In-line through focal holography of stained T4 bacteriophages. (a) Single defocused image ($\Delta f = -8 \mu\text{m}$) of the acquired ROI. (b) Simulated image for the same defocus. (c) Difference between the experimental and simulated images. (d) Focal series parameters, showing the beginning and ending defoci and the defocus step. (e) The resulting calculated phase image. The phase sensitivity is 0.02 rad. The scale bar on all images corresponds to 100 nm.

The tail of the phage has a very high contrast in the phase image in figure 4.1e but the 4 nm period helicoidal motif of the tail is not visible (the pixel size is 0.88 nm). This is not due to electron irradiation as the staining protects the sample from high electron doses. It is most probably due to a lack of phase sensitivity although the background looks clear. The baseplate of the upper T4 is visible even with the background contamination. The baseplate of the other T4 bottom left on the other hand is not, as more protein contamination is present around the phage and its baseplate. Finally, tail fibers which are usually visible with negative staining are not detected. As we will see later, we assume it is due to the very low phase shift induced by these fibers requiring a higher phase sensitivity. Nevertheless, the very high contrast and SNR prompted us to test on an unstained sample.

4.2.2 Unstained sample in-line holography

Similar to our approach in off-axis holography, we began experimenting in-line holography at room temperature. We aimed at comparing the phase images obtained by in-line and off-axis holography to optimize the reconstruction parameters for the iterative algorithm. An example is shown in figure 4.2a with a 7-image focal series acquired on the I2TEM. The defocus step is 100 nm, from -300 to +300 nm. The electron dose per image is $21.8 \text{ e}^-/\text{\AA}^2$ for a 3 seconds exposure time, resulting in a total dose of $152.6 \text{ e}^-/\text{\AA}^2$ for the series. We tried not to surpass this total dose when acquiring 7 or 5 images per stack.

Determining the good parameters for image alignment and phase image reconstruction required many trials and errors. The final image-independent parameters used in one analysis can be used as a starting point on many datasets with or without (if the conditions are the same) optimization. “Wrong” phase images (not shown) consist on a very grainy background and/or phages with very low contrast. The phase image in figure 4.2c is the result of an optimal set of parameters.

The phase map shown in figure 4.2c shows a flat and constant background on which the T4 phage with 3 gold beads appear very bright. The phase sensitivity of this image is 0.024 rad, much better than what was obtained by off-axis holography. The phage itself is well defined and the morphologies of both its capsid and its tail are clearly visible. The phage baseplate is even discernable. However, the tail rings do not show up. This result agrees with the room temperature off-axis holography experiments as well as with the room temperature ptychography experiments performed on the T4 bacteriophage (see §5.2), which only revealed the general morphology of the phage with a limited spatial resolution of a few nanometers.

When plotting the phase profiles across the capsid and the tail in figure 4.2b, we see an almost flat background as qualitatively observed in the phase image. The capsid phase shift maximum is 0.7 rad, which is lower than the phase shift measured in off-axis holography experiments i.e. between 2 and 2.5 rad. This is also the case for the 0.15 rad maximum phase shift observed at the tail, which is lower than the maximum phase shift of 0.25 ± 0.05 rad measured in off-axis experiments. As presented in the previous chapter, the phase shift is quantitatively and directly measured by the off-axis interferential method. In contrary, the phase shift measurements provided by in-line holography should be taken with caution, as the difference we measure between the two holography methods reflects the non-quantitative aspect of in-line holography.

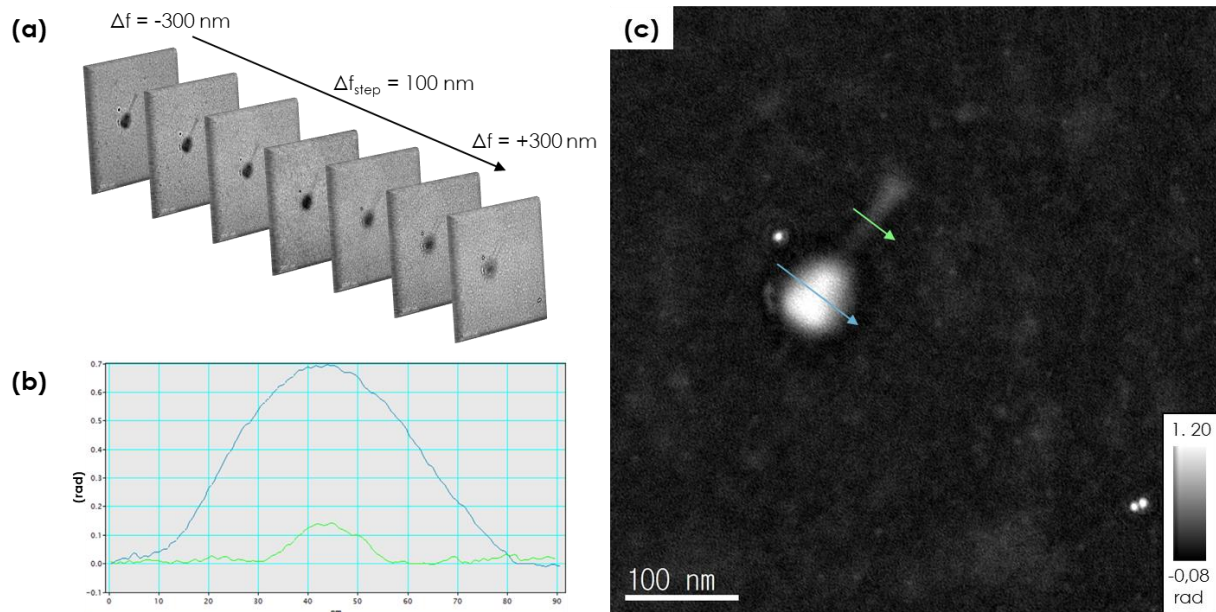


Figure 4.2 Room temperature in-line electron holography of an unstained T4 bacteriophage. (a) Raw focal-series images and acquisition parameters. (b) Phase profile of the capsid (blue) and the tail (green) in the phase image (c). The experiment was done on the I2TEM microscope in Lorentz mode.

Despite limited spatial resolution, bacteriophages are however better distinguished with this approach than when looking at unstained phages in conventional bright-field TEM. In addition, in-line holography yields phase images with less high frequency noise compared to off-axis experiments as demonstrated by the higher phase sensitivity.

4.3 CRYOGENIC IN-LINE HOLOGRAPHY

4.3.1 T4 and T5 bacteriophages cryo-in-line experiments

We first tested in-line electron holography in cryogenic conditions on the Jeol JEM 2100 of the CBI. This microscope is equipped with a LaB6 electron gun, operating at 200kV and is fitted with a 4k by 4k CCD camera. It is also equipped with Serial-EM [226] for semi-automated low-dose image acquisition. This program works under the Digital Micrograph[®] platform. We used an energy filter for our acquisitions, the Gatan Imaging Filter (GIF Quantum model 964), which magnifies the image by ~ 12 times while reducing the noise by eliminating inelastically scattered electrons [227].

We performed in-line holography on T4 bacteriophages deposited on lacey grids. To limit irradiation damage and remain in low dose condition, for all data sets, we acquired focal series consisting of 5 images instead of 7 as in our previous experiment on unstained phages. The example shown in figure 4.3 consists in a series acquired at defoci between $-3 \mu\text{m}$ to $+3 \mu\text{m}$ with a $1.5 \mu\text{m}$ focus step. The dose per image was $13 \text{ e}^-/\text{\AA}^2$, with an exposure time of 0.8 seconds for each. The $3 \mu\text{m}$ under-focused image is shown in figure 4.3a for reference. After images alignment, a region of interest, shown in figure 4.3b, was extracted. The obtained stack was used for the iterative reconstruction with the FRWR algorithm. The phase and amplitude images are shown in figure 4.3c and 4.3d respectively.

In cryogenic conditions, where the frozen sample is directly deposited on lacey grids, getting rid of the background effect due to the ice is difficult. Nevertheless, we were able to obtain a clear enough background when the ice layer was sufficiently thin. The low frequency noise does not affect the phase sensitivity, which is equal to 0.033 rad. Looking at the details, the capsid decoration protein named ‘Hoc’ is visible as well as the tail fibers in the phase image 4.3c, whereas there were not discernable neither at room temperature nor in cryogenic off-axis electron holography.

In this experiment, we observed for the first time alternating periodic dark and light motifs in the phase signal of the T4 tail. In addition to the phase image, the amplitude image reported in figure 4.3d is similar to the in-focus image. However, the borders of the phages are clearer and more defined than in the in-focus image which gives the impression that the contrast is better. The contrast $((I_{\max}-I_{\min})/(I_{\max}+I_{\min}))$, calculated on the amplitude images give 0.9 whereas that of the cryo-EM is equal to 1. This should be looked into in more details and discussed with in-line holography specialists. In our analysis, we focused on the phase image as the amplitude one does not bring any additional information compared to BF TEM image.

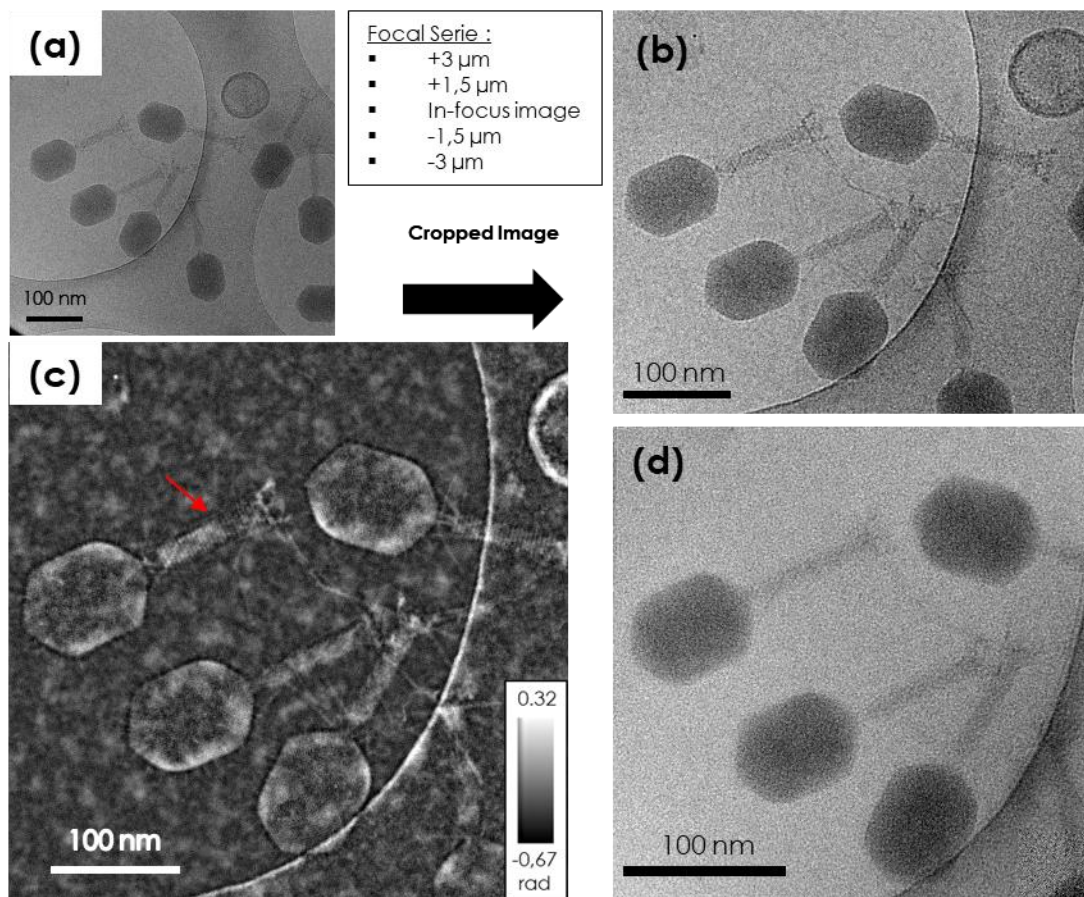


Figure 4.3 Cryogenic in-line holography of the T4 bacteriophage on the Jeol 2100 at the CBI. (a) A BF defocused image ($\Delta f=-3 \mu\text{m}$) of the focal series. After alignment, the phase is calculated in a ROI shown in (b). (c) Final phase image of the T4 phages. (d) Amplitude image.

This cryo in-line experiment was then reproduced on the Talos Arctica microscope equipped with a K2 DDD at the CBI laboratory to evidence the effect of a direct detector compared to the CCD one of the Jeol 2100. We benefited of the help and expertise of Vanessa Soldan and Stéphanie Balor to acquire data sets on this advanced TEM.

To take advantage of the K2 camera, we acquired multi-framed movies that were later motion-corrected using Relion's implementation of MotionCorr2 [228]. The figure 4.4 illustrate our experiment that consisted in acquiring a non-linear 7-image focal series ($\pm 9 \mu\text{m}$; $\pm 4 \mu\text{m}$; $\pm 1 \mu\text{m}$; focus) of the T4 bacteriophage with a total exposure dose of $79.1 \text{ e}^-/\text{\AA}^2$. The focus was adjusted manually for each defocused image. When using a non-linear series, we can adjust a parameter in the FRWR alignment steps to account for the changing focus step.

The $\Delta f = -4 \mu\text{m}$ under-focused image is reported in figure 4.4a for reference. After initial alignment using the FRWR plugin in Digital Micrograph-1.8[®] followed by FFT fitting, we proceeded to the iterative reconstruction. The intermediate steps, namely iterations 0; 83 and 381 are shown in figure 4.4a. The iteration "0" consists of the first iteration where all the images of the focal series were used. The final phase image reported in figure 4.4b was obtained after 981 iterations. In this experiment, we obtained a phase sensitivity, i.e. the standard deviation of the phase measured in ice (area with a constant phase signal), of 0.04 rad. Compared to the BF image in 4.4a, we notice a much higher contrast and a SNR improvement allowing to reveal the fine structure of the different parts of the T4 phages.

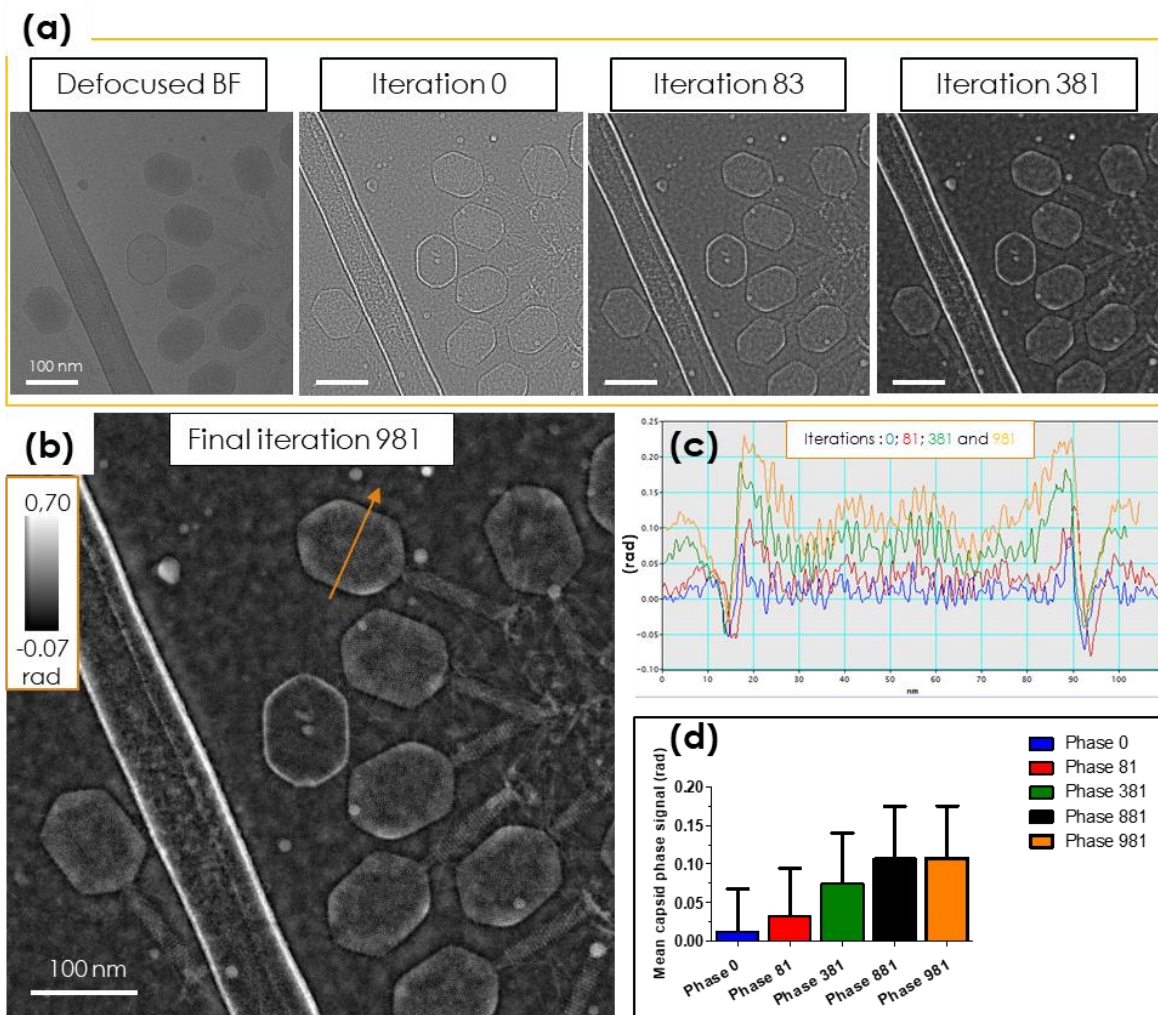


Figure 4.4 Cryo in-line electron holography of T4 bacteriophages on the Talos Arctica equipped with a K2 detector. (a) BF image ($\Delta f = -4 \mu\text{m}$) followed by 4 different phase reconstruction iterations using the FRWR algorithm. (b) Final phase image (iteration number 981). (c) Phase profile of the T4 phage with the orange arrow in (b) for different iterations. The x axis represents the 'x' coordinate along the profile in nm and the y axis represents the phase shift in radians. (d) Bar plot of the mean internal capsid phase signal for different reconstruction iterations.

We measured phase-shift evolution across a phage capsid (orange arrow in figure 4.4b) as a function of the number of iterations (figure 4.4c). We notice an increase of the phase values, as we progress through the iterations while the background noise is reduced. This is clearly evidenced in the phase jump at the capsid edge, which is equal to 0.12 rad at the iteration “0” and 0.25 rad the iteration “981”. It corresponds to an increase of the image contrast and phase value with the number of iterations up to an optimal that can be estimated by plotting the mean phase value of the capsid studied in figure 4.4c as a function of the number of iterations (figure 4.4d). For iteration “0”, the phase is about 0.01 rad with an error of 0.05 rad; after 881 iterations, the mean phase value reaches 0.107 rad with an error of 0.067 rad, while 100 additional iterations do not further improve the reconstruction, indicating the algorithm has converged. The error bars shown in the figure 4.4d are significant relative to the measured phase shifts (this noise can be attenuated by combining in-line and off-axis holography, as we will demonstrate in the part 5.1 of this manuscript).

When studying in detail the T4 bacteriophage capsid, we can clearly distinguish the DNA, especially at the periphery of the capsid where its periodical structure is visible (figure 4.5a). This level of contrast of the DNA structure is not usually seen except in few cases when condensing the DNA into toroids, making it is easier to see [229,230].

The periodic structure corresponding to the 4 nm periodical stacking of the pb18 proteins rings is visible on the phase image of the T4 bacteriophage tail in figure 4.5b. It is similar to the model in figure 4.5c, obtained by stacking 4 hexamers of the gp18, with a visualization of the electrostatic potential of the rings.

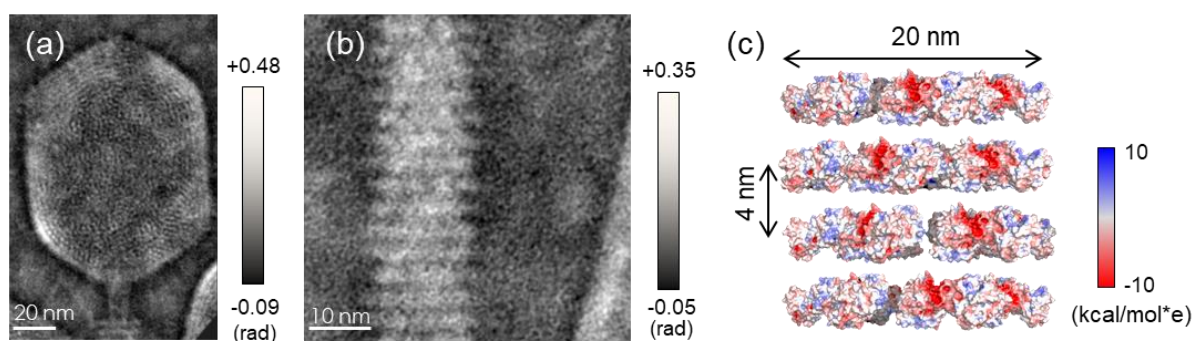


Figure 4.5 In depth structural study of the T4 bacteriophage. (a) Zoom on the T4 capsid. (b) Zoom on the tail of the T4 phage. The visible part is called the tail sheath (outside tube). (c) 4 gp18 trimers with the surface electrostatic potential (pdb id: 3FOH) computed on chimeraX [231].

Interestingly, we observe an additional helical periodic contrast on the tails in the phase images (figure 4.5b). These alternating bright and dark group of helices are even more conspicuous upon averaging phase images from different reconstructions as reported in figure 4.6a or treating the image with a low-pass filter as shown in figure 4.6b. This helicoidal contrast is therefore neither a high frequency noise nor a phase reconstruction artifact. We measure an angle of around 32° between the direction of the helix and the tail axis (figure 4.6c). We hypothesized that the helicoidal contrasts we observed in the phase image was related to the tail sheath charge distribution. Indeed, the phase shift is influenced by the local electrostatic potential and the gp18 protein shows a negatively charged domain at the surface of the tail sheath. Considering that (1) the reported rotation angle of the tail sheath rings around the tail axis is 17.2° [62]; (2) the tail diameter is 21 nm and (3) the ring to ring periodicity is 4.5 nm (the last two parameters being measured on the Talos Arctica with the same calibration as for the in-line data), we estimated that the negative charges on the gp18 protein should align with a projected angle of 34.5° relative to the tail axis, which is in good agreement with our

measurement. The small difference could be due to calibration errors of the K2 or in the angle measurements itself.

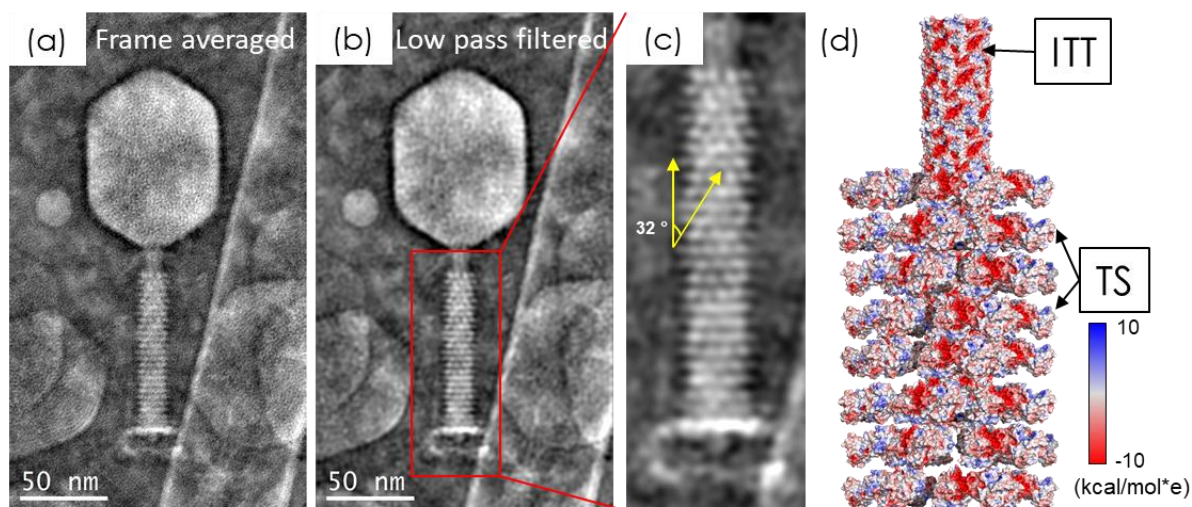


Figure 4.6 Analysis of the tail undulating phase signal. (a) Manually frame averaged phase image of 6 T4 bacteriophages. (b) Low-pass filtered image of (a). (c) Magnification of the tail of the bacteriophage shown in (b). The yellow arrow shows the angle of the gp18 helices relative to the tail axis. (d) Electrostatic potential of the internal tail tube [ITT] (pdb id: 5W5F) [68] and the tail sheath [TS] (pdb id: 3FOH) [231] surrounding it.

Cryogenic in-line holography on T5 bacteriophages

To confirm the potentialities of the cryogenic in-line holography experiments, we reproduced the experiments on different bacteriophages. The T5 was selected, which is more challenging to study because of its narrower and more flexible tail that is more difficult to image than the T4 one. Our goal was to visualize the tail and capsid detailed morphology and to detect phase shift signals similar to those measured on the T4 tail and attributed to the electric charge distribution.

We prepared vitrified T5 grids using a Lacey support (©Ted Pella), and performed the experiment on the Talos Arctica microscope at CBI using the same procedure for acquisition and reconstruction used for the T4.

The T5 bacteriophage presents two tail conformations. The first one, shown in figure 4.7a (left), corresponds to a T5 with a capsid full of its DNA and in which the tape measure protein (TMP) is present in the tail to block DNA ejection. In the second conformation, shown in the figure 4.7a (right), the TMP is no longer in the tail and the capsid is empty as the DNA has been injected out of the phage. The two conformations are shown in the defocused BF cryo-EM image in figure 4.7b.

Based on our previous experience, we were able to further improve the phase sensitivity by almost a factor of 2 compared to what was achieved on the T4 and reach 0.023 rad for a total electron dose of $50 \text{ e}^-/\text{\AA}^2$. The background was clearer with less noise as shown in figure 4.7c.

We then compared contrast and SNR in the BF image and the phase image. The intensity and phase profiles of the BF ($\Delta f = -9 \text{ }\mu\text{m}$) and phase images for the tail of DNA-containing or empty phages, as observed in figures 4.7d,f and figures 4.7e,g respectively, are plotted in a single graph in figure 4.7h. The profiles of the intensity of the $9 \text{ }\mu\text{m}$ under-focused images show a very small difference between the full and empty tail due to the low contrast difference between the background and the tail, with both slightly emerging from the noise. On the contrary, there is a clear difference between the phase signals of the full and empty

tails: a decay of the phase value along the axis of the empty tail is clearly evidenced as expected from the absence of the TMP.

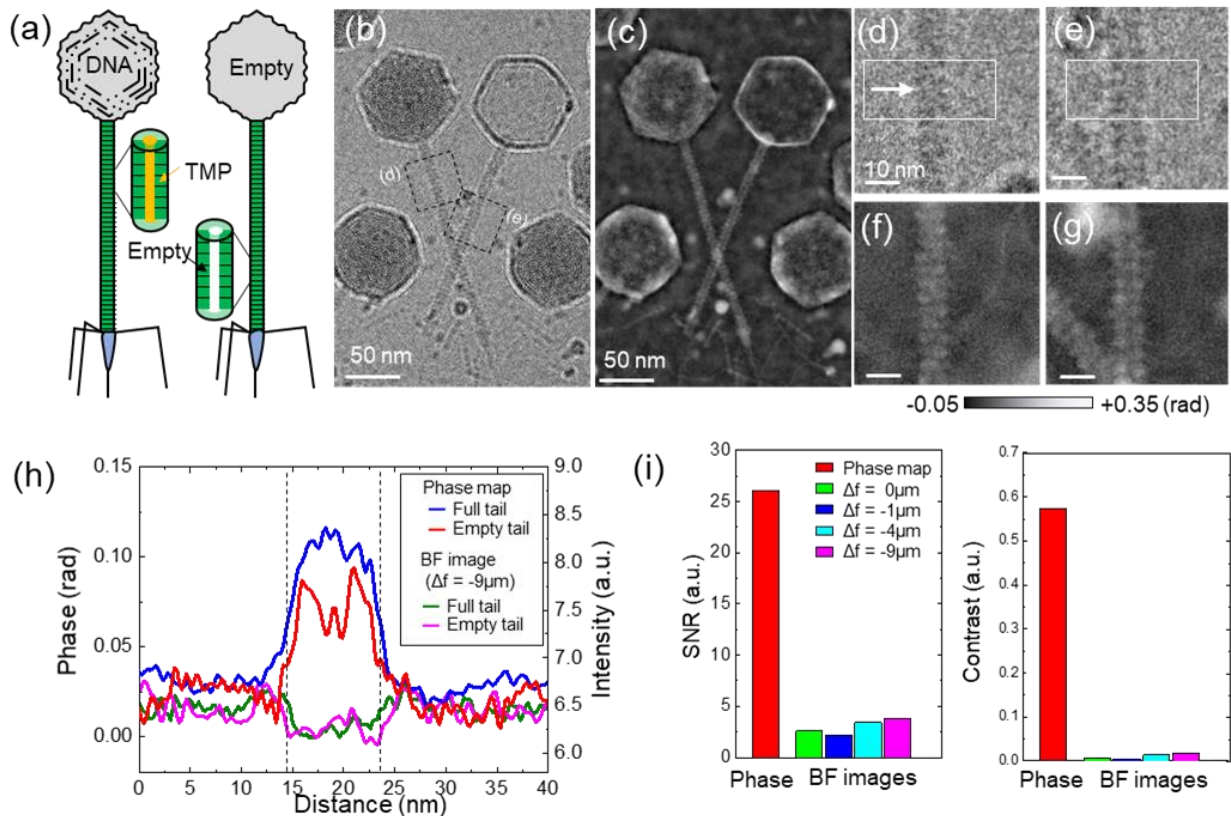


Figure 4.7 T5 bacteriophage focal series in-line electron holography. (a) Representation of the full (left) and empty (right) states of T5 bacteriophage with a zoom at their respective tail structure. (b) Under-focus BF image ($\Delta f = -4\mu\text{m}$) by cryo-EM. (c) Phase image of the area shown in (b). (d-e) Cryo-BF images of the full and empty T5 tails respectively. (f-g) Phase images of the full and empty T5 tails respectively. (h) Plot of the $9\mu\text{m}$ under-focused BF images of (d) and (e) intensities as well as the phase shift signal of the same two tails shown in (f) and (g). (i) Left: SNR comparison between the phase image and the under-focused and in-focus BF images. Right: Contrast comparison between the phase image and the under-focused and in-focus BF images.

The SNR and contrast of all under-focused and focused BF images were calculated and compared to the phase signal in figure 4.7i. A 10-times increase of the SNR and a 38-time increase in contrast is evidenced in the phase image compared to the -4 and $-9\mu\text{m}$ under-focused images. We may infer from these measurements that if SPA of biological macromolecules were performed on phase images extracted from in-line holography, 10 times fewer images would be required for a reconstruction with similar contrast.

We also closely studied the capsid to investigate the structural information that can be extracted from phase images. Figure 4.8a shows the capsid phase image with, superimposed on the left side of it, the electrostatic potential calculated using ChimeraX[®] from the pdb structure (pdb id: 6OMC) [215]. A periodic “bumpy” profile due to the protein distribution appears at the capsid surface when zooming on the electrostatic potential map (figure 4.8b). A similar profile is visible in the experimental phase image as shown in figure 4.8c and in the phase profile extracted at the capsid surface of the phase image and reported in figure 4.8d. We therefore claim these in-line phase images allow revealing bumps with a 10 nm periodicity at the surface of the capsid and demonstrate the reliability of in-line holography to detect very fine structural information.

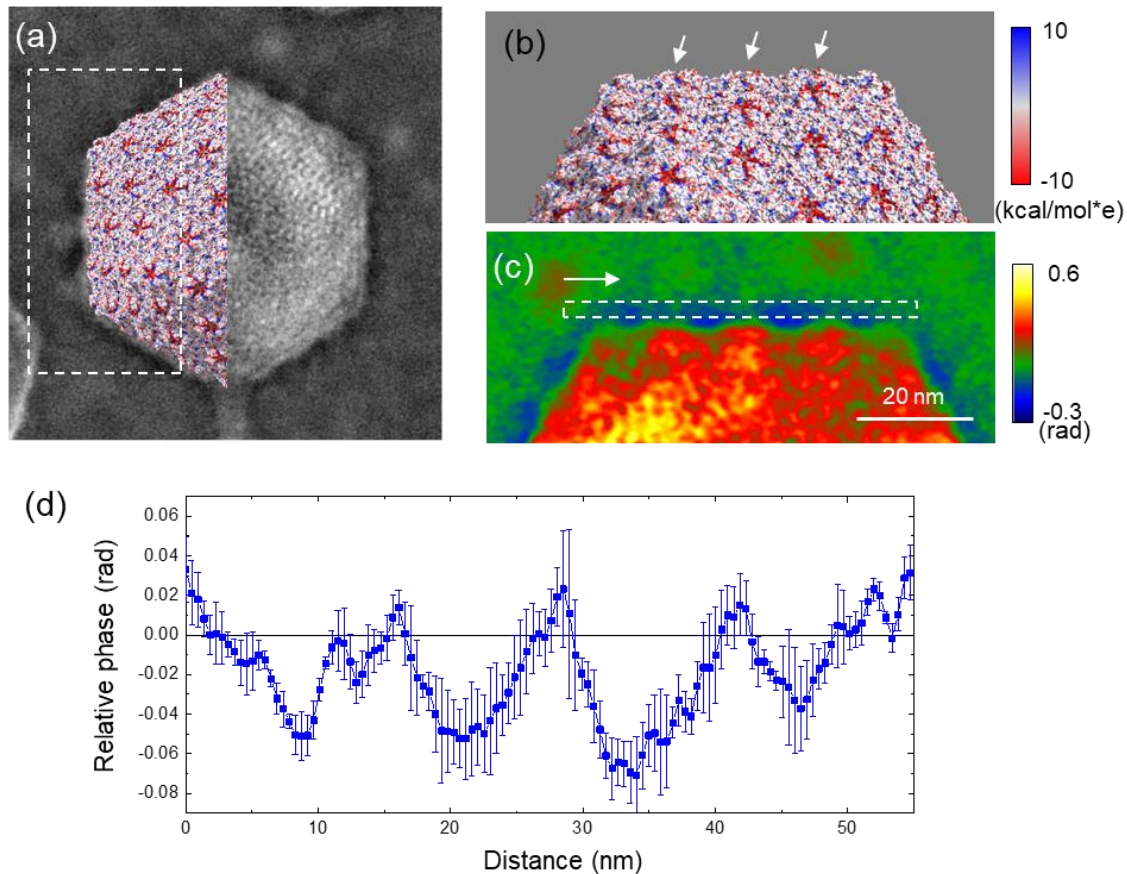


Figure 4.8 In-depth analysis of the T5 capsid's surface. (a) T5 capsid phase image with an overlap of the surface electrostatic potential calculated using ChimeraX using the pbd structure (id: 6OMC) [215]. (b) Zoom from (a) on the electrostatic potential at the side of the T5 phage showing the surface topology of the capsid. (c) Colored in-line phase image of the area shown in (a) showing the same topology as observed on the already published structure. (d) Phase profile of the selected area in (c) showing the relative phase variation.

The large improvements of both SNR and contrast evidence the benefits of the focal-series in-line holography for achieving true single particle imaging. We were able to reproduce, even improve our first results on T4 showing the large potentialities of in-line holography.

Surface charge analysis of the T4 bacteriophage

When studying the phase images of both the T4 and T5 bacteriophages capsids, we notice similar contrasts surrounding the capsid that are different for full and empty capsids.

Defocused BF images: the $-9\ \mu\text{m}$ under-focused images of the full and empty capsids are reported in figure 4.9a and 4.9b respectively. We observe that the dark Fresnel fringe is much darker when the capsid is empty. This can also be observed in the white Fresnel fringe of the $9\ \mu\text{m}$ over-focused images of the empty capsid (figure 4.9d), which is brighter than the one of the full capsids (figure 4.9c).

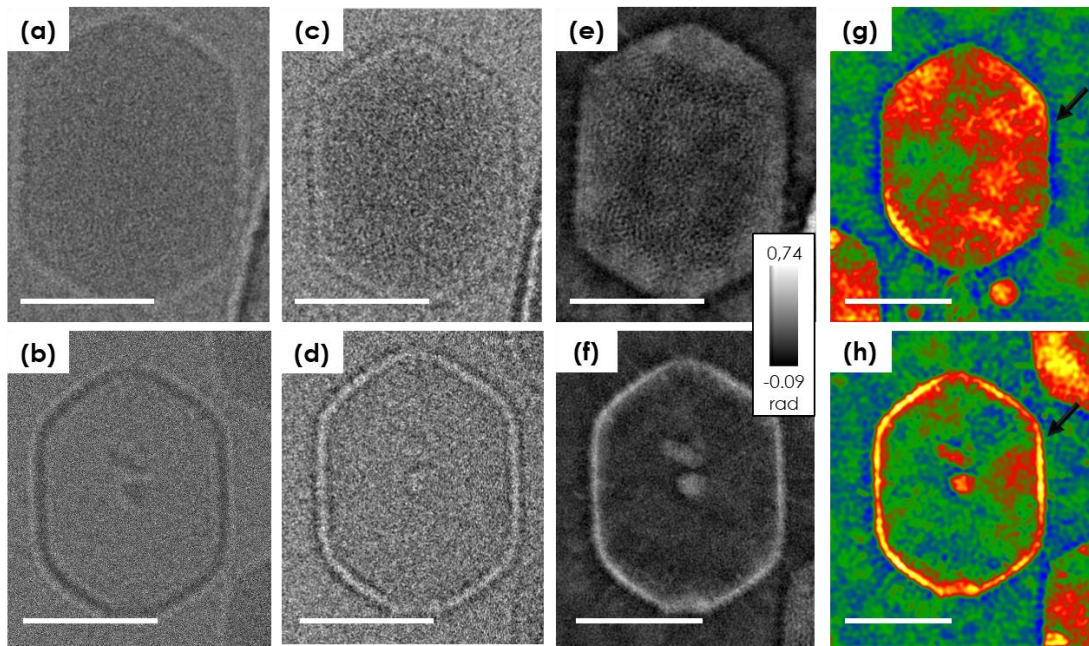


Figure 4.9: Analysis of the peripheral capsid phase signal (a) Under-focused cryo-EM BF image of a full capsid ($\Delta f = -9 \mu\text{m}$). (b) Under-focused cryo-EM BF image of an empty capsid ($\Delta f = -9 \mu\text{m}$). (c) Over-focused cryo-EM BF image of a full capsid ($\Delta f = +9 \mu\text{m}$). (d) Over-focused cryo-EM BF image of an empty capsid ($\Delta f = +9 \mu\text{m}$). (e) Raw phase image of a full capsid. (f) Raw phase image of an empty capsid. (g) Colored phase image of a full capsid. (h) Colored phase image of an empty capsid. The scales bars length is 50 nm.

Phase images: compared to the BF defocused images, a noticeable difference in the interiors of the full and empty capsids is observed in the phase images. Furthermore, the full capsid in figure 4.9e shows a dark crown around its edge that is even more visible when transforming it to a colored image in figure 4.9g. This contrast becomes bright around the empty capsid as shown in figure 4.9f and figure 4.9h. An indicator that this is not an artifact is its reproducibility as we were able to observe the same difference between an empty and a full capsid with the T5 bacteriophages shown in figure 4.7c (zoom not shown). The T4 bacteriophage has a negatively charged capsid [232], inside of which the negative DNA is stabilized thanks to the presence of cations and others proteins. We believe that the internal content (DNA & proteins) as well as the capsid itself result in an almost neutral charge, while the release of the capsid content leaves the capsid with its negative charge uncompensated, which results into the change of contrast observed in the phase images in figures 4.9f and 4.9h. However, the quantification of the charge is not reliable enough to prove this assumption. Similar experiments should be carried out in cryogenic off-axis holography to get more accurate data. For the time being, the latter is under development due to the numerous problems we are facing with the cryo-stage.

In conclusion, we show with experiments performed on two types of bacteriophages, that cryogenic in-line electron holography allows recovering structural information with better contrast and SNR compared to cryo-EM BF images. Additionally, our experiments also reveal a phase signal around the capsid that we believe is related to its content-dependent charge distribution.

4.3.2 Testing cryogenic in-line holography for individual particle imaging of pre-40S ribosome particles

The pre40S particles

In an attempt to extend the cryogenic in-line holography application to smaller biological samples, and as we were working on reconstructing pre-40S particles using single particle reconstruction (SPA) (see the annex chapter), we acquired in-line focal series of pre-40S particles. Pre-40S are immature 40S particles, which compose, together with the 60S particles, the eukaryotic ribosome [233]. The fully assembled ribosome (yeast) is shown in the figure 4.10a. The pre-40S is a mix of pre-ribosomal RNA (pre-rRNA), ribosomal proteins (r-proteins) and assembly factors (AF). Its maturation starts in the nucleus and finishes in the cytoplasm. In the cytoplasm, the maturation state of the pre-40S, which can be known from the AF that are present in the structure can be divided in three stages: early, intermediate and late [234]. The ribosomes, as well as the pre-40S particles has been well studied by cryo-EM, but many aspects of the maturation mechanisms are still shallow.

The pre-40S 3D structure can be divided into 3 main parts as shown in the model in figure 4.10b: The “head” (blue), the “platform” (yellow) and the “body” (grey). The head is the most flexible part of the pre-40S making it harder to reconstruct. They were obtained during the SPA reconstruction of the pre-40S particles (see the annex chapter).

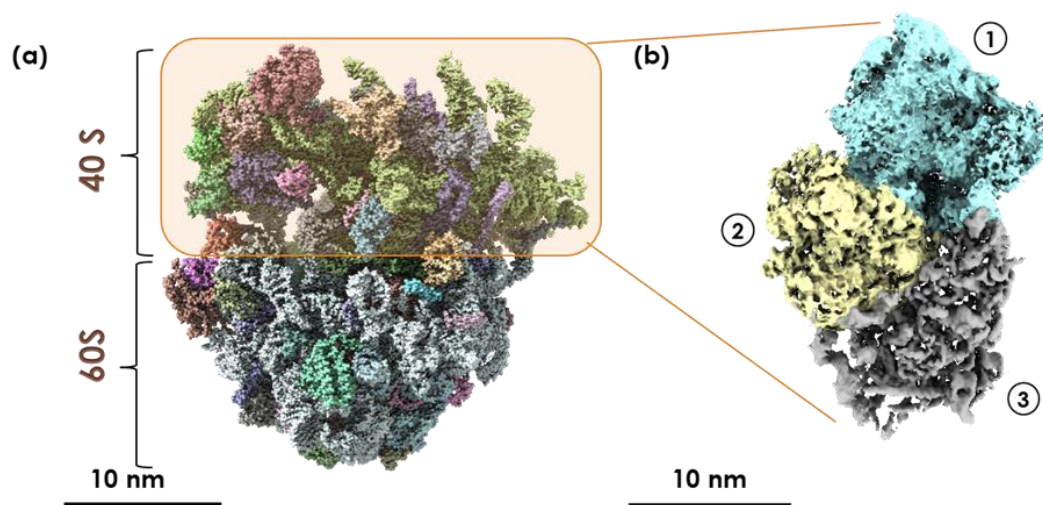


Figure 4.10 (a) Structure of the full yeast 80S ribosome (pdb: 4V7R) solved by X-ray diffraction by Ben Shem et al. [235]. (b) 3D structure of the pre-40S particles with different colors showing the head (1), the platform (2) and the main body (3). This structure was obtained by SPA.

Cryogenic in-line holography of the pre-40S particles

The low Z number particles give a low contrast in TEM. It is then very difficult to assess the sample shape and orientation just with defocused images. 2D classification of a high number of images followed by class averaging helps to enhance contrast and to determine the orientation of the particles before reconstructing the 3D volume (not shown).

In-line electron holography at low resolution allows enhancing the SNR and the contrast as shown in the T4 and T5 bacteriophages studies. Having more SNR should then enable the acquisition of much less images and a faster reconstruction analysis (due to smaller number of images to process) as well as enabling to determine the orientation of each particle

with the naked eye in the ideal cases. In addition to our primary objective, Dr. Célia Plisson-Chastang with whom we worked on the pre40S SPA, aimed to detect a 200 nucleotides long RNA sequence called 'TTS1'. This sequence is a 3' extension to the 18S rRNA that is cleaved by an enzyme, 'Nob1' in the late maturation steps of the pre-40S [236]. Since this extension is very flexible, it is difficult to observe by SPA averaging, but could be with in-line holography.

We therefore performed acquisitions on the Talos Arctica at the CBI. The example shown in figure 4.11 is a series of 5 images ($\pm 4 \mu\text{m}$; $\pm 1 \mu\text{m}$; focus) of pre-40S particles on Quantifoil[®] grids with a carbon support of 2 to 3 nm thick. The dose per image was $9 \text{ e}^-/\text{\AA}^2$.

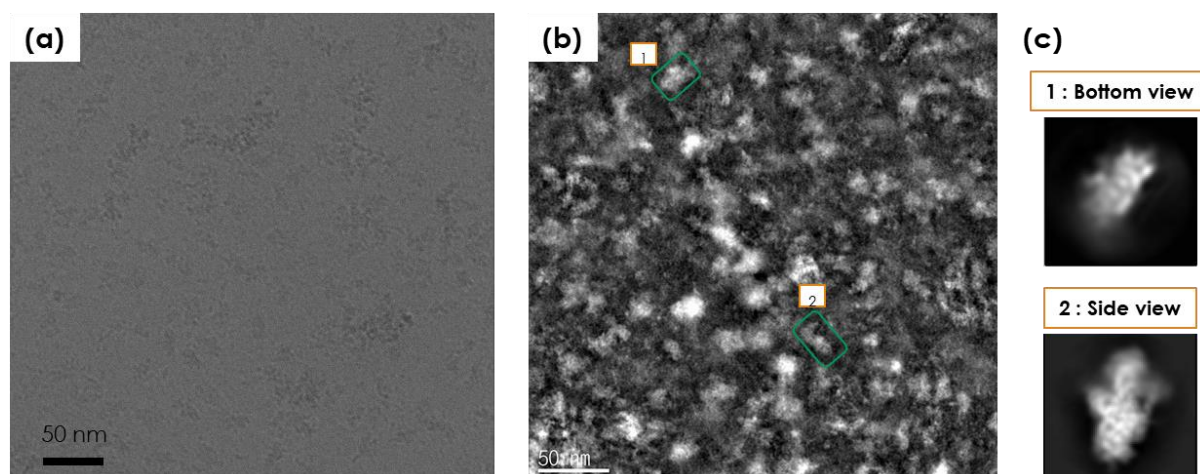


Figure 4.11 Pre-40S focal series in-line electron holography. (a) BF image of a focal-series ($\Delta f = -4 \mu\text{m}$). (b) Phase image of a ROI of the focal series. (c) 2 2D classes from the SPA corresponding to two particles in the phase image (green squares).

A single defocused image is shown in figure 4.11a where not much is visible due to the low SNR value and weak contrast. More contrasted features appear in the phase image in figure 4.11b. Nonetheless, the non-homogeneous background in this image suggests non-optimal acquisition or analysis parameters or a not sufficiently clean sample preparation. We could however identify a few particles based on already known 2D orientation classes of the pre-40S particles, two of which are shown in figure 4.11c (zoom on green squares in figure 4.11b).

Further improvements are required to be able to analyze such images by SPA. It is necessary to test different defocus steps and different defocus values, as well as the optimization of FRWR parameters, which we did not have the opportunity to do. To date, we have neither been able to effectively improve the contrast of phase images to reveal the particles, nor detect the 200 nucleotides extension of 20S rRNA. We nevertheless see the potential of in-line holography to increase particle contrast, which could help resolve 3D structures with fewer particles or reconstruct small proteins that are difficult to pick with the low SNR of bright-field TEM images.

CHAPTER 5: ALTERNATIVE PHASE IMAGING TECHNIQUES: HYBRID ELECTRON HOLOGRAPHY AND ELECTRON PTYCHOGRAPHY

5.1 HYBRID ELECTRON HOLOGRAPHY

5.1.1 The advantages and limitations of combining off-axis and in-line electron holography

As we showed in chapters 3 and 4, off-axis holography and focal series in-line holography have great potentials for biological applications. Even though they both require additional work and improvements on their own, it is also possible to combine them. Off-axis holography excels in retrieving low frequency information whereas in-line is more efficient for retrieving the high frequencies [175]. The off-axis method has however a better phase sensitivity at low resolution. Moreover, off-axis electron holography is a quantitative method [153], whereas in-line holography, which has a better phase sensitivity at high spatial resolution, is semi-quantitative [76]. Therefore, combining the two in a “hybrid holography” experiment should reduce the noise across the entire frequency spectrum while reliably maintaining good spatial resolutions. We therefore launched the first so-called “hybrid holography” experiment on the I2TEM microscope.

As mentioned in chapter 2, hybrid electron holography, combining the off-axis and in-line approaches, has been introduced for the first time by C. Ozsoy-Keskinbora et al. in 2014 without further publication since then [175]. In their article, they were able to improve the phase sensitivity and to broaden the collected frequency spectrum by combining the two methods.

Similar to off-axis and in-line holography, many challenges, some common for biological observations in holography and other specific to our experimental setup had to be addressed.

- First, the use of the same microscope is required to image the sample while using the same illumination conditions for both acquisitions. This eliminates the possibility of using cryo-EM dedicated microscope - as we did for cryogenic in-line - if it is not equipped with biprism(s) for off-axis experiments. In our case, we used the I2TEM for room temperature

experiments but did not succeed in acquiring cryo-EM data due to the temperature issues discussed in chapter 3.

- Second, a robust workflow is essential to combine both methods. Our approach is explained in the following part 5.1.2.
- Third, combining the two approaches requires acquiring more images on the same area and therefore reducing the dose for each experiment in order to keep a low total dose i.e. reducing the electron dose per image. This is performed by taking 3 or 5 images per stack for the in-line experiments, but also by reducing the dose in off-axis since the phase sensitivity will be given mainly by in-line (see §5.1.3).
- Fourth, the image stack analysis and reconstruction using the same FRWR algorithm in the in-line experiments is time consuming as already presented.

The experimental conditions for off-axis and in-line holography are also slightly different: in in-line holography, the incident electron beam must have a round shape, which is not a suitable configuration for off-axis holography because this reinforces phase noise due to lack of beam coherence from the center of the beam to its periphery. In off-axis electron holography, this lack of coherence is reduced by giving an elliptical shape to the beam with the minor axis of the ellipse perpendicular to the axis of the biprism [175].

Taking all the limitations and challenges into account, we tested the hybrid holography approach on the I2TEM in Lorentz mode and at room temperature. The images were acquired using the One View camera. For a good in-line reconstruction, we used a smaller magnification (0.41 nm pixel resolution) than what we usually use for off-axis (0.1 nm pixel resolution). Our experiments were performed on the T4 bacteriophage, using TEM lacey grids with a 3 to 4 nm thick carbon support. Bacteriophages were purified using the chloroform method.

5.1.2 Experimental procedure

Our experimental approach for hybrid holography was based on one of the two proposed by C. Ozsoy-Keskinbora et al. [175]. We first setup the I2TEM and align the beam in the off-axis configuration. The biprisms are inserted and aligned so both overlap on the camera image plane. The incident beam is set elliptical for all acquisitions.

Before locating a sample, the objective astigmatism is first corrected and the focus is set to zero. Furthermore, to stabilize the sample and the hologram fringes, both the stage goniometer and the gun deflectors have to be calibrated to compensate for the respective drifts. We then remove the biprisms from the FOV and set the low magnification “*search mode*” to locate our sample. An area “as clean as possible” with isolated samples is selected to prevent overlapping with other materials in the off-axis holography acquisition. During all those steps, the dose is kept as low as possible to prevent damaging the sample before image recording.

An example of a series of 3 images from under-focused to over-focused is acquired as displayed in the example in figure 5.1 (1). After the in-line part, the beam configuration is switched to “*search mode*” to further reduce irradiation damages and the biprisms are inserted into the FOV. The sample is then centered, and the alignment switched to the “*record mode*” at focus. The fringe stabilization and, when possible, sample stage drift correction, are started. An off-axis hologram is then recorded (figure 5.1(2)).

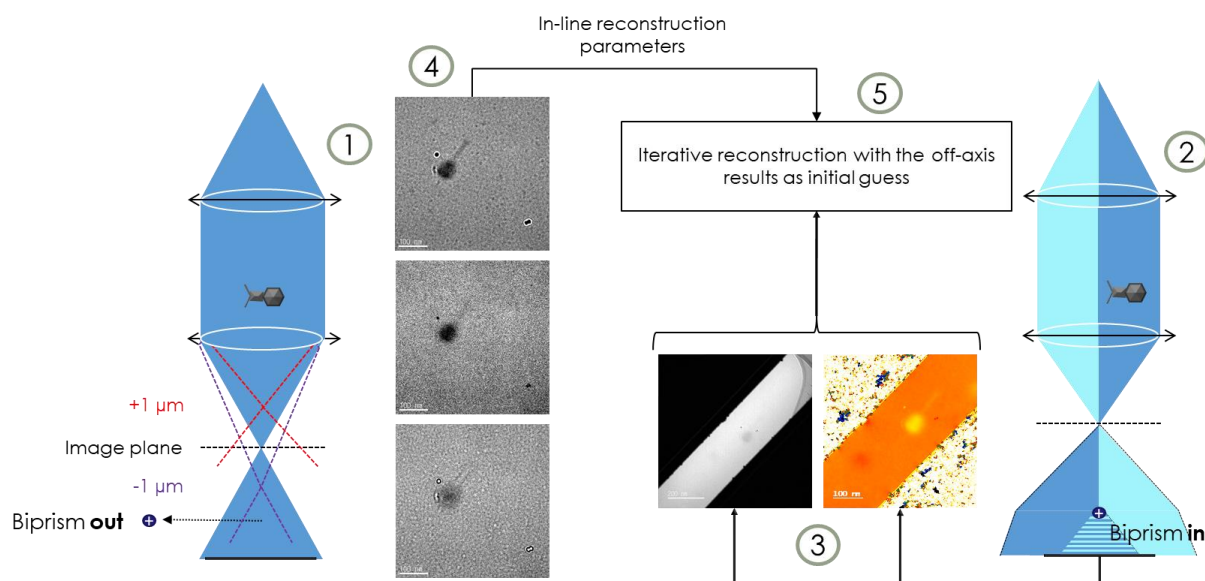


Figure 5.1 Hybrid holography workflow. Only one of the two biprisms of the I2TEM are shown in this figure for simplicity. (1) In-line acquisition. (2) Off-axis acquisition. (3) Off-axis hologram analysis. (4) In-line focal-series alignment and analysis. (5) Hybrid analysis.

The hologram obtained from off-axis holography is analyzed to extract the amplitude and phase images, shown in figure 5.1(3). The off-axis phase image is unwrapped and will be used as starting phase image for the hybrid reconstruction. The images of the focal series are then aligned precisely and the iterative reconstruction is run (figure 5.1 (4)). The optimized parameters (alignment and algorithm parameters), are then used for the hybrid analysis. In a final step, the iterative algorithm ‘FRWR’ is run again to analyze the aligned in-line stack using as starting amplitude and phase images, which were “empty” for the first run of the classical in-line analysis, the off-axis amplitude and unwrapped phase images. The final amplitude and phase images obtained using the combined techniques result in a lower phase noise images with an improved contrast and SNR compared to the BF-TEM.

5.1.3 Combining off-axis and in-line holography: first test on the T4 bacteriophage

Inspired by the results obtained by C. Ozsoy-Keskinbora et al., on hybrid holography we reproduced their experiment on a biological T4 sample. As a first step, we disregarded the electron dose to evaluate the phase noise reduction in the hybrid mode and the recovery of both low and high frequencies at such doses.

The hybrid experiment was performed on the I2TEM as previously stated. A $-300 \mu\text{m}$ under-focused image showing the full FOV is shown in figure 5.2a. A whole phage is observed despite the low inherent contrast and no details of the tail or head show up. One gold bead is visible next to the phage as well as two others more distant. In this example, we analyzed the region in the red square. The structure of the T4 is shown in figure 5.2b, taken from Yap et al. [206]. Three circles highlight the thickest areas in the bacteriophage capsid.

We used the two-biprisms configuration for the off-axis holography acquisitions and acquired a 4 minutes hologram. The total dose for the hologram was of $680 \text{ e}^-/\text{\AA}^2$ which is a high dose for a biological unstained specimen studied at room temperature. The aim of this

first attempt is not however to achieve high resolution. The amplitude and phase images obtained from off-axis electron holography are shown in figure 5.2c (left and right respectively). The amplitude image in figure 5.2c (left) displays a lower contrast compared to the defocused image in figure 5.2a. On the contrary, the phase image (figure 5.2c right) reveals a well contrasted and defined phase over a clean and homogeneously flat background signal. The phase sensitivity in this experiment is 0.04 rad. This high phase sensitivity is mainly due to the high electron dose, leading to more contrasted fringes. The thin and flat 3 nm ultrathin carbon support and the absence of contamination also allow to achieve the low phase noise.

Following the hologram acquisition, we acquired a focal series of 7 images (as we disregarded the cumulated dose) ranging from $-300\ \mu\text{m}$ under-focus to $+300\ \mu\text{m}$ over-focus with a constant step of $100\ \mu\text{m}$ (linear serie). Each image was acquired with 3 seconds exposure time corresponding to an electron dose of $8.5\ \text{e}^-/\text{\AA}^2$ per image. The series was then aligned using the FRWR plugin implemented in 'Digital Micrograph' by Gatan[®]. The aligned images are merged into a stack and the FRWR algorithm was run using to the different experimental parameters as described in chapter 4. The resulting images are shown in figure 5.2d. The amplitude image (left), shows the T4 virion together with gold beads. The beads exhibit Fresnel fringes which were not observed previously. These fringes seem to also be present in the phase image in figure 5.2d (right). The T4 is clearly visible in the phase image and the background is homogeneous with a mean value of 0.025 rad. However, as on our other in-line results in chapter 4, small weak white spots show up in the background. The phase sensitivity is 0.026 rad, which is better than the sensitivity obtained in the off-axis experiment (0.04 rad).

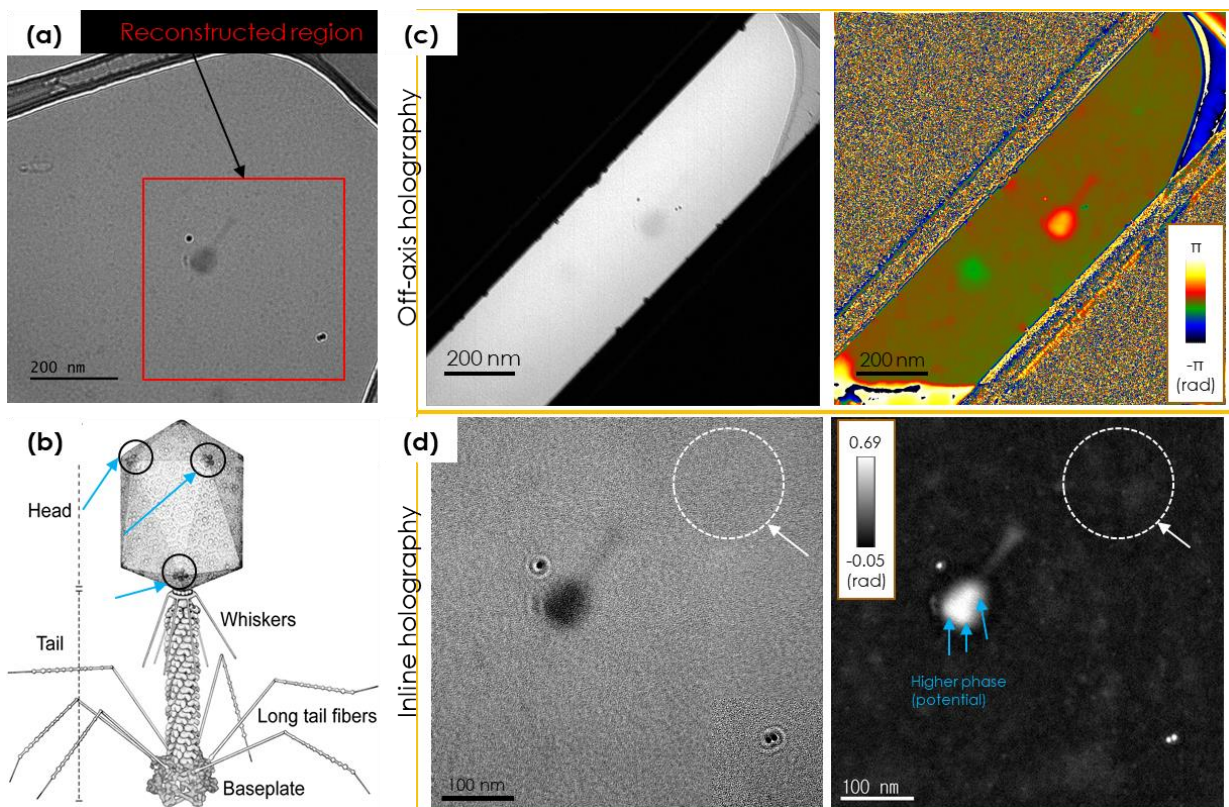


Figure 5.2 Hybrid holography of the T4 bacteriophage. (a) Defocused ($-300\ \mu\text{m}$) image of the total FOV. The area analyzed by in-line and off-axis is shown in the red square. (b) T4 structure from Yap et al. [206], with three circles showing the thickest areas of the bacteriophage. (c) Raw amplitude (left) and phase (right) images obtained by analyzing the off-axis holography hologram. (d) Raw amplitude (left) and phase (right) images obtained by analyzing the in-line holography focal series using the FRWR algorithm. The dotted circle highlights the background signal that is present everywhere on the image.

We noticed an intense phase signal with a triangle shape inside the capsid. This coincides with its thickest areas that are marked by circles in figure 5.2b. This signal is easier to notice in in-line compared to off-axis.

In a second step, we used the amplitude and phase images obtained by the off-axis experiment as starting images for the FRWR algorithm. The comparison between the hybrid and both the off-axis and in-line phase images is shown in figure 5.3. The off-axis image, cropped in the figure 5.3a shows a visible and well contrasted phase with one gold bead on its left, as well as two other beads with negative phase shifts (“ghost” image). As discussed in the previous paragraph, the phase sensitivity is high for an off-axis holography experiment (meaning a low phase noise value): 0.04 rad (figure 5.3d). In this experiment, we used a smaller magnification than usual (0.41 nm pixel resolution) and a larger fringe spacing leading to a theoretical spatial resolution of 0.82 nm with the chosen FT mask. Nevertheless, no detail of the rings in the T4 tail is evidenced. The inability to see the tail rings is likely caused by the high electron dose damaging the structure.

The colored in-line phase image in figure 5.3b shows lighter blue patches across the image. The phase sensitivity is nonetheless high i.e. 0.026 rad as already mentioned (figure 3.4d). No tail ring signal emerges in the magnified phase image and the baseplate area appears noisy compared to the off-axis image.

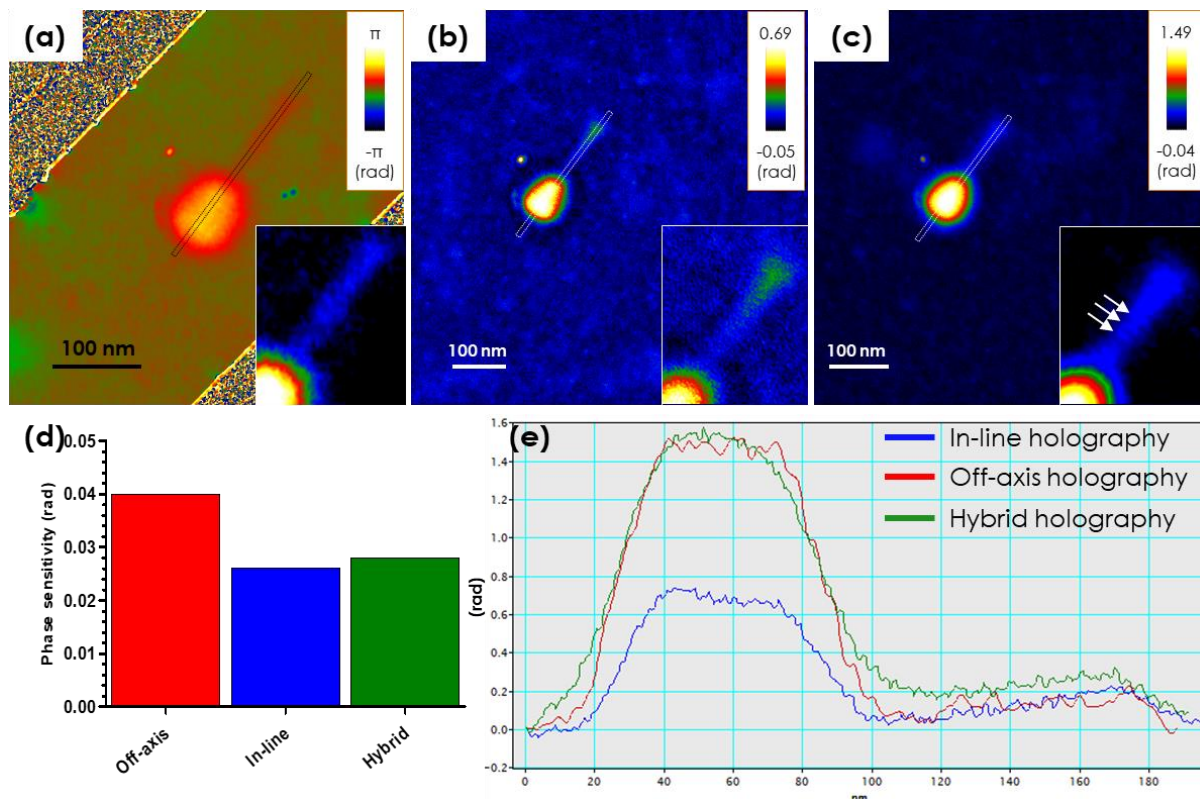


Figure 5.3 Comparison of the off-axis, in-line and hybrid electron holography results. (a) Colored phase image of the off-axis holography analysis. A magnification of the tail is inserted in the bottom right and its contrast enhanced by modifying the contrast limits of the image. (b) Colored phase image of the in-line holography analysis. A magnification of the tail is highlighted in the bottom right. (c) Colored phase image of the hybrid holography analysis. A magnification of the tail is highlighted in the bottom right. The three arrows show a pattern resembling the tail rings. (d) Histogram comparing the phase sensitivity of the three electron holography methods. (e) Phase profiles of the T4 bacteriophages (dotted rectangles in (a), (b) and (c)) of the off-axis (red), in-line (blue) and hybrid (green) phase images. The y axis is in rad and the x is in nm.

The hybrid phase obtained by combining the previous two results lead to the phase image shown in figure 5.3c. At first sight, the image background looks much cleaner although the phase sensitivity is similar to the one obtained in-line, with 0.028 rad (figure 5.3d). The T4 capsid phase shift signal is more homogeneous and the tail is similar to the off-axis one with a more defined shape. When zooming on the tail, we can see three ring-like repetitions. The measured distance between them is ~ 8 nm which is two times the expected ring periodicity. However, the rest of the tail does not contain this signal.

Three phase profiles taken along the phage in figure 5.3a, b and c are plotted on the same graph in figure 5.3e. These profiles evidence the difference between the phase shifts measured by in-line and off axis experiments. We measured a maximum phase shift of 0.7 rad in the capsid for in-line holography compared to 1.5 rad measured by off-axis holography, again illustrating the fact that the former is not quantitative in that matter. It is interesting to note that the off-axis holography phase shift is lower than the expected 2.4 rad, hinting at the damage of the capsid which does not seem to occur at doses less than $450 \text{ e}^-/\text{\AA}^2$ (see chapter 3).

Hybrid holography enables to retain the correct phase shift information as it recovers the value we got from off-axis. The difference between hybrid and off-axis holography is the smoother capsid profile obtained with the hybrid method which also reveals less noisy phase variation. The phase shift values measured in the hybrid phase image on the tail are slightly more important than the ones measured by in-line and off-axis experiments with a phase shift around 0.25 rad for the hybrid phase image compared to 0.2 rad for off-axis and in-line. Detecting more signal could be the reason we could observe the tail ring-like features in figure 5.3c. It is however difficult to analyze quantitatively these images, especially at the tail as it is damaged by electron irradiation.

In summary, our results on hybrid electron holography show a slight improvement compared to the in-line and off axis experiments. These results are however not conclusive as we did not achieve high resolution phase images. The signal gain can be seen on the phase profiles of the tail, the latter not being so clear.

5.1.4 Perspectives

More relevant results are expected by performing the hybrid experiments at lower electron dose thanks to the use of the K3 DDD with improved detection. The next step would then be to reproduce the experiment at room temperature first, then at cryogenic temperature, with a dose between 60 and $80 \text{ e}^-/\text{\AA}^2$, using the K3 camera. At low temperatures we could also explore doses up to $120 \text{ e}^-/\text{\AA}^2$ to reduce the phase noise as much as possible. We suggest studying the same T4 bacteriophage deposited on the quantifoil grids with a graphene layer. We should be able to assess the limits of hybrid holography in the best conditions that we now master. The limitation is that we have to first choose one or two data sets to analyze. It is done by analyzing the off-axis holograms and evaluating the phase images before the in-line holography series reconstruction as the in-line and hybrid steps are long and difficult. We can then focus on optimizing the analysis parameters of the FRWR algorithm for the selected datasets. It would be interesting, after succeeding in imaging the T4, to also perform hybrid experiment on the T5 bacteriophage to attempt to image its tail. For the future experiments, the number of images per focal series has to be maximum of 5, or if not possible, 3 as it should be enough for an amplitude and phase reconstruction. An equilibrium between the electron dose in off-axis and in-line has then to be found.

5.2 OTHER TEM METHODS FOR THE STUDY OF BIOLOGICAL SAMPLES: ADF-STEM AND ELECTRON PTYCHOGRAPHY

5.2.1 Introduction

STEM has found in the recent years many applications in the biological field. For example, STEM imaging in the annular dark field (ADF) mode is a unique method used for determining the molecular mass of isolated protein assemblies [24]. Most STEM current applications in biology are in cryogenic conditions. Cryo-STEM can help detect protein-bound metallic ions like iron (Fe) in ferritin without the need to access high resolutions [237]. The cryo-STEM approach is particularly useful in tomography as it permits access to more tilt angles due to an improved depth resolution [135]. Cryo-STEM was also combined with a focal-series acquisition (not to be confused with the in-line analysis) as a way to improve in-depth information. Using this approach S. Trepout et al. imaged the flagellum in the protist *Trypanosoma brucei* using sections up to 750 nm thick [136].

Finally, two major techniques are currently being developed with already some very promising published results. The first one is integrated differential contrast STEM (iDPC STEM). iDPC STEM is a phase imaging technique that enables the detection of light atoms, providing images in which the contrast is proportional to the atomic number of the atoms [238]. It also provides a higher SNR than annular dark field STEM (ADF-STEM). iDPC STEM proved very promising as it enables imaging of very thick samples. X. Li et al. demonstrated the potentiality of this STEM method on resin embedded human hepatocellular cells (HepG2) at very low doses obtaining highly contrasted phase images down to $1 \text{ e}^-/\text{\AA}^2$ electron dose, as well as using sections up to 600 nm thick with a constant dose while still having enough contrast [239]. A breakthrough was achieved with 3D high resolution reconstructions of the keyhole limpet hemocyanin (KLH) at 6.5 Å and the TMV at 3.5 Å using iDPC STEM acquisition and SPA [240].

4D-STEM is another STEM technique under development. It is different from conventional bright field (BF) and dark field (DF) STEM, as it consists on acquiring diffraction patterns with a focused probe [241] on overlapping areas of the sample. One analysis scheme is called electron ptychography. This technique enables the phase retrieval of the electron exit wave enhancing the contrast. The difference in the TEM alignments is the use of an under-focused probe. Ptychography is currently being developed in Oxford in cryo-EM [180] and recent SPA reconstruction were also published [181]. These articles and electron ptychography were further discussed in the part 2.6.5.

In this part of the chapter, we therefore present our results obtained using BF and HAADF STEM, as well as electron ptychography on the T4 bacteriophage.

5.2.2 STEM imaging of the T4 bacteriophage

We wanted to explore ADF-STEM on unstained bacteriophages to compare with the other techniques we tested. We therefore performed STEM experiments on the probe corrected Jeol ARM 200F microscope located at the Raimond Castaing center to study the unstained T4 bacteriophage at room temperature.

In these experiments, many configurations with different probe sizes and camera lengths were tested. First, two probe sizes were selected while fixing the camera length at 12 cm as reported in figure 5.4a and b. The probe sizes were “5C” and “3C” based on the Jeol terminology, the “5C” corresponding to a 0.09 nm probe size, the “3C” to a larger probe (unknown). When using smaller probe size, the borders of our object appears more clearly. With the 0.09 nm probe, the capsid borders appear clear and yield the same signal as the interior of the capsid (insert in figure 5.4a). On the contrary, the larger probe size gives a lower contrast of the capsid borders and the tail (insert in figure 5.4b). We therefore mainly performed the STEM experiments using the 0.09 nm probe size as it gives better contours to our bacteriophages and enables to reveal the tail fibers. With this probe size, and a 40 μm condenser aperture, we had a probe current of around 155 pA.

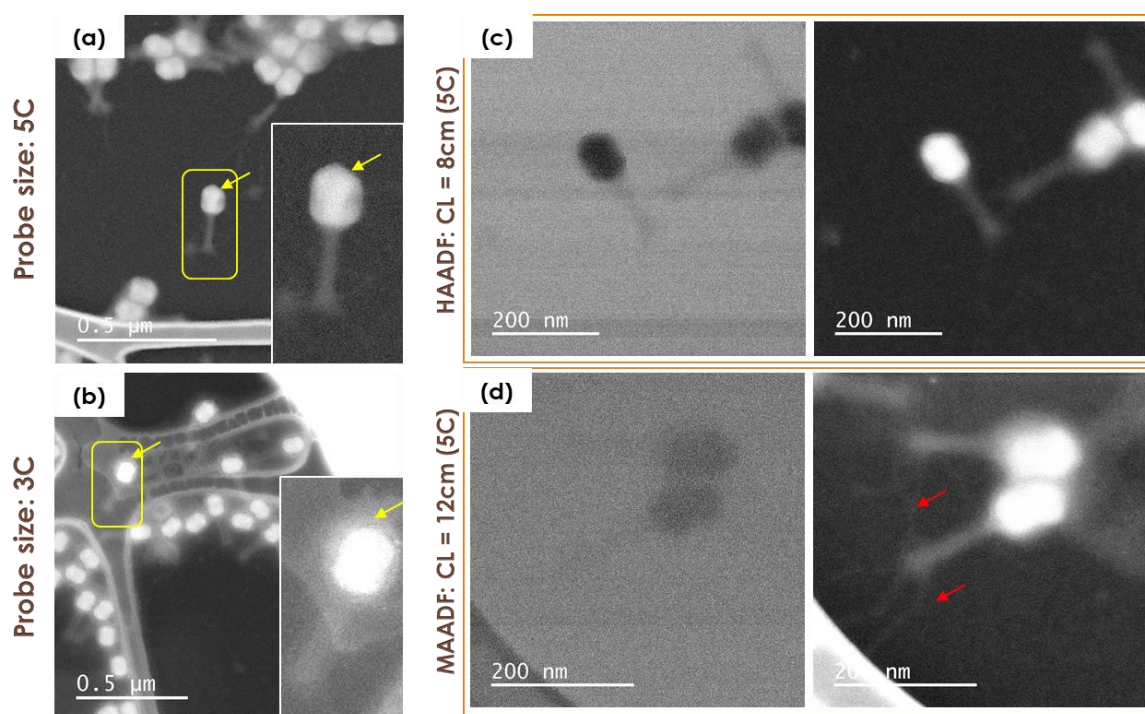


Figure 5.4 STEM imaging of the T4 bacteriophage. (a) Low magnification image of the T4 using a 5C probe size (Jeol annotation). (b) Low magnification image of the T4 using a 3C probe (Jeol annotation). A zoom into isolated bacteriophages in the yellow squares in (a) and (b) are shown in the insets at the bottom right corners. The yellow arrows point at the capsid borders of the phages. (c) BF (left) and DF (right) images of the T4 bacteriophage using an 8 cm camera length (0.61 nm pixel resolution) and a 5C probe size. (d) BF (left) and DF (right) images of the T4 bacteriophage using a 12 cm camera length (0.46 nm pixel resolution) and a 5C probe size. The red arrows point at the T4 tail fibers.

We then acquired images with a 0.09 nm spot size (5C) using two different camera length values: 8 cm for HAADF images and 12 cm for MAADF. Examples of each are shown in figures 5.4c and d respectively. The images on the left are the BF and those on the right are the dark field (DF) collected by the annular detectors. The intensity of the DF phage signal, which is dependent on the Z number of the material is higher than in the BF, leading to more contrasted phages. The HAADF DF image is more contrasted than the MAADF one. This is apparent when looking at the signal intensity of the capsid, which have a higher signal in HAADF (profiles not shown). On the other hand, the tail fibers are slightly more visible in the MAADF DF images (red arrows in figure 5.4d right).

These experiments show that DF-STEM enhances the contrast of unstained bacteriophages compared to a parallel beam configuration image, as well as showing structures like the tail fibers in MAADF that are not visible in parallel beam. Moreover, we showed a very high contrast at the capsid and tail, especially in HAADF which suggests that bacteriophages could be an ideal sample to further explore this method. Intriguingly, the only uses of STEM for SPA 3D reconstructions have been carried out with iDPC cryo-STEM [240], and to our knowledge there is no report on the use of this technique on bacteriophages. It would then be interesting to start by exploring medium resolution SPA on these samples. Having access to a dedicated cryo-STEM microscope is however required.

5.2.3 4D-STEM ptychography of the T4 bacteriophage

Electron ptychography is a recent 4D-STEM technique that is developing quite rapidly with few applications for the study of biological materials [177,180,181]. We were thus interested in exploring this method and compare it with both in-line and off-axis electron holography. We proposed to Prof A. Kirkland's group to perform ptychography experiments on our samples. As he agreed to collaborate, we sent our T4 solution to Dr. Emanuella Liberti who prepared the samples on graphene supports, provided by the Prof. Sara Bals' group the day before the STEM session. Ptychography experiments were carried out both at high and low dose.

The high dose experiment was done on isolated bacteriophages. An example with the corresponding BF image is shown in figure 5.5a. The total dose was $332 \text{ e}^-/\text{\AA}^2$ with an overlap ratio of 0.9 when scanning the probe. The analysis was done using the ePIE iterative algorithm [243] with 10 iterations. The amplitude image figure 5.5b (left) shows a well contrasted bacteriophage similar to the BF image. We notice however, a darker part of the T4 head. The phase image of the T4, in figure 5.5b (right), provides lower contrast than the amplitude image. In this example, the probe size is about 16 nm and the phase error is 0.1096 rad, similar to the sensitivity obtained in low dose off-axis holography experiment. The tail rings are not resolved in these experimental conditions.

The low dose experiment in figure 5.5c and 5d was carried out with $66 \text{ e}^-/\text{\AA}^2$ total dose using a 0.8 overlap ratio smaller than the one used for the high dose experiment. The BF image obtained is shown in figure 5.5c. Based on our experiments, this dose is low enough not to damage the T4 rings as they appear in cryo-EM at similar dose. The ptychography data were analyzed using the same algorithm with 10 iterations. The amplitude image in figure 5.5d (left) shows a well contrasted bacteriophage similarly to the high dose experiment. A very dark signal also appears in the capsid ruling out the possibility of artefact damage due to the total electron dose which is less than $70 \text{ e}^-/\text{\AA}^2$. The phase image in figure 5.5d right is less contrasted than the one at higher dose (figure 5.5b right). The T4 tail is visible with a weak signal while the capsid contour is not continuous. The defocused probe size is about 10 nm in this case. The phase sensitivity is 0.127 rad, slightly weaker than the one obtained at higher dose.

We assume that the dark signal in the capsid is due to the dose rate (number of electrons per second) instead of the total dose, as it is much higher than in a classic TEM experiment.

These ptychography results, on top of our experience with off-axis holography tells us that we should not expect to see the tail rings at room temperature. The resolution is always limited due to multiple factors, mainly the electron dose rate and the phase noise. This first experiment suggests that ptychography, although performant in cryogenic conditions, may not

provide contrasted-enough phase images at room temperature. Lowering the dose further reduces the contrast and the noise is relatively high compared to the 0.06 rad we target in electron holography.

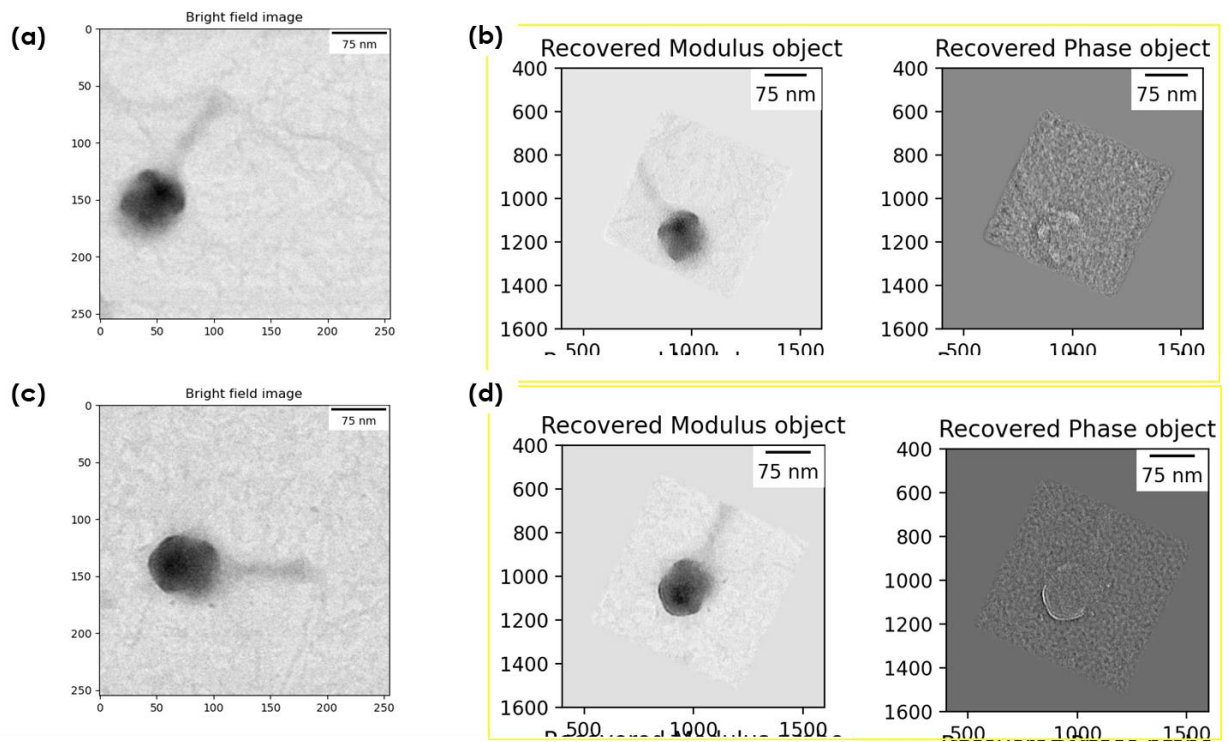


Figure 5.5 Electron ptychography of the T4 bacteriophage. (a) BF image of the first example; total dose in ptychography is $332 \text{ e}/\text{\AA}^2$. (b) Ptychography analysis of a cropped ROI of the bacteriophage in (a) showing the amplitude, or 'modulus' image on the left, and the phase image on the right. (c) BF image of the second example; total dose in ptychography is $66 \text{ e}/\text{\AA}^2$. (d) Ptychography analysis of a cropped ROI of the bacteriophage in (c) showing the amplitude, or 'modulus' image on the left, and the phase image on the right. The data in this figure were analyzed and provided by Abner Velazco-Torrejon.

CHAPTER 6: CONCLUSIONS AND THE FUTURE OF ELECTRON HOLOGRAPHY

Several exploratory studies were carried out during this thesis to develop the study of biological materials by electron holography. Many challenges arose, some preventing us from obtaining better results and carrying out further experiments. Among them, the installation of the K3 direct electron detector in the CEMES took five months, during which the microscope was not accessible for any experiments (off-axis and hybrid electron holography). Furthermore, we encountered a problem with the low temperature sample holder for the cryogenic off-axis holography. The temperature could not be stabilized under -170°C and rose to around -164°C , which most of the time induced crystallization or even ice sublimation for reasons that are still unclear.

Despite these major obstacles, this thesis provides a new assessment of the applicability of electron holography techniques to the imaging of biological objects and identifies key elements to be considered for future developments in this field. We were able to make significant improvements to electron holography compared to existing publications. This chapter summarizes the work carried out and the results obtained in each part of the thesis.


At the end of this chapter, we discuss future plans for each part and the improvements that still need to be made for electron holography to become a practical bioimaging technique capable to achieve advanced results.

6.1 OFF-AXIS ELECTRON HOLOGRAPHY

In this part of this chapter, we first determine the current capabilities and limitations of off-axis holography carried out at room temperature.

When performing the off-axis experiment with a high-dose acquisition mode on a CMOS camera, we achieved medium resolutions without reaching 4 nm, therefore not sufficient to resolve our target: imaging the tail rings on T4 phages. It appears to be difficult to go beyond this spatial resolution due to the high sensitivity of unstained samples to electron irradiation. This limits the acceptable electron dose and therefore the SNR of the resulting phase images.

In addition, our studies also highlight specific constraints linked to the off-axis electron holography method. Hence, the superposition of the electron wave phase shifted after interaction with the sample, with the reference wave ideally passing through vacuum areas but most often passing through the support, makes the cleanness and the thinness of the supports particularly crucial to obtain satisfactory holograms, as reference wave has to be homogeneous



without phase shift variations due to possible thickness changes or contaminations. For similar reasons, data acquisition is very sensitive to contamination of the sample solution with impurities. Furthermore, the higher sensitivity of off-axis holography to low Z atoms makes it more vulnerable to contaminations compared to negative stained or cryo-EM, which can tolerate some contamination levels.

We were able to image the phage structure and clearly distinguish the capsid, the tail and the baseplate using the One view camera. We determined that the T4 capsid induced a phase shift around 2.2 ± 0.2 rad, whereas the phase shift due to the tail was 0.2 ± 0.05 rad, which increases to 0.5 rad following its contraction after ejection of the phage DNA. On the other hand, the phase shift of the capsid drops to 1.6 rad when the dose is too high (1000 and $680 \text{ e}^-/\text{\AA}^2$ for off-axis and hybrid phase images respectively), signaling major electron beam damages. Nevertheless, it was difficult to obtain a good fringe contrast and acceptable phase sensitivities at low electron dose with this CMOS.

The SNR was significantly improved by the use of a direct electron detector compared to the CMOS one. The K3 camera allowed us to record holograms that resulted in phase images with a SNR increased by more than two times. This improvement led to visualizing the T4 bacteriophage morphology even for electron doses down to $15 \text{ e}^-/\text{\AA}^2$.

We reproduced our results using the K3 on the T5 bacteriophage whose tail is thinner than the T4 one and can only be observed in low dose conditions before any significant beam damage occurs. The T5 capsid induced a 2.2 ± 0.1 rad phase shift, comparable to the T4 one. These measurements show that the projected electrostatic potentials inside both phage capsids (see equations 1.5 and 1.6) are similar as their thicknesses are also similar: 86 nm for the T4 and 90 nm for the T5. On the other hand, the T5 tail produces a phase shift of 0.25 ± 0.05 rad.

In phages treated with the spermine which neutralize the DNA, the phase shift is changing to 1.6 ± 0.2 rad. This is the first time the effect of the DNA charge changes is evidenced using off-axis holography. Nonetheless, it is difficult to exactly measure the charge variation as the mean inner potential (MIP) is not constant inside the capsid.

Regarding phase sensitivity, we achieved an average 0.06 rad at room temperature at high electron doses ($80 \text{ e}^-/\text{\AA}^2 < \text{dose} < 450 \text{ e}^-/\text{\AA}^2$) and 0.1 rad at low electron doses ($< 80 \text{ e}^-/\text{\AA}^2$). The 0.06 rad sensitivity we targeted to visualize the tail rings, was achieved in many images acquired at high doses but at the cost of sample damage and remained difficult to obtain at low doses.

Off-axis holography results were further improved when carried out at cryogenic temperature. The shape of the phage is better defined in the phase images, particularly its baseplate. We measured a smaller phase shift at the capsid, around 0.9 ± 0.1 rad compared to room temperature. This is mainly the result of the inclusion of the phage in continuous layer of vitreous ice which reduced the measured phase shift of the beam passing through both the ice and the phage (see §3.3.4) in addition to a likely decrease in the MIP of phage atoms when they are vitrified at liquid nitrogen temperature.

In low temperature experiments, the required low electron dose and the ice thickness of the ice in which the sample is embedded significantly reduce the SNR of the phase images and therefore limit the potential of off-axis electron cryo-holography for the study of biological materials.

6.2 FOCAL-SERIES IN-LINE ELECTRON HOLOGRAPHY

The in-line electron holography studies were carried out in parallel to the off-axis holography experiments. After an initial test on a stained sample, we performed the experimental work on unstained T4 samples at room temperature on the I2TEM fitted with the One View CMOS, and successfully tested the reconstruction method using the FRWR iterative algorithm. We then moved to cryo-temperature using the automated cryo-EM microscope Talos Arctica.

Room temperature experiments at high electron doses gave results similar to the off-axis studies. Although the morphology of the phage was visible, the tail rings were not identifiable. We achieved a phase sensitivity of ~ 0.02 rad and measured a 0.7 rad phase shift at the T4 capsid and 0.15 rad at its tail, values lower than what was measured in off-axis holography. We concluded that room temperature observations of unstained samples by electron holography cannot reach a resolution of 4 nm. This went also to confirm the non-quantitative aspect of in-line holography.

Experiments were then conducted in cryo-conditions on a Jeol JEM 2100 equipped with a CCD camera. Very promising results with low phase noise were obtained with a phase sensitivity of 0.03 rad. Contrary to what was measured in off-axis holography, the phase shifts detected at the capsid at cryogenic temperature were the same as those obtained at room temperature using in-line holography.

Our first cryo-experiments were reproduced on the new Talos Arctica dedicated cryo-EM microscope equipped with a K2 DDD. State of the art results were obtained with a large contrast and SNR improvement compared to classical BF images. In particular, we evidenced the tail helicoidal structure corresponding to a 17° rotation of each ring around the tail axis in agreement with its model. Remarkably, this was evidenced by a contrast likely produced by electrostatic charges at the surface of the tail sheath. We also measured a difference in the phase shift surrounding the capsid depending on if it is full or empty. We believe this phase shift difference depends on the total capsid charge, which is modified when DNA is expelled from it. More work is however needed to further understand and quantify these phase signal differences.

We also attempted to visualize pre-40S ribosomal particles by cryo- in-line holography on the Talos Arctica. We did obtain images with enhanced contrast, but could neither obtain sufficiently satisfactory images of the particles nor visualize the 200 nucleotides extension of the 20S pre-rRNA we expected to evidence. The image acquisition parameters (defocus, defocus step...) have to be optimized to obtain better images to be able to confidently identify the proteins.

The duration and complexity of cryo- in-line holography experiments, in particular due to the image analysis process, led to a limited number of experiments. This chapter nonetheless showed the performances of the in-line holography technique, which does not require a dedicated TEM equipment (biprism set-up). With advanced and automated algorithms, we believe in-line holography should progress to become a very powerful technique for structure reconstruction, and possibly global charge analysis.

6.3 HYBRID ELECTRON HOLOGRAPHY

Following the off-axis and in-line holography results, we tested the combination of both approaches in a so-called hybrid electron holography method reported by Ozsoy-Keskinbora et al. [175]. The goal was to acquire both off-axis holograms and a focal series of the same field of view using the same beam conditions. The hybrid approach is expected to combine the ‘low frequency’ performances of the off-axis method with the ‘high frequency’ ones of the in-line method.

We were able to perform a first experiment at room temperature on the T4 bacteriophage on the I2TEM. The hybrid electron holography results show an improved phase image with a high phase sensitivity (0.028 rad) indicating that the off-axis phase noise is reduced when combined with in-line. We also retained the phase shift values from off-axis holography with the capsid one being 1.5 rad in both off-axis and hybrid. Finally, a slightly higher phase shift at the tail was measured and a ring-like motif was observed. We therefore succeeded in demonstrating some improvements of the “usual” in-line or off-axis holography method with the hybrid approach. However, these improvements were limited by the higher total electron dose required to acquire the off-axis holograms and the focal series, which damage the irradiation sensitive structures.

Unfortunately, we could not replicate this experiment at low dose and neither in cryogenic conditions, the latter being a challenge because of the temperature issues we are facing with the cooling stage of the biprism-equipped I2TEM.

6.4 ELECTRON PTYCHOGRAPHY ON THE T4 BACTERIOPHAGE

We also sought to compare electron holography with electron ptychography. Dr. E. Liberti of the A. Kirkland’s group in Oxford with whom we have collaborated, first carried out electron ptychography experiment at room temperature, which was untested previously, as well as low temperature in order to reproduce on T4 virions the results achieved in 2020 on rotavirus double layered particles as well as HIV-1 virus-like particles by Zhou et al. [180]. An aliquot of the T4 bacteriophage solution was sent to the Oxford group. The T4 were deposited on graphene/quantifoil grids. In all cases, the capsid appeared dark in BF STEM images. The resulting phase image did not evidence any improvement over off-axis or in-line holography phase images even at low doses. The tail fibers were detected in the BF images, as also observed in our own STEM HAADF experiments on the Jeol ARM 200 kV at the Castaing platform in Toulouse, while they could not be observed by electron holography. Electron ptychography experiments performed on T4 under cryogenic conditions are still to be carried out.

This collaboration on electron ptychography highlighted the limits of phase imaging techniques at room temperatures and the necessity electron ptychography to be carried out at cryogenic electron microscopy and low electron dose to achieve higher resolutions.

6.5 THE FUTURE OF ELECTRON HOLOGRAPHY

Despite the many technical hurdles that we faced to perform off-axis electron holography, especially in cryogenic conditions, the results achieved during these three years encourage us to draw a map for future experiments and improvements as a continuation of this thesis. The goal remains to obtain high resolution phase images by interferometric TEM experiments at cryo-temperatures similarly to what is achieved in cryo-EM BF images.

Off-axis electron holography

The DNA charge effect on the phase shift of the T5 capsid is definitely an element worth investigating. Our data were limited due to the duration where the I2TEM was non-operating (K3 installation delay) and our focus on cryo-off-axis holography after. The target will be to recreate this with the T4 bacteriophages at room temperature, then at cryogenic temperature.

However, the development of off-axis holography under cryogenic conditions on the I2TEM suffers severe technical limitations. The first challenge for the continuation of this project will be to solve the temperature increase upon inserting the sample cryo-holder, either by finding a way to make the tip of the stage thermally isolated, or by replacing the cryogenic holder by a more performant one.


The other challenge will be to improve phase noise at low electron doses and in cryogenic conditions. It is indeed essential to find ways to reduce the noise and improve the phase sensitivity to reach $2\pi/1000$ (about 10^{-3} rad), as regularly achieved in off-axis electron holography experiments performed on inorganic materials and devices. This noise comes, on one hand, from the low electron dose required for the study of biological materials and from the amorphous ice when working on vitrified samples. Another aim is to succeed in preparing samples embedded in thinner ice of constant thickness.

In-line electron holography

Developing cryo- in-line holography on biological objects is easier as it does not require a dedicated EM unlike off-axis electron holography. The main difficulty is the time consuming and difficult analysis that sometimes required many runs to achieve a relevant phase image.

To make the in-line holography experiment more practical and therefore more widely used, image reconstruction procedures should be developed to make them more “user-friendly” and more robust. We guess that the use of IA will be a major asset for the development of this method. Furthermore, optimizing the microscope acquisition parameters should be further mastered for different particle sizes as to facilitate future in-line acquisitions. This would be done by further testing on smaller samples like the pre-40S particles we worked on.

The combination of cryogenic electron tomography with in-line holography by acquiring a focal-series at different tilts can also be a way to achieve high resolution 3D structural images. The reconstruction will first consist in obtaining the phase images for each tilt and then treating the data as in a tomography experiment. It however presents many challenges. The limited electron dose is one of them, as the dose increases with the number of images to acquire. Alternatives with 3 images per series with a few selected tilts or 5 images



per series with less tilts will have to be tested to determine the best acquisition conditions as well as good parameters for the FRWR reconstruction.

Hybrid electron holography

After the first room temperature hybrid electron holography experiment carried out at high dose, two must-do experiments need to be performed. First, a low dose room temperature experiment would help us evaluate the capabilities of hybrid holography by looking at the structural information achieved for the tail and the tail fibers of the T4 bacteriophage. The next step would be performing cryogenic hybrid holography.

For that, the difficulties explained in the off-axis part regarding low temperatures has to be addressed. The phase noise would not be the major issue as in-line will reduce the noise as we saw with our results. One possibility would be to split the electron dose between the two methods: first acquire a 3 or 5 images series for in-line holography with a total dose of $30 \text{ e}^-/\text{\AA}^2$, and then perform off-axis holography with a similar dose of $30 \text{ e}^-/\text{\AA}^2$.

Summary of the performances of EM techniques for the study of biological materials

A summary of the different microscopy techniques tested in this thesis is presented in the table 6.1.

- Cryo-EM combined to single particle analysis is the most resolutive EM technique for 3D structure determination as it has a complete and robust analysis workflow.
- Regarding low resolution studies, room temperature off-axis electron holography is still not as resolved as negative staining TEM, but has the advantage of achieving contrasted phase images of biological unstained sample, therefore avoiding the artifacts due to the addition of contrasting agents. However, this must be balanced with the high sensitivity of unstained samples to electron irradiations. Furthermore, in both cases, the sample is dehydrated and not in its native state.
- Cryogenic in-line electron holography appears to have a major potential to acquire phase images with high contrast. It would therefore improve upon classical cryo-EM by adding even more contrast. This opens up the prospect of combining this approach with SPA in the future. Along this line, the work performed independently on electron ptychography by Peter Nellist and Angus Kirkland's groups has yielded promising results by achieving 18.6 \AA resolution using 498 particles on one of the 3 reconstructed datasets [EMD-35917] [181].

| Method | Best spatial resolution | Data collection | Analysis method | ADVANTAGES | LIMITATIONS |
|---|---|---|---|--|--|
| Negative Stained TEM | 18-20 Å | Defocused images (contrast due to the staining agent) | Visual inspection Low resolution SPA | <ul style="list-style-type: none"> • Easy and fast workflow • Can be used on any TEM • The stain protects the sample from beam damage | <ul style="list-style-type: none"> • Effects of the contrasting solution on the sample (pH, salt concentration...) • Resolution limited by the contrasting agent |
| Cryo-EM (SPA) | 1-3 Å | Defocused images (about 10^5 images) | <ul style="list-style-type: none"> • SPA (randomly oriented particles) | <ul style="list-style-type: none"> • High Resolution 3D reconstruction of biological specimens • Frozen samples are hydrated and well preserved | <ul style="list-style-type: none"> • Low SNR and contrast per image • High number of images needed for 3D reconstruction |
| Off-Axis Holography | <u>RT:</u> <ul style="list-style-type: none"> • 3-6 nm (spatial resolution) on the K3 • 0.06 rad (phase sensitivity) <u>Cryo:</u> <ul style="list-style-type: none"> • $\sim 4 < r < 10$ nm • 0.1 rad (phase resolution) | In-focus interference fringes images (holograms) | Amplitude and phase extraction by Fourier analysis (qHolo by C. Gatel) | <ul style="list-style-type: none"> • High phase contrast without the need of contrasting agent • Low frequency information collection | <ul style="list-style-type: none"> • Limited resolution at RT • Very sensitive to contaminations • Limited information at high frequency |
| In-line Holography (focal series method) | <u>Cryo:</u> <ul style="list-style-type: none"> • 1.4-4 Å • 0.02 rad (phase sensitivity) | Focal series images | Amplitude and phase extraction (FRWR/FRIH iterative algorithm by C. Koch) | <ul style="list-style-type: none"> • Does not require a vacuum area • Compatible with low electron dose • High frequency information collection | <ul style="list-style-type: none"> • Limited information at low frequency • Complex image analysis process |
| 4D-STEM ptychography | <u>RT:</u> <ul style="list-style-type: none"> • 1.6-8 nm | Diffraction Images (under-focused beam) | Amplitude and phase extraction (ePIE iterative algorithm) | <ul style="list-style-type: none"> • Can be performed in low dose conditions • High phase contrast without the use of staining molecules | <ul style="list-style-type: none"> • Limited resolution at RT • High dose rate |

Table 6.1 Comparison of the techniques discussed in this manuscript showing their current resolution limit, the type of data that is collected, the analysis methods and then the main advantages and disadvantages.



ANNEX: SUMMARY TABLES

| Off-axis hologram | Fringe spacing | Specifications | Total electron dose | Phase sensitivity |
|---|----------------|---------------------------------|--------------------------------------|-------------------|
| Negatively stained T4 (figure 3.4) | - | π -shift | - | 0.65 rad |
| Unstained T4 (figure 3.5) | 1.29 nm | π -shift + drift correction | 680 e ⁻ /Å ² | 0.04 rad |
| Unstained T4 (figure 3.6) | 0.86 nm | π -shift + drift correction | 387 e ⁻ /Å ² | 0.06 rad |
| Unstained contracted tail T4 (figure 3.8) | 0.85 nm | π -shift + drift correction | 505 e ⁻ /Å ² | 0.13rad |
| Unstained contrasted T4 (figure 3.9) | 2.2 nm | π -shift + drift correction | 194 e ⁻ /Å ² | 0.09 rad |
| Unstained T4 - K3 DDD (figure 3.11) | 0.57 nm | π -shift + drift correction | 213 e ⁻ /Å ² | 0.06 rad |
| Unstained T5 - K3 DDD (figure 3.12) | 0.54 nm | π -shift + drift correction | 142.5 e ⁻ /Å ² | 0.09 rad |
| Unstained T4 - K3 DDD (figure 3.14) | 1.46 nm | π -shift + drift correction | 31.2 e ⁻ /Å ² | 0.08 rad |
| Unstained T5 - K3 DDD (figure 3.15a) | 0.54 nm | π -shift | 59.7 e ⁻ /Å ² | 0.08 rad |
| Unstained T5 - K3 DDD (figure 3.15b) | 0.54 nm | π -shift | 59.7 e ⁻ /Å ² | 0.06 rad |
| Vitrified T4 (figure 3.20b) | 0.64 nm | π -shift | 47.3 e ⁻ /Å ² | 0.16 rad |
| Vitrified T4 (figure 3.20d) | 0.64 nm | π -shift | 47.4 e ⁻ /Å ² | 0.16 rad |
| Vitrified T4 (figure 3.21) | 0.64 nm | π -shift | 101 e ⁻ /Å ² | 0.08 rad |
| Vitrified T5 (figure 3.22) | 0.7 nm | π -shift | 51.8 e ⁻ /Å ² | 0.085 rad |
| Resin embedded yeast cell slice (figure 3.25) | 1.9 nm | π -shift | 203.6 e ⁻ /Å ² | 0.16 rad |

Annex Table 1. Summary of the off-axis holography results presented in chapter 3.

| Focal series | Defocus values | Total electron dose | Phase range | Phase sensitivity |
|--|---|----------------------------------|-------------------|-------------------|
| Negatively stained T4 (figure 4.1) | $\pm 8 \mu\text{m}$; $\pm 6 \mu\text{m}$; $\pm 4 \mu\text{m}$; $\pm 2 \mu\text{m}$; Focus | - | [-0.04; 1.1 rad] | 0.02 rad |
| Unstained T4 (figure 4.2) | $\pm 300 \text{ nm}$; $\pm 200 \text{ nm}$; $\pm 100 \text{ nm}$; Focus | $152.6 \text{ e}^-/\text{\AA}^2$ | [-0.08; 1.20 rad] | 0.024 rad |
| Vitrified T4 - Jeol 2100 (figure 4.3) | $\pm 3 \mu\text{m}$; $\pm 1.5 \mu\text{m}$; Focus | $65 \text{ e}^-/\text{\AA}^2$ | [-0.67; 0.32 rad] | 0.033 rad |
| Vitrified T4 - Talos Artica (figure 4.4) | $\pm 9 \mu\text{m}$; $\pm 4 \mu\text{m}$; $\pm 1 \mu\text{m}$; Focus | $79.1 \text{ e}^-/\text{\AA}^2$ | [-0.07; 0.7 rad] | 0.04 rad |
| Vitrified T5 - Talos Artica (figure 4.7) | $\pm 9 \mu\text{m}$; $\pm 4 \mu\text{m}$; $\pm 1 \mu\text{m}$; Focus | $50 \text{ e}^-/\text{\AA}^2$ | [-0.05; 0.35 rad] | 0.023 rad |
| Vitrified pre-40S (figure 4.11) | $\pm 4 \mu\text{m}$; $\pm 1 \mu\text{m}$; Focus | $45 \text{ e}^-/\text{\AA}^2$ | - | - |

Annex Table 2. Summary of the in-line holography results presented in chapter 4.

ANNEX CHAPTER: SPA OF DOUBLE MUTANT PRE-40S PARTICLES FOR THE STUDY OF THE MATURATION PROCESS

7.1 INTRODUCTION

7.1.1 Understanding the 40S subunit maturation process

In parallel to developing electron holography, I worked in a collaboration with Célia Plisson-Chastang at the CBI on determining the 3D structure of yeast pre-40S particles. The general aim was to understand the effect of a double mutation of the ribosomal protein Rps20 on the maturation process of the particles. A general presentation of the ribosome and the pre-40S particles can be found in chapter 4, part 4.3.2. Here, we will focus on the 40S subunit maturation, the understanding of which is the objective of this project.

The small ribosomal subunit, or 40S subunit, is one of the two large macromolecular particles that make the ribosome. Synthesis of the 40S ribosomal subunit mostly takes place in the nucleus where the precursors to the 18S ribosomal RNA, the core element of the 40S ribosomal subunit, are gradually matured while they concomitantly assemble with ribosomal proteins. This process is assisted at each step by assembly factors (AF), which transiently associate with the nascent ribosomal subunit. The last maturation steps take place after export of the precursor 40S (pre-40S) subunits into the cytoplasm. They lead to the association of the last ribosomal proteins and to the release of all the AFs, yielding fully mature 40S subunits [244]. Our study is in the continuation of results presented in the publication by Mitterer et al. on early cytoplasmic pre-40S particles. This publication addressed that mechanism of maturation steps taking place just after nuclear export of these particles, seeking to establish the relationships between ribosomal proteins and AFs present at these steps [233]. They determined that the ribosomal protein Rps20 interacts with Rsp3, enabling the AF called Ltv1 to recruit the Hrr25 kinase, which phosphorylates Ltv1. In parallel, they found that Rps20 structure makes a loop that goes inside the ribosome and interacts with the AF Rio2 on the other side of the subunit, the intersubunit side (oriented toward the 60S subunit when the ribosome is fully assembled). The relative positioning of Rps3 and Rps20 ribosomal proteins as well as the Rio2 AF is shown in figure 7.1a taken from Mitterer et al. [233]. The two AFs Rio2 and Ltv1 are then released in a co-dependent manner under the control of a checkpoint ensuring the correct progress of the maturation. The complete summary is shown in figure 7.1b taken from Mitterer et al. [233].

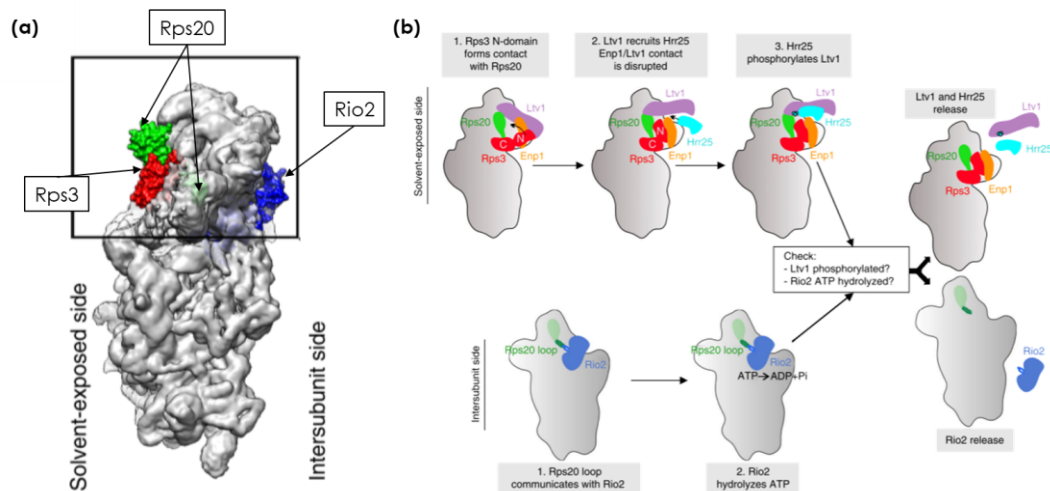


Figure 7.1 (a) 3D electron density map of the pre-40S showing the Rps20, Rps3 and Rio2 proteins. (b) Summary of the Ltv1 and Rio2 release process in the maturation of the pre-40S. Both figures were taken from Mitterer et al. [233].

In their study, they generated either point mutations or the complete deletion of the Rps20 loop (Rps20 Δ loop), which spans amino acids 68 to 78. They were able to determine that the loop mutant slowed cell growth and created a 40S synthesis defect. The latter, was subject to a SPA analysis generating two different 3D maps [233].

Here, we focused on cells expressing the double point mutations of Rps20 D113K/E115K. These two amino acids are known to interact with lysine 3 and lysine 7 in Rps3 [233]. This mutation is viable, but cells display slow growth. This mutant made it possible to purify short-lived maturation intermediates that are usually difficult to obtain as these steps evolve fast.

Our goal in this project was to reconstruct the 3D structure of the resulting pre-40S particles by SPA to determine which proteins and AFs are present or not in the structure, with a focus on the head part to understand the effect of these mutations on the pre-40S structure. To reach this goal, it was necessary to achieve a sufficiently high resolution on the head. We expect this structural insight to help us understand, together with the previous experiments, the mechanisms of the pre-40S particle maturation, especially the role of the Rps20/Rps3 interaction.

7.1.2 Single particle analysis (SPA)

SPA was used in this study to reconstruct and analyze the 3D structure of pre-40S particles. The general principle of SPA is explained previously in the part 2.3 of the manuscript. Here, we go more deeply into the details of the SPA analysis and its algorithms as it is our main analysis method.

SPA requires a large number of images, containing between 10^5 and 10^6 particles, which is necessary to overcome the low SNR in the images and obtain enough signal after averaging [82]. For the SPA workflow, many reconstruction programs exist containing algorithms for each step of the process. The most popular to date is Relion, an open source program published by Sjors Scheres in 2012 [102]. We are currently at the 4th version of the program [245]. A unique algorithm to Relion, useful for flexible particles is the multi-body refinement [246]. It is used for 3D structure refinement of big particles comprised of many rigid

independently moving parts called “rigid bodies”, as well as determining their relative motions. Another program is cryoSPARC, developed by Structura Biotechnology Inc. and available for free for non-profit academic use [101]. Two other programs are cisTEM [247], a very visual program easy to use and understand, and Scipion [248], a package containing many software that enable to perform SPA. In the present work, Scipion was used to perform deep learning based post-processing of 3D volumes with DeepEMhancer after the main analysis. The program we mainly used in this chapter is Relion 4 [245]. The workflow is presented in figure 7.2. Any calculation, like 2D classification for example is referred to as a “job”.

Image processing

All cryo-EM data have been acquired using a DDD camera (Ametek Gatan K2), which gives us multi-framed movies instead of the single-framed micrographs. This allows correcting the sample drift and greatly improves signal for high spatial frequencies. After importing the movies, we correct the drift (beam-induced motion and stage drift) frame by frame using the MOTIONCOR2 algorithm [228]. In addition to estimating inter-frame motion, the algorithm estimates the heterogeneous per-movie motion of particles. Therefore, MOTIONCOR2 also estimates the motion of the particles by dividing the micrograph into smaller patches [82]. After motion correction, we proceed to CTF estimation. In Relion, two algorithms exist, GCTF [249], optimized to use GPU and thus running faster, and CTFFIND, which is the open source option integrated in Relion [250]. This step aims to estimate the defocus and the astigmatism by fitting a model of the microscope CTF on the amplitude spectrum of each micrograph, which is obtained by taking the absolute of the FT of a micrograph or movie. CTF estimation yields us the defocus as well as different other interesting parameters like the estimated maximum resolution for each micrograph.

An optional step following the CTF estimation is to do an image subset selection based on the estimated maximum resolution (refer to the figure 7.2). It is possible to filter our data using the subset selection at different steps of the SPA using different criteria. Another optional method after the subset selection is manual picking. Before having the current powerful algorithms for particle picking, microscopists used to manually pick all particles on their micrographs. Nowadays, it is only useful to get to know the data, and to determine the diameter of the mask used to pick the particles for the automatic picking.

In all cases, the next mandatory step after CTF estimation, as shown in figure 7.2, is automatic particle picking. For the first auto-picking job, we use the Laplacian-of-Gaussian (LoG) filter that was added in Relion 3 onwards [108]. For this step, no template is required, but only the minimum and maximum particle diameter, as well as a threshold to avoid picking contaminations, which are usually well contrasted.

Particle picking and 2D classification

Particle picking determines the coordinates of every object in the micrographs that the algorithm determined as being a particle. This allows to extract the particles from the micrographs into individual images. In this step, we specify a box size (in pixels) for the particles. We can also bin the particles to accelerate the calculations before un-binning at a later step when resolution becomes limited by particle binning.

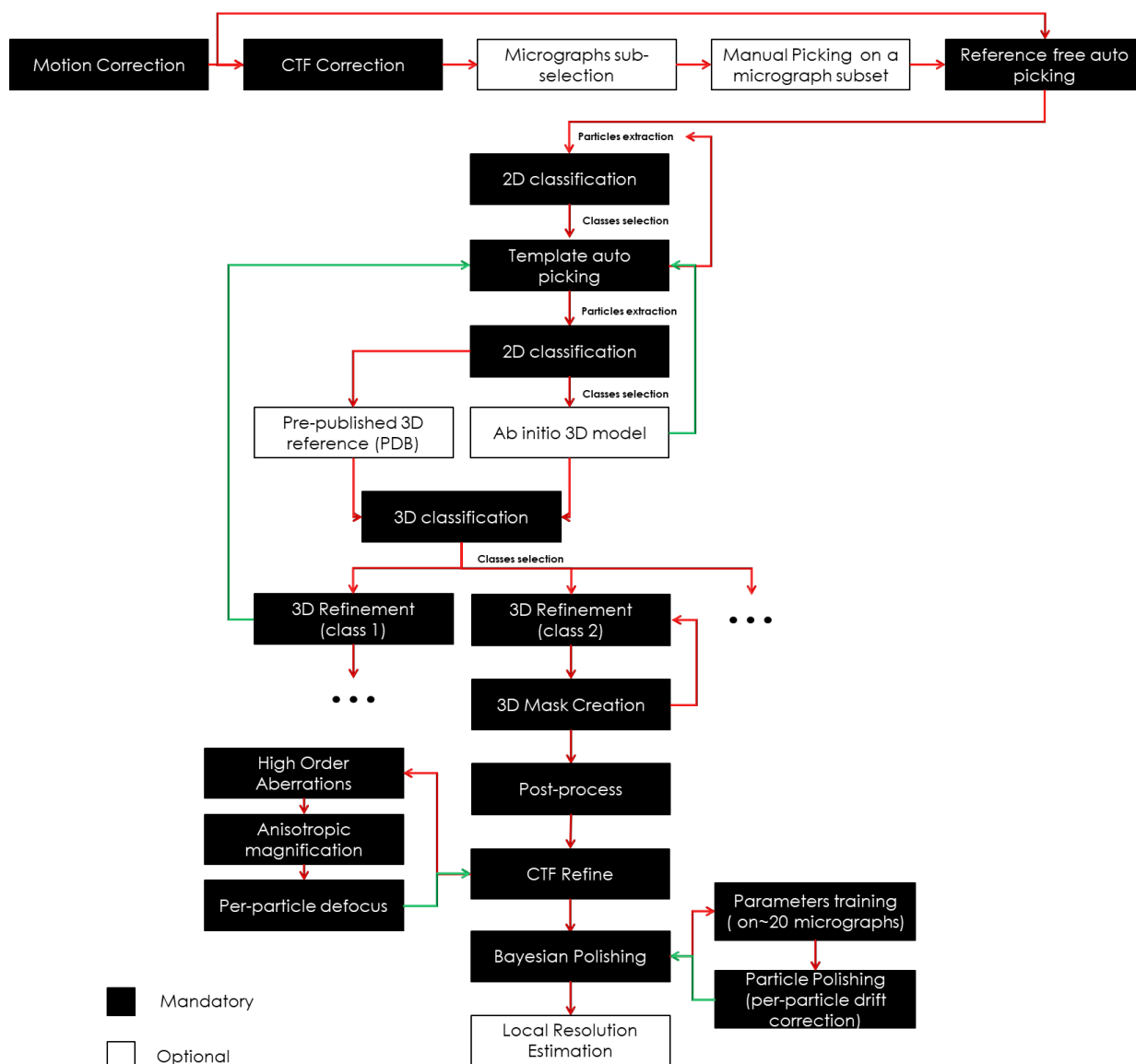


Figure 7.2 SPA workflow describing our work done on Relion 4 for the pre-40S particle reconstruction. The additional steps done on other programs are not included.

It is then possible to proceed to the first 2D classification, which aims to classify the particles according to their projection orientation. The addition of the aligned images in each class provides higher SNR images that can be used as 2D templates for the reference-based auto-picking. Using the subset selection job, we select a few classes that have different orientations (not all the good classes). Then we use the selected classes as templates for a template-based auto-picking and extract the particles. The 2D classification and auto-picking steps can be repeated if needed. It is also possible to perform the auto-picking taking the first 3D reconstruction to generate 2D templates, and then repeat the steps mentioned in this paragraph (figure 7.2). When the 2D classes are satisfactory, we select all the good classes using subset selection.

3D reconstruction and classification

3D reconstruction is performed by aligning the images on the projections of a reference 3D model. A first option is to use a similar published structure and low-pass filter

it, for example the structure of another mutant of the protein [100]. A second option is to generate a low-resolution ab-initio structure. The latter is based on a stochastic gradient descent (SGD) algorithm that was first used in cryoSPARC [101].

SGD is an optimization algorithm that will try to find local minima corresponding to the most probable 3D structure in an iterative manner, from randomly selected images at each iteration. This algorithm, compared to classical gradient descent is more effective in not getting trapped in a local minimum, that is a wrong structure to which the algorithm converges [82]. This is illustrated in figure 7.3 as the stochastic algorithm was able to escape the local minimum (purple disk) for a better more stable one (black disk) unlike the classic one that has a chance to get trapped depending on the initial starting conditions. We should mention that this method can fail if data quality is bad, or if the particles do not have enough orientations. In the last few years, a few deep learning algorithms have been developed for Ab-initio map calculation [117].

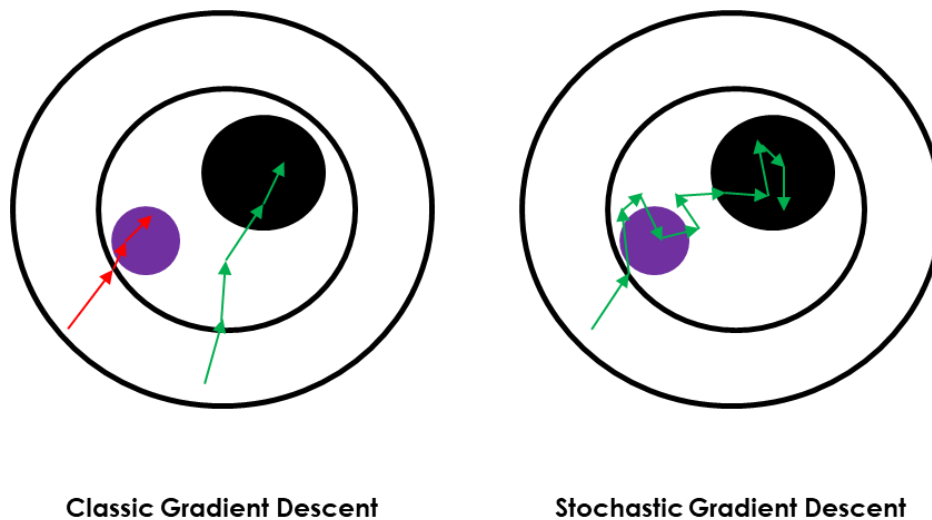



Figure 7.3 Comparison of the GD (left) and the SGD (right) algorithms.

After obtaining the reference, we can start the first 3D classification. For this, we need the last 2D class selection, as well as our 3D reference. Depending on our sample, we choose a specific number of 3D classes to be determined. Too many classes will lead to a low number of particles per class and longer calculation times. Too few and we may miss the structural heterogeneity in our sample. As with 2D classification, we use the subset selection to select each good 3D class with a separate job. We then proceed similarly for each selected class.

The following step is to refine the 3D map using the 3D refinement job. This step requires very few inputs, namely the initial angular sampling for orientation determination, the reference and the 3D class [111]. During this job, the estimated resolution and the average changes between iteration in the optimal orientations and class assignments of all the particles are monitored. The resolution is calculated by the gold standard Fourier shell correlation method by refining two independent half parts of the data set and calculating the FSC [251]. Whenever one of the two criteria (resolution and class assignment) no longer improves during new iterations, the angular orientation sampling becomes smaller. The algorithm stops when the orientation sampling becomes smaller than the estimated angular accuracy calculated by the algorithm [111]. The two-half datasets are combined for the final iteration. The refined map will be generated and its final resolution will be provided. This 3D refined map will then need to be sharpened. Therefore, we need to create a mask that envelopes the particle, while removing the outside noise without cutting parts of our 3D map. The sharpening is done with



the post-processing job. It will lead to a more accurate resolution estimation as the noise decreases the FSC curve in the 3D refinement (noise is not correlated) [252].

Two major steps remain and can be done in any order to further improve our map resolution. The first is CTF refinement, which consists in correcting the higher-order aberrations, the anisotropic magnification [253] and per-particle defocus by running it once for each [108]. A 3D refinement followed by post-process is performed after the 3 CTF refinement jobs and should lead to an improvement of the resolution. How well the per-particle defocus algorithm performs depends on how flat the ice was. The second process is the Bayesian polishing. This job estimates individual particle motion due to beam damage [253]. Before running the polishing, a “training step” is required to determine the input parameters. After polishing, another 3D refinement followed by a post-process step are performed. An optional step is, if useful, to calculate the local resolution on our 3D map.

To visualize 3D structures, we use two main software: UCSF chimeraX [254,255], the successor of UCSF chimera [256] which is the one we used in our study, as well as Pymol [257], with most functionality accessible with the open source license.

7.2 SPA ANALYSIS OF THE PRE-40S PARTICLE

7.2.1 SPA analysis of the full pre-40S particle

A summary of this SPA analysis is presented at the end of this chapter for reference.

Image acquisition on pre-40S extracted from the Rps20 D113K/E115K double-mutant yeast strain was performed over two days. In total, we obtained 9891 multi-framed movies with 40 frames per movie. CTFfind was then used to estimate the defocuses of the motion-corrected movies that ranged from 2000 to 45000 Å (figure 7.3a). The defocuses per movie are well distributed along the defocus range with the highest number of movies around 15000 Å. The resolution per micrograph also provided by the CTFfind algorithm is presented in figure 7.3b. The resolutions ranged from 2.8 to 6.7 Å. As most had a resolution below 5 Å, we went ahead and selected the movies with maximum resolution of 4.5 Å. We therefore ended up with a total of 6933 movie that we used for the rest of the analysis.

Our reference-free auto-picking gave us 1169810 particles. With this number of particles, we decided to bin the extracted particles to facilitate the calculation. We therefore created 2D classes and selected those who corresponded to different orientations for the template-based auto-picking. We therefore ended up with an average of 144 particle per micrograph. This led to the 26 2D classes shown in the figure 7.4a, with a total of 367449 particles. The classes are ordered from the highest number of particles (top left) to the lowest (bottom right). The most populated classes on the first line show a tendency of our particles to adopt a preferential orientation.

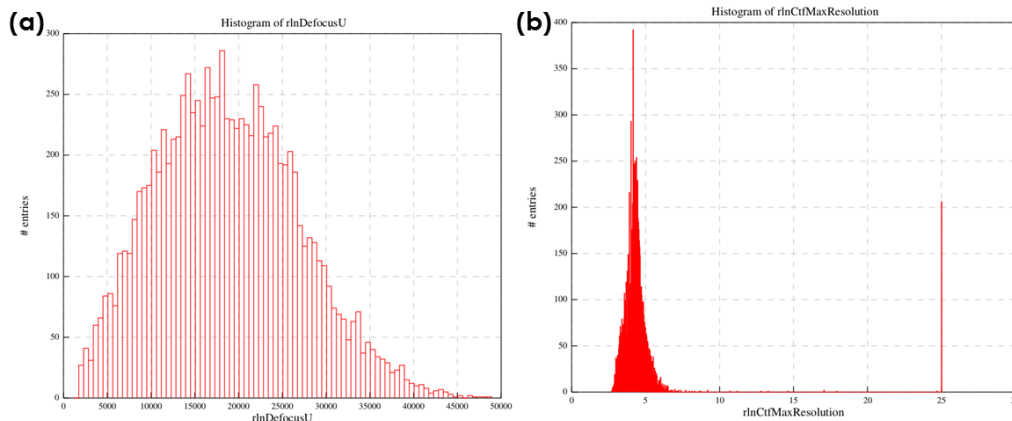


Figure 7.3 CTF estimation using the CTFFind algorithm. (a) Histogram distribution of the number of movies as a function of the measured defocus. (b) Histogram distribution of the number of movies as a function of the estimated resolution.

For the 3D classification, we used a previously published reference, the C1-S20 Δ loop structure reconstructed by Mitterer et al. (pdb: 6RBD) [233] and created a 3D volume map by using the 'molmap' command on chimeraX. We chose to obtain 3 classes. The results are shown in figure 7.4b. Out of the three maps, the class number 3 was by far the best as the head looked a lot more like what we are expecting. The classes 1 and 2 had head parts (upper part) that looked deformed and not resolved at all. The particles that were used to obtain the class three were therefore selected for further analysis. Using the 'subset selection' job, we re-extracted the particles of class 3 from the movies and unbinned them. In total, 142920 particles were remaining.

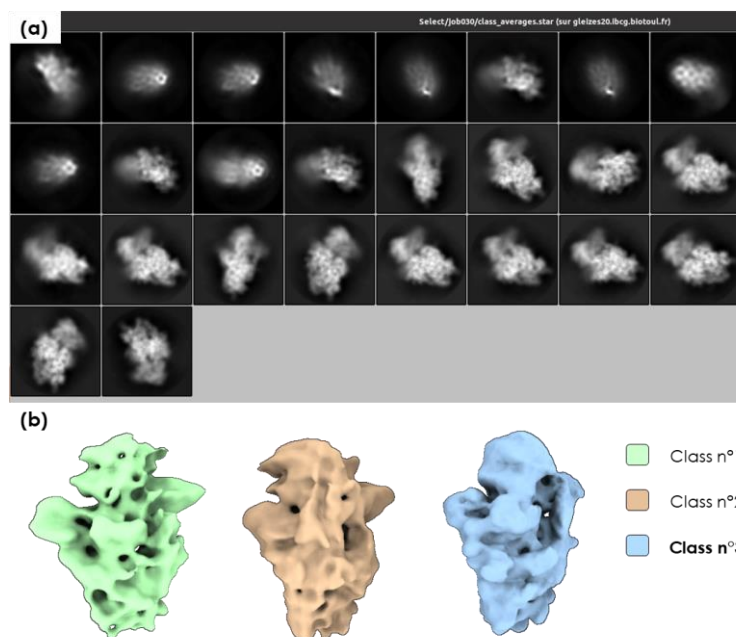


Figure 7.4 (a) Final 2D classes obtained by template-based auto-picking. (b) First 3D classes obtained from the particles selected using the 2D classes in (a).

We next performed a first 3D refinement step on these selected particles on Relion. The results are presented in figure 7.5, visualized on chimeraX. The difference between figures 7.5a and 7.5b is the level of contour. The resolution, given by the gold standard FSC, is 4.29 Å. The body of the pre-40S is very well resolved and the structure is very well defined when

looking at the structure with low contour. The 20S rRNA is visible (red arrows) as well as some secondary structures like the α -helix (yellow arrow). However, the head of the pre-40S has a poor resolution at this stage. Lowering the contours does not show any detail as the head disappears.

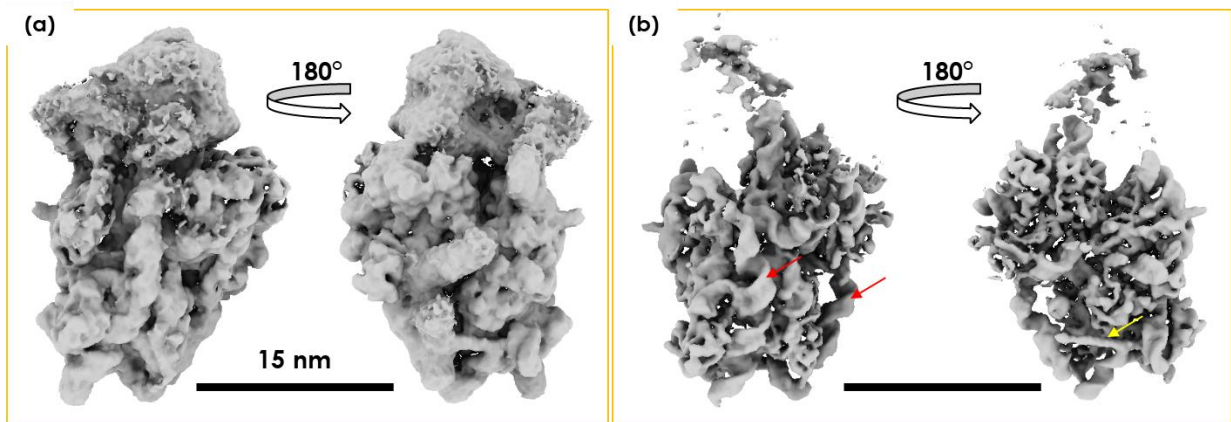


Figure 7.5 3D map obtained after 3D refinement by using the particles selected from the 3rd 3D class in figure 7.4b. (a) 2 views rotated by 180° with low contour levels. (b) 2 views rotated by 180° with high contour levels.

To improve the map, the 3D refine was followed by a post-processing. For that step, a mask has to be created prior to the job. The mask surrounds the particle, thus removing some noise, without cutting part of the protein. We also applied a 20 Å lowpass filter on the mask. Post-process yielded the results presented in the figure 7.6. The Fourier shell correlation (FSC) is presented in figure 7.6a. The red line, which is the correlation of phase randomized masked maps (addition of high resolution noise) drops fast before the other curves, signifying that there is no over-fitting in the post-process [252]. In other terms, if the masked curves drop before the phase randomized one, it indicated that the real structure contains a lot of high resolution noise that comes from over-fitting in our 3D structure. The resolution is given by the black line (overlapping with the blue one) which corresponds to the masked FSC calculation. In our case, the resolution, estimated for an FSC threshold of 0.143 [258] is at 3.8 Å.

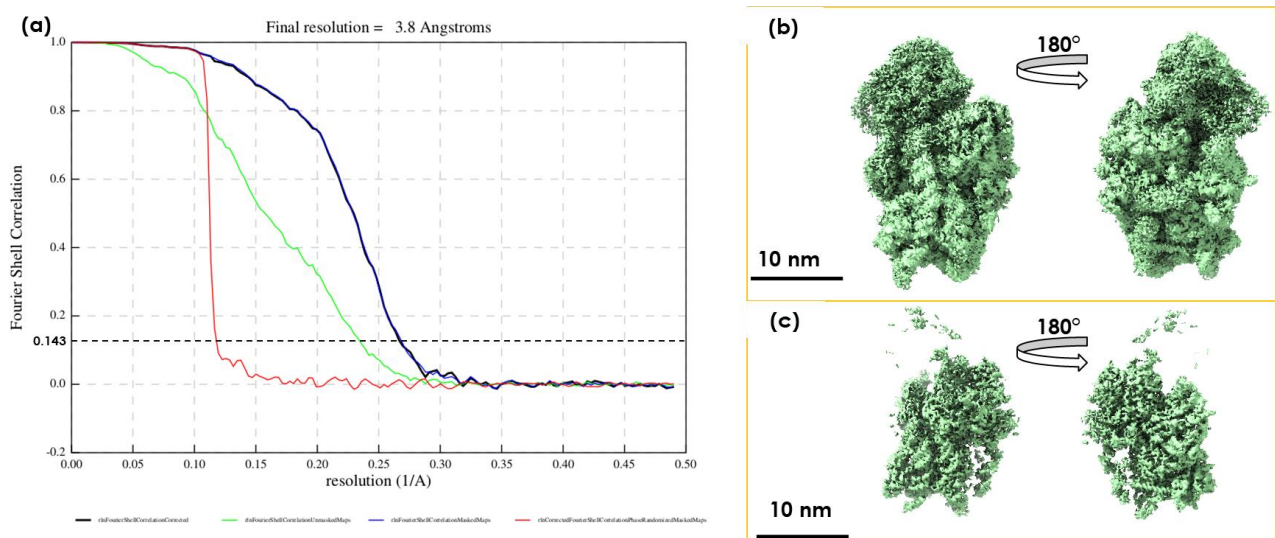


Figure 7.6 Post-process results following the first 3D refine. (a) FSC plot showing a random noise (red) plot, an unmasked map FSC (green) and a masked particles FRC (blue and black). The black curve is a correction made on the blue curve to account for the mask effect on the FSC [258]. (b) Low contour and (c) high contour 3D volume of the post-processed particles.

The low contour level map in figure 7.6b shows more details than the refined structure in the previous figure. However, the head is still not clear and no specific feature can be observed beyond what the 3D refined structure showed us. Lowering the contour levels will make the head disappear as evidenced by the structures in figure 7.6c. The body is however more detailed as we can now see the RNA strand of the 20S rRNA.

To further improve the resolution, CTF refinement was carried out. Following these 3 jobs, a 3D refinement as well as a post-process were done to check for a resolution improvement. The results of the post-processing are shown in figure 7.7. The unmasked phase randomized (red) curve in figure 7.7a indicated a good post-process and resolution estimation. The latter was therefore improved by 0.4 Å (3.4 Å resolution). This can be observed when comparing the low contour image (figure 7.7b) and the high contour image (figure 7.7c) with those of the previous post-process (figure 7.6b and 7.6c). However, the structures still show no sign of improvement at the head level, indicating that the resolution improvement was at the body level.

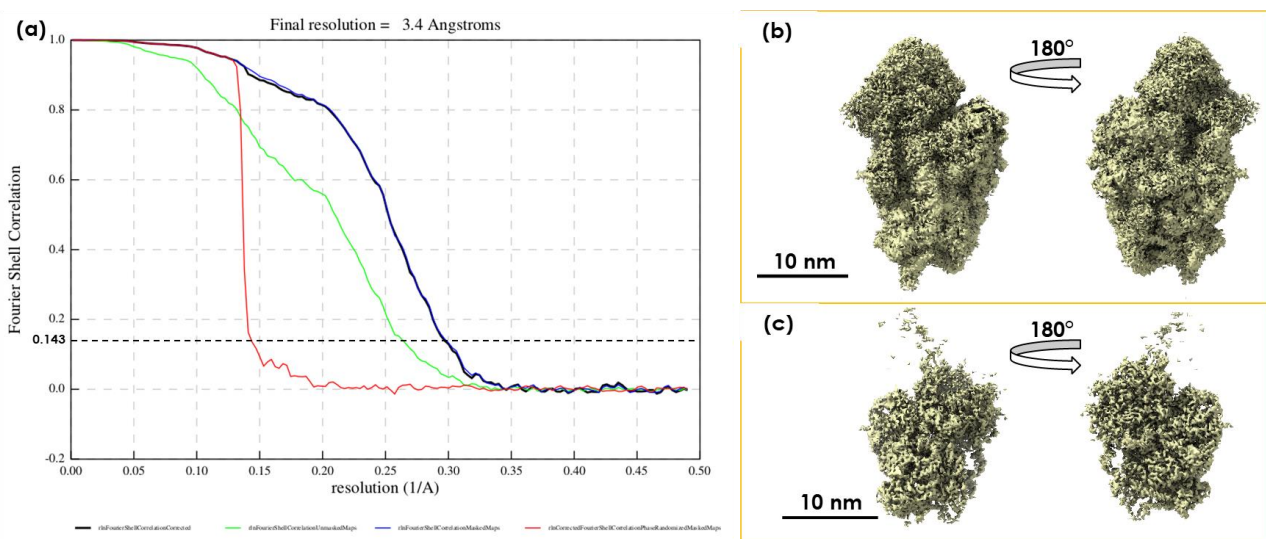


Figure 7.7 Post-process results following the CTF refinement. (a) FSC plot showing a random noise (red) plot, an unmasked particle FSC (green) and a masked particles FRC (blue and black). The black curve is a correction made on the blue curve to account for the mask effect on the FSC. (b) Low contour and (c) high contour 3D volume of the post-processed particles.

In Relion, it is possible to further improve the resolution by estimating the motion of each and every single particle across all the movies and correcting for it. The algorithm is called Bayesian polishing [108]. Particle polishing is done in two steps, first a training is needed, which is done on a subset of particles. It is recommended on Relion's tutorial to use around 4000 particles. The training will give us three parameters required for the main algorithm: particle velocity, diversion (spatial correlation length of the velocity), and acceleration. The main algorithm will then estimate, much more accurately than the initial motion correction the movements of the particles. When the initial data is already well resolved, like in our case, this is expected to further improve the resolution. The polishing was followed by a 3D refine and a post-processing. The FSC curve is shown in figure 7.8a showing a 3.1 Å resolution, a 0.3 Å improvement over the last post-process.

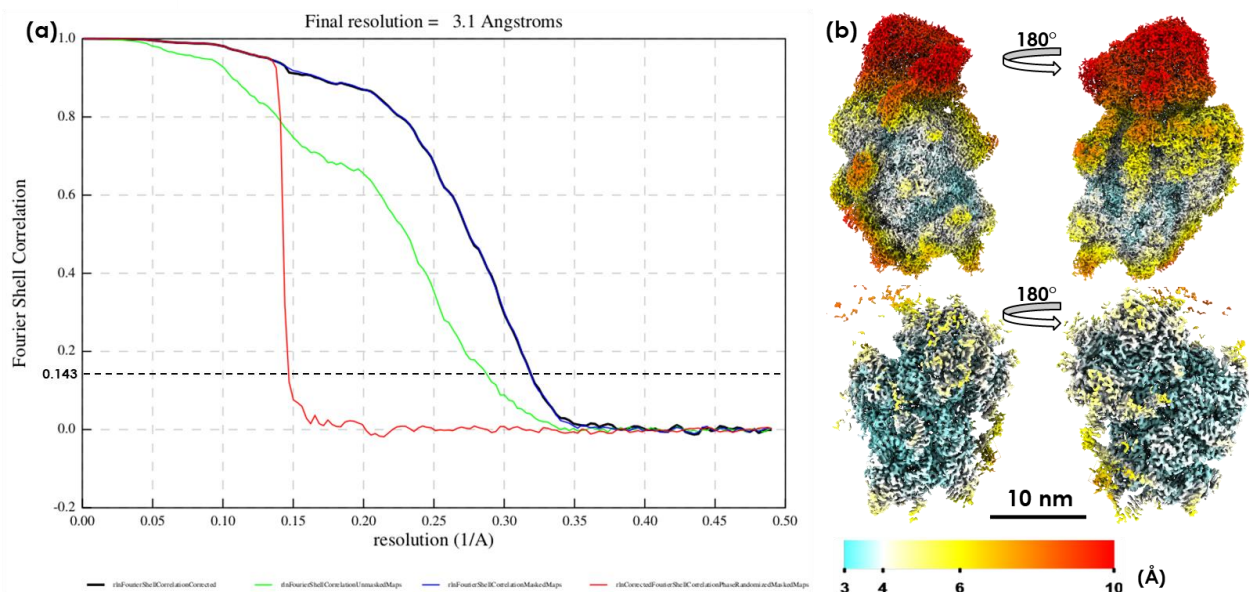


Figure 7.8 Post-process results following the Bayesian polishing. (a) FSC plot showing a random noise (red) plot, an unmasked particle FSC (green) and a masked particles FRC (blue and black). The black curve is a correction made on the blue curve by the algorithm which usually does not make much difference. (b) Low contour and (c) high contour 3D volumes of the post-processed particles. The particles are colored corresponding to the local resolution calculated on Relion.

As our interest was to look at the head structure, we calculated the local resolution across the 3D volume on Relion. The post-process volume was then colored according to local resolution. The results are shown in figure 7.8b with low contours (top) and high contours (bottom). As expected the body was well resolved with the resolutions between 3 and 4 Å. The flexible parts, namely the solvent exposed parts of the pre-40S body were slightly less resolved with values between 5 and 10 Å. However, the head had resolutions between 9 and 12 Å, which correspond to rather low resolutions for such structural analysis. This called for the specific improvement of the head resolution through focused analysis.

7.2.2 Resolution enhancement of the Pre-40S head

To enhance the head resolution, the body was subtracted using the corresponding job on Relion, leaving only the head density.

We started with the 142929 particles used to build the 3D reconstruction presented above. A 3D classification was then run with one class as the output. Due to the structural heterogeneity on the head, the final iteration was over-fitted. We therefore took the 12th iteration, shown in figure 7.9a (up) as a reference for a 3D refinement.

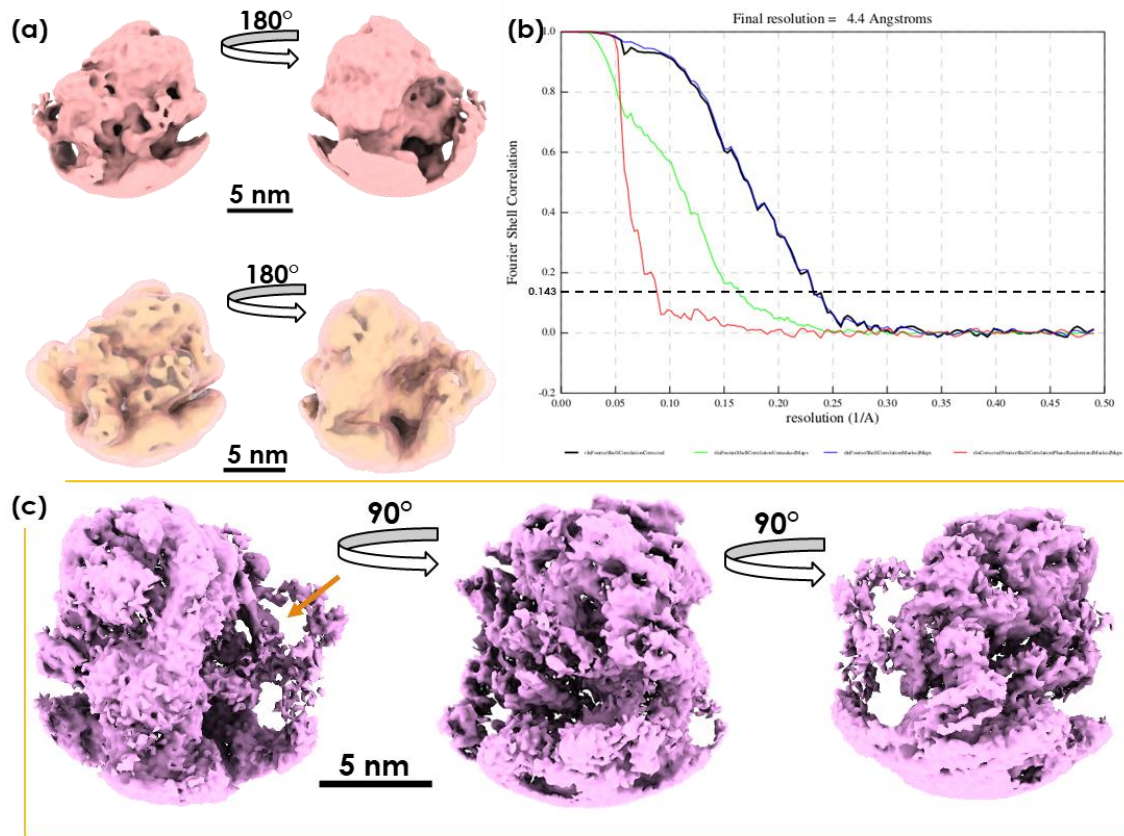


Figure 7.9 (a) Up: 12th iteration of the head model obtained by 3D classification with one class as the output. Down: 3D refined structure using the initial particles within the mask that was generated for the post-processing job. (b) Post-processing FSC of the 3D refined structure in (a) down, showing a resolution of 4.4 Å. (c) Post-processed head shown at 3 different angles.

The particles were 3D refined based on the obtained map. The resulting structure had a 6.15 Å resolution. The mask was then created for post-processing by manually subtracting the parts of the mask corresponding to the body on chimeraX. The 3D refined structure (yellow) as well as the mask (transparent pink) are shown in figure 7.9a (down). Subsequent post-processing led to a 4.4 Å resolution. The FSC graph, shown in figure 7.9b, validates the post-processing job. The resulting 3D structure is displayed in figure 7.9c. The head looks a bit hollow, especially the beak part (orange arrow). To determine the heterogeneity of the heads, the particles composing the post-processed structure were subjected to a 4 class 3D classification. The first job was run with the “Perform image alignment” option on ‘no’. Therefore, the particles were only classified without further alignment. The obtained classes are shown in figure 7.10a (up). All classes showed a good 3D structure with different resolutions, with the exception of class 2. This second class was the most populated one with 53000 particles as shown in the histogram in figure 7.10b. To try to understand why, a 3D classification with three output classes was run with the particles from class 2 (results not shown). All the obtained classes were poorly defined, signifying that the second class in the figure 7.10a (up) contains either very heterogenous orientations and conformations of the head, or (beam) damaged particles. The best class that is the third one contains 27502 particles less than the classes 2 and 4.

A second job was run with the “Perform image alignment” option on ‘yes’. This translates to a classification as well as a particle alignment during this process. However, the obtained classes, shown in figure 7.10a (down), looked worse than the initial 3D refinement

map shown in figure 7.9a (down), with the exception of class 4. As a test, classes 1 and 4 were refined and post-processed (results not shown). Class 1, with 43654 particles (figure 7.10b), gave a 4.9 Å resolution map while class 4, with 24843 particles (figure 7.10b) gave a 4.7 Å resolution.

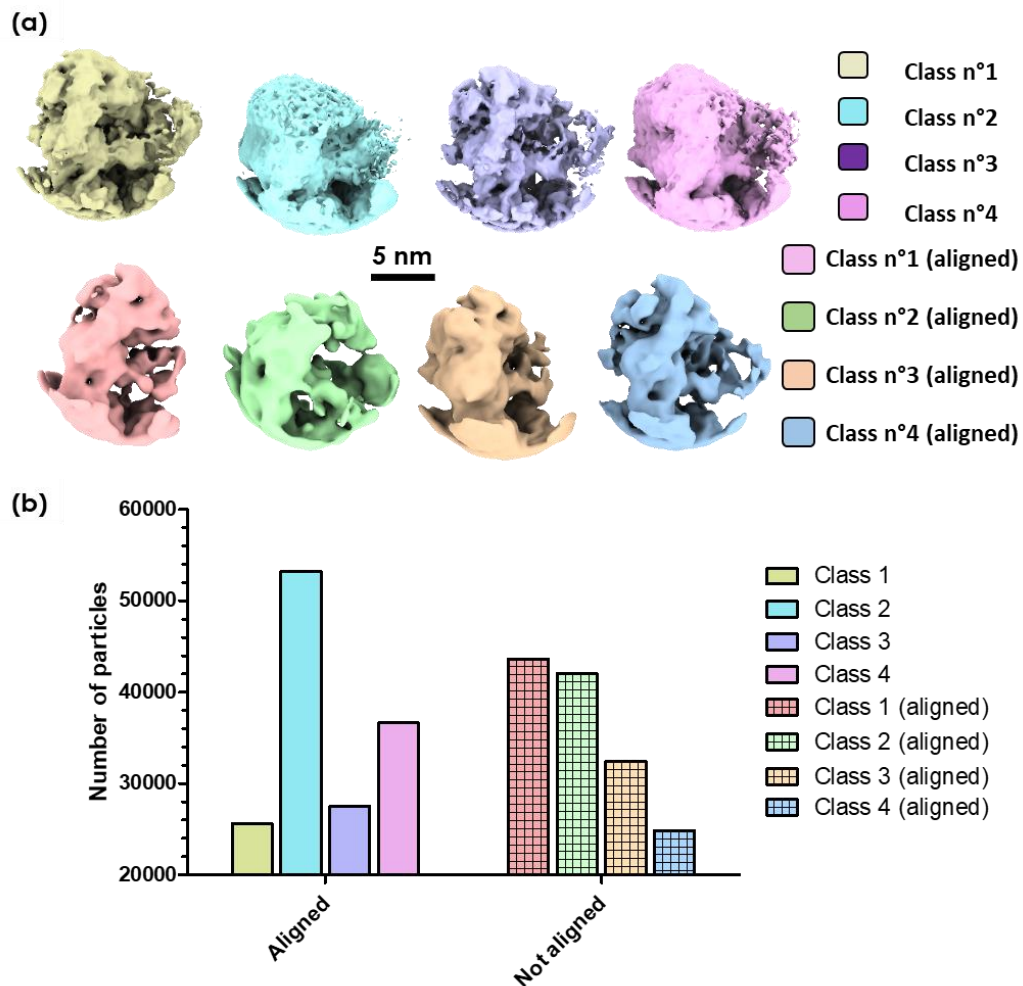


Figure 7.10 3D classification of the 3D refined particles in figure 7.9a (down). Up: The 4 classes obtained by the ‘non-aligned’ 3D classification. Down: The 4 classes obtained by the ‘aligned’ 3D classification. (b) Histogram of the distribution of the number of particles of the ‘aligned’ and ‘non-aligned’ classes.

The classes 1 and 4 of the aligned 3D classification, in addition to those obtained without alignment were then 3D refined and post-processed. The results of the class 3 of the non-aligned 3D classification are shown in the figure 7.11. The 3D refined of this class led to a 7.1 Å resolution. The 3D map is shown in figure 7.11a. At this resolution, we can start to see some proteins, like the AF Rio2 that is shown by the red arrow, an ATPase (enzyme hydrolyzing ATP) that is essential for pre-40S maturation [259]. We can clearly see its two α -helices density. The post-processing of this structure lead to a 4.7 Å resolution structure as shown in the FSC curves in figure 7.11b. We therefore went from an initial resolution of the head that was around 10Å to less than a half showing that our approach was very efficient.

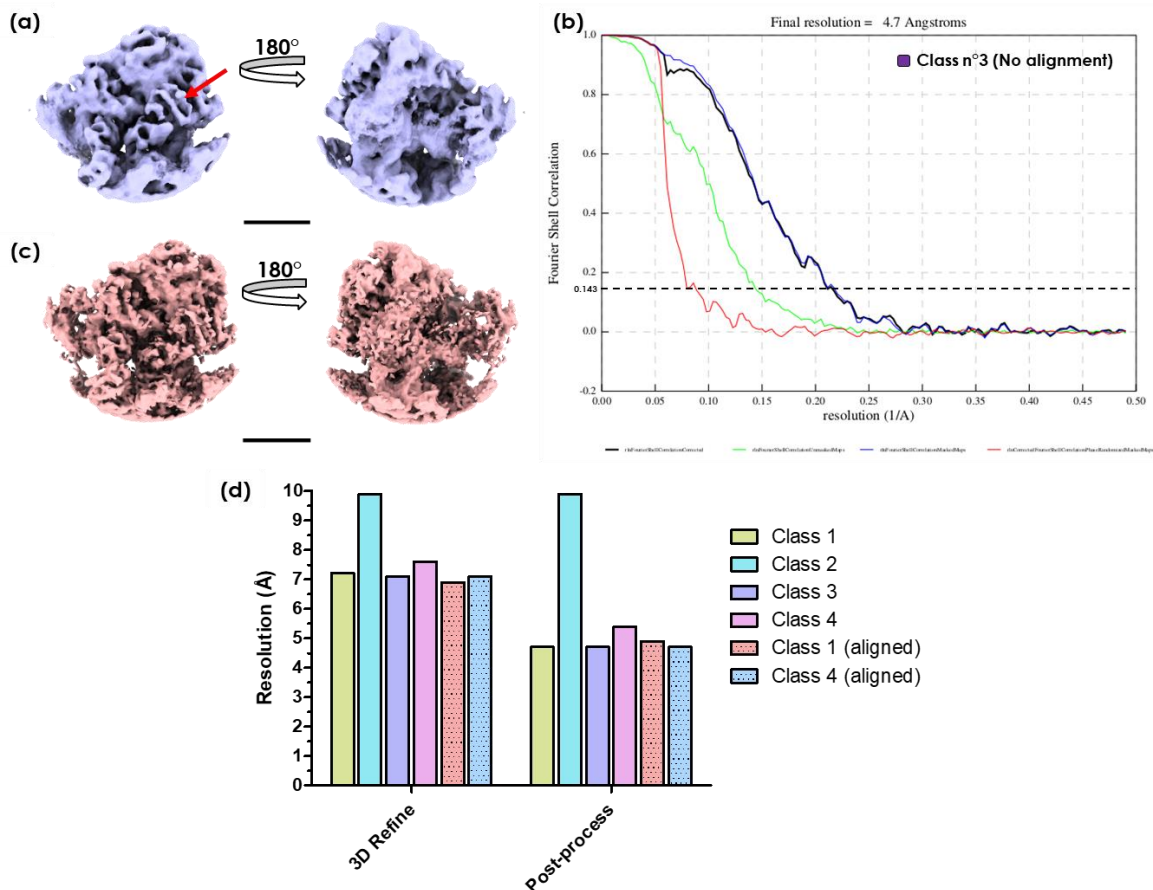


Figure 7.11 (a) 3D refinement of the third class of the non-aligned 3D classification shown in figure 7.10a. The red arrow shows the density corresponding to the Rio2 protein. (b) FSC of the post processing of the map in (a). The achieved resolution is 4.7 Å. (c) Post-processed map of the structure in (a). (d) Histogram of the 3D refine and post-processed 3D maps resolutions of the different classes shown in the figure 7.10a except the classes 2 and 3 of the aligned 3D classification. Scale bars correspond to 5 nm.

The 3D electron density map is shown in figure 7.11c. The improvements made compared to the 3D refined structure are easily seen when comparing the two. The resolutions of the refined and post-processed classes presented in figure 7.10 is shown in figure 7.11d. The second class of the non-aligned classification shows a similar resolution to the initial head before subtraction of the body signal. The post-processing of this class shows no improvements in the resolution. All the other classes possess more or less similar resolutions after 3D refinement as well as after post-processing. The best classes were the first and third classes of the non-aligned 3D classification. The first class had a 7.2 Å resolution for the 3D refined map, and a 4.7 Å resolution for the post-processed map.

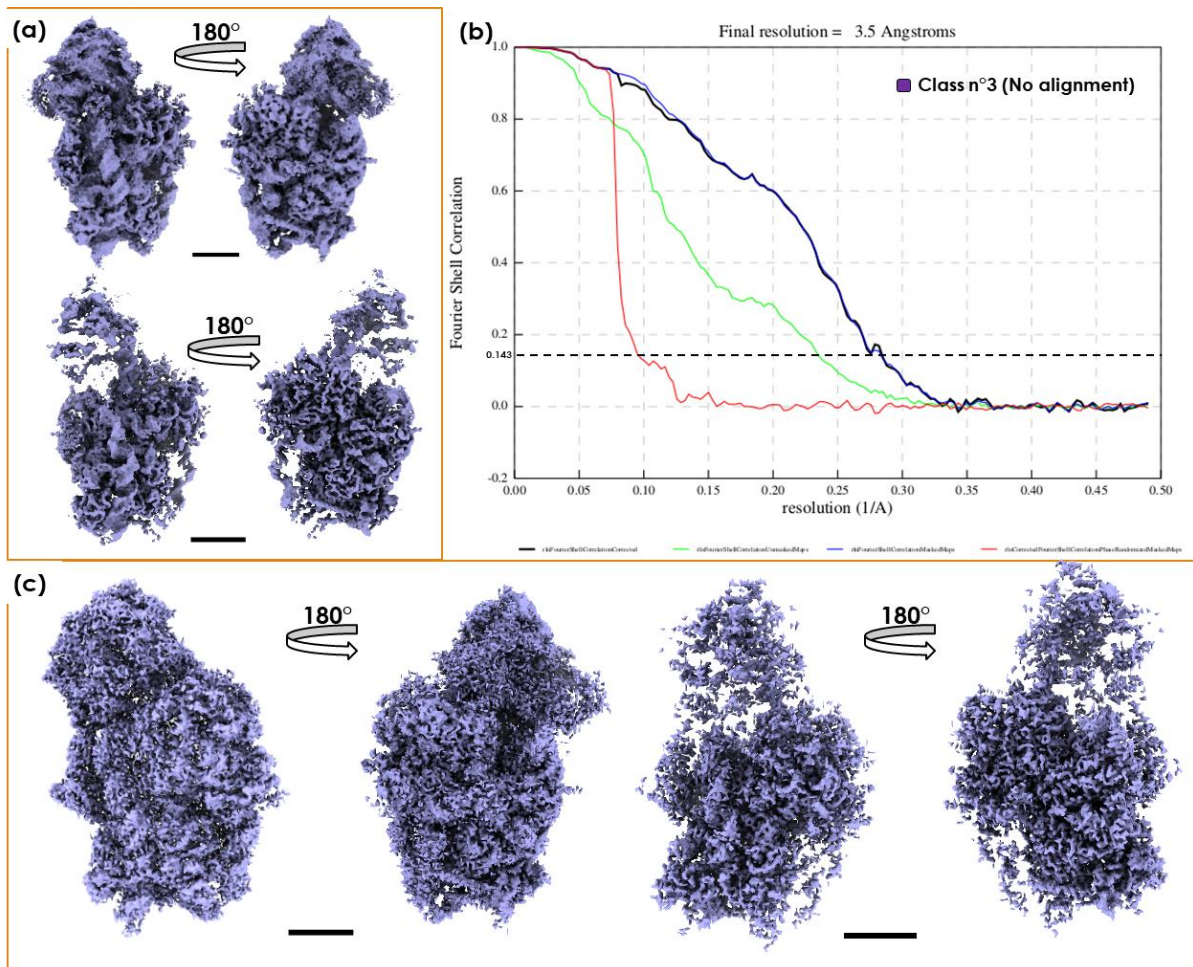


Figure 7.12 (a) 3D refinement of the reverted class 3 (non-aligned) with high (up) and low (down) contours. (b) FSC curve of the post-processing of the map shown in (a), showing a 3.5 Å resolution. (c) Post-processed maps refinement of the reverted and refined class 3 (non-aligned) with high (left) and low (right) contours. Scale bars correspond to 5 nm.

All the classes shown in figure 7.11d were then reverted to obtain the 3D map of the corresponding entire pre-40S particles. The figure 7.12a shows the 3D refine of the reverted particles of the class 3 of the non-aligned classification. The upper part shows a much better head compared to the full particle results we obtained in our initial SPA workflow. The head is nonetheless not fully visible when lowering the contour levels. The body details are also still visible. For this class, the resolution is 4.2 Å. The FSC graph of the post-process in figure 7.12b shows a 3.5 Å resolution, a bit lower than the 3.1 Å resolution of the full particle in the figure 7.8. This indicates that the alignment that was based on the head part, slightly reduced the body resolutions. The high (left) and low (right) contour 3D maps are shown in figure 7.12c. Comparing with the figure 7.8b (down), we see that we have more signal coming from the head when lowering the contours, further confirming the better head resolution. These reverted and post-processed maps were then used for our structural analysis in chimeraX.

The main SPA presented in this paragraph is summarized in the figure 7.13, and focuses on the class 3 for simplicity. For the full detailed SPA analysis, refer to figure 7.2.

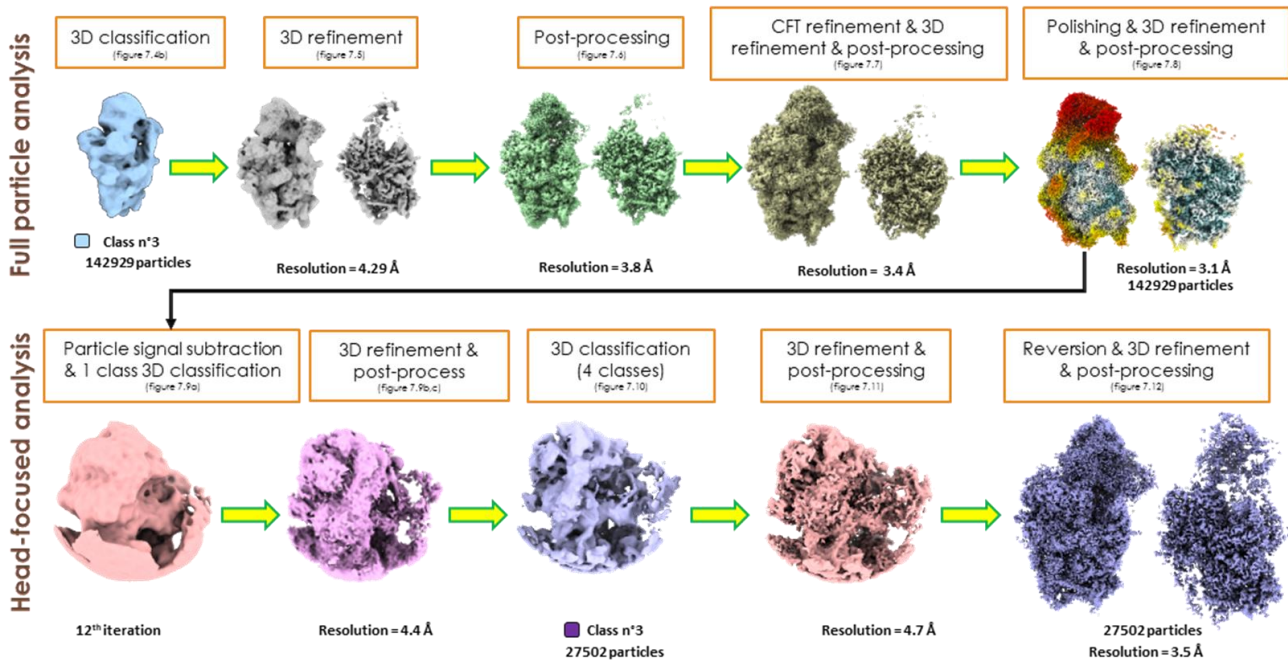


Figure 7.13 Summary of the 3D maps generated and refined during the SPA of the pre-40S with a focus on the class 3 head on the second line.

Deep-Learning post-processing of the 3D refined non-aligned heads and reverted particles

In parallel to post-processing of the head with Relion, we performed deep learning based post-processing using the DeepEMhancer algorithm [260]. It is based on a convolutional neural network that has been trained using EMDB data with pairs of images: a cryo-EM map as input and a tightly masked post-processed map using LocScale [261] as an output.

The 4 classes obtained from the non-aligned 3D classification of the head particles were post-processed using DeepEMhancer. The results are shown in figure 7.14. As previously observed, the second class still exhibits a bad structure after this deep learning post-process. Classes 1, 3 and 4 all exhibit improved electron density maps, especially the third class that yielded the best resolution with Relion. The beak in classes 1 and 3 is only visible when increasing the contours compared to what is displayed in figure 7.14.

The deep learning approach was successful as it provided high resolution head structures without any noise, in contrast to the Relion post-process where denoising in chimeraX is required by the means of the 'hide dust' command. We therefore used these structures, in addition to those obtained in Relion, for our structural analysis.

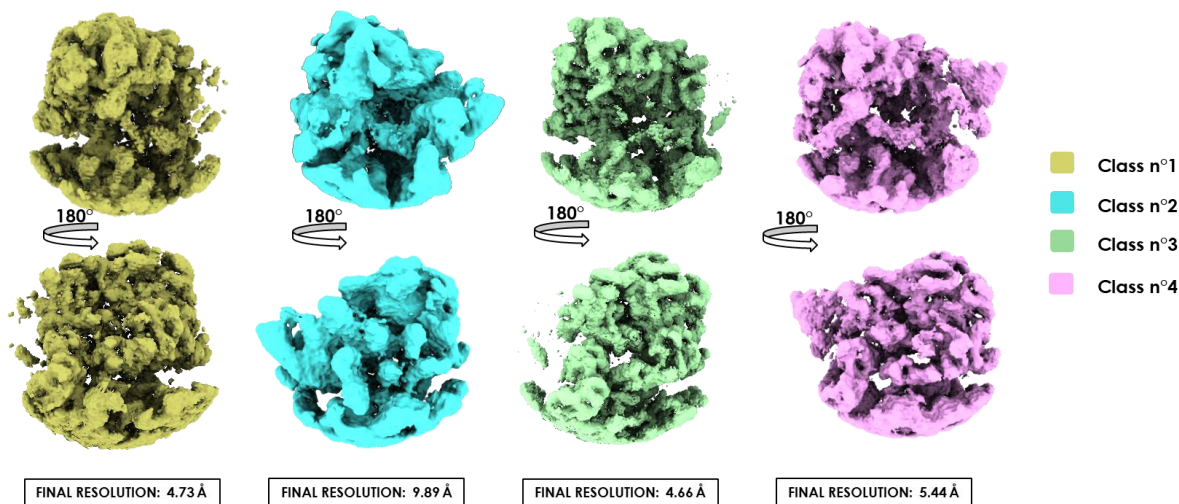


Figure 7.14 Post-processed 3D maps of the 3D refinements of the four classes obtained by the non-aligned 3D classification. The resolutions are those obtained by the Relion post-process as DeepEMhancer does not provide neither the FSC graph nor the resolution value.

Multi-body refinement of the pre-40S

In order to assess the flexibility of the pre-40S and improve the head resolution, we tested multibody refinement [115] using the reverted 3D refined third class displayed in figure 7.12a.

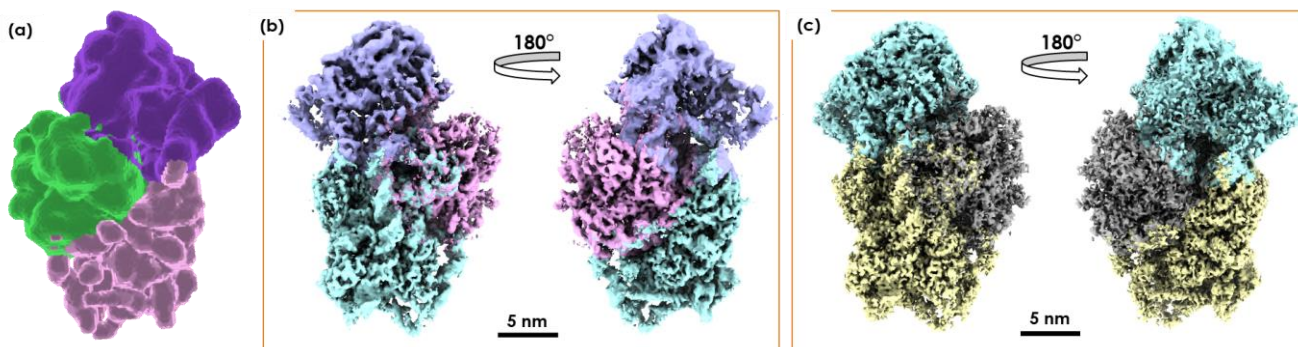


Figure 7.15 Multibody refinement of the 3D refine in figure 7.12a. (a) Simultaneous visualization of the 3 masks obtained by cutting the original one (full particle) generated in Relion, by using the 'erase' tool in chimeraX. (b) Refinement results of the 3 bodies. All are shown simultaneously in this figure. (c) Post-process of the 3 bodies shown in (b). Similarly, the bodies are shown simultaneously in this figure.

Figure 7.15 shows how pre-40S were divided into three parts, called 'bodies': the head (purple), the platform (green) and the body (pink). The corresponding masks for the three bodies were created in chimeraX (figure 7.15a). The masks were all lowpass filtered at 15 Å. The refined structure of the three bodies is shown in the figure 7.15b. The global resolution obtained is 3.5 Å, the same as for the 3D refined reverted class 3. This absence of improvement proves that our approach based on the classification of the heads helped sorting out the heterogeneity and thus improved the resolution. The post-processing of each body was then done. The three parts are shown simultaneously in the figure 7.15c. The resolutions of the three bodies are 3.5 Å for the body, 4.6 Å for the head and 3.6 Å for the platform. The head resolution is also the same as the one obtained in the Relion post-processing of the same class. Although multibody refinement did not improve the resolution, it still gave us an

understanding of the pre-40S flexibility. The flexibility movies will eventually be deposited on HAL archives.

7.2.3 Analysis and Discussion

Having obtained a detailed map of both the head and the body, we undertook a preliminary analysis by rigid fitting of a pdb structure these maps. We first compared this new map with the two structures of pre-40S particles isolated from two Rps20 Δ loop mutant strains, in which the amino acids (aa) of the loop are deleted (aa 68-78), published by Mitterer et al [233]. We found that our 3D map was similar to the C1-S20 Δ loop mutant (pdb: 6RBD). Hence, we used this pdb structure as our comparison model. It should be noted that we looked into all the classes (head alone and reverted) in addition to the DeepEMhancer post-processed heads. No major structural differences were observed between classes. The differences were mostly due to the pre-40S flexibility leading to variations of the position of the head relative to the body. The following results compare the 6RBD pdb structure to the class 3 of the 3D classification.

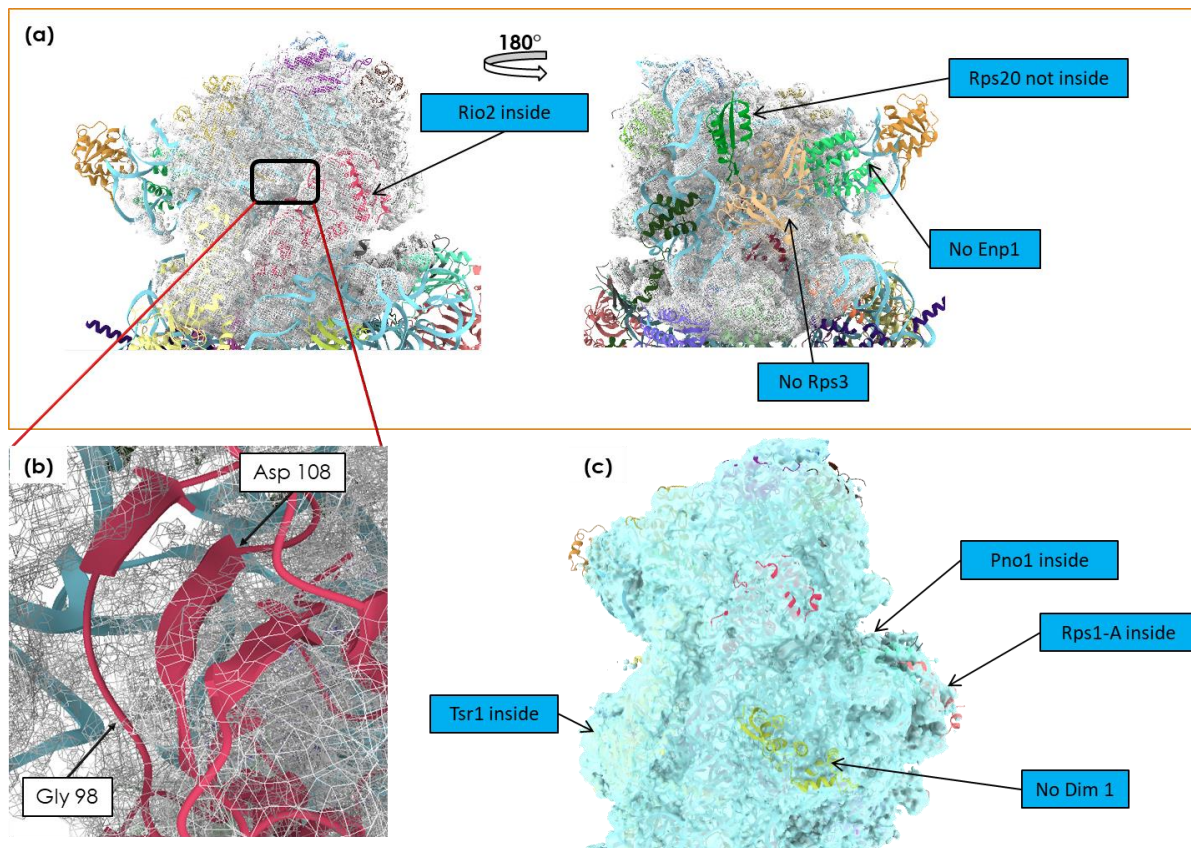


Figure 7.16 (a) Analysis of the class 3 of the DeepEMhancer post-processing (mesh representation) against the pdb 6RBD structure of the pre-40S. (b) Zoom-in into the Rio2 density showing a sequence (aa 98-108) outside the map. (c) Fit of the 6RBD structure into the full reverted class 3 (figure 7.15).

First, the pdb structure was fitted inside of the class 3 head obtained by deep learning post-processing. The results are shown in the figure 7.16a. We notice the absence of three proteins. The first is Enp1, an assembly factor (AF) that plays a role in the dissociation of the Ltv1 AF [233]. On the other hand, we can see that both Rps20 and Rps3 are missing. Regarding Rio2, we can see the protein in the map, but a sequence, aa 98-108, shown in figure

7.16b is out of the density map. The function of this sequence has yet to be established. Its displacement could be related to the absence or the mispositioning of Rps20, with whom Rio2 interact [233]. Regarding the body, we see in figure 7.16c the absence on the subunit interface of the AF Dim1, whereas Dim2/Pno1 and Tsr1 are present.

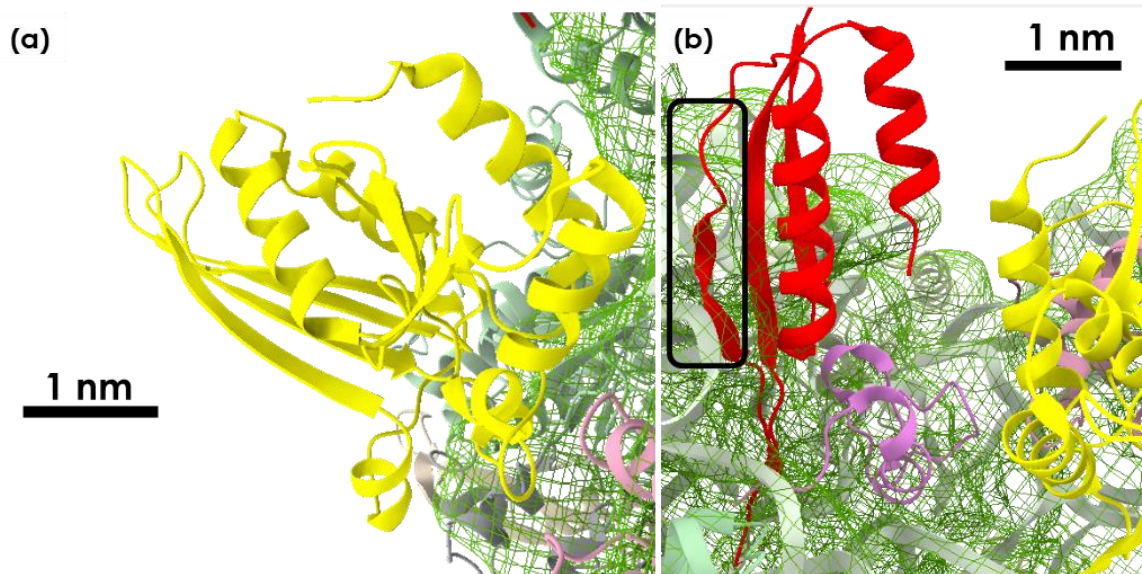


Figure 7.17 In-depth look at the electron density maps around (a) Rps3 (yellow) and (b) Rps20 (red). The red arrow in (a) shows a non-structured flexible sequence that is outside of the density. The rectangle in (b) shows a sequence of Rps20 inside of the electron density map.

We checked whether some parts of the map were empty when fitting the reference pdb 6RBD model, which could indicate the presence of the non-found proteins, but in a different position or conformation than in the 6RBD pdb model. Rps3 appeared to be completely excluded from the density map with no other possible conformations (figure 7.17a). A partial density corresponding to Rps20 could be detected (figure 7.17b), more specifically the sequence inside the black rectangle, as well as the internal loop that extends towards the other side of the pre-40S head. The rest of Rps20 was absent in our 3D structure.

Despite the partial appearance of Rps20 density in the map, we know that this Rps20 mutant is fully incorporated into pre-40S particles [233]. We think that Rps20 is not stably associated, or very flexible, which could explain its partial absence in the map. In addition, both the *rps20* mutant we used (*rps20* D113/K115>K) and the *rps3* mutant (K7/K10>ED) that also affect the Rps20/Rps3 interactions are viable, which indicates that 40S particles are indeed matured despite these mutations [233]. Since both Rps20 and Rps3 are essential for assembly of the 40S subunit, some correctly assembled intermediates are expected to be present in these mutated strains. However, these “normal” intermediates may be a minor species among the purified particles due to their much shorter lifetime compared to the misassembled intermediates characterized here.

The low number of particles (143,000 for the full particle reconstruction, 27,000 in class 3) (figure 7.13) also plays a role in the low resolution of the beak. Indeed, we would need a total of around one million particles in order to detect it, in addition to the unstable Rps20 and Rps3 within subgroups of classified particles. To do so, we would need to purify pre-40S particles again, try to increase their concentration on cryo-EM grids and acquire more images, thus more particles. Although it is very unlikely, we cannot completely refute the possibility of this being a purification artifact.

Fitting and analyzing our 3D map using the C2 Δ loop structure (pdb: 6RBE), the second one obtained by Mitterer et al. [233], did not add much information as the position of Rio2 did not correspond to this conformation, but rather to the one in the 6RBD map we presented in figure 7.16. Other AF who are only present in the C2 Δ loop structure are not present in our structure.

To further analyze these observations, we need, as a next step, to locally adjust all the chains of the 6RBD pdb model into our cryo-EM maps using Coot [262], since ChimeraX is only capable of rigid fitting the structure by translating and rotating the whole particle. This will soon be tested in addition to new acquisitions on other mutants by Dr. Célia Plisson-Chastang to try and further characterize the structural aspects of yeast pre-40S maturation.



RESUMÉ ÉTENDU DE LA THÈSE

Développement de la cryo-holographie électronique pour l'étude des matériaux biologiques

Directeurs de thèse : Dr. Etienne Snoeck (CEMES-CNRS)
Dr. Pierre-Emmanuel Gleizes (MCD-CBI)

Objectifs et contexte de la thèse

L'objectif général de cette thèse était d'étudier les potentialités de nouvelles méthodes de microscopie électronique pour l'étude de matériaux biologiques. Nous nous sommes concentrés principalement sur l'étude de deux techniques majeures d'holographie électronique, à savoir l'holographie électronique off-axis et l'holographie in-line par séries focales, avec pour objectif d'identifier leurs limitations et pousser les limites de quelques travaux déjà réalisés. Nous avons travaillé à optimiser ces méthodes en exploitant le potentiel de leur rapport signal sur bruit amélioré et de leur contraste accru.

Nos équipes du CEMES et du CBI à Toulouse utilisent la microscopie électronique pour l'étude de matériaux inorganiques et biologiques respectivement. Le groupe du CEMES possède une très bonne expertise en holographie électronique, et celui du CBI est expert en cryo-EM. Récemment, C. Gatel et al. ont fait progresser la méthode d'holographie électronique off-axis [8] pour atteindre une sensibilité de phase de 2 milliradians avec une caméra CMOS (complementary metal oxide semiconductor) avec une configuration de type CCD (Charge-Coupled Device) sur le microscope I2TEM au CEMES. Cela permet la détection de déphasages très faibles, comme ceux produits par des matériaux de très faible numéro atomique (Z), y compris des échantillons biologiques. La sensibilité de phase est encore meilleure avec l'utilisation de caméra à détection directe. Ces progrès ont été menés sur un microscope électronique unique dédié à l'holographie électronique, l'I2TEM, équipé d'un système à double prisme. L'objectif de ces travaux est de combiner les connaissances des deux équipes pour explorer les capacités de l'holographie électronique off-axis pour l'étude des échantillons biologiques. Le sujet de la thèse a été étendu incluant d'abord l'holographie électronique in-line, puis hybride. Par rapport à l'holographie off-axis, l'holographie in-line peut être menée sur des microscopes électroniques avec des optiques standards, comme le Talos Arctica, mais impose une analyse d'image complexe.

Ce travail exploratoire a dû faire face à des obstacles techniques importants. Malgré cela, cette thèse a abouti à de nouveaux résultats offrant une nouvelle évaluation de l'applicabilité des technologies modernes d'holographie électronique aux objets biologiques. Elle a permis



d'identifier des éléments clés à prendre en compte pour des développements futurs dans ce domaine.

Les échantillons tests utilisés pour cette thèse sont les bactériophages T4 et T5, bien connus et faciles à produire. L'avantage d'utiliser de tels échantillons est leur résistance accrue à l'irradiation électronique par rapport à d'autres objets plus petits (les protéines par exemple) qui nécessitent des études par MET avec des doses inférieures à $40 \text{ e}^-/\text{Å}^2$. Les phages T5 ont été préparés et purifiés par le Dr. Amélie Leforestier au LPS-CNRS de l'université Paris Saclay à Orsay alors que les phages T4 ont été produits au CBI dans le cadre de cette thèse. Des collaborations ont été menées avec plusieurs autres groupes, notamment l'équipe du Prof. Sara Bals au laboratoire EMAT en Belgique qui nous a fourni des grilles en graphène permettant d'améliorer les résultats de l'holographie off-axis.

Organisation du manuscrit de thèse

Le manuscrit est divisé en deux premiers chapitres bibliographiques. Le **chapitre 1** aborde les bases théoriques et méthodologiques de la microscopie électronique essentielles pour comprendre les principes avancés de la microscopie électronique (ME) tels que ceux concernant l'onde électronique et le transfert d'informations de phase et d'amplitude, ainsi que le microscope électronique lui-même.

Le **chapitre 2** se concentre principalement sur la partie biologique pour expliquer la composition des macromolécules biologiques, la microscopie électronique cryogénique (cryo-EM), la tomographie électronique cryogénique (cryo-ET), et aussi les principes des techniques d'holographie électronique. La dernière partie de ce chapitre décrit en détail les protocoles de préparation des échantillons utilisés au cours de cette thèse.

La partie résultat de ce manuscrit commence avec les **chapitres 3 et 4** et concerne les expériences d'holographie off-axis et in-line, respectivement. Ils sont les principaux chapitres de cette thèse. Les deux sont divisés en une introduction pour chaque méthode, les résultats des expériences à température ambiante, puis les résultats des expériences à température cryogénique. Des détails sur les performances, les limitations et les inconvénients des deux techniques sont discutés.

Le **chapitre 5** aborde les capacités améliorées de l'holographie hybride, qui combine l'holographie électronique off-axis et in-line pour obtenir de meilleures informations sur un spectre de fréquences spatiales plus large. Un paragraphe est ensuite consacré aux résultats de ptychographie obtenus par un groupe d'Oxford avec nos bactériophages T4.

Une **conclusion générale** compare et discute les méthodes d'holographie utilisées dans cette thèse avec les capacités actuelles des méthodes de microscopie électronique connues utilisées en biologie.

Un **chapitre annexe** est inclus en fin de manuscrit. Il présente une analyse classique de microscopie électronique cryogénique sur laquelle j'ai travaillé mais qui ne fait pas partie de l'axe principal de la thèse. Il concerne la détermination de la structure de particules ribosomiques pré-40S mutées par analyse de particules isolés (SPA). Ce chapitre n'est pas inclus dans ce résumé en français.

CHAPITRE 1 : MICROSCOPIE ÉLECTRONIQUE EN TRANSMISSION

Les électrons ont une double identité : la dualité onde-particule. Ce qui intéresse essentiellement l'holographie électronique sont la phase et la longueur d'onde du faisceau électronique. La longueur d'onde des électrons décroît avec l'augmentation des vitesses d'accélération. Elle est de 0.038 Å pour une tension d'accélération de 100 kV, et 0.01 Å pour 1.5 million de volt.

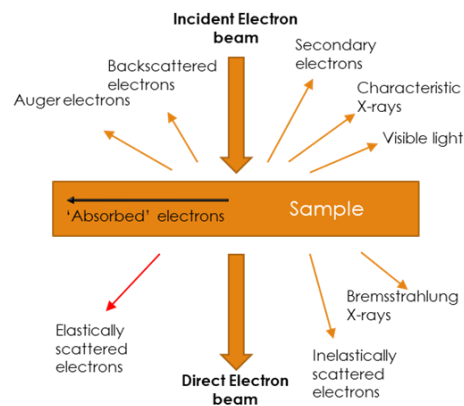


Figure 1 : Représentation des différentes radiations résultant des interactions électron-échantillon.

Différents phénomènes physiques résultent de l'interaction électrons-matière. Les différents rayonnements émis sont reportés dans la figure 1. Dans le cas de la microscopie électronique à transmission (MET), les électrons diffusés élastiquement contribuent au signal, et ceux diffusés inélastiquement contribuent au bruit.

La deuxième partie de ce chapitre décrit les différentes parties d'un microscope électronique, notamment le canon, la lentille objectif, ainsi que les détecteurs. On y présente ensuite l'ITEM, le microscope utilisé pour toutes les expériences d'holographie off-axis et hybride. La troisième et dernière partie décrit la formation d'image et le transfert d'information dans un microscope électronique. Tous ces principes sont décrits dans la version originale du chapitre en début du manuscrit.

CHAPITRE 2 : HOLOGRAPHIE ÉLECTRONIQUE : UNE SOLUTION POUR L'OBSERVATION DES ÉCHANTILLONS BIOLOGIQUES ?

La biologie cellulaire étudie les cellules et leurs organites à l'échelle nanométrique et micrométrique et vise à résoudre la structure des macromolécules à haute résolution. Les macromolécules biologiques comprennent en particulier les protéines et les acides nucléiques (ADN, ARN), qui peuvent s'assembler en structures homo- ou hétéromériques complexes.

Pour observer ces échantillons plusieurs techniques ont vu le jour, en tout premier la cristallographie des rayons X qui a joué un rôle majeur dans la détermination de la structure 3D des macromolécules biologiques. Cette méthode présente des limitations liées à la cristallisation des échantillons et à la concentration élevée nécessaire [70]. Une autre technique, la RMN, essentielle pour l'étude de la structure des molécules biologiques, reste limitée aux petites protéines (moins de 100 kDa) en raison de ses contraintes techniques [85]. En microscopie électronique, la coloration négative des échantillons est largement utilisée pour des observations à basse résolution [92] et l'accès aux hautes résolutions n'a été possible qu'avec la cryo-microscopie électronique (cryo-EM) qui a connu des évolutions technologiques majeures depuis une quinzaine d'années, permettant d'atteindre des résolutions inférieures à 2 Å [56,103] et de résoudre avec succès des structures hautement complexes grâce à l'introduction de détecteurs électroniques directs (DDD) et l'amélioration des logiciels d'analyse et de reconstruction 3D. Cette reconstruction se fait par analyse de particules isolées (SPA) dans le cas de protéines présentant des orientations aléatoires dans la glace, ou par tomographie dans le cas d'échantillons avec orientation préférentielles ou de grandes tailles comme les cellules. Pour ces techniques de microscopie électronique à haute résolution, la faiblesse du rapport signal sur bruit (SNR) et du contraste impose l'acquisition et l'analyse d'un très grand nombre d'images. Le faible contraste des images de microscopie électronique est dû au fait que l'onde électronique interagit faiblement avec les atomes de faible numéros atomiques qui composent la matière biologique, et son amplitude n'est que très légèrement modifiée contrairement à sa phase. La mesure de la phase de l'onde, ainsi que le besoin d'éliminer les aberrations optiques dues aux lentilles des microscopes électroniques, ont été à l'origine du développement de l'holographie électronique par Denis Gabor en 1947 [144]. Le développement des canons à électrons à émission de champ froid (C-FEG) a par la suite largement participé à l'essor de l'holographie électronique.

L'holographie électronique off-axis, différente de celle développée par Gabor, est une technique d'interférence qui a nécessité le développement d'un outil, le biprisme, permettant aux électrons d'interférer. Le biprisme dans un MET développé par G. Mollenstedt et H. Duker en 1955 [151] est un filament conducteur que l'on polarise pour réaliser l'interférence entre les faisceaux passant de part et d'autre de celui-ci.

Le principe de l'holographie off-axis se base sur la modification de la phase de l'onde électronique qui interagit avec la matière. La figure 2 montre un front de l'onde électronique qui est une surface où tous les points sont à la même phase. Lors de l'interaction avec un objet, la phase de l'onde sera modifiée selon l'épaisseur et la composition atomique locale ». Le biprisme polarisé positivement, fait interférer l'onde ayant interagit avec le matériau avec une partie de l'onde passée dans le vide, appelée onde de référence, pour donner une figure d'interférence, constituée de franges, appelée hologramme (figure 2 bas). Ces franges oscillent comme le montre le profil en figure 2.

Pour obtenir une image de phase d'un objet on réalise une transformée de Fourier (FT) de l'hologramme. Cette FT est composée d'une bande centrale et de deux bandes latérales. Un masque circulaire est appliqué sur une des bandes latérales et une transformée de Fourier inverse est réalisée sur cette zone. Un calcul permet d'extraire l'image d'amplitude (équivalent d'une image filtrée sans perte d'énergie (« zero-loss ») en TEM classique [216]) et l'image de phase, laquelle est plus contrastée.

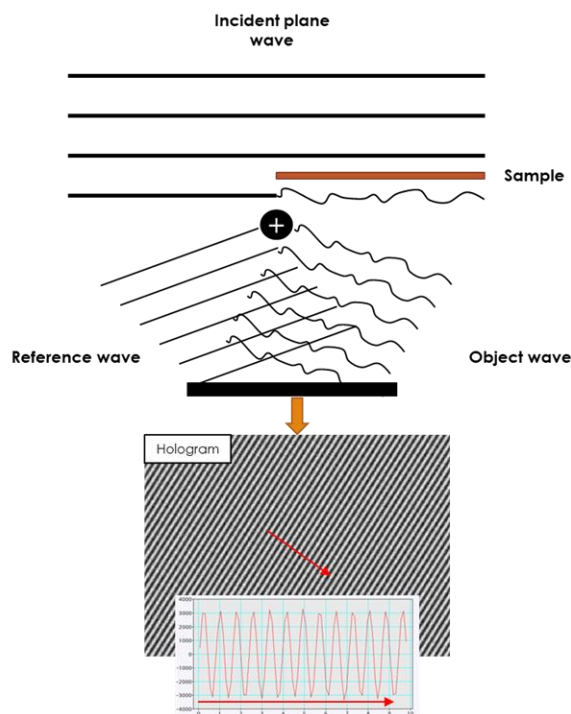


Figure 2 Représentation de l'interférence induite par le biprisme entre le faisceau de référence non modifié et le faisceau qui passe par l'objet. Le schéma d'interférence est représenté en bas de la figure, montrant une alternance de franges noires et blanches. Un profil représenté par la flèche rouge est indiqué sous l'image, montrant la nature ondulatoire des franges d'interférence.

À l'origine les premières expériences étaient menées en holographie électronique in-line où l'échantillon est placé au centre du faisceau d'électron. La mesure de la phase de l'onde consiste à acquérir une série d'images de la même zone en changeant le focus de sous-focalisé à sur-focalisé. L'analyse se fait en plusieurs étapes : un alignement précis doit être réalisé en corrigeant les variations de drift, de la rotation et du grandissement entre les images ; ensuite, les paramètres de défocalisation de chaque image et le pas de défocalisation sont précisément déterminés grâce à un fit des transformés de Fourier des images.

Deux autres techniques ont aussi été explorées dans ce travail de thèse. La première est l'holographie hybride, qui consiste à combiner l'holographie off-axis et in-line en imageant, sous les mêmes conditions d'illumination, la même région contenant notre échantillon. La deuxième est la ptychographie électronique, technique maîtrisée par nos collaborateurs à l'université d'Oxford en Angleterre. Cette technique de 4D-STEM a ainsi été testée sur les bactériophages T4 à température ambiante.

Concernant les échantillons, nous avons étudié les bactériophage T4 et T5, à cause de leurs structures bien connues et la facilité de production et de purification des échantillons. Cette dernière a été faite en premier temps sur le T4 par lyse des bactéries au chloroforme, précipitation des débris par centrifugation et échange du tampon par ultrafiltration sur vivacon[®]. Dans un deuxième temps, nous avons opté pour un protocole de purification sans chloroforme impliquant deux étapes de centrifugation différentielle d'abord pour éliminer les bactéries et les fragments bactériens, puis culoter les phages avant de les re-suspendre dans du tampon. Ce second protocole aboutit à des solutions bien plus propres.

Plusieurs types de grilles ont été testées. Au final, nous avons travaillé à température ambiante avec les grilles de carbone ultrafin (Ted Pella[®]) et des grilles de graphène sur Quantifoil gracieusement fournies par nos collaborateurs de l'équipe du Prof. Sara Bals au

laboratoire EMAT en Belgique. Pour les expériences de cryo-EM, nous avons utilisé des grilles Lacey.

CHAPITRE 3 : HOLOGRAPHIE ÉLECTRONIQUE OFF-AXIS SUR LES BACTÉRIOPHAGES

Contexte et développements relatifs aux travaux

Contrairement à la RMN et à la cryo-EM, l'holographie électronique off-axis, et sa capacité à détecter des petits déphasages de l'onde électronique, devrait être en mesure de visualiser à la fois de petites et de grandes protéines. Bien que la plupart des expériences précédentes utilisant l'holographie aient été réalisées sur des virus, quelques tests utilisant la méthode off-axis ont été réalisés sur différents types d'objets objets comme les fibrilles de collagène et la ferritine [43]. Dans cette thèse, nous avons principalement utilisé les bactériophages T4 et T5 comme échantillons modèles. Dans notre cas, nous avons tenté de cibler des résolutions permettant de visualiser les structures périodiques de 4 nm dans la queue de ces bactériophages.

Les acquisitions d'holographie off-axis sur l'I2TEM ont nécessité le développement et l'optimisation de programmes pour des acquisitions stables et automatisées. Tous les développements de logiciels ont été réalisés au CEMES par le Dr. Christophe Gatel et sont présentés dans les paragraphes suivants.

Correction de dérive : comme dans d'autres techniques d'imagerie directe, la dérive de l'échantillon est un problème majeur car les acquisitions peuvent durer quelques dizaines de secondes, et une dérive d'échantillon floute l'image. Pour éviter d'acquérir plusieurs images et de les aligner en post-traitement, un processus de correction de dérive en temps réel a été développé par C. Gatel dans le cadre de la thèse du Dr. Julien Dupuy [195].

Décalage en π : une technique dite de "décalage en π " a également été développée par C. Gatel [8], qui améliore considérablement le contraste final des franges. Elle consiste à imposer un décalage en π des franges d'interférence pendant l'exposition au milieu du temps d'acquisition, en ajustant le courant des déflectrices du canon ou du condenseur de l'I2TEM et en soustrayant les deux piles d'hologrammes acquises avant et après le "décalage en π " des franges [196].

Lenses-BD : Enfin, un programme majeur intégré à Digital Micrograph[®] est "Lenses-BD". Ce dernier code, également développé par C. Gatel, pallie le manque d'automatisation dans l'I2TEM en permettant de sauvegarder deux ensembles de paramètres, dans notre cas un ensemble de paramètres de faible grossissement et faible dose que nous avons appelé "*mode recherche*", et un ensemble de paramètres de fort grossissement et dose plus élevée appelé "*mode enregistrement*". Pour l'analyse des hologrammes, nous utilisons un programme commercialisé également développé par C. Gatel appelé "*qHolo*" [8].

Ayant optimisé tous les paramètres expérimentaux précédents, la seule difficulté notable est de limiter la dose totale d'électrons à laquelle l'échantillon est exposé, tout en conservant un rapport signal sur bruit suffisant permettant de détecter de petits déphasages. Cela nécessite de régler la mise au point, de corriger le mouvement des franges et de la dérive de l'échantillon à un endroit différent à proximité de l'échantillon, avant de lancer l'acquisition sur l'échantillon, le tout effectué en "*mode enregistrement*". Cela doit être fait manuellement car

aucune automatisation n'existe pour la séquence : ajustement de l'image - déplacement de l'échantillon - acquisition finale.

Ces procédures sont cruciales pour les études d'holographie électronique sur des échantillons biologiques, qui nécessitent une configuration TEM à faible dose. En effet, la réduction de la dose d'électrons réduit également le contraste des franges, et l'automatisation est donc essentielle pour optimiser efficacement l'acquisition d'hogrammes électroniques sur des échantillons à contraste très faible.

Les défis pour l'holographie électronique off-axis

Dans des conditions idéales d'échantillons insensibles aux dommages du faisceau et avec un détecteur parfait, l'holographie off-axis a la capacité de détecter des déphasage jusqu'à $2\pi/1000$ [197] avec une dose d'électrons suffisante pour obtenir un signal sur bruit (SNR) élevé. La limite de détection de phase φ_{lim} est définie par la formule suivante :

$$\Delta\varphi_{lim} = MTF(q) \times \sqrt{\left(\frac{2\alpha}{DQE(q) \times N_0 V^2}\right)}$$

avec 'q' la fréquence spatiale.

Cette limite dépend de la fonction de modulation de transfert (MTF) et de l'efficacité de détection quantique (DQE) de la caméra (qui dépend des fréquences spatiale captées), de la dose d'électrons, définie par N_0 qui est le nombre moyen d'électrons par pixel, V_0 qui est le contraste de frange, et du rapport α entre la zone à l'intérieur du masque de bande latérale (défini lors de la reconstruction) et de la surface totale de l'espace de Fourier [40].

Optimisation de divers paramètres pour l'holographie off-axis

Nous nous sommes fixés l'objectif d'atteindre une résolution de 4 nm permettant d'observer la périodicité des molécules en forme d'anneaux qui constituent la queue du phage T4.

Concernant l'échantillon, nous avons testé les options suivantes :

1. Le choix de l'échantillon parmi les bactériophages T4, T5 et T7 (résultats non-inclus pour le T7). Le phage T4 a été notre échantillon principal. Il est doté d'une capsid (tête) de 100 nm x 85 nm, d'une queue de 100 nm de long et 20 nm de diamètre et d'un "baseplate" (pied). La queue est formée d'une superposition d'anneaux, chacun constitué d'un hexamère de la protéine gp18. Les anneaux sont distants de 4 nm et chacun est tourné de 17.2° par rapport au précédent [62].
2. La méthode de purification : extraction par chloroforme ou extraction par ultracentrifugation.
3. Le choix du support des objets pour les expériences MET : graphène commercial, carbone ultrafin commercial, ou graphène sur Quantifoil (collaboration avec l'équipe du Prof. Sara Bals)

Concernant les paramètres relatifs au microscope, nous avons testé les options suivantes :

1. Le "mode normal" qui consiste à insérer le porte-échantillon au niveau de la lentille objectif, ou le "mode Lorentz" qui consiste à insérer le porte-échantillon au-dessus de la

lentille objectif. Ce dernier a finalement été retenu après nos tests préliminaires. Il offre l'avantage de permettre un champ de vue bien plus large qu'en mode normal.

2. La dose électronique a été subdivisée en « faibles doses » ($20-80 \text{ e}^-/\text{\AA}^2$) et « fortes doses » ($80-450 \text{ e}^-/\text{\AA}^2$).
3. Le temps d'acquisition des hologrammes (moins de 20 s en faible dose et plus de 20 s en dose élevée).
4. L'interfrange des hologrammes (0.6-0.9 nm ou 0.9-1.2 nm).
5. La température : température ambiante ou cryogénique.
6. La caméra : CMOS (One View de Gatan[®]) ou à détection directe d'électrons (K3 de Gatan[®]).

Avant l'observation d'échantillons non colorés, nous avons testé plusieurs paramètres du microscope en utilisant des échantillons de T4 colorés négativement. Nous avons également mesuré le contraste que nous pouvions obtenir sous un faisceau d'électrons accélérés à 300 kV et déterminé les paramètres d'acquisition optimaux pour obtenir une image de phase à haut rapport signal sur bruit (SNR). Nous avons ainsi déterminé que le mode "Lorentz" était bien plus adapté pour des échantillons de la taille du T4, et que les agents contrastants induisent un bruit de phase trop important pour atteindre les résolutions espérées dans nos images de phase.

Holographie off-axis à forte dose du bactériophage T4 avec une caméra CMOS

Après avoir testé le graphène commercial et le carbone ultrafin, nous avons choisi les grilles graphène-quantifoil de nos collaborateurs de Belgique comme grilles pour l'holographie off-axis à température ambiante. En utilisant ces grilles et la méthode de purification par ultracentrifugation pour préparer les échantillons de T4, nous avons obtenus les résultats présentés ci-dessous.

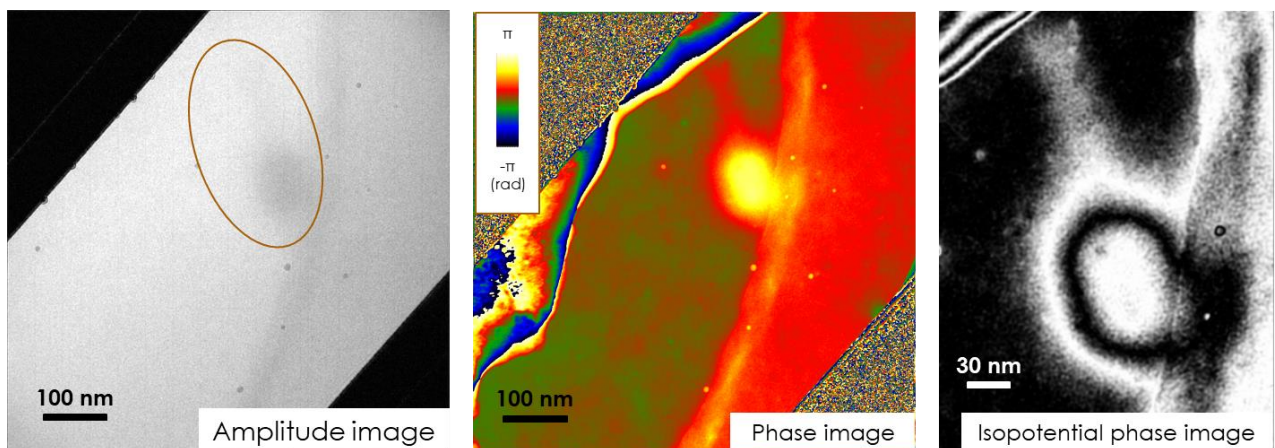


Figure 3 Holographie off-axis du bactériophage T4 sur du graphène sur carbone à trous à l'aide d'une caméra CMOS. L'espacement des franges est de 0.86 nm. L'image d'amplitude montre la position du phage (cercle). L'image de phase montre le bactériophage bien contrasté avec sa capsid touchant le carbone. L'isophase est représentée ($\cos [-4 \times \text{phase}]$) avec un examen plus approfondi de la queue et de la plaque de base.

Dans cette expérience, le temps d'exposition est de 50 secondes avec une dose totale d'électrons de $387 \text{ e}^-/\text{\AA}^2$ permettant d'obtenir un contraste de frange de 24% et un interfrange de 0,86 nm conduisant à une résolution de 1,7 nm avec le masque numérique sélectionné. Dans l'image présentée dans la figure 3, le phage est posé sur du graphène propre, sa capsid

touchant le bord d'un trou du carbone. Le phage est visible sur l'image d'amplitude mais sans suffisamment d'information car le contraste est trop faible. L'image de phase de sensibilité de 0,06 rad révèle un signal très uniforme et continu ce qui indique une surface propre et plate avec une phase moyenne proche de zéro. Les différentes parties du phage (capside, queue et « *baseplate* ») sont clairement visibles. Le profil de la capsidie et de la queue (voir le manuscrit) présente un signal de phase plus important par rapport aux expériences précédentes réalisées avec une dose considérablement plus élevée, avec des maximums de 2,4 rad et 0,25 rad respectivement. Cependant, nous n'avons pas pu visualiser clairement les anneaux de la queue, qui sont probablement endommagés à cette forte dose d'irradiation. L'image montrant les isophases permet de mieux visualiser la queue sans révéler plus de détails. Sur cette image en figure 3 (droite), la « *baseplate* » est beaucoup plus contrastée que sur l'image de phase brute, mais le bruit en rend une partie floue.

Holographie off-axis à faible dose du bactériophage T4 avec une camera DDD

Une expérience à faible dose a été réalisée sur les bactériophages T4 sur une grille avec support graphène à température ambiante (figure 4). L'espacement des franges dans l'hologramme a été fixé à 1,46 nm, ce qui, en théorie, est suffisant pour visualiser les anneaux de la queue. La dose totale d'électrons de $31,2 \text{ e}^-/\text{\AA}^2$ est suffisante pour obtenir des images d'amplitude et de phase où la capsidie et la queue du phage sont clairement visibles. Cependant, à une dose aussi faible, le bruit de phase est élevé (0,08 rad), ce qui réduit la sensibilité en phase. Il est donc difficile d'observer des structures à haute résolution comme les anneaux de la queue que nous voulions imager. Il apparaît également que le support de graphène autour du phage n'est pas d'épaisseur uniforme. Néanmoins, les profils de phase pour la capsidie et la queue (figure 4) ont montré un déphasage maximal de 2,6 rad pour la capsidie et de 0,25 rad pour la queue, en accord avec les expériences réalisées à haute dose.

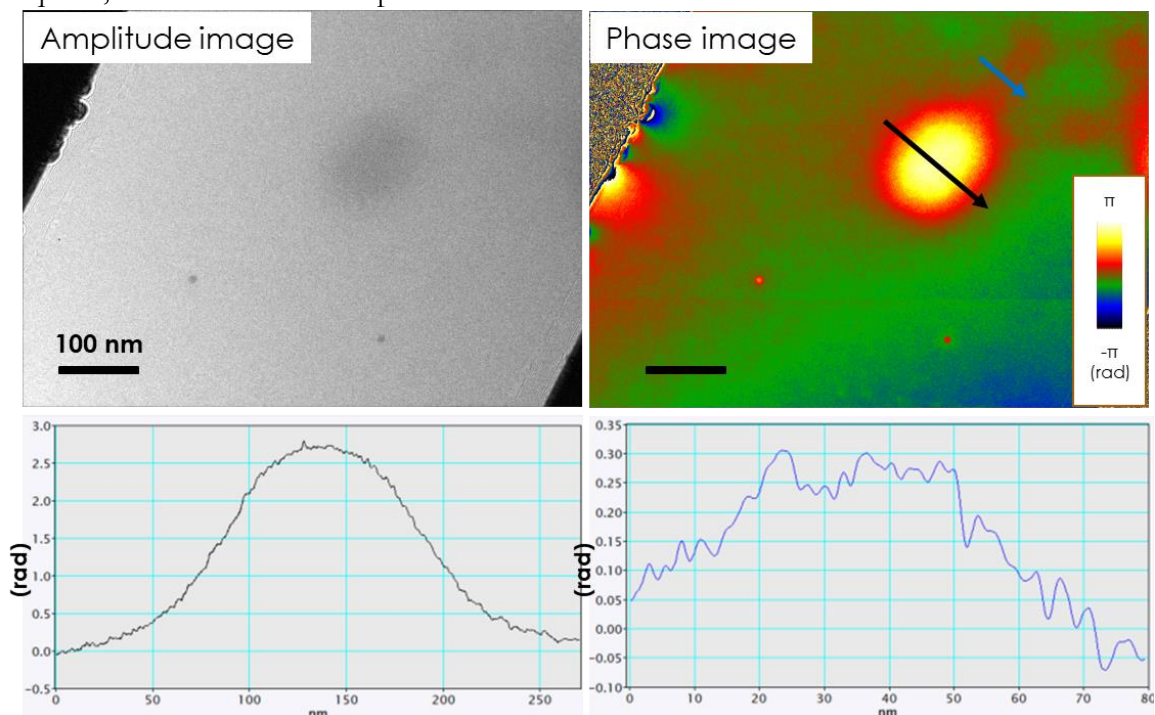


Figure 4 Holographie off-axis à faible dose d'un bactériophage T4 sur du graphène à l'aide de la caméra K3. L'image d'amplitude montre une augmentation de l'épaisseur du graphène de gauche à droite. L'image de phase montre un phage avec sa queue, mais pas de « *baseplate* » claire. Les profils de déphasage montrent des valeurs de phase similaires à celles d'une expérience à haute dose. L'axe "y" est en rad et l'axe "x" en nm. La sensibilité de la phase est de 0,08 rad.

Ces expériences ont été aussi réalisées avec le bactériophage T5. Deux observations supplémentaires ont été faites :

1. La queue du T5 est très facilement endommagée par les électrons. Il faut donc travailler à faible dose pour étudier ces virions.
2. Le déphasage induit par la capsidie diminue lorsque l'ADN est neutralisé par la spermine (poly-cations) démontrant la capacité de l'holographie off-axis à détecter des variations de charge.

Holographie électronique off-axis à température cryogénique

Après avoir mené des expériences sur les phages à température ambiante, des expériences d'holographie off-axis ont été réalisées dans des conditions cryogéniques. Pour pouvoir travailler à basse température et à faible dose, nous avons mis au point un protocole d'expérience décrit dans le chapitre 3, et nous avons testé le refroidissement du porte-échantillon et des deux pièges à azote liquide de l'I2TEM, avant d'expérimenter sur un échantillon réel. Plus important encore, l'installation de la caméra K3 a permis d'obtenir, à de faibles doses, des hologrammes présentant un contraste de franges nettement amélioré.

Pour le "*mode recherche*" (faible grandissement), la dose est toujours réglée à $\sim 0,008 \text{ e}^- / \text{\AA}^2 \cdot \text{s}$. La dose et les paramètres de lentilles sont ensuite réglés dans le "*mode acquisition*" (fort grandissement) avec une dose cible autour de $65 \text{ e}^- / \text{\AA}^2$. Le principal problème de l'I2TEM concerne le porte-échantillon. Dans les microscopes Hitachi, la pointe du porte-échantillon entre en contact avec le goniomètre (dans ce que l'on appelle "l'oreille") qui permet le déplacement du porte-objet dans la direction "y". Sans ce contact, lorsque le porte-échantillon n'est pas complètement inséré, seuls les mouvements dans la direction "x" sont possibles. En cryo-EM, nous avons remarqué une augmentation de la température due à ce contact qui passe de -175°C lorsque porte-échantillon est partiellement insérée à -164°C lorsqu'il est en contact avec l'oreille. Or, en dépit de publications indiquant que la température de cristallisation de la glace est plus élevée [95,210], nous avons couramment rencontré un problème de cristallisation de la glace dans nos expériences sur l'I2TEM à des températures de -164°C . Nous avons néanmoins pu faire quelques acquisitions dans les rares zones où cette cristallisation n'avait pas lieu.

Afin de déterminer les limites de dose électronique permettant l'étude de ces phages sans endommager leur structure, et notamment les anneaux de la queue, nous avons étudié sur le Jeol 2100 au CBI, l'évolution des dommages induits par l'irradiation électronique en fonction de la dose. Nos résultats indiquent que la structure de la queue est endommagée à partir de $70 \text{ e}^- / \text{\AA}^2$ même si la forme générale du phage reste intacte à cette dose, voire au-delà. Cette approche qui n'est cependant pas très précise car nous n'étudions pas l'objet en continu pendant son exposition au faisceau électronique, nous permet néanmoins d'avoir une estimation de la dose maximale que peut supporter le phage avant que sa structure ne soit trop endommagée.

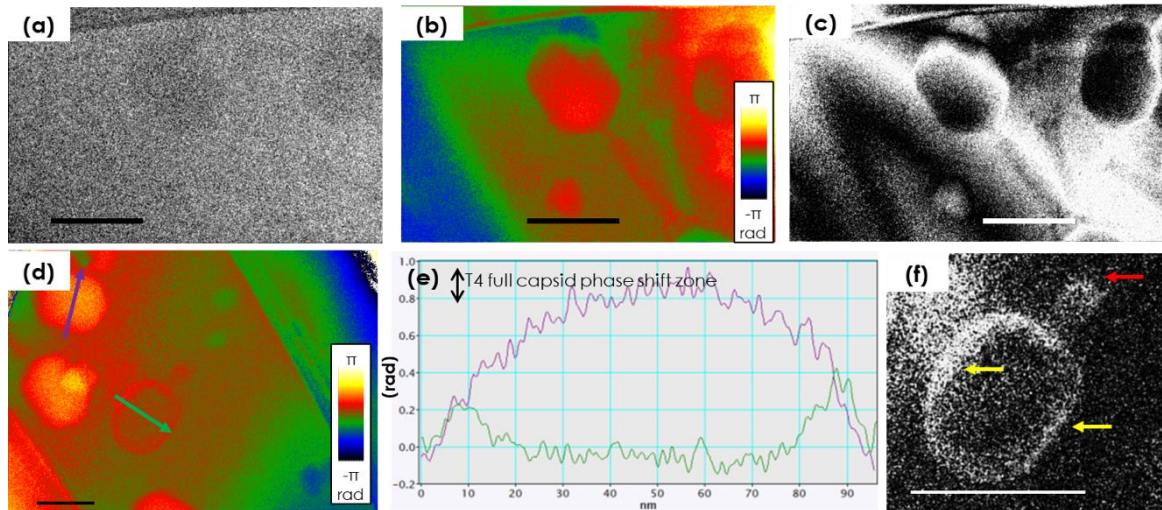


Figure 5 Holographie électronique cryogénique off-axis à faible dose d'électrons du bactériophage T4. (a-b-c) Analyse du premier hologramme. (a) Image d'amplitude du premier hologramme. (b) Image de phase du premier hologramme. (c) Image isophasse ($\cos [5 \times \text{phase}]$) de la phase montrée en (b). (d) Image de phase du deuxième hologramme. (e) Profils de phase des capsides vides (profil et flèche verts) et pleines (profil et flèche violets). La double flèche indique la zone des valeurs de déphasage maximales des capsides. (f) Image isophasse ($\cos [-5 \times \text{phase}]$) du phage à capside vide de (d) montrant la capside et la queue. Les barres d'échelle sont toutes de 100 nm.

La figure 5 montre deux images obtenues lors d'une expérience d'holographie cryogénique off-axis réalisée à faible dose sur un échantillon congelé. L'hologramme a été acquis pendant 20 secondes avec une dose totale égale à $47,3 \text{ e}^-/\text{\AA}^2$. L'image d'amplitude de la figure 5a présente un contraste très faible et est assez bruyante dû à la présence de la glace amorphe qui entoure l'objet. À l'inverse, l'image de phase de la figure 5b est beaucoup plus contrastée, avec la capside, la queue et la *baseplate* visibles et bien définies, même si une grande hétérogénéité de phase apparaît en arrière-plan. La sensibilité de phase de cette image est de 0,16 rad, une valeur bien supérieure à la sensibilité de 0,06 rad que nous visons. Ce bruit élevé rend impossible la visualisation des anneaux de queue du T4. Le calcul des isophases révèle les phages voisins avec des déphasages similaires (figure 5c).

Des expériences à des doses élevées ont été effectuées et ont permis d'obtenir de meilleures sensibilités en phase à des doses de l'ordre de $100 \text{ e}^-/\text{\AA}^2$. Des expériences similaires ont été menées sur le phage T5 donnant lieu aux mêmes conclusions, mais avec quelques résultats présentant de meilleures sensibilités en phase que celles obtenues sur le T4.


Les mesures de déphasage obtenues sur la capside des phages T4 et T5, à basse température donnent des valeurs inférieures à celles mesurées à température ambiante. Le déphasage mesuré après interaction avec le matériau étudié dépend du potentiel électrostatique du (des) matériaux traversé(s) :

$$\varphi = C_E \cdot V \cdot t,$$

avec C_E une constante qui dépend de l'énergie des électrons, V le potentiel électrostatique du (des) matériaux, et t l'épaisseur traversée. Le déphasage mesuré en cryo-EM est diminué par le potentiel électrostatique de la glace vitreuse comme suit :

$$\varphi_{\text{measured Cryo}} = C_E (V_{\text{capside}} - V_{\text{ice}}) \cdot t_1$$

avec t_1 l'épaisseur de la capside (voire la partie 3.3.2, pour l'analyse complète).



Il explique la diminution du déphasage observé à basse température. La baisse du potentiel interne liée à la l'augmentation de densité du matériaux [216,217] contribue également à cette diminution du déphasage.

Pour illustrer l'effet de la dose sur le bruit de phase, nous avons calculé le rapport signal/bruit (SNR) pour les images de phase en cryo-EM en fonction de la dose d'électrons. En examinant les images de phase du bactériophage T4, nous pouvons constater une amélioration du SNR de 7 autour de $46 \text{ e}^-/\text{\AA}^2$, jusqu'à 11,8 pour $100 \text{ e}^-/\text{\AA}^2$. Cela s'explique par la diminution du bruit de phase d'environ 0,15 à 0,07 rad. Alors que la dose d'électrons est un paramètre critique du SNR, nous notons qu'il n'y a pas de corrélation stricte entre la sensibilité de phase et la dose d'électrons, puisque nous avons pu obtenir quelques exceptions de "bonne" sensibilité de phase pour des doses faibles (par exemple à $38,8 \text{ e}^-/\text{\AA}^2$).

Dans ce chapitre, nous avons donc montré, en plus des capacités de l'holographie off-axis à température ambiante, l'une des premières expériences d'holographie cryogénique off-axis sur un échantillon biologique en utilisant une caméra DDD (K3) et un microscope équipé d'un C-FEG (FEG froid) dédié à l'holographie électronique. Ces expériences montrent la possibilité d'acquérir des hologrammes à faible dose d'électrons et d'extraire des images de phase avec une sensibilité d'environ 0,1 rad.

CHAPITRE 4 : HOLOGRAPHIE ÉLECTRONIQUE IN-LINE SUR LES BACTÉRIOPHAGES

Avec un chercheur post-doctoral ayant travaillé deux ans dans notre groupe au laboratoire CEMES, nous avons testé l'holographie électronique par séries focales in-line comme méthode alternative pour obtenir des images de phase à contraste élevé. Les expériences ont été réalisées sur des bactériophages T4 et T5 à température ambiante, mais aussi à température cryogénique sur le Talos Arctica, un cryo-microscope dédié, entièrement automatisé et équipé d'une caméra à détection directe d'électrons K2 (Ametek Gatan), récemment installé au laboratoire du CBI.

Un des avantages des expériences d'holographie in-line est qu'elles peuvent être réalisées sur n'importe quel microscope et que divers logiciels libres pour la reconstruction d'images sont disponibles en accès libre. Pour l'analyse d'image et la reconstruction d'image de phase, nous avons utilisé le code FRWR, qui signifie "Full-Resolution Wave Reconstruction", un logiciel développé par le Prof. Christoph Koch [165].

Par rapport à l'holographie off-axis, en raison de sa flexibilité et de son adaptabilité, l'holographie in-line, a été développée par de nombreux groupes et est plus largement utilisée, bien qu'il n'y ait que peu de résultats publiés sur un microscope cryo-EM de dernière génération. Par ailleurs, nous n'avons pas connaissance de l'utilisation de la variante "série focale" de l'holographie in-line sur des objets biologiques.

Holographie in-line à température ambiante

Comme pour les expériences off-axis, nous avons mené les premières expériences in-line sur des bactériophages T4 colorés négativement, étudiés sur un microscope HF2000 fonctionnant à 200 kV et équipé d'une caméra CCD. L'image de phase obtenue à partir de

L'analyse d'une série de 9 clichés montre un bactériophage avec un haut contraste, mais ne révélant pas sa structure à haute résolution à cause des dommages créés par une dose électronique trop élevée. La sensibilité en phase de 0.02 rad est néanmoins meilleure que celle de l'holographie off-axis.

Nous avons ensuite mené des expériences d'holographie in-line sur un échantillon non coloré à température ambiante sur l'I2TEM équipé d'une caméra CMOS de type CCD. Le déphasage maximal de la capsid est de 0,7 rad, inférieur au déphasage mesuré dans les expériences d'holographie off-axis, (i.e. entre 2 et 2,5 rad). Le déphasage mesuré au niveau de la queue du phage est de 0,15 rad également inférieur à celui mesuré dans les expériences off-axis ($0,25 \pm 0,05$ rad). Ceci traduit l'aspect semi-quantitatif de l'holographie in-line.

Malgré une résolution spatiale limitée, les bactériophages non-colorés sont toutefois mieux définis lorsqu'ils sont imagés avec par holographie in-line que par MET conventionnelle en champ clair. En outre, l'holographie in-line produit des images de phase avec moins de bruit à haute fréquence que les expériences off-axis, comme le montre la sensibilité de phase plus élevée.

Holographie in-line cryogénique

Nous avons mené nos premières expériences d'holographie électronique in-line dans des conditions cryogéniques sur le Jeol JEM 2100 du CBI. Ce microscope est équipé d'un canon à électrons LaB6 fonctionnant à 200 kV et d'une caméra CCD de 4k X 4k montée derrière un filtre d'énergie (Gatan Imaging Filter Quantum model 964). L'acquisition semi-automatique d'images à faible dose a été réalisée avec Serial-EM [226].

Ces expériences ont été réalisées sur des bactériophages T4 déposés sur des grilles en lacey. La série d'image a été acquise à des focalisations comprises entre $-3 \mu\text{m}$ et $+3 \mu\text{m}$ avec un pas de $1,5 \mu\text{m}$. La dose par image était de $13 \text{ e}^-/\text{\AA}^2$, avec un temps d'exposition de 0,8 seconde pour chacune. Cette expérience a abouti à une image à haute résolution montrant un rapport signal sur bruit et un contraste élevé, la sensibilité en phase étant de 0.033 rad.

Cette expérience a ensuite été reproduite sur le microscope Talos Arctica équipé d'un DDD K2 au CBI et d'un canon FEG. Avec la K2, les prises de vue ont été réalisées sous forme de films, ce qui a permis la correction de la dérive de l'échantillon grâce au logiciel MotionCorr2 dans Relion [228]. L'expérience a consisté à acquérir une série focale non linéaire de 7 images à des focalisations de : $\pm 9 \mu\text{m}$; $\pm 4 \mu\text{m}$; $\pm 1 \mu\text{m}$ et au focus, du bactériophage T4 avec une dose d'exposition totale de $79,1 \text{ e}^-/\text{\AA}^2$. La mise au point a été ajustée manuellement pour chaque image défocalisée.

L'image sous-focalisée de $4 \mu\text{m}$ ($\Delta f = -4 \mu\text{m}$) est reportée dans la figure 6a à titre de référence. Après avoir aligner les images de la série à l'aide du plugin FRWR, la valeur de focalisation exacte de chaque image ainsi que d'autres paramètres sont déterminées par modélisation de la FFT des images ; les valeurs données par le microscope ne sont pas précises. Nous procédons ensuite à la reconstruction itérative. Les étapes intermédiaires, à savoir les itérations 0 ; 83 et 381, sont illustrées à la figure 6a. L'itération "0" est la première itération au cours de laquelle toutes les images de la série focale sont utilisées. L'image de phase finale présentée dans la figure 6b a été obtenue après 981 itérations. Dans cette expérience, nous avons obtenu une sensibilité de phase de 0,04 rad. Par rapport à l'image en champ clair dans la figure 6a, nous remarquons un contraste beaucoup plus élevé et une amélioration du SNR permettant de révéler la structure fine des différentes parties des phages T4.

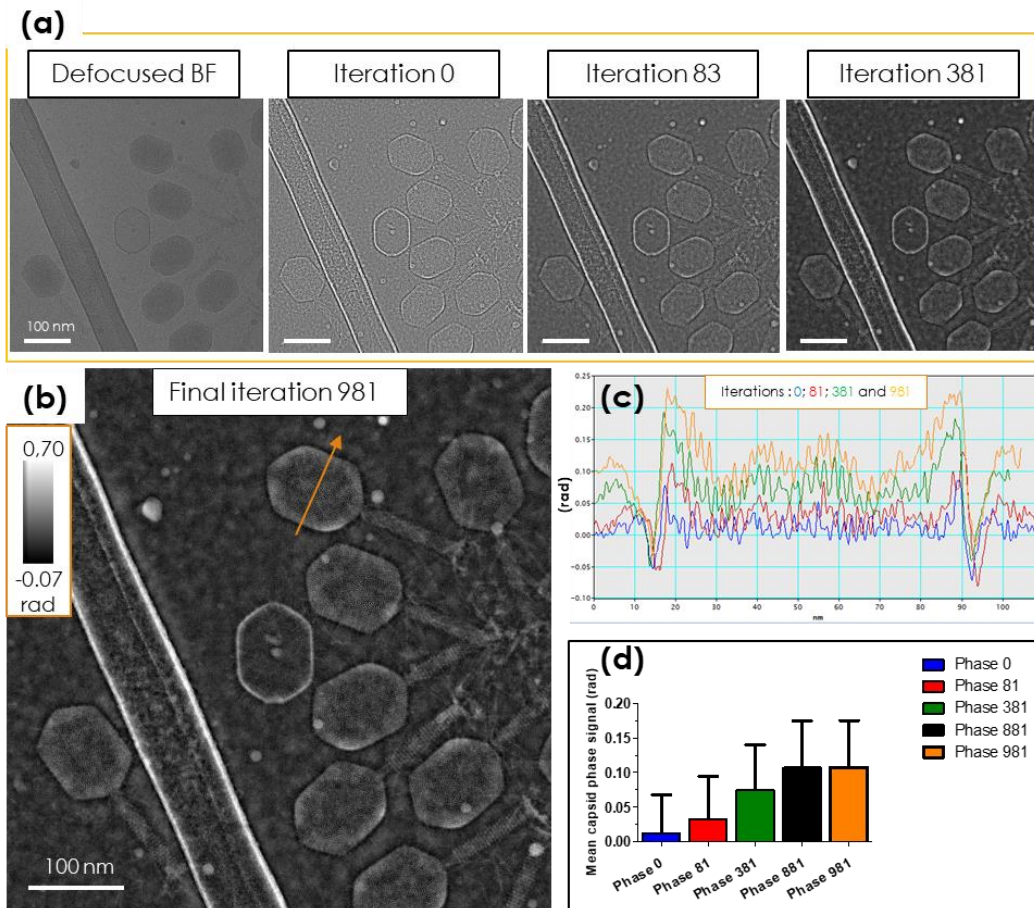


Figure 6 Cryo holographie électronique in-line de bactériophages T4 sur le Talos Arctica équipé d'un détecteur K2. (a) Image BF ($\Delta f = -4 \mu\text{m}$) suivie de 4 itérations différentes de reconstruction de phase à l'aide de l'algorithme FRWR. (b) Image de phase finale (itération 981). (c) Profil de phase du phage T4 (flèche orange) pour les différentes itérations montrées dans (a). L'axe x représente la coordonnée "x" le long du profil en nm et l'axe y représente le déphasage en radians. (d) Histogramme du signal de phase moyen de la capsid pour différentes itérations de reconstruction.

Nous avons mesuré l'évolution du déphasage à travers une capsid de phage (flèche orange dans la figure 6b) en fonction du nombre d'itérations (figure 6c). Nous observons une augmentation des valeurs de phase, au fur et à mesure des itérations, alors que le bruit de fond est réduit. Ceci est clairement illustré par le saut de phase au bord de la capsid, qui est égal à 0,12 rad à l'itération "0" et à 0,25 rad à l'itération "981". Il correspond à une augmentation du contraste de l'image et de la valeur de la phase avec le nombre d'itérations jusqu'à un optimum qui peut être estimé en traçant un profil de la moyenne de phase de la capsid étudiée dans la figure 6c en fonction du nombre d'itérations (figure 6d). Pour l'itération "0", la phase est d'environ 0,01 rad avec une erreur de 0,05 rad ; après 881 itérations, la valeur moyenne de la phase atteint 0,107 rad avec une erreur de 0,067 rad, alors que 100 itérations supplémentaires n'améliorent pas la reconstruction, indiquant que l'algorithme a convergé.

En étudiant en détail la capsid du bactériophage T4, on distingue clairement l'ADN, notamment à la périphérie de la capsid où sa structure périodique est visible. La structure périodique correspondant à l'empilement périodique de 4 nm des anneaux de protéines pb18 est visible sur l'image de phase de la queue du bactériophage T4 avec les hélices dues à la rotation des anneaux.

Cette expérience d'holographie in-line cryogénique a été reproduite sur les bactériophages T5 et a donné des images de phase avec des sensibilités de 0,023 rad pour des doses électroniques de $50 \text{ e}^-/\text{\AA}^2$ (voir le chapitre 3 pour une description et analyse détaillées).

En étudiant les images de phase des capsides des bactériophages T4 et T5, nous remarquons des contrastes qui sont différents lorsque les capsides sont pleines ou vides. Ceci est illustré dans la figure 7 :

- Images en champ clair défocalisées : dans les images sous-focalisées à $-9 \mu\text{m}$ des capsides pleines et vides (figures 7a et 7b respectivement), la frange de Fresnel sombre est beaucoup plus foncée lorsque la capside est vide. Ceci peut également être observé dans la frange de Fresnel blanche des images sur-focalisées de $9 \mu\text{m}$ de la capside vide (figure 7d), qui est plus lumineuse que celle de la capside pleine (figure 7c). Il est cependant difficile de tirer conclusion d'observations à partir d'images de champ claire d'où il est nécessaire de regarder les images de phases

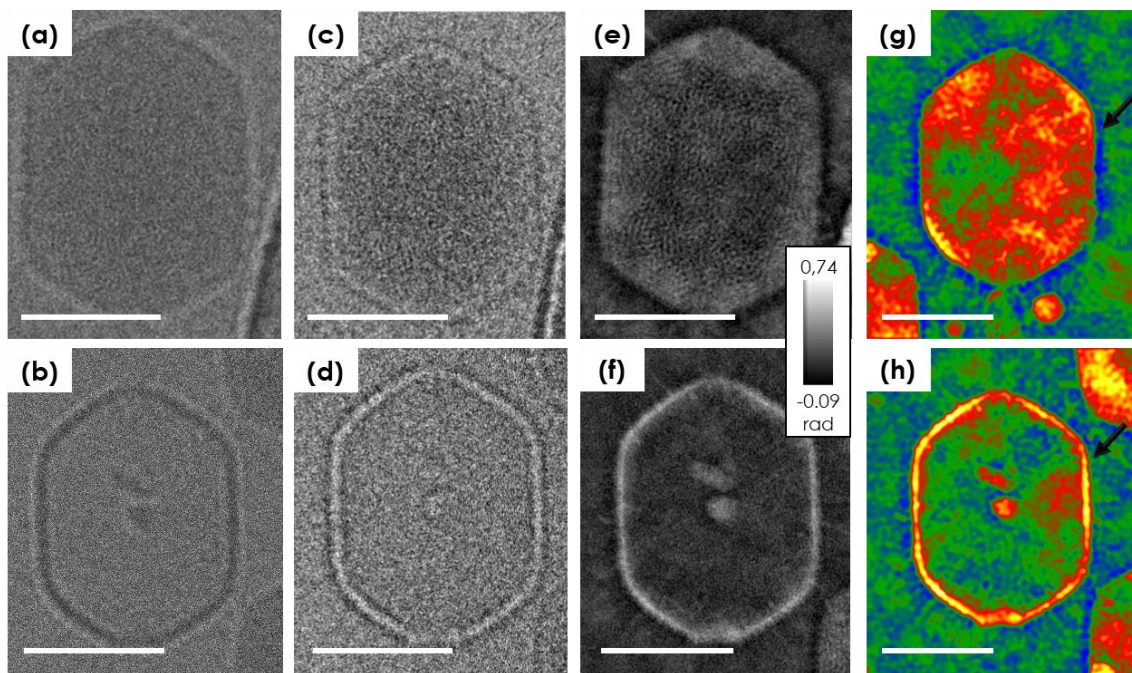



Figure 7 Analyse du signal de phase de la périphérie de capsides T4 (a, b) Image champ clair sous focalisée ($\Delta f = -9 \mu\text{m}$) en cryo-EM d'une capside pleine. (a) et d'une capside vide (b). (c) Image en champ clair sur-focalisée ($\Delta f = +9 \mu\text{m}$) d'une capside pleine (c) et d'une capside vide (d). (e, f) Image de phase brute d'une capside pleine (e) et d'une capside vide (f). (g, h) Images de phase colorée d'une capside pleine (g) et d'une capside vide (h). La longueur des barres d'échelle est de 50 nm.

- Images de phase : par rapport aux images en champ clair défocalisées, une différence notable est observée dans les images de phase dans les intérieurs des capsides pleines et vides. En outre, la capside pleine de la figure 7e présente une couronne sombre sur son pourtour qui est encore plus visible sur l'image en fausse couleur de la figure 7g. Ce contraste devient brillant autour de la capside vide, comme le montrent les figures 7f et 7h. Cette différence de contraste des images de phase entre une capside vide et une pleine a été mainte fois observée excluant un artefact d'imagerie ou d'analyse d'image. Le bactériophage T4 possède une capside chargée négativement [232], à l'intérieur de laquelle l'ADN négatif est stabilisé grâce à la présence de cations et d'autres protéines. La somme des charges contenues dans la capside (ADN et protéines) et de la capside elle-même est « quasi » neutre (mesures effectuées avec ChimeraX en calculant le potentiel électrostatique de surface). La libération du contenu de la capside la laisse vide avec sa charge négative non compensée. Ce changement de charges entre capside



pleine, quasi neutre, capsidie vide, négativement chargée est à l'origine du changement de contraste observé dans les images de phase des figures 7f et 7h. L'holographie in-line n'est cependant pas suffisamment quantitative, pour pouvoir quantifier la variation de charge. Des expériences similaires devraient être réalisées en holographie cryogénique off-axis pour obtenir des données plus quantitatives.

En conclusion, nous avons montré, grâce à des expériences réalisées sur deux types de bactériophages, que l'holographie électronique cryogénique in-line permet d'obtenir des informations structurales avec un meilleur contraste et un meilleur rapport signal/bruit comparé aux images en champ clair en cryo-EM. En outre, nos expériences ont permis de mettre en évidence une différence de phase de la capsidie lorsque celle-ci est pleine ou vide que nous avons reliée aux variations de charges associée à l'expulsion de l'ADN contenue dans celle-ci.

CHAPITRE 5 : TECHNIQUES ALTERNATIVES D'IMAGERIE DE PHASE : HOLOGRAPHIE ÉLECTRONIQUE HYBRIDE ET PTYCHOGRAPHIE ÉLECTRONIQUE

Comme nous l'avons montré dans les chapitres 3 et 4, l'holographie off-axis et l'holographie en série focale in-line ont un grand potentiel pour les applications biologiques. Bien qu'elles nécessitent toutes deux des travaux et des améliorations supplémentaires, il est également possible de les combiner. L'holographie off-axis excelle dans l'extraction d'informations à basse fréquence, tandis que l'holographie in-line est plus efficace pour l'extraction des hautes fréquences [175]. En outre, l'holographie électronique off-axis est une méthode quantitative [153], tandis que l'holographie in-line, qui a une meilleure sensibilité à la phase à haute résolution spatiale, est semi-quantitative [76]. Par conséquent, la combinaison des deux dans une expérience d'"holographie hybride" devrait réduire le bruit sur l'ensemble du spectre de fréquences tout en maintenant de manière fiable une bonne résolution spatiale. Nous avons donc lancé la première expérience d'"holographie hybride" sur le microscope I2TEM.

Tout comme pour l'holographie off-axis et in-line, de nombreux défis ont dû être relevés, certains communs aux observations biologiques en holographie et d'autres spécifiques à notre dispositif expérimental :

1. Tout d'abord, l'utilisation du même microscope est nécessaire pour imager le même échantillon sous les mêmes conditions d'illumination (faisceaux, dose électronique...) pour les deux acquisitions. Ceci impose donc d'utiliser un MET équipé d'un biprisme (l'I2TEM dans notre cas).
2. Combiner les deux approches nécessite l'acquisition d'un plus grand nombre d'images sur la même zone et de réduire la dose pour chaque expérience afin de maintenir une dose totale faible.
3. L'analyse et la reconstruction sera faite à l'aide du même algorithme FRWR utilisé dans les expériences in-line, ce qui est chronophage et nécessite une bonne expertise.

En tenant compte de ces contraintes, nous avons testé l'approche de l'holographie hybride sur l'I2TEM en mode Lorentz et à température ambiante. Les images ont été acquises

à l'aide de la caméra CMOS One View. Nos expériences ont été réalisées sur le bactériophage T4, en utilisant des grilles TEM lacey avec un support en carbone de 3 à 4 nm d'épaisseur. Les bactériophages ont été purifiés par la méthode du chloroforme.

Procédure d'acquisition et d'analyse en holographie hybride

La procédure d'acquisition démarre avec holographie in-line. Le faisceau incident est établi elliptique pour toutes les acquisitions. Les biprismes sont insérés et alignés.

Avant de localiser un échantillon, l'astigmatisme de la lentille objectif est d'abord corrigé et la mise au point est réglée au focus. Pour stabiliser l'échantillon et les franges de l'hologramme, le goniomètre de la platine et les déflecteurs du canon sont calibrés pour compenser les dérives respectives. Les biprismes sont ensuite retirés du champ de vision et le mode "recherche" à faible grossissement est sélectionné afin de localiser notre échantillon. Une zone "aussi propre que possible" avec des échantillons isolés est sélectionnée pour éviter le chevauchement avec d'autres matériaux lors de l'acquisition en holographie off-axis. Pendant toutes ces étapes, la dose est maintenue aussi faible que possible pour éviter d'endommager l'échantillon avant l'acquisition.

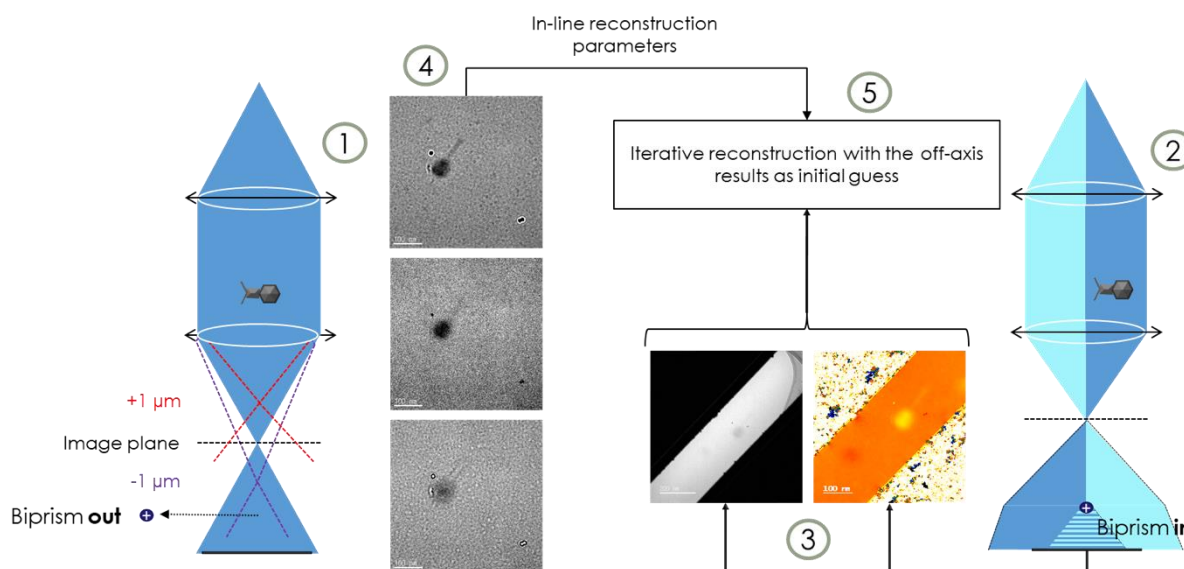


Figure 8 Processus d'holographie hybride. Pour des raisons de simplicité, un seul des deux biprismes de l'I2TEM est représenté sur cette figure. (1) Acquisition in-line. (2) Acquisition off-axis. (3) Analyse de l'hologramme off-axis. (4) Alignement et analyse de la série focale. (5) Analyse hybride.

Une série focale de 3 images (sous-focalisée ; au focus ; sur-focalisée) est acquise comme le montre l'exemple de la figure 8 (1). Après les acquisitions in-line, la configuration du faisceau est commutée en "mode recherche" pour réduire les dommages causés par l'irradiation, et les biprismes sont insérés. L'échantillon est alors centré et l'alignement passe en mode "acquisition" afin de mettre au point l'objet (au focus). La stabilisation des franges et, si possible, la correction de la dérive de la platine de l'échantillon sont lancées. Un hologramme off-axis est alors enregistré (figure 5.1(2)).

L'hologramme obtenu par holographie off-axis est analysé pour extraire les images d'amplitude et de phase, comme le montre la figure 5.1(3). L'image de phase off-axis est linéarisée et sera utilisée comme image de phase de départ pour la reconstruction hybride. Les images de la série focale sont ensuite alignées avec précision et la reconstruction itérative est

lancée (figure 5.1 (4)). Les paramètres optimisés (paramètres d'alignement et d'algorithmes) sont ensuite utilisés pour l'analyse hybride.

Dans une dernière étape, l'algorithme itératif "FRWR" est exécuté à nouveau pour analyser la série obtenue en holographie in-line en utilisant comme images d'amplitude et de phase de départ, qui étaient "vides" lors de la première exécution de l'analyse classique, l'amplitude off-axis et l'image de phase linéarisée. Les images finales d'amplitude et de phase obtenues donnent des images à faible bruit de phase avec un contraste et un rapport signal/bruit améliorés par rapport au BF-TEM.

Holographie hybride à température ambiante

Nous avons utilisé la configuration à deux biprismes pour les acquisitions holographiques off-axis et avons acquis un hologramme de 4 minutes. La dose totale pour l'hologramme était de $680 \text{ e}^-/\text{\AA}^2$, ce qui est une dose élevée pour un échantillon biologique non coloré étudié à température ambiante. L'objectif de cette première tentative n'était cependant pas d'atteindre une haute résolution, mais d'évaluer les contraintes et les performances de l'holographie hybride.

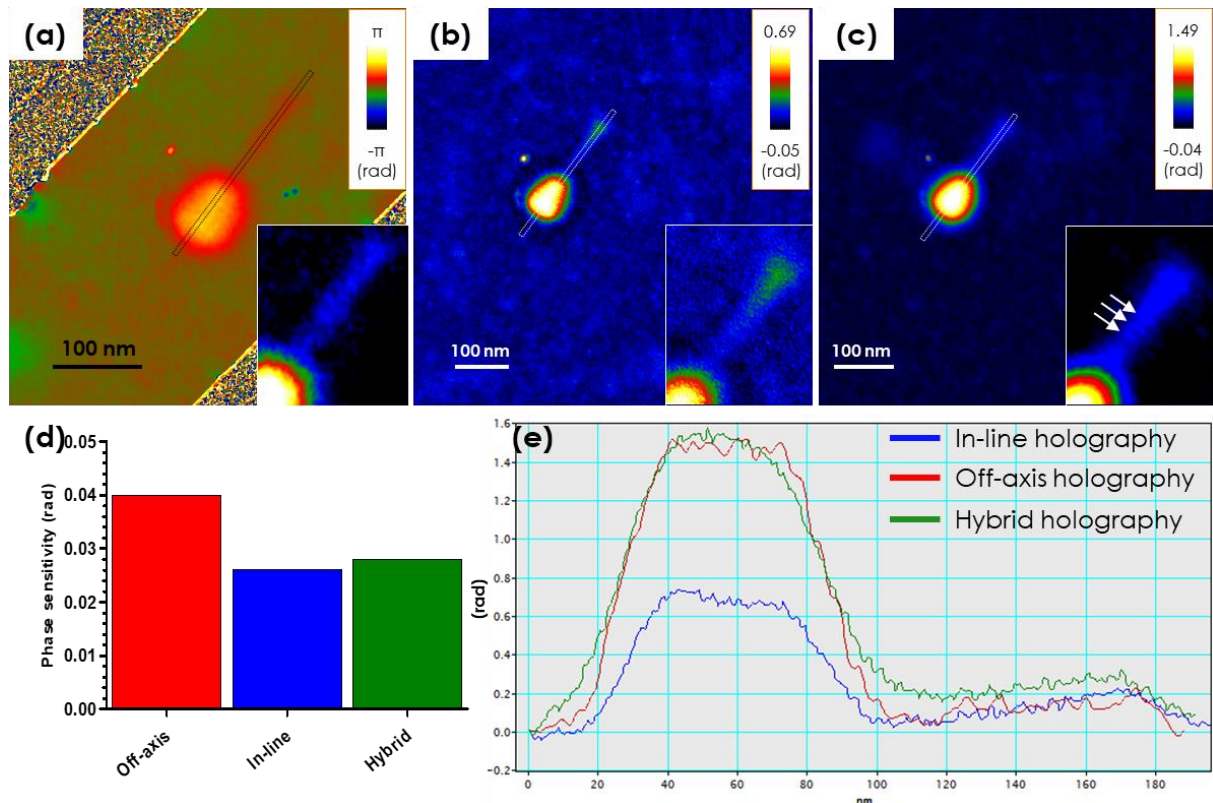


Figure 9 Comparaison des résultats de l'holographie électronique off-axis, in-line et hybride. (a) Image de phase colorée de l'analyse de l'hologramme off-axis. Un agrandissement de la queue est inséré en bas à droite et son contraste est amélioré en modifiant les limites de contraste de l'image. (b) Image de phase colorée de l'analyse de la série focale in-line. Un agrandissement de la queue est mis en bas à droite. (c) Image de phase colorée de l'analyse d'holographie hybride. Un agrandissement de la queue est mis en évidence en bas à droite. Les trois flèches montrent un motif ressemblant aux anneaux de la queue. (d) Histogramme comparant la sensibilité de phase des trois méthodes d'holographie électronique. (e) Profils de phase des bactériophages T4 (rectangles en pointillés dans (a), (b) et (c)) des images de phase off-axis (rouge), in-line (bleu) et hybrides (vert). L'axe y est en rad et l'axe x est en nm.

La comparaison entre l'image de phase issue de la méthode hybride avec celles obtenues par holographie off-axis et in-line est illustrée en figure 9. L'image off-axis dans la figure 9a montre un phage visible et bien contrasté avec une bille d'or sur sa gauche, ainsi que deux autres billes avec des déphasages négatifs (image "fantôme"). Comme nous l'avons vu, la sensibilité de phase est plus élevée dans une expérience d'holographie off-axis, les images de phase présentent une faible valeur de bruit de phase, 0,04 rad dans l'image de la figure 9d. Dans cette expérience, nous avons utilisé un grossissement plus faible que dans les expériences précédentes (taille de pixel de 0,41 nm) et un espacement des franges plus important, ce qui conduit à une résolution spatiale théorique de 0,82 nm. Néanmoins, aucun détail des anneaux de la queue du T4 n'est mis en évidence. L'impossibilité de voir les anneaux de la queue résulte probablement de la dose trop élevée d'électrons qui endommage la structure.

L'image de phase colorée in-line de la figure 9b montre des contrastes clairs sur toute l'image. La sensibilité de la phase est néanmoins élevée, à savoir 0,026 rad. Aucun signal d'anneau de queue n'apparaît sur l'image de phase agrandie et la zone du *baseplate* semble bruyante par rapport à l'image off-axis.

L'image de phase hybride obtenue conduit à l'image de phase présentée à la figure 9c. À première vue, le fond de l'image semble beaucoup plus propre bien que la sensibilité de phase 0,028 rad soit similaire à celle obtenue in-line, (figure 9d). Le signal de déphasage de la capsid T4 est plus homogène et la morphologie de la queue est similaire à celle obtenue par holographie off-axis avec une forme plus définie. En zoomant sur la queue, on peut voir trois répétitions similaires aux anneaux. La distance mesurée entre elles est de ~ 8 nm, soit deux fois la périodicité attendue des anneaux.

Trois profils de phase pris le long du phage dans la figure 9a, b et c sont reportés sur le même graphique dans la figure 9e. Ces profils mettent en évidence la différence entre les déphasages mesurés par les expériences in-line et off-axis. Nous avons mesuré un déphasage maximal de 0,7 rad dans la capsid pour l'holographie in-line et de 1,5 rad lorsque mesuré par l'holographie off-axis. Cette différence illustre à nouveau le fait que l'holographie in-line n'est pas quantitative.

L'holographie hybride permet de conserver l'information correcte sur le déphasage, car elle récupère la valeur obtenue par holographie off-axis. L'holographie hybride permet d'obtenir un profil de capsid plus lisse que celui obtenu par holographie off-axis et une variation de phase moins bruyante. Les valeurs de déphasage mesurées dans l'image de phase hybride sur la queue sont légèrement plus importantes que celles mesurées par les expériences in-line et off-axis, avec un déphasage d'environ 0,25 rad pour l'image de phase hybride contre 0,2 rad pour les expériences off-axis et in-line. Il est cependant difficile d'analyser quantitativement ces images, en particulier au niveau de la queue qui est endommagée par la trop forte dose d'irradiation électronique qu'impose la combinaison des deux techniques d'holographie.

En résumé, nos résultats sur l'holographie électronique hybride sont légèrement améliorés par rapport aux expériences in-line et off-axis. Le gain de signal est visible sur les profils de phase et dans les images de la queue. Ces résultats ne sont toutefois pas concluants car nous n'avons pas obtenu d'images de phase à haute résolution.

Les techniques d'imagerie de phase en STEM

Deux autres techniques de microscopie STEM sont également développées pour l'étude de matériaux biologiques et des résultats très novateurs ont été publiés.

La première est le STEM à contraste différentiel intégré (iDPC STEM). iDPC STEM est une technique d'imagerie de phase pour laquelle le contraste est proportionnel au numéro atomique des atomes [238] et qui permet la détection d'atomes légers. La technique iDPC STEM s'est avérée très prometteuse car elle permet d'obtenir d'étudier des échantillons très épais.

La 4D-STEM est une autre technique STEM en cours de développement. Elle diffère de du STEM conventionnel à champ clair (BF) et à champ sombre (DF), et consiste à acquérir des clichés de diffraction avec une sonde focalisée convergente [241] sur des zones de l'échantillon qui se chevauchent. Cette méthode d'imagerie de phase en STEM, la ptychographie électronique, permet de récupérer la phase de l'onde de sortie des électrons.

Dans cette partie du chapitre, nous présentons donc nos résultats obtenus en utilisant BF et ADF STEM, ainsi que la ptychographie électronique sur le bactériophage T4.

Imagerie du bactériophage T4 par ADF-STEM

Afin d'explorer HAADF-STEM sur des bactériophages non colorés pour les comparer aux autres techniques que nous avons testées, des expériences ont été réalisées en STEM sur le microscope Jeol ARM 200F corrigé « sonde », situé au centre Raimond Castaing (Toulouse), pour étudier le bactériophage T4 non coloré à température ambiante.

Dans ces expériences, de nombreuses configurations avec différentes tailles de sonde et longueurs de caméra ont été testées. Ces expériences ont montré que le STEM à champ sombre (DF-STEM) améliore le contraste des bactériophages non colorés par rapport à une image obtenue en configuration de faisceau parallèle. De plus le DF-STEM révèle des structures telles que les fibres de la queue en configuration de collection des électrons diffractés à des angles moyens (MAADF), qui ne sont pas visibles en faisceau parallèle. De plus, nous avons mis en évidence un contraste élevé au niveau de la capsid et de la queue, en particulier en HAADF.

Imagerie du bactériophage T4 par 4D-STEM

La ptychographie électronique est une technique 4D-STEM récente qui se développe assez rapidement avec quelques applications pour l'étude des matériaux biologiques [177,180,181]. Nous avons voulu explorer cette méthode et la comparer à l'holographie électronique in-line et off-axis. Nous avons proposé au groupe du professeur A. Kirkland de réaliser des expériences de ptychographie sur nos échantillons. Nous avons ainsi envoyé une solution de T4 préparée au CBI au Dr Emanuella Liberti à Oxford qui a préparé les échantillons sur des supports en graphène, fournis par le groupe du Pr. Sara Bals. Les expériences de ptychographie ont été réalisées sur des phages T4 isolées à la fois à haute et à basse dose électronique.

La première expérience a été faite avec une dose totale de $332 \text{ e}^-/\text{\AA}^2$ avec un rapport de chevauchement de 0,9 lors du balayage de la sonde. L'expérience à faible dose a été réalisée avec une dose totale de $66 \text{ e}^-/\text{\AA}^2$ en utilisant un rapport de recouvrement de 0,8. L'analyse des données a été effectuée à l'aide de l'algorithme itératif ePIE [243] avec 10 itérations pour chaque jeu de données. Les images de phases obtenues présentaient un faible contraste et les anneaux de la queue du T4 n'étaient pas visibles à cette dose.

Ces résultats de ptychographie, en plus de notre expérience en l'holographie off-axis sur les échantillons T4, nous indiquent que les anneaux de queue ne sont pas observables à température ambiante. La résolution est toujours limitée par de multiples facteurs,

principalement la dose d'électrons en STEM et le bruit de phase. Cette première expérience suggère que la ptychographie, bien que performante dans des conditions cryogéniques, ne fournit pas des images de phase suffisamment contrastées à température ambiante. La réduction de la dose réduit plus encore le contraste et augmente le bruit.

CHAPITRE 6 : CONCLUSIONS ET PERSPECTIVES


Plusieurs études exploratoires ont été menées au cours de cette thèse pour caractériser les potentialités des méthodes d'holographie électronique pour l'étude des matériaux biologiques. Nous avons rencontré de nombreux défis, certains limitant le nombre d'expériences et nous empêchant d'obtenir de meilleurs résultats. Malgré ces obstacles, cette thèse a permis de réaliser une nouvelle évaluation de l'applicabilité des techniques d'holographie électronique à l'imagerie d'objets biologiques et d'identifier les éléments clés à prendre en compte pour les développements futurs dans ce domaine. Nous avons pu par ailleurs apporter des améliorations significatives à l'holographie électronique par rapport aux publications existantes.

Holographie électronique off-axis : La propreté de la solution de l'échantillon ainsi que celle du support, et la finesse de ce dernier sont apparues comme des paramètres particulièrement cruciaux pour obtenir des hologrammes suffisamment contrastés permettant d'obtenir des images de phase avec des rapport signal/bruit (SNR) suffisants. L'holographie électronique, surtout off-axis, est plus sensible aux contaminations contrairement aux expériences de MET sur des objets en coloration négative et à la cryo-EM en champ clair qui ont des niveaux de tolérances supérieurs à la contamination.

Les expériences d'holographie off-axis à haute dose, ont fourni des images à moyenne résolution ne permettant pas d'atteindre une résolution de 4 nm, et donc insuffisantes pour imager les anneaux de la queue des phages T4 qui étaient un de nos objectifs. Le rapport signal/bruit (SNR) des images a été considérablement amélioré avec la K3 comparé à la CMOS (un SNR 2 fois supérieur). Cette dernière nous a permis de visualiser la morphologie du bactériophage T4 avec des doses d'électrons aussi faibles que $31 \text{ e}^-/\text{Å}^2$.

Nous avons mesuré un déphasage du faisceau d'environ $2,2 \pm 0,2$ rad au niveau de la capsid du T4 et de $0,2 \pm 0,05$ rad au niveau de la queue. Ce dernier augmente à $0,5$ rad suite à sa contraction, après l'éjection de l'ADN. L'importante sensibilité de l'échantillon à l'irradiation électronique impose de travailler à faible dose au risque de l'endommager. Pour le bactériophage T5, la queue plus fine ne peut être observée que dans des conditions de faible dose. Les images de phase obtenues avec la K3 indiquent un déphasage de $2,2 \pm 0,1$ rad sur la capsid T5, et un déphasage de $0,25 \pm 0,05$ rad sur la queue.

Nous avons obtenu une sensibilité de phase moyenne de $0,06$ rad à température ambiante à des doses d'électrons élevées ($80 \text{ e}^-/\text{Å}^2 < \text{dose} < 450 \text{ e}^-/\text{Å}^2$) et en moyenne de $0,1$ rad à des faibles doses d'électrons ($< 80 \text{ e}^-/\text{Å}^2$). La sensibilité de $0,06$ rad nécessaire pour permettre de visualiser les anneaux de la queue a été obtenue dans de nombreuses images



acquises à des doses élevées, mais au prix de dommages d'irradiation importants de l'échantillon. Imager ces anneaux reste difficile à réaliser à faible dose.

Les résultats de l'holographie off-axis sont améliorés lorsque les expériences sont réalisées à basse température. La morphologie du phage est mieux définie dans les images de phase, en particulier la capsidie plutôt oblongue à température ambiante, qui apparaît avec icosaédrique à basse température et la *baseplate* est visible. Nous avons mesuré un déphasage plus faible au niveau de la capsidie, d'environ $0,9 \pm 0,1$ rad par rapport la mesure obtenue à température ambiante. Ceci est principalement dû à l'inclusion du phage dans une couche continue de glace vitreuse qui réduit le déphasage mesuré du faisceau traversant à la fois la glace et le phage, en plus d'une diminution intrinsèque du potentiel moyen interne des atomes du phage avec la baisse de température.

Dans les expériences à basse température, il est nécessaire de travailler à faible dose électronique pour éviter d'endommager la structure de l'objet et la couche de la glace dans laquelle est inclus l'échantillon. Cette nécessaire faible dose et la couche de glace vitreuse réduisent fortement le rapport signal sur bruit des images de phase induisant des bruits de phase supérieur à 0.1 rad. Les expériences d'holographie à basse température font ainsi face à un dilemme où la réduction de la dose nécessaire pour pas endommager la structure de l'objet biologique induit une augmentation significative du bruit de phase.

Holographie électronique in-line par séries focales

Les expériences d'holographie in-line à température ambiante avec des doses électroniques élevées ont donné des résultats similaires aux études off-axis. Bien que la morphologie du phage soit révélée, les anneaux de la queue de celui-ci ne sont pas identifiables. Nous avons obtenu une sensibilité de phase d'environ 0,02 rad et mesuré un déphasage de 0,7 rad au niveau de la capsidie T4 et de 0,15 rad au niveau de sa queue. Ces valeurs de déphasages sont inférieures à celles mesurées en holographie off-axis. Nous avons conclu de ce travail que les observations d'échantillons non colorés à température ambiante par holographie électronique ne peuvent pas permettre d'atteindre une résolution de 4 nm, même avec le faible niveau de bruit obtenu en holographie in-line. Ceci est dû au fait que les échantillons non colorés sont également non-protégés et donc plus sensibles aux dommages dus à l'irradiation.

Les expériences d'holographie in-line cryogéniques ont été effectuées sur le nouveau microscope cryogénique Talos Arctica équipé d'une caméra à détection directe d'électrons K2. Des résultats de haute qualité ont été obtenus. Des images de phases présentant une amélioration importante du contraste et du rapport signal/bruit par rapport aux images en champ clair classiques ont été obtenues. Ces images révèlent clairement la structure hélicoïdale de la queue du phage T4, correspondant à la rotation de 17° de chaque anneau autour de l'axe de la queue, en accord avec la structure connue de celui-ci. Nous avons également mesuré une différence dans le déphasage entourant la capsidie lorsqu'elle est pleine ou vide. Nous argumentons que cette différence de déphasage dépend de la charge totale de la capsidie, qui est modifiée lorsque l'ADN en est expulsé. Une analyse quantitative de la variation de charge nécessite des expériences supplémentaires.

Holographie électronique hybride

Nous avons pu réaliser des premières expériences d'holographie électronique hybride à température ambiante sur le bactériophage T4 sur l'I2TEM. Les résultats montrent une image de phase améliorée avec une sensibilité de phase élevée (0,028 rad) indiquant que le bruit de phase off-axis est réduit lorsque sont combinés l'holographie in-line et off-axis. Nous avons

obtenu les valeurs de déphasage de 1,5 rad pour la capsid en accord avec les mesures d'holographie off-axis, Enfin, un déphasage légèrement plus élevé a été mesuré au niveau de la queue et un motif en forme d'anneau a été observé. Nous avons donc réussi à démontrer des améliorations apportées par l'approche hybride par rapport à l'holographie in-line ou off-axis. Toutefois, ces améliorations ont été limitées par la dose totale d'électrons plus élevée nécessaire pour acquérir à la fois les nécessaires hologrammes off-axis et ceux de la série focale, qui endommagent les structures sensibles à l'irradiation.

Ptychographie électronique

Des études de ptychographie électronique ont été réalisées sur le bactériophage T4 par une équipe d'Oxford avec qui nous collaborons. L'image de phase résultante n'a pas montré d'amélioration par rapport aux images de phase d'holographie off-axis ou in-line, même à faible dose. Cette collaboration sur la ptychographie électronique a mis en évidence les limites des techniques d'imagerie de phase à température ambiante et la nécessité de réaliser la ptychographie électronique dans des conditions cryogéniques.

Synthèse

L'holographie off-axis a montré des limitations en raison du bruit et de sa sensibilité aux contaminations. L'holographie électronique nécessite une source d'électrons cohérente et nous avons montré l'apport d'une caméra DDD et un mode avec un champ de vision large pour imager des échantillons de la taille des bactériophages avec des faibles doses d'électron. Des méthodes de réduction du bruit restent nécessaires pour obtenir un rapport signal/bruit élevé par rapport aux méthodes classiques en champ clair.

Nous avons montré la possibilité de mesurer la charge de la capsid par holographie qui est la seule méthode le permettant. Cet aspect prometteur nécessite davantage d'expériences pour quantifier ces charges.


L'holographie in-line outre le fait qu'elle ne nécessite pas des microscopes dédiés, permet d'obtenir des images de phase très résolues de meilleure SNR que celles obtenues par holographie off-axis ce qui constitue un point fort de cette méthode.

Enfin, l'holographie hybride a montré ses capacités à préserver les informations de phases obtenues par l'off-axis ainsi que la sensibilité en phase de l'in-line. Cette méthode, bien que très chronophage, a également montré un grand potentiel.

Perspectives

Malgré les limites qu'on a établis en holographie off-axis, plusieurs pistes restent à explorer pour éventuellement améliorer cette technique.

- La réalisation d'échantillons vitrifiés dans une glace plus fine et d'épaisseur constante est un point clef pour obtenir des images de phase de SNR suffisant.
- La voie de l'holographie hybride en cryo semble très prometteuse en termes de sensibilité à hautes et basses fréquences bien qu'elle impose de cumuler les doses électroniques des expériences de l'holographie in-line et off-axis.
- La mesure de la charge locale par holographie mérite d'être explorée plus en détail car elle pourrait apporter des lumières sur l'importance des variations de charges dans les processus biologiques.



L'holographie in-line a montré son fort potentiel à cause de son applicabilité sur tout type de microscope. Il serait donc intéressant :

- De poursuivre les expériences avec des objets de différentes tailles comme les pré-40S. Cela nécessitera un travail d'optimisation et du temps d'analyse. Le but sera alors d'explorer l'apport du gain de contraste et de SNR par rapport aux méthodes de reconstruction SPA.
- D'étudier d'autres codes de reconstruction que « FRWR » afin d'évaluer et comparer leurs performances.
- D'automatiser la partie analyse.

BIBLIOGRAPHY

- [1] E. Abbe, Beiträge zur Theorie des Mikroskops und der mikroskopischen Wahrnehmung, *Archiv f. mikrosk. Anatomie* 9 (1873) 413–468. <https://doi.org/10.1007/BF02956173>.
- [2] M. Lelek, M.T. Gyparaki, G. Beliu, F. Schueder, J. Griffié, S. Manley, R. Jungmann, M. Sauer, M. Lakadamyali, C. Zimmer, Single-molecule localization microscopy, *Nature Reviews Methods Primers* 2021 1:1 1 (2021) 1–27. <https://doi.org/10.1038/s43586-021-00038-x>.
- [3] H. Jubb, A.P. Higuero, A. Winter, T.L. Blundell, Structural biology and drug discovery for protein-protein interactions, *Trends in Pharmacological Sciences* 33 (2012) 241–248. <https://doi.org/10.1016/J.TIPS.2012.03.006>.
- [4] Q. Li, C. Kang, Mechanisms of Action for Small Molecules Revealed by Structural Biology in Drug Discovery, *International Journal of Molecular Sciences* 21 (2020) 1–18. <https://doi.org/10.3390/IJMS21155262>.
- [5] The Nobel Prize in Physics 1914 - NobelPrize.org, (n.d.). <https://www.nobelprize.org/prizes/physics/1914/summary/>.
- [6] The Nobel Prize in Chemistry 1962 - NobelPrize.org, (n.d.). <https://www.nobelprize.org/prizes/chemistry/1962/summary/>.
- [7] The Nobel Prize in Chemistry 2017 - NobelPrize.org, (n.d.). <https://www.nobelprize.org/prizes/chemistry/2017/summary/>.
- [8] C. Gatel, Quantitative field mapping at the nanoscale by transmission electron microscopy, (2020). <https://hal.science/tel-02974885> (accessed April 11, 2023).
- [9] A. Harscher, *Electron holography of biological objects: basics and examples of applications*, 1999.
- [10] J.J.T.M.A. F.R.S., XL. Cathode Rays, *The London, Edinburgh, and Dublin Philosophical Magazine and Journal of Science* 44 (1897) 293–316. <https://doi.org/10.1080/14786449708621070>.
- [11] I. Orion, M. Laitman, The Double-Slit Experiment and Particle-Wave Duality: Toward a Novel Quantum Interpretation, *Journal of Modern Physics* 01 (2010) 90–92. <https://doi.org/10.4236/jmp.2010.110013>.
- [12] L. De Broglie, Waves and Quanta, *Nature* 1923 112:2815 112 (1923) 540–540. <https://doi.org/10.1038/112540a0>.
- [13] C. Davisson, L.H. Germer, Diffraction of electrons by a crystal of nickel, *Physical Review* 30 (1927) 705–740. <https://doi.org/10.1103/PHYSREV.30.705/FIGURE/1/THUMB>.
- [14] C. Jönsson, Electron Diffraction at Multiple Slits, Citation: *American Journal of Physics* 42 (1974) 4. <https://doi.org/10.1119/1.1987592>.
- [15] Y. Garini, B.J. Vermolen, I.T. Young, From micro to nano: recent advances in high-resolution microscopy, *Current Opinion in Biotechnology* 16 (2005) 3–12. <https://doi.org/10.1016/J.COPBIO.2005.01.003>.


-
- [16] R. Heintzmann, G. Ficz, Breaking the Resolution Limit in Light Microscopy, in: *Methods in Cell Biology*, Academic Press, 2007: pp. 561–580. [https://doi.org/10.1016/S0091-679X\(06\)81026-5](https://doi.org/10.1016/S0091-679X(06)81026-5).
- [17] S.C.M. Reinhardt, L.A. Masullo, I. Baudrexel, P.R. Steen, R. Kowalewski, A.S. Eklund, S. Strauss, E.M. Unterauer, T. Schlichthaerle, M.T. Strauss, C. Klein, R. Jungmann, Ångström-resolution fluorescence microscopy, *Nature* 617 (2023) 711–716. <https://doi.org/10.1038/s41586-023-05925-9>.
- [18] A. Tonomura, *The Quantum World Unveiled by Electron Waves*, WORLD SCIENTIFIC, 1998. <https://doi.org/10.1142/2976>.
- [19] R.F. Egerton, Choice of operating voltage for a transmission electron microscope, *Ultramicroscopy* 145 (2014) 85–93. <https://doi.org/10.1016/j.ultramic.2013.10.019>.
- [20] Stephen J. Pennycook, Peter D. Nellist, *Scanning Transmission Electron Microscopy*, Springer New York, New York, NY, 2011. <https://doi.org/10.1007/978-1-4419-7200-2>.
- [21] S. Sadayama, H. Sekiguchi, A. Bright, N. Suzuki, K. Yamada, K. Kaneko, Physical: Full length High-resolution three-dimensional scanning transmission electron microscopy characterization of oxide-nitride-oxide layer interfaces in Si-based semiconductors using computed tomography, (2011). <https://doi.org/10.1093/jmicro/dfz029>.
- [22] R.F. Egerton, P. Li, M. Malac, Radiation damage in the TEM and SEM, *Micron* 35 (2004) 399–409. <https://doi.org/10.1016/j.micron.2004.02.003>.
- [23] D.B. Williams, C.B. Carter, *Transmission Electron Microscopy*, Springer US, Boston, MA, 2009. <https://doi.org/10.1007/978-0-387-76501-3>.
- [24] A.A. Sousa, R.D. Leapman, Development and application of STEM for the biological sciences, *Ultramicroscopy* 123 (2012) 38–49. <https://doi.org/10.1016/j.ultramic.2012.04.005>.
- [25] T.J. Pennycook, G.T. Martinez, P.D. Nellist, J.C. Meyer, High dose efficiency atomic resolution imaging via electron ptychography, *Ultramicroscopy* 196 (2019) 131–135. <https://doi.org/10.1016/j.ultramic.2018.10.005>.
- [26] C.A. Scarff, M.J.G. Fuller, R.F. Thompson, M.G. Iadaza, Variations on negative stain electron microscopy methods: Tools for tackling challenging systems, *Journal of Visualized Experiments* 2018 (2018). <https://doi.org/10.3791/57199>.
- [27] B. Fultz, J. Howe, *Transmission Electron Microscopy and Diffractometry of Materials*, Springer Berlin Heidelberg, Berlin, Heidelberg, 2013. <https://doi.org/10.1007/978-3-642-29761-8>.
- [28] S. Hatanaka, J. Yamasaki, J. Yamasaki, Quantitative measurement of spatial coherence of electron beams emitted from a thermionic electron gun, *JOSA A*, Vol. 38, Issue 12, Pp. 1893-1900 38 (2021) 1893–1900. <https://doi.org/10.1364/JOSAA.437843>.
- [29] J. Orloff, Survey of electron sources for high-resolution microscopy, *Ultramicroscopy* 28 (1989) 88–97. [https://doi.org/10.1016/0304-3991\(89\)90278-7](https://doi.org/10.1016/0304-3991(89)90278-7).
- [30] B. Cho, K. Shigeru, C. Oshima, W(310) cold-field emission characteristics reflecting the vacuum states of an extreme high vacuum electron gun, *REVIEW OF SCIENTIFIC INSTRUMENTS* 84 (2013) 13305. <https://doi.org/10.1063/1.4776182>.

- [31] G.A. Schwind, G. Magera, L.W. Swanson, Comparison of parameters for Schottky and cold field emission sources, Citation: *Journal of Vacuum Science & Technology B: Microelectronics and Nanometer Structures Processing, Measurement, and Phenomena* 24 (2006) 2897. <https://doi.org/10.1116/1.2366675>.
- [32] X. Shao, A. Khurshed, A Review Paper on “Graphene Field Emission for Electron Microscopy,” *Applied Sciences* 2018, Vol. 8, Page 868 8 (2018) 868. <https://doi.org/10.3390/APP8060868>.
- [33] P.T.E. Roberts, J.N. Chapman, A.M. MacLeod, A CCD-based image recording system for the CTEM, *Ultramicroscopy* 8 (1982) 385–396. [https://doi.org/10.1016/0304-3991\(82\)90061-4](https://doi.org/10.1016/0304-3991(82)90061-4).
- [34] B.D.A. Levin, Direct detectors and their applications in electron microscopy for materials science, *Journal of Physics: Materials* 4 (2021) 042005. <https://doi.org/10.1088/2515-7639/ac0ff9>.
- [35] A.R. Faruqi, G. McMullan, Direct imaging detectors for electron microscopy, *Nuclear Instruments and Methods in Physics Research, Section A: Accelerators, Spectrometers, Detectors and Associated Equipment* 878 (2018) 180–190. <https://doi.org/10.1016/J.NIMA.2017.07.037>.
- [36] H. Shigematsu, F.J. Sigworth, Noise models and cryo-EM drift correction with a direct-electron camera, *Ultramicroscopy* 131 (2013) 61. <https://doi.org/10.1016/J.ULTRAMIC.2013.04.001>.
- [37] A.-C. Milazzo, G. Moldovan, J. Lanman, J. Liang, J.C. Bouwer, S. Klienfelder, S.T. Peltier, M.H. Ellisman, A.I. Kirkland, N.-H. Xuong, Characterization of a Direct Detection Device Imaging Camera for Transmission Electron Microscopy, (2010). <https://doi.org/10.1016/j.ultramic.2010.03.007>.
- [38] R.A. McLeod, M. Malac, Characterization of detector modulation-transfer function with noise, edge, and holographic methods, *Ultramicroscopy* 129 (2013) 42–52. <https://doi.org/10.1016/J.ULTRAMIC.2013.02.021>.
- [39] G. Moldovan, B. Jeffery, A. Nomerotski, A. Kirkland, Imaging modes for direct electron detection in TEM with column parallel CCD, *Nuclear Instruments and Methods in Physics Research Section A: Accelerators, Spectrometers, Detectors and Associated Equipment* 607 (2009) 13–16. <https://doi.org/10.1016/j.nima.2009.03.105>.
- [40] S.L.Y. Chang, C. Dwyer, J. Barthel, C.B. Boothroyd, R.E. Dunin-Borkowski, Performance of a direct detection camera for off-axis electron holography, *Ultramicroscopy* 161 (2016) 90–97. <https://doi.org/10.1016/J.ULTRAMIC.2015.09.004>.
- [41] C. Hetherington, Aberration correction for TEM, *Materials Today* 7 (2004) 50–55. [https://doi.org/10.1016/S1369-7021\(04\)00571-1](https://doi.org/10.1016/S1369-7021(04)00571-1).
- [42] J.C. Meyer, Transmission electron microscopy (TEM) of graphene, in: *Graphene*, Elsevier, 2014: pp. 101–123. <https://doi.org/10.1533/9780857099334.2.101>.
- [43] P. Simon, H. Lichte, P. Formanek, M. Lehmann, R. Huhle, W. Carrillo-Cabrera, A. Harscher, H. Ehrlich, Electron holography of biological samples, *Micron* 39 (2008) 229–256. <https://doi.org/10.1016/j.micron.2006.11.012>.
- [44] L. Reimer, *Transmission Electron Microscopy*, Springer Berlin Heidelberg, Berlin, Heidelberg, 1989. <https://doi.org/10.1007/978-3-662-21579-1>.
- [45] H. Lichte, Electron Holography: Phases matter, *Journal of Electron Microscopy* 62 (2013). <https://doi.org/10.1093/jmicro/dft009>.

- [46] J. Ruprecht, J. Nield, Determining the structure of biological macromolecules by transmission electron microscopy, single particle analysis and 3D reconstruction, *Progress in Biophysics and Molecular Biology* 75 (2001) 121–164. [https://doi.org/10.1016/S0079-6107\(01\)00004-9](https://doi.org/10.1016/S0079-6107(01)00004-9).
- [47] R. Danev, W. Baumeister, Cryo-EM single particle analysis with the volta phase plate, *eLife* 5 (2016). <https://doi.org/10.7554/ELIFE.13046>.
- [48] R.M. Glaeser, Invited Review Article: Methods for imaging weak-phase objects in electron microscopy, *Review of Scientific Instruments* 84 (2013). <https://doi.org/10.1063/1.4830355>.
- [49] M. Malac, S. Hettler, M. Hayashida, E. Kano, R.F. Egerton, M. Beleggia, Phase plates in the transmission electron microscope: operating principles and applications, *Microscopy* 70 (2021) 75–115. <https://doi.org/10.1093/JMICRO/DFAA070>.
- [50] M. Khoshouei, M. Radjainia, W. Baumeister, R. Danev, Cryo-EM structure of haemoglobin at 3.2 Å determined with the Volta phase plate, *Nat Commun* 8 (2017) 16099. <https://doi.org/10.1038/ncomms16099>.
- [51] O. Schwartz, J.J. Axelrod, S.L. Campbell, C. Turnbaugh, R.M. Glaeser, H. Müller, Laser phase plate for transmission electron microscopy, *Nature Methods* 16 (2019) 1016–1020. <https://doi.org/10.1038/s41592-019-0552-2>.
- [52] P.S. Shen, The 2017 Nobel Prize in Chemistry: cryo-EM comes of age, *Analytical and Bioanalytical Chemistry* 410 (2018) 2053–2057. <https://doi.org/10.1007/s00216-018-0899-8>.
- [53] T. Chen, N. Hongdilokkul, Z. Liu, D. Thirunavukarasu, F.E. Romesberg, The Expanding World of DNA and RNA, *Current Opinion in Chemical Biology* 34 (2016) 80. <https://doi.org/10.1016/J.CBPA.2016.08.001>.
- [54] J.D. Watson, F.H.C. Crick, Molecular Structure of Nucleic Acids: A Structure for Deoxyribose Nucleic Acid, *Nature* 1953 171:4356 171 (1953) 737–738. <https://doi.org/10.1038/171737a0>.
- [55] R.P. Bywater, Why twenty amino acid residue types suffice(d) to support all living systems, *PLOS ONE* 13 (2018) e0204883. <https://doi.org/10.1371/JOURNAL.PONE.0204883>.
- [56] K.M. Yip, N. Fischer, E. Paknia, A. Chari, H. Stark, Atomic-resolution protein structure determination by cryo-EM, *Nature* 2020 587:7832 587 (2020) 157–161. <https://doi.org/10.1038/s41586-020-2833-4>.
- [57] K. Zhang, X. Li, Z. Wang, G. Li, B. Ma, H. Chen, N. Li, H. Yang, Y. Wang, B. Liu, Systemic Expression, Purification, and Initial Structural Characterization of Bacteriophage T4 Proteins Without Known Structure Homologs, *Frontiers in Microbiology* 12 (2021). <https://doi.org/10.3389/fmicb.2021.674415>.
- [58] D.M. Lin, B. Koskella, H.C. Lin, Phage therapy: An alternative to antibiotics in the age of multi-drug resistance, *World Journal of Gastrointestinal Pharmacology and Therapeutics* 8 (2017) 162. <https://doi.org/10.4292/WJGPT.V8.I3.162>.
- [59] C. Brives, J. Pourraz, Phage therapy as a potential solution in the fight against AMR: obstacles and possible futures, *Palgrave Communications* 2020 6:1 6 (2020) 1–11. <https://doi.org/10.1057/s41599-020-0478-4>.

- [60] H. Ling, X. Lou, Q. Luo, Z. He, M. Sun, J. Sun, Recent advances in bacteriophage-based therapeutics: Insight into the post-antibiotic era, *Acta Pharmaceutica Sinica B* 12 (2022) 4348–4364. <https://doi.org/10.1016/J.APSB.2022.05.007>.
- [61] V.B. Rao, A. Fokine, Q. Fang, Q. Shao, Bacteriophage T4 Head: Structure, Assembly, and Genome Packaging, *Viruses* 15 (2023) 527. <https://doi.org/10.3390/V15020527>.
- [62] M.L. Yap, M.G. Rossmann, Structure and function of bacteriophage T4, *Future Microbiology* 9 (2014) 1319–1337. <https://doi.org/10.2217/fmb.14.91>.
- [63] P. Hyman, M. van Raaij, Bacteriophage T4 long tail fiber domains, *Biophysical Reviews* 10 (2018) 463–471. <https://doi.org/10.1007/s12551-017-0348-5>.
- [64] Y. Zivanovic, F. Confalonieri, L. Ponchon, R. Lurz, M. Chami, A. Flayhan, M. Renouard, A. Huet, P. Decottignies, A.R. Davidson, C. Breyton, P. Boulanger, Insights into Bacteriophage T5 Structure from Analysis of Its Morphogenesis Genes and Protein Components, (2014). <https://doi.org/10.1128/JVI.02262-13>.
- [65] C.A. Arnaud, G. Effantin, C. Vivès, S. Engilberge, M. Bacia, P. Boulanger, E. Girard, G. Schoehn, C. Breyton, Bacteriophage T5 tail tube structure suggests a trigger mechanism for Siphoviridae DNA ejection, *Nature Communications* 8 (2017). <https://doi.org/10.1038/s41467-017-02049-3>.
- [66] F. Guo, Z. Liu, P.A. Fang, Q. Zhang, E.T. Wright, W. Wu, C. Zhang, F. Vago, Y. Ren, J. Jakana, W. Chiu, P. Serwer, W. Jiang, Capsid expansion mechanism of bacteriophage T7 revealed by multistate atomic models derived from cryo-EM reconstructions, *Proceedings of the National Academy of Sciences of the United States of America* 111 (2014) E4606–E4614. https://doi.org/10.1073/PNAS.1407020111/SUPPL_FILE/PNAS.1407020111.SM02.MPG.
- [67] M. Pérez-Ruiz, M. Pulido-Cid, J.R. Luque-Ortega, J.M. Valpuesta, A. Cuervo, J.L. Carrascosa, Assisted assembly of bacteriophage T7 core components for genome translocation across the bacterial envelope, *Proceedings of the National Academy of Sciences of the United States of America* 118 (2021) e2026719118. https://doi.org/10.1073/PNAS.2026719118/SUPPL_FILE/PNAS.2026719118.SAPP.PDF.
- [68] W. Zheng, F. Wang, N.M.I. Taylor, R.C. Guerrero-Ferreira, P.G. Leiman, E.H. Egelman, Refined Cryo-EM Structure of the T4 Tail Tube: Exploring the Lowest Dose Limit, *Structure* 25 (2017) 1436–1441.e2. <https://doi.org/10.1016/j.str.2017.06.017>.
- [69] P.G. Leiman, F. Arisaka, M.J. Van Raaij, V.A. Kostyuchenko, A.A. Aksyuk, S. Kanamaru, M.G. Rossmann, Morphogenesis of the T4 tail and tail fibers, *Virology Journal* 7 (2010). <https://doi.org/10.1186/1743-422X-7-355>.
- [70] E. Ortiz Ortega, H. Hosseinian, M.J. Rosales López, A. Rodríguez Vera, S. Hosseini, Characterization Techniques for Morphology Analysis, in: 2022: pp. 1–45. https://doi.org/10.1007/978-981-16-9569-8_1.
- [71] Y. Shi, A Glimpse of Structural Biology through X-Ray Crystallography, *Cell* 159 (2014) 995–1014. <https://doi.org/10.1016/J.CELL.2014.10.051>.
- [72] J.C. Kendrew, G. Bodo, H.M. Dintzis, R.G. Parrish, H. Wyckoff, D.C. Phillips, A Three-Dimensional Model of the Myoglobin Molecule Obtained by X-Ray Analysis, *Nature* 181 (1958) 662–666. <https://doi.org/10.1038/181662a0>.

-
- [73] M.F. PERUTZ, M.G. ROSSMANN, A.F. CULLIS, H. MUIRHEAD, G. WILL, A.C.T. NORTH, Structure of Hæmoglobin: A Three-Dimensional Fourier Synthesis at 5.5-Å. Resolution, Obtained by X-Ray Analysis, *Nature* 185 (1960) 416–422. <https://doi.org/10.1038/185416a0>.
- [74] R.P.D. Bank, PDB Statistics: PDB Data Distribution by Experimental Method and Molecular Type, (n.d.). <https://www.rcsb.org/stats/summary> (accessed September 29, 2023).
- [75] V.I. Mikla, V.I. Rusin, P.A. Boldizhar, Advances in Imaging from the First X-Ray Images, *Journal of Optoelectronics and Advanced Materials* 14 (2014) 1–22. <https://doi.org/10.1016/B978-0-12-417021-6.00001-0>.
- [76] W. Koch, A. Lubk, F. Grossmann, H. Lichte, R. Schmidt, Coherent and incoherent effects on the imaging and scattering process in transmission electron microscopy and off-axis electron holography, *Ultramicroscopy* 110 (2010) 1397–1403. <https://doi.org/10.1016/j.ultramic.2010.07.002>.
- [77] Y. Cheng, Single-particle cryo-EM—How did it get here and where will it go, *Science* 361 (2018) 876–880. <https://doi.org/10.1126/science.aat4346>.
- [78] W.C. Dickinson, Dependence of the F 19 Nuclear Resonance Position on Chemical Compound, *Phys. Rev.* 77 (1950) 736–737. <https://doi.org/10.1103/PhysRev.77.736.2>.
- [79] W.G. Proctor, F.C. Yu, The Dependence of a Nuclear Magnetic Resonance Frequency upon Chemical Compound, *Phys. Rev.* 77 (1950) 717–717. <https://doi.org/10.1103/PhysRev.77.717>.
- [80] A.W. Overhauser, Polarization of Nuclei in Metals, *Physical Review* 92 (1953) 411. <https://doi.org/10.1103/PhysRev.92.411>.
- [81] J.A. Purslow, B. Khatiwada, M.J. Bayro, V. Venditti, NMR Methods for Structural Characterization of Protein-Protein Complexes, *Frontiers in Molecular Biosciences* 7 (2020) 9. <https://doi.org/10.3389/FMOLB.2020.00009/BIBTEX>.
- [82] A. Singer, F.J. Sigworth, Computational Methods for Single-Particle Electron Cryomicroscopy, *Annual Review of Biomedical Data Science* 3 (2020) 163–190. <https://doi.org/10.1146/annurev-biodatasci-021020-093826>.
- [83] D. Dai, X. Wang, Y. Liu, X.-L. Yang, C. Glaubit, V. Denysenkov, X. He, T. Prisner, J. Mao, Room-temperature dynamic nuclear polarization enhanced NMR spectroscopy of small biological molecules in water, *Nature Communications* 12 (2021) 6880. <https://doi.org/10.1038/s41467-021-27067-0>.
- [84] S. Kaieda, B. Setlow, P. Setlow, B. Halle, Mobility of core water in *Bacillus subtilis* Spores by 2H NMR, *Biophysical Journal* 105 (2013) 2016–2023. <https://doi.org/10.1016/J.BPJ.2013.09.022>.
- [85] X. Robbins Puthenveetil, O. Vinogradova, Solution NMR: A powerful tool for structural and functional studies of membrane proteins in reconstituted environments, *J. Biol. Chem* 294 (2019) 15914–15931. <https://doi.org/10.1074/jbc.REV119.009178>.
- [86] M. Guéron, P. Plateau, Water Signal Suppression in NMR of Biomolecules, *eMagRes* 2007 (2007). <https://doi.org/10.1002/9780470034590.EMRSTM0590>.
- [87] H. Ruska, Die Sichtbarmachung der bakteriophagen Lyse im Übermikroskop, *Die Naturwissenschaften* 28 (1940) 45–46. <https://doi.org/10.1007/BF01486931/METRICS>.

- [88] E. Peankuch, G.A. Kausche, Isolierung und  bermikroskopische Abbildung eines Bakteriophagen, *Naturwissenschaften* 28 (1940) 46–46. <https://doi.org/10.1007/BF01486932>.
- [89] H.-W. Ackermann, Pfankuch E, Kausche GA. Isolation and supra-microscopic representation of a bacteriophage. *Naturwissenschaften* 1940; 28, Bacteriophage 1 (2011) 186–187. <https://doi.org/10.4161/BACT.1.4.17625>.
- [90] H.-W. Ackermann, The first phage electron micrographs, *Bacteriophage* 1 (2011) 225–227. <https://doi.org/10.4161/BACT.1.4.17280>.
- [91] S. Brenner, R.W. Horne, A negative staining method for high resolution electron microscopy of viruses, *Biochimica et Biophysica Acta* 34 (1959) 103–110. [https://doi.org/10.1016/0006-3002\(59\)90237-9](https://doi.org/10.1016/0006-3002(59)90237-9).
- [92] J.R. Gallagher, A.J. Kim, N.M. Gulati, A.K. Harris, Negative-Stain Transmission Electron Microscopy of Molecular Complexes for Image Analysis by 2D Class Averaging, *Current Protocols in Microbiology* 54 (2019). <https://doi.org/10.1002/CPMC.90>.
- [93] D.J. De Rosier, A. Klug, Reconstruction of Three Dimensional Structures from Electron Micrographs, 217 (1966).
- [94] K.A. Taylor, R.M. Glaeser, Electron Microscopy of Frozen Hydrated Biological Specimens, *JOURNAL OF ULTRASTRUCTURE RESEARCH* 55 (1976) 448–456.
- [95] J. Dubochet, J. Lepault, R. Freeman, J.A. Berriman, J.-C. Homo, Electron microscopy of frozen water and aqueous solutions, *Journal of Microscopy* 128 (1982) 219–237. <https://doi.org/10.1111/j.1365-2818.1982.tb04625.x>.
- [96] R. Henderson, P.N.T. Unwin, Three-dimensional model of purple membrane obtained by electron microscopy, *Nature* 1975 257:5521 257 (1975) 28–32. <https://doi.org/10.1038/257028a0>.
- [97] J. Frank, J. Zhu, P. Penczek, Y. Li, S. Srivastava, A. Verschoor, M. Radermacher, R. Grassucci, R.K. Lata, R.K. Agrawal, A model of protein synthesis based on cryo-electron microscopy of the E. coli ribosome, *Nature* 1995 376:6539 376 (1995) 441–444. <https://doi.org/10.1038/376441a0>.
- [98] H. Liu, L. Jin, S.B.S. Koh, I. Atanasov, S. Schein, L. Wu, Z.H. Zhou, Atomic structure of human adenovirus by Cryo-EM reveals interactions among protein networks, *Science* 329 (2010) 1038–1043. https://doi.org/10.1126/SCIENCE.1187433/SUPPL_FILE/LIU.SOM.PDF.
- [99] W. Kühlbrandt, The Resolution Revolution, *Science* 343 (2014) 1443–1444. <https://doi.org/10.1126/science.1251652>.
- [100] E. Nogales, S.H.W. Scheres, Cryo-EM: A Unique Tool for the Visualization of Macromolecular Complexity, *Molecular Cell* 58 (2015) 677–689. <https://doi.org/10.1016/J.MOLCEL.2015.02.019>.
- [101] A. Punjani, J.L. Rubinstein, D.J. Fleet, M.A. Brubaker, cryoSPARC: algorithms for rapid unsupervised cryo-EM structure determination, *Nature Methods* 2017 14:3 14 (2017) 290–296. <https://doi.org/10.1038/nmeth.4169>.
- [102] S.H.W. Scheres, A Bayesian View on Cryo-EM Structure Determination, *Journal of Molecular Biology* 415 (2012) 406. <https://doi.org/10.1016/J.JMB.2011.11.010>.

- [103] T. Nakane, A. Kotecha, A. Sente, G. McMullan, S. Masiulis, P.M.G.E. Brown, I.T. Grigoras, L. Malinauskaitė, T. Malinauskas, J. Miebling, T. Uchański, L. Yu, D. Karia, E.V. Pechnikova, E. de Jong, J. Keizer, M. Bischoff, J. McCormack, P. Tiemeijer, S.W. Hardwick, D.Y. Chirgadze, G. Murshudov, A.R. Aricescu, S.H.W. Scheres, Single-particle cryo-EM at atomic resolution, *Nature* 587 (2020) 152–156. <https://doi.org/10.1038/s41586-020-2829-0>.
- [104] T. Dahmane, M. Damian, S. Mary, J.L. Popot, J.L. Banères, Amphipol-assisted in vitro folding of G protein-coupled receptors, *Biochemistry* 48 (2009) 6516–6521. <https://doi.org/10.1021/BI801729Z>.
- [105] J.L. Banères, J.L. Popot, B. Mouillac, New advances in production and functional folding of G-protein-coupled receptors, *Trends in Biotechnology* 29 (2011) 314–322. <https://doi.org/10.1016/J.TIBTECH.2011.03.002>.
- [106] D. Kampjut, J. Steiner, L.A. Sazanov, Cryo-EM grid optimization for membrane proteins, *ISCIENCE* 24 (2021) 102139. <https://doi.org/10.1016/j.isci.2021.102139>.
- [107] C. Thangaratnarajah, J. Rheinberger, C. Paulino, S.M. Lea, P.A. Williams, Cryo-EM studies of membrane proteins at 200 keV This review comes from a themed issue on Cryo-electron microscopy Edited by Challenges with membrane proteins, *Current Opinion in Structural Biology* 76 (2022) 102440. <https://doi.org/10.1016/j.sbi.2022.102440>.
- [108] J. Zivanov, T. Nakane, B.O. Forsberg, D. Kimanius, W.J. Hagen, E. Lindahl, S.H. Scheres, New tools for automated high-resolution cryo-EM structure determination in RELION-3, *eLife* 7 (2018). <https://doi.org/10.7554/eLife.42166>.
- [109] R. Langer, J. Frank, A. Feltynowski, W. Hoppe, A. des Bilddifferenzverfahrens usw, Anwendung des Bilddifferenzverfahrens auf die Untersuchung von Strukturänderungen dünner Kohlefolien bei Elektronenbestrahlung, *Berichte Der Bunsengesellschaft Für Physikalische Chemie* 74 (1970) 1120–1126. <https://doi.org/10.1002/BBPC.19700741107>.
- [110] M. van Heel, J. Frank, Use of multivariate statistics in analysing the images of biological macromolecules, *Ultramicroscopy* 6 (1981) 187–194. [https://doi.org/10.1016/S0304-3991\(81\)80197-0](https://doi.org/10.1016/S0304-3991(81)80197-0).
- [111] S.H.W. Scheres, RELION: Implementation of a Bayesian approach to cryo-EM structure determination, *Journal of Structural Biology* 180 (2012) 519–530. <https://doi.org/10.1016/j.jsb.2012.09.006>.
- [112] K.R. Vinothkumar, R. Henderson, Single particle electron cryomicroscopy: trends, issues and future perspective, *Quarterly Reviews of Biophysics* 49 (2016) e13. <https://doi.org/10.1017/S0033583516000068>.
- [113] B. Li, D. Zhu, H. Shi, X. Zhang, Effect of charge on protein preferred orientation at the air–water interface in cryo-electron microscopy, *Journal of Structural Biology* 213 (2021). <https://doi.org/10.1016/J.JSB.2021.107783>.
- [114] Y. Zi Tan, P.R. Baldwin, J.H. Davis, J.R. Williamson, C.S. Potter, B. Carragher, D. Lyumkis, Addressing preferred specimen orientation in single-particle cryo-EM through tilting, *Nature Methods* 2017 14:8 14 (2017) 793–796. <https://doi.org/10.1038/NMETH.4347>.
- [115] T. Nakane, D. Kimanius, E. Lindahl, S.H. Scheres, Characterisation of molecular motions in cryo-EM single-particle data by multi-body refinement in RELION, *eLife* 7 (2018). <https://doi.org/10.7554/eLife.36861>.

- [116] A. Punjani, D.J. Fleet, 3D variability analysis: Resolving continuous flexibility and discrete heterogeneity from single particle cryo-EM, *Journal of Structural Biology* 213 (2021) 107702. <https://doi.org/10.1016/J.JSB.2021.107702>.
- [117] E.D. Zhong, T. Bepler, B. Berger, J.H. Davis, CryoDRGN: reconstruction of heterogeneous cryo-EM structures using neural networks, *Nature Methods* 2021 18:2 18 (2021) 176–185. <https://doi.org/10.1038/s41592-020-01049-4>.
- [118] E.D. Zhong, A. Lerer, J.H. Davis, B. Berger, CryoDRGN2: Ab initio neural reconstruction of 3D protein structures from real cryo-EM images, in: 2021 IEEE/CVF International Conference on Computer Vision (ICCV), IEEE, 2021: pp. 4046–4055. <https://doi.org/10.1109/ICCV48922.2021.00403>.
- [119] A. Punjani, D.J. Fleet, 3DFlex: determining structure and motion of flexible proteins from cryo-EM, *Nature Methods* (2023). <https://doi.org/10.1038/s41592-023-01853-8>.
- [120] Y. Liu, X. Meng, Z. Liu, J. Struct, B. Author, Deformed grids for single-particle cryo-electron microscopy of specimens exhibiting a preferred orientation, *J Struct Biol* 182 (2013) 255–258. <https://doi.org/10.1016/j.jsb.2013.03.005>.
- [121] J.R. Meyerson, P. Rao, J. Kumar, S. Chittori, S. Banerjee, J. Pierson, M.L. Mayer, S. Subramaniam, Self-assembled monolayers improve protein distribution on holey carbon cryo-EM supports, *Scientific Reports* 4 (2014) 7084. <https://doi.org/10.1038/srep07084>.
- [122] V. Lučić, A. Leis, W. Baumeister, Cryo-electron tomography of cells: connecting structure and function, *Histochem Cell Biol* 130 (2008) 185–196. <https://doi.org/10.1007/s00418-008-0459-y>.
- [123] C. Berger, N. Premaraj, R.B.G. Ravelli, K. Knoop, C. López-Iglesias, P.J. Peters, Cryo-electron tomography on focused ion beam lamellae transforms structural cell biology, *Nature Methods* 2023 20:4 20 (2023) 499–511. <https://doi.org/10.1038/s41592-023-01783-5>.
- [124] H. Moor, Theory and Practice of High Pressure Freezing, *Cryotechniques in Biological Electron Microscopy* (1987) 175–191. https://doi.org/10.1007/978-3-642-72815-0_8.
- [125] P.D. Sanz, L. Otero, High-Pressure Freezing, *Emerging Technologies for Food Processing* (2014) 515–538. <https://doi.org/10.1016/B978-0-12-411479-1.00028-0>.
- [126] R.K. Hylton, M.T. Swulius, Challenges and triumphs in cryo-electron tomography, *iScience* 24 (2021) 102959. <https://doi.org/10.1016/j.isci.2021.102959>.
- [127] T.R. Umrekar, E. Cohen, T. Drobnič, N. Gonzalez-Rodriguez, M. Beeby, CryoEM of bacterial secretion systems: A primer for microbiologists, *Molecular Microbiology* 115 (2021) 366–382. <https://doi.org/10.1111/MMI.14637>.
- [128] M. Obr, W.J.H. Hagen, R.A. Dick, L. Yu, A. Kotecha, F.K.M. Schur, Exploring high-resolution cryo-ET and subtomogram averaging capabilities of contemporary DEDs, *Journal of Structural Biology* 214 (2022). <https://doi.org/10.1016/J.JSB.2022.107852>.
- [129] Subtomogram averaging in the cryo-ET workflow, (n.d.). <https://blog.delmic.com/subtomogram-averaging-in-the-cryo-et-workflow> (accessed September 29, 2023).
- [130] P.S. Erdmann, Z. Hou, S. Klumpe, S. Khavnekar, F. Beck, F. Wilfling, J.M. Plitzko, W. Baumeister, In situ cryo-electron tomography reveals gradient organization of

ribosome biogenesis in intact nucleoli, *Nature Communications* 2021 12:1 12 (2021) 1–9. <https://doi.org/10.1038/s41467-021-25413-w>.

[131] F.K.M. Schur, M. Obr, W.J.H. Hagen, W. Wan, A.J. Jakobi, J.M. Kirkpatrick, C. Sachse, H.-G. Kräusslich, J.A.G. Briggs, An atomic model of HIV-1 capsid-SP1 reveals structures regulating assembly and maturation, *Science* 353 (2016) 506–508. <https://doi.org/10.1126/science.aaf9620>.

[132] B. Turoňová, W.J.H. Hagen, M. Obr, S. Mosalaganti, J.W. Beugelink, C.E. Zimmerli, H.-G. Kräusslich, M. Beck, Benchmarking tomographic acquisition schemes for high-resolution structural biology, *Nature Communications* 11 (2020) 876. <https://doi.org/10.1038/s41467-020-14535-2>.

[133] B. Turoňová, F.K.M. Schur, W. Wan, J.A.G. Briggs, Efficient 3D-CTF correction for cryo-electron tomography using NovaCTF improves subtomogram averaging resolution to 3.4 Å, *Journal of Structural Biology* 199 (2017) 187–195. <https://doi.org/10.1016/j.jsb.2017.07.007>.

[134] R.M. Sanchez, Y. Zhang, W. Chen, L. Dietrich, M. Kudryashev, Subnanometer-resolution structure determination in situ by hybrid subtomogram averaging - single particle cryo-EM, *Nature Communications* 11 (2020) 3709. <https://doi.org/10.1038/s41467-020-17466-0>.

[135] S.G. Wolf, L. Houben, M. Elbaum, Cryo-scanning transmission electron tomography of vitrified cells, *Nature Methods* 11 (2014) 423–428. <https://doi.org/10.1038/nmeth.2842>.

[136] S. Trepout, C. Messaoudi, S. Perrot, P. Bastin, S. Marco, Scanning transmission electron microscopy through-focal tilt-series on biological specimens, *Micron* 77 (2015) 9–15. <https://doi.org/10.1016/j.micron.2015.05.015>.

[137] M. Eibauer, M. Pellanda, Y. Turgay, A. Dubrovsky, A. Wild, O. Medalia, Structure and gating of the nuclear pore complex, *Nature Communications* 6 (2015). <https://doi.org/10.1038/NCOMMS8532>.

[138] K. Cowtan, Phase Problem in X-ray Crystallography, and Its Solution, in: eLS, Wiley, 2003. <https://doi.org/10.1038/npg.els.0002722>.

[139] G.L. Taylor, Introduction to phasing, *Acta Crystallographica Section D: Biological Crystallography* 66 (2010) 325. <https://doi.org/10.1107/S0907444910006694>.

[140] J. Jumper, R. Evans, A. Pritzel, T. Green, M. Figurnov, O. Ronneberger, K. Tunyasuvunakool, R. Bates, A. Žídek, A. Potapenko, A. Bridgland, C. Meyer, S.A.A. Kohl, A.J. Ballard, A. Cowie, B. Romera-Paredes, S. Nikolov, R. Jain, J. Adler, T. Back, S. Petersen, D. Reiman, E. Clancy, M. Zielinski, M. Steinegger, M. Pacholska, T. Berghammer, S. Bodenstein, D. Silver, O. Vinyals, A.W. Senior, K. Kavukcuoglu, P. Kohli, D. Hassabis, D. Hassabis, Highly accurate protein structure prediction with AlphaFold, *Nature* 2021 596:7873 596 (2021) 583–589. <https://doi.org/10.1038/s41586-021-03819-2>.

[141] M. Baek, F. Dimairo, I. Anishchenko, J. Dauparas, S. Ovchinnikov, G.R. Lee, J. Wang, Q. Cong, L.N. Kinch, R.D. Schaeffer, C. Millán, H. Park, C. Adams, C.R. Glassman, A. Degiovanni, J.H. Pereira, A.V. Rodrigues, A.A. Van Dijk, A.C. Ebrecht, D.J. Opperman, T. Sagmeister, C. Buhlheller, T. Pavkov-Keller, M.K. Rathinaswamy, U. Dalwadi, C.K. Yip, J.E. Burke, K.C. Garcia, P.D. Adams, R.J. Read, D. Baker, Accurate prediction of protein structures and interactions using a three-track neural network, *Science* 373 (2021) 871–876.

- [142] I. Barbarin-Bocahu, M. Graille, The X-ray crystallography phase problem solved thanks to AlphaFold and RoseTTAFold models: A case-study report, *Acta Crystallographica Section D: Structural Biology* 78 (2022) 517–531. <https://doi.org/10.1107/S2059798322002157/JC5047SUP1.PDF>.
- [143] A. Perrakis, T.K. Sixma, AI revolutions in biology, *EMBO Reports* 22 (2021). <https://doi.org/10.15252/embr.202154046>.
- [144] D. GABOR, A New Microscopic Principle, *Nature* 161 (1948) 777–778. <https://doi.org/10.1038/161777a0>.
- [145] J.M. Cowley, *Twenty forms of electron holography*, 1992.
- [146] T. Latychevskaia, Spatial coherence of electron beams from field emitters and its effect on the resolution of imaged objects, *Ultramicroscopy* 175 (2017) 121–129. <https://doi.org/10.1016/j.ultramicro.2016.11.008>.
- [147] J. Upatnieks, E.N. Leith, Reconstructed Wavefronts and Communication Theory*, *JOSA*, Vol. 52, Issue 10, Pp. 1123-1130 52 (1962) 1123–1130. <https://doi.org/10.1364/JOSA.52.001123>.
- [148] K. Harada, Interference and interferometry in electron holography, *Microscopy* 70 (2021) 3. <https://doi.org/10.1093/JMICRO/DFAA033>.
- [149] T. Latychevskaia, P. Formanek, C.T. Koch, A. Lubk, Off-axis and inline electron holography: Experimental comparison, *Ultramicroscopy* 110 (2010) 472–482. <https://doi.org/10.1016/j.ultramicro.2009.12.007>.
- [150] F. Wang, D. Wang, L. Rong, Y. Wang, J. Zhao, Single-shot dual-wavelength in-line and off-axis hybrid digital holography, *Applied Physics Letters* 112 (2018) 091903. <https://doi.org/10.1063/1.5013923>.
- [151] G. Möllenstedt, H. Düker, Fresnelscher Interferenzversuch mit einem Biprisma für Elektronenwellen, *Die Naturwissenschaften* 42 (1955) 41. <https://doi.org/10.1007/BF00621530/METRICS>.
- [152] H. Lichte, P. Formanek, A. Lenk, M. Linck, C. Matzeck, M. Lehmann, P. Simon, Electron Holography: Applications to Materials Questions, *Annual Review of Materials Research* 37 (2007) 539–588. <https://doi.org/10.1146/annurev.matsci.37.052506.084232>.
- [153] M. Hÿtch, C. Gatel, Phase detection limits in off-axis electron holography from pixelated detectors: gain variations, geometric distortion and failure of reference-hologram correction, *Microscopy* 70 (2021) 47–58. <https://doi.org/10.1093/jmicro/dfaa044>.
- [154] K. Harada, A. Tonomura, Y. Togawa, T. Akashi, T. Matsuda, Double-biprism electron interferometry, *Applied Physics Letters* 84 (2004) 3229–3231. <https://doi.org/10.1063/1.1715155>.
- [155] B. Haas, J.-L. Rouvière, V. Boureau, R. Berthier, D. Cooper, Direct comparison of off-axis holography and differential phase contrast for the mapping of electric fields in semiconductors by transmission electron microscopy., *Ultramicroscopy* 198 (2019) 58–72. <https://doi.org/10.1016/j.ultramicro.2018.12.003>.
- [156] C. Gatel, A. Lubk, G. Pozzi, E. Snoeck, M. Hÿtch, Counting elementary charges on nanoparticles by electron holography, *Physical Review Letters* 111 (2013). <https://doi.org/10.1103/PhysRevLett.111.025501>.

-
- [157] E. Snoeck, R.E. Dunin-Borkowski, F. Dumestre, P. Renaud, C. Amiens, B. Chaudret, P. Zurcher, Quantitative magnetization measurements on nanometer ferromagnetic cobalt wires using electron holography, *Applied Physics Letters* 82 (2002) 88. <https://doi.org/10.1063/1.1532754>.
- [158] F. Zheng, A. Kovács, T. Denneulin, J. Caron, T. Weßels, R.E. Dunin-Borkowski, Magnetic Field Mapping using Off-Axis Electron Holography in the Transmission Electron Microscope, *Journal of Visualized Experiments* (2020). <https://doi.org/10.3791/61907>.
- [159] T. Denneulin, F. Houdellier, M. Hÿtch, Differential phase-contrast dark-field electron holography for strain mapping, *Ultramicroscopy* 160 (2016) 98–109. <https://doi.org/10.1016/j.ultramic.2015.10.002>.
- [160] T. Latychevskaia, F. Wicki, J.N. Longchamp, C. Escher, H.W. Fink, Direct Observation of Individual Charges and Their Dynamics on Graphene by Low-Energy Electron Holography, *Nano Letters* 16 (2016) 5469–5474. https://doi.org/10.1021/ACS.NANOLETT.6B01881/SUPPL_FILE/NL6B01881_SI_004.AVI.
- [161] J.-N. Longchamp, T. Latychevskaia, C. Escher, H.-W. Fink, Low-energy electron holographic imaging of individual tobacco mosaic virions, *Applied Physics Letters* 107 (2015) 133101. <https://doi.org/10.1063/1.4931607>.
- [162] C.T. Koch, Towards full-resolution inline electron holography, *Micron* 63 (2014) 69–75. <https://doi.org/10.1016/j.micron.2013.10.009>.
- [163] E.J. Kirkland, Improved high resolution image processing of bright field electron micrographs. I. Theory, *Ultramicroscopy* 15 (1984) 151–172. [https://doi.org/10.1016/0304-3991\(84\)90037-8](https://doi.org/10.1016/0304-3991(84)90037-8).
- [164] I. Biran, L. Houben, H. Weissman, M. Hildebrand, L. Kronik, B. Rybtchinski, Real-Space Crystal Structure Analysis by Low-Dose Focal-Series TEM Imaging of Organic Materials with Near-Atomic Resolution, *Advanced Materials* 34 (2022). <https://doi.org/10.1002/ADMA.202202088>.
- [165] C.T. Koch, A flux-preserving non-linear inline holography reconstruction algorithm for partially coherent electrons, *Ultramicroscopy* 108 (2008) 141–150. <https://doi.org/10.1016/j.ultramic.2007.03.007>.
- [166] C.T. Koch, Inline and hybrid electron holography for mapping charges, potentials, and strain phase, (n.d.).
- [167] M.R.S. Huang, A. Eljarrat, C.T. Koch, Quantifying the data quality of focal series for inline electron holography, *Ultramicroscopy* 231 (2021). <https://doi.org/10.1016/j.ultramic.2021.113264>.
- [168] G.B. Stevens, M. Krüger, T. Latychevskaia, P. Lindner, A. Plückthun, H.W. Fink, Individual filamentous phage imaged by electron holography, *European Biophysics Journal* 40 (2011) 1197–1201. <https://doi.org/10.1007/s00249-011-0743-y>.
- [169] M. Cheung, H. Adaniya, C. Cassidy, M. Yamashita, T. Shintake, Low-energy in-line electron holographic imaging of vitreous ice-embedded small biomolecules using a modified scanning electron microscope, *Ultramicroscopy* 209 (2020). <https://doi.org/10.1016/j.ultramic.2019.112883>.
- [170] J.N. Longchamp, S. Rauschenbach, S. Abb, C. Escher, T. Latychevskaia, K. Kern, H.W. Fink, Imaging proteins at the single-molecule level, *Proceedings of the National*

Academy of Sciences of the United States of America 114 (2017) 1474–1479. <https://doi.org/10.1073/pnas.1614519114>.

[171] T. Matsumoto, T. Tanji, A. Tonomura, Visualization of DNA in solution by Fraunhofer in-line electron holography. II: Experiments, *Optik* (1995).

[172] A. Pant, M. Banerjee, K. Khare, Quantitative phase imaging of single particles from a cryoEM micrograph, *Optics Communications* 506 (2022) 127588. <https://doi.org/10.1016/J.OPTCOM.2021.127588>.

[173] T. Latychevskaia, H.-W. Fink, Simultaneous reconstruction of phase and amplitude contrast from a single holographic record, *Optics Express*, Vol. 17, Issue 13, Pp. 10697–10705 17 (2009) 10697–10705. <https://doi.org/10.1364/OE.17.010697>.

[174] P. Morin, M. Pitaval, E. Vicario, *Low Energy Off-Axis Holography in Electron Microscopy*, 1996.

[175] C. Ozsoy-Keskinbora, C.B. Boothroyd, R.E. Dunin-Borkowski, P.A. Van Aken, C.T. Koch, Hybridization approach to in-line and off-axis (electron) holography for superior resolution and phase sensitivity, *Scientific Reports* 4 (2014). <https://doi.org/10.1038/srep07020>.

[176] P.M. Pelz, W.X. Qiu, R. Bücker, G. Kassier, R.J.D. Miller, Low-dose cryo electron ptychography via non-convex Bayesian optimization, *Scientific Reports* 7 (2017). <https://doi.org/10.1038/s41598-017-07488-y>.

[177] J. Song, C.S. Allen, S. Gao, C. Huang, H. Sawada, X. Pan, J. Warner, P. Wang, A.I. Kirkland, Atomic Resolution Defocused Electron Ptychography at Low Dose with a Fast, Direct Electron Detector, *Scientific Reports* 9 (2019). <https://doi.org/10.1038/s41598-019-40413-z>.

[178] J.G. Lozano, G.T. Martinez, L. Jin, P.D. Nellist, P.G. Bruce, Low-Dose Aberration-Free Imaging of Li-Rich Cathode Materials at Various States of Charge Using Electron Ptychography, *Nano Letters* 18 (2018) 6850–6855. <https://doi.org/10.1021/acs.nanolett.8b02718>.

[179] F. Hüe, J.M. Rodenburg, A.M. Maiden, P.A. Midgley, Extended ptychography in the transmission electron microscope: possibilities and limitations, *Ultramicroscopy* 111 (2011) 1117–1123. <https://doi.org/10.1016/J.ULTRAMIC.2011.02.005>.

[180] L. Zhou, J. Song, J.S. Kim, X. Pei, C. Huang, M. Boyce, L. Mendonça, D. Clare, A. Siebert, C.S. Allen, E. Liberti, D. Stuart, X. Pan, P.D. Nellist, P. Zhang, A.I. Kirkland, P. Wang, Low-dose phase retrieval of biological specimens using cryo-electron ptychography, *Nature Communications* 11 (2020). <https://doi.org/10.1038/s41467-020-16391-6>.

[181] X. Pei, L. Zhou, C. Huang, M. Boyce, J.S. Kim, E. Liberti, Y. Hu, T. Sasaki, P.D. Nellist, P. Zhang, D.I. Stuart, A.I. Kirkland, P. Wang, Cryogenic electron ptychographic single particle analysis with wide bandwidth information transfer, *Nature Communications* 2023 14:1 14 (2023) 1–10. <https://doi.org/10.1038/s41467-023-38268-0>.

[182] S. Payne, *Methods to Study Viruses*, in: *Viruses*, Elsevier, 2017: pp. 37–52. <https://doi.org/10.1016/b978-0-12-803109-4.00004-0>.

[183] G. Bourdin, B. Schmitt, L.M. Guy, J.E. Germond, S. Zuber, L. Michot, G. Reuteler, H. Brüssow, Amplification and purification of T4-Like Escherichia coli phages for phage therapy: From laboratory to pilot scale, *Applied and Environmental Microbiology* 80 (2014) 1469–1476. <https://doi.org/10.1128/AEM.03357-13>.

-
- [184] E. Kutter, A. Sulakvelidze, *Bacteriophages*, CRC Press, 2004. <https://doi.org/10.1201/9780203491751>.
- [185] C. Li, A.P. Tardajos, D. Wang, D. Choukroun, K. Van Daele, T. Breugelmans, S. Bals, A simple method to clean ligand contamination on TEM grids, *Ultramicroscopy* 221 (2021). <https://doi.org/10.1016/j.ultramic.2020.113195>.
- [186] A. Kumar, N. Sengupta, S. Dutta, Simplified Approach for Preparing Graphene Oxide TEM Grids for Stained and Vitrified Biomolecules, *Nanomaterials* 11 (2021) 1–22. <https://doi.org/10.3390/NANO11030643>.
- [187] J. Dubochet, M. Adrian, J.-J. Chang, J.-C. Homo, J. Lepault, A.W. McDowell, P. Schultz, Cryo-electron microscopy of vitrified specimens, *Quarterly Reviews of Biophysics* 21 (1988) 129–228. <https://doi.org/10.1017/S0033583500004297>.
- [188] G. Weissenberger, R.J.M. Henderikx, P.J. Peters, Understanding the invisible hands of sample preparation for cryo-EM, *Nature Methods* 18 (2021) 463–471. <https://doi.org/10.1038/s41592-021-01130-6>.
- [189] H.D. White, K. Thirumurugan, M.L. Walker, J. Trinick, A second generation apparatus for time-resolved electron cryo-microscopy using stepper motors and electrospray, *Journal of Structural Biology* 144 (2003) 246–252. <https://doi.org/10.1016/j.jsb.2003.09.027>.
- [190] L. Rima, M. Zimmermann, A. Fränkl, T. Clairfeuille, M. Lauer, A. Engel, H.A. Engel, T. Braun, cryoWriter: a blotting free cryo-EM preparation system with a climate jet and cover-slip injector, *Faraday Discussions* 240 (2022) 55–66. <https://doi.org/10.1039/D2FD00066K>.
- [191] R.B.G. Ravelli, F.J.T. Nijpels, R.J.M. Henderikx, G. Weissenberger, S. Thewessem, A. Gijbers, B.W.A.M.M. Beulen, C. López-Iglesias, P.J. Peters, Cryo-EM structures from sub-nl volumes using pin-printing and jet vitrification, *Nature Communications* 11 (2020) 2563. <https://doi.org/10.1038/s41467-020-16392-5>.
- [192] E. Nwanochie, V.N. Uversky, Structure Determination by Single-Particle Cryo-Electron Microscopy: Only the Sky (and Intrinsic Disorder) is the Limit, *International Journal of Molecular Sciences* 20 (2019) 4186. <https://doi.org/10.3390/ijms20174186>.
- [193] R. Konrat, NMR contributions to structural dynamics studies of intrinsically disordered proteins, *Journal of Magnetic Resonance* 241 (2014) 74. <https://doi.org/10.1016/J.JMR.2013.11.011>.
- [194] C.J. Wilson, W.Y. Choy, M. Karttunen, AlphaFold2: A Role for Disordered Protein/Region Prediction?, *International Journal of Molecular Sciences* 23 (2022) 23. <https://doi.org/10.3390/IJMS23094591/S1>.
- [195] C. Gatel, J. Dupuy, F. Houdellier, M.J. Hÿtch, Unlimited acquisition time in electron holography by automated feedback control of transmission electron microscope, *Applied Physics Letters* 113 (2018) 133102. <https://doi.org/10.1063/1.5050906>.
- [196] V.V. Volkov, M.G. Han, Y. Zhu, Double-resolution electron holography with simple Fourier transform of fringe-shifted holograms, *Ultramicroscopy* 134 (2013) 175–184. <https://doi.org/10.1016/J.ULTRAMIC.2013.06.018>.
- [197] E. Voelkl, D. Tang, Approaching routine $2\pi/1000$ phase resolution for off-axis type holography, *Ultramicroscopy* 110 (2010) 447–459. <https://doi.org/10.1016/J.ULTRAMIC.2009.11.017>.

- [198] R.S. Pantelic, J.C. Meyer, U. Kaiser, H. Stahlberg, The application of graphene as a sample support in transmission electron microscopy, *Solid State Communications* 152 (2012) 1375–1382. <https://doi.org/10.1016/j.ssc.2012.04.038>.
- [199] Y. Han, X. Fan, H. Wang, F. Zhao, C.G. Tully, J. Kong, N. Yao, N. Yan, High-yield monolayer graphene grids for near-atomic resolution cryoelectron microscopy, *Proceedings of the National Academy of Sciences* 117 (2020) 1009–1014. <https://doi.org/10.1073/pnas.1919114117>.
- [200] L. Lin, J. Zhang, H. Su, J. Li, L. Sun, Z. Wang, F. Xu, C. Liu, S. Lopatin, Y. Zhu, K. Jia, S. Chen, D. Rui, J. Sun, R. Xue, P. Gao, N. Kang, Y. Han, H.Q. Xu, Y. Cao, K.S. Novoselov, Z. Tian, B. Ren, H. Peng, Z. Liu, Towards super-clean graphene, *Nature Communications* 10 (2019). <https://doi.org/10.1038/s41467-019-09565-4>.
- [201] W. Xie, L.T. Weng, K.M. Ng, C.K. Chan, C.M. Chan, Clean graphene surface through high temperature annealing, *Carbon* 94 (2015) 740–748. <https://doi.org/10.1016/j.carbon.2015.07.046>.
- [202] H.A. Mehedi, D. Ferrah, J. Dubois, C. Petit-Etienne, H. Okuno, V. Bouchiat, O. Renault, G. Cunge, High density H₂ and He plasmas: Can they be used to treat graphene?, *Journal of Applied Physics* 124 (2018). <https://doi.org/10.1063/1.5043605>.
- [203] P. Schweizer, C. Dolle, D. Dasler, G. Abellán, F. Hauke, A. Hirsch, E. Spiecker, Mechanical cleaning of graphene using in situ electron microscopy, *Nature Communications* 11 (2020). <https://doi.org/10.1038/s41467-020-15255-3>.
- [204] A. Tyagi, V. Mišeikis, L. Martini, S. Forti, N. Mishra, Z.M. Gebeyehu, M.A. Giambra, J. Zribi, M. Frégnaux, D. Aureau, M. Romagnoli, F. Beltram, C. Coletti, Ultra-clean high-mobility graphene on technologically relevant substrates, *Nanoscale* 14 (2022) 2167–2176. <https://doi.org/10.1039/D1NR05904A>.
- [205] A. Fokine, M.Z. Islam, Z. Zhang, V.D. Bowman, V.B. Rao, M.G. Rossmann, Structure of the Three N-Terminal Immunoglobulin Domains of the Highly Immunogenic Outer Capsid Protein from a T4-Like Bacteriophage, *J Virol* 85 (2011) 8141–8148. <https://doi.org/10.1128/JVI.00847-11>.
- [206] M.L. Yap, T. Klose, F. Arisaka, J.A. Speir, D. Veessler, A. Fokine, M.G. Rossmann, Role of bacteriophage T4 baseplate in regulating assembly and infection, *Proceedings of the National Academy of Sciences* 113 (2016) 2654–2659. <https://doi.org/10.1073/pnas.1601654113>.
- [207] J. Dupuy, Contrôle dynamique et optimisation des observations en microscopie électronique en transmission, (2021).
- [208] L. Barberi, F. Livolant, A. Leforestier, M. Lenz, Local structure of DNA toroids reveals curvature-dependent intermolecular forces, *Nucleic Acids Research* 49 (2021) 3709–3718. <https://doi.org/10.1093/nar/gkab197>.
- [209] U. Weierstall, H. Lichte, Electron holography with a superconducting objective lens, *Ultramicroscopy* 65 (1996) 13–22. [https://doi.org/10.1016/S0304-3991\(96\)00050-2](https://doi.org/10.1016/S0304-3991(96)00050-2).
- [210] J.A. McMILLAN, S.C. LOS, Vitreous Ice: Irreversible Transformations During Warm-Up, *Nature* 206 (1965) 806–807. <https://doi.org/10.1038/206806a0>.
- [211] M.F. Moody, L. Makowski, X-ray diffraction study of tail-tubes from bacteriophage T2L, *Journal of Molecular Biology* 150 (1981) 217–244. [https://doi.org/10.1016/0022-2836\(81\)90450-2](https://doi.org/10.1016/0022-2836(81)90450-2).

-
- [212] S. Krimm, T.F. Anderson, Structure of normal and contracted tail sheaths of T4 bacteriophage, *Journal of Molecular Biology* 27 (1967) 197–202. [https://doi.org/10.1016/0022-2836\(67\)90015-0](https://doi.org/10.1016/0022-2836(67)90015-0).
- [213] R.M. Glaeser, K.A. Taylor, Radiation damage relative to transmission electron microscopy of biological specimens at low temperature: a review, *Journal of Microscopy* 112 (1978) 127–138. <https://doi.org/10.1111/j.1365-2818.1978.tb01160.x>.
- [214] J. Cheng, X. Zhang, Optimizing weighting functions for cryo-electron microscopy, *Biophys Rep* 7 (2021) 152–158. <https://doi.org/10.52601/bpr.2021.210001>.
- [215] A. Huet, R.L. Duda, P. Boulanger, J.F. Conway, Capsid expansion of bacteriophage T5 revealed by high resolution cryoelectron microscopy, *Proceedings of the National Academy of Sciences of the United States of America* 116 (2019) 21037–21046. <https://doi.org/10.1073/pnas.1909645116>.
- [216] M.N. Yesibolati, S. Laganà, H. Sun, M. Beleggia, S.M. Kathmann, T. Kasama, K. Mølhav, Mean Inner Potential of Liquid Water, *Phys. Rev. Lett.* 124 (2020) 065502. <https://doi.org/10.1103/PhysRevLett.124.065502>.
- [217] A. Harscher, H. Lichte, Inelastic Mean Free Path and Mean Inner Potential of Carbon Foil and Vitrified Ice measured with Electron Holography., in: *Electron Microscopy General Interest and Instrumentation*, IOP Publishing Ltd, Bristol, 1998.
- [218] M.T.B. Clabbers, M.W. Martynowycz, J. Hattne, B.L. Nannenga, T. Gonen, Electron-counting MicroED data with the K2 and K3 direct electron detectors, *Journal of Structural Biology* 214 (2022) 107886. <https://doi.org/10.1016/J.JSB.2022.107886>.
- [219] M. Sun, C.M. Azumaya, E. Tse, D.P. Bulkeley, M.B. Harrington, G. Gilbert, A. Frost, D. Southworth, K.A. Verba, Y. Cheng, D.A. Agard, Practical considerations for using K3 cameras in CDS mode for high-resolution and high-throughput single particle cryo-EM, *Journal of Structural Biology* 213 (2021) 107745. <https://doi.org/10.1016/j.jsb.2021.107745>.
- [220] H.-J. Cho, J.-K. Hyun, J.-G. Kim, H.S. Jeong, H.N. Park, D.-J. You, H.S. Jung, Measurement of ice thickness on vitreous ice embedded cryo-EM grids: investigation of optimizing condition for visualizing macromolecules, *J Anal Sci Technol* 4 (2013) 7. <https://doi.org/10.1186/2093-3371-4-7>.
- [221] A. Aufschnaiter, S. Büttner, The vacuolar shapes of ageing: From function to morphology, *Biochimica et Biophysica Acta (BBA) - Molecular Cell Research* 1866 (2019) 957–970. <https://doi.org/10.1016/J.BBAMCR.2019.02.011>.
- [222] Z. Trebichalská, J. Javůrek, M. Tatičková, D. Kyjovská, S. Kloudová, P. Otevřel, A. Hampl, Z. Holubcová, High-Resolution 3D Reconstruction of Human Oocytes Using Focused Ion Beam Scanning Electron Microscopy, *Frontiers in Cell and Developmental Biology* 9 (2021). <https://doi.org/10.3389/fcell.2021.755740>.
- [223] H. Zhang, C. Wang, G. Zhou, Ultra-Microtome for the Preparation of TEM Specimens from Battery Cathodes, *Microscopy and Microanalysis : The Official Journal of Microscopy Society of America, Microbeam Analysis Society, Microscopical Society of Canada* 26 (2020) 867–877. <https://doi.org/10.1017/S1431927620024368>.
- [224] E. Carlino, In-line holography in transmission electron microscopy for the atomic resolution imaging of single particle of radiation-sensitive matter, *Materials* 13 (2020). <https://doi.org/10.3390/ma13061413>.
- [225] J.-N. Longchamp, C. Escher, H.-W. Fink, Ultraclean freestanding graphene by platinum-metal catalysis, *Journal of Vacuum Science & Technology B, Nanotechnology and*

Microelectronics: Materials, Processing, Measurement, and Phenomena 31 (2013) 020605. <https://doi.org/10.1116/1.4793746>.

[226] D.N. Mastronarde, Automated electron microscope tomography using robust prediction of specimen movements, (2005). <https://doi.org/10.1016/j.jsb.2005.07.007>.

[227] R.R. Schröder, W. Hofmann, J.F. Ménéret, Zero-loss energy filtering as improved imaging mode in cryoelectron microscopy of frozen-hydrated specimens, *Journal of Structural Biology* 105 (1990) 28–34. [https://doi.org/10.1016/1047-8477\(90\)90095-T](https://doi.org/10.1016/1047-8477(90)90095-T).

[228] S.Q. Zheng, E. Palovcak, J.P. Armache, K.A. Verba, Y. Cheng, D.A. Agard, MotionCor2: Anisotropic correction of beam-induced motion for improved cryo-electron microscopy, *Nature Methods* 14 (2017) 331–332. <https://doi.org/10.1038/nmeth.4193>.

[229] A. Leforestier, F. Livolant, Structure of toroidal DNA collapsed inside the phage capsid, *Proceedings of the National Academy of Sciences* 106 (2009) 9157–9162. <https://doi.org/10.1073/pnas.0901240106>.

[230] N.V. Hud, K.H. Downing, Cryoelectron microscopy of λ phage DNA condensates in vitreous ice: The fine structure of DNA toroids, *Proc. Natl. Acad. Sci. U.S.A.* 98 (2001) 14925–14930. <https://doi.org/10.1073/pnas.261560398>.

[231] A.A. Aksyuk, P.G. Leiman, L.P. Kurochkina, M.M. Shneider, V.A. Kostyuchenko, V.V. Mesyanzhinov, M.G. Rossmann, The tail sheath structure of bacteriophage T4: a molecular machine for infecting bacteria, *The EMBO Journal* 28 (2009) 821–829. <https://doi.org/10.1038/EMBOJ.2009.36>.

[232] M.F. Khan, H. Dong, Y. Chen, M.A. Brook, Low Discrimination of Charged Silica Particles at T4 Phage Surfaces, *Biosens J* 4 (2015) 125. <https://doi.org/10.4172/2090-4967.1000125>.

[233] V. Mitterer, R. Shayan, S. Ferreira-Cerca, G. Murat, T. Enne, D. Rinaldi, S. Weigl, H. Omanic, P.E. Gleizes, D. Kressler, C. Plisson-Chastang, B. Pertschy, Conformational proofreading of distant 40S ribosomal subunit maturation events by a long-range communication mechanism, *Nature Communications* 10 (2019). <https://doi.org/10.1038/s41467-019-10678-z>.

[234] R. Shayan, D. Rinaldi, N. Larburu, L. Plassart, S. Balor, D. Bouyssié, S. Lebaron, J. Marcoux, P.E. Gleizes, C. Plisson-Chastang, Good Vibrations: Structural Remodeling of Maturing Yeast Pre-40S Ribosomal Particles Followed by Cryo-Electron Microscopy, *Molecules* 2020, Vol. 25, Page 1125 25 (2020) 1125. <https://doi.org/10.3390/MOLECULES25051125>.

[235] A. Ben-Shem, L. Jenner, G. Yusupova, M. Yusupov, Crystal structure of the eukaryotic ribosome, *Science* 330 (2010) 1203–1209. https://doi.org/10.1126/SCIENCE.1194294/SUPPL_FILE/BEN-SHEM.SOM.PDF.

[236] A.C. Lamanna, K. Karbstein, Nob1 binds the single-stranded cleavage site D at the 3'-end of 18S rRNA with its PIN domain, *Proc. Natl. Acad. Sci. U.S.A.* 106 (2009) 14259–14264. <https://doi.org/10.1073/pnas.0905403106>.

[237] N. Elad, G. Bellapadrona, L. Houben, I. Sagi, M. Elbaum, Detection of isolated protein-bound metal ions by single-particle cryo-STEM, *Proc. Natl. Acad. Sci. U.S.A.* 114 (2017) 11139–11144. <https://doi.org/10.1073/pnas.1708609114>.

[238] E. Yücelen, I. Lazić, E.G.T. Bosch, Phase contrast scanning transmission electron microscopy imaging of light and heavy atoms at the limit of contrast and resolution, *Sci Rep* 8 (2018) 2676. <https://doi.org/10.1038/s41598-018-20377-2>.

- [239] X. Li, I. Lazić, X. Huang, M. Wirix, L. Wang, Y. Deng, T. Niu, D. Wu, L. Yu, F. Sun, Imaging biological samples by integrated differential phase contrast (iDPC) STEM technique, *Journal of Structural Biology* 214 (2022). <https://doi.org/10.1016/j.jsb.2022.107837>.
- [240] I. Lazić, M. Wirix, M.L. Leidl, F. De Haas, D. Mann, M. Beckers, E.V. Pechnikova, K. Müller-Caspary, R. Egoavil, E.G.T. Bosch, C. Sachse, Single-particle cryo-EM structures from iDPC-STEM at near-atomic resolution, *Nat Methods* 19 (2022) 1126–1136. <https://doi.org/10.1038/s41592-022-01586-0>.
- [241] C. Ophus, Four-Dimensional Scanning Transmission Electron Microscopy (4D-STEM): From Scanning Nanodiffraction to Ptychography and Beyond, *Microsc Microanal* 25 (2019) 563–582. <https://doi.org/10.1017/S1431927619000497>.
- [242] C. Ricolleau, J. Nelayah, T. Oikawa, Y. Kohno, N. Braidy, G. Wang, F. Hue, D. Alloyeau, High Resolution Imaging and Spectroscopy Using C S-corrected TEM with Cold FEG JEM-ARM 200 F, (2012).
- [243] A.M. Maiden, J.M. Rodenburg, An improved ptychographical phase retrieval algorithm for diffractive imaging, *Ultramicroscopy* 109 (2009) 1256–1262. <https://doi.org/10.1016/J.ULTRAMIC.2009.05.012>.
- [244] M. Ameismeier, I. Zemp, J. van den Heuvel, M. Thoms, O. Berninghausen, U. Kutay, R. Beckmann, Structural basis for the final steps of human 40S ribosome maturation, *Nature* 2020 587:7835 587 (2020) 683–687. <https://doi.org/10.1038/s41586-020-2929-x>.
- [245] D. Kimanius, L. Dong, G. Sharov, T. Nakane, S.H.W. Scheres, New tools for automated cryo-EM single-particle analysis in RELION-4.0, *Biochemical Journal* 478 (2021) 4169. <https://doi.org/10.1042/BCJ20210708>.
- [246] T. Nakane, S.H.W. Scheres, Multi-body Refinement of Cryo-EM Images in RELION, in: *Methods in Molecular Biology* (Clifton, N.J.), 2021: pp. 145–160. https://doi.org/10.1007/978-1-0716-0966-8_7.
- [247] T. Grant, A. Rohou, N. Grigorieff, CisTEM, user-friendly software for single-particle image processing, *eLife* 7 (2018). <https://doi.org/10.7554/ELIFE.35383>.
- [248] J.M. de la Rosa-Trevín, A. Quintana, L. del Cano, A. Zaldívar, I. Foche, J. Gutiérrez, J. Gómez-Blanco, J. Burguet-Castell, J. Cuenca-Alba, V. Abrishami, J. Vargas, J. Otón, G. Sharov, J.L. Vilas, J. Navas, P. Conesa, M. Kazemi, R. Marabini, C.O.S. Sorzano, J.M. Carazo, Scipion: A software framework toward integration, reproducibility and validation in 3D electron microscopy, *Journal of Structural Biology* 195 (2016) 93–99. <https://doi.org/10.1016/J.JSB.2016.04.010>.
- [249] K. Zhang, Gctf: Real-time CTF determination and correction, *Journal of Structural Biology* 193 (2016) 1–12. <https://doi.org/10.1016/J.JSB.2015.11.003>.
- [250] A. Rohou, N. Grigorieff, CTFIND4: Fast and accurate defocus estimation from electron micrographs, *Journal of Structural Biology* 192 (2015) 216–221. <https://doi.org/10.1016/j.jsb.2015.08.008>.
- [251] R. Henderson, A. Sali, M.L. Baker, B. Carragher, B. Devkota, K.H. Downing, E.H. Egelman, Z. Feng, J. Frank, N. Grigorieff, W. Jiang, S.J. Ludtke, O. Medalia, P.A. Penczek, P.B. Rosenthal, M.G. Rossmann, M.F. Schmid, G.F. Schröder, A.C. Steven, D.L. Stokes, J.D. Westbrook, W. Wriggers, H. Yang, J. Young, H.M. Berman, W. Chiu, G.J. Kleywegt, C.L. Lawson, Outcome of the First Electron Microscopy Validation Task Force Meeting, *Structure* 20 (2012) 205–214. <https://doi.org/10.1016/j.str.2011.12.014>.

- [252] S. Chen, G. McMullan, A.R. Faruqi, G.N. Murshudov, J.M. Short, S.H.W. Scheres, R. Henderson, High-resolution noise substitution to measure overfitting and validate resolution in 3D structure determination by single particle electron cryomicroscopy, *Ultramicroscopy* 135 (2013) 24–35. <https://doi.org/10.1016/J.ULTRAMIC.2013.06.004>.
- [253] J. Zivanov, T. Nakane, S.H.W. Scheres, A Bayesian approach to beam-induced motion correction in cryo-EM single-particle analysis, *Urn:Issn:2052-2525* 6 (2019) 5–17. <https://doi.org/10.1107/S205225251801463X>.
- [254] E.F. Pettersen, T.D. Goddard, C.C. Huang, E.C. Meng, G.S. Couch, T.I. Croll, J.H. Morris, T.E. Ferrin, UCSF ChimeraX: Structure visualization for researchers, educators, and developers, *Protein Science* 30 (2021) 70–82. <https://doi.org/10.1002/pro.3943>.
- [255] T.D. Goddard, C.C. Huang, E.C. Meng, E.F. Pettersen, G.S. Couch, J.H. Morris, T.E. Ferrin, UCSF ChimeraX: Meeting modern challenges in visualization and analysis, *Protein Science* 27 (2018) 14–25. <https://doi.org/10.1002/pro.3235>.
- [256] E.F. Pettersen, T.D. Goddard, C.C. Huang, G.S. Couch, D.M. Greenblatt, E.C. Meng, T.E. Ferrin, UCSF Chimera—A visualization system for exploratory research and analysis, *J Comput Chem* 25 (2004) 1605–1612. <https://doi.org/10.1002/jcc.20084>.
- [257] J.E. Lineback, A.L. Jansma, PyMOL as an Instructional Tool To Represent and Manipulate the Myoglobin/Hemoglobin Protein System, *Journal of Chemical Education* 96 (2019) 2540–2544. <https://doi.org/10.1021/acs.jchemed.9b00143>.
- [258] S.H.W. Scheres, Processing of Structurally Heterogeneous Cryo-EM Data in RELION, in: *Methods in Enzymology*, Elsevier, 2016: pp. 125–157. <https://doi.org/10.1016/bs.mie.2016.04.012>.
- [259] S. Ferreira-Cerca, V. Sagar, T. Schäfer, M. Diop, A.-M. Wesseling, H. Lu, E. Chai, E. Hurt, N. LaRonde-LeBlanc, ATPase-dependent role of the atypical kinase Rio2 on the evolving pre-40S ribosomal subunit, *Nat Struct Mol Biol* 19 (2012) 1316–1323. <https://doi.org/10.1038/nsmb.2403>.
- [260] R. Sanchez-Garcia, J. Gomez-Blanco, A. Cuervo, J.M. Carazo, C.O.S. Sorzano, J. Vargas, DeepEMhancer: a deep learning solution for cryo-EM volume post-processing, *Communications Biology* 4 (2021). <https://doi.org/10.1038/s42003-021-02399-1>.
- [261] A.J. Jakobi, M. Wilmanns, C. Sachse, Model-based local density sharpening of cryo-EM maps, *eLife* 6 (2017) e27131. <https://doi.org/10.7554/eLife.27131>.
- [262] P. Emsley, B. Lohkamp, W.G. Scott, K. Cowtan, Features and development of Coot, *Acta Crystallogr D Biol Crystallogr* 66 (2010) 486–501. <https://doi.org/10.1107/S0907444910007493>.



SHORT ABSTRACT

Résumé

Cette thèse présente une évaluation des capacités de l'imagerie de phase par holographie électronique pour l'observation d'échantillons biologiques, en couplant les méthodologies les plus avancées dans ce domaine et la cryomicroscopie électronique qui permet l'observation des échantillons dans un état quasi-natif. Nous avons étudié les possibilités de l'holographie « off-axis » et l'holographie « in-line » à température ambiante et en condition cryogénique. La préparation des échantillons et les conditions expérimentales en MET ont été optimisées en mettant l'accent sur la mise en œuvre d'un protocole à faible dose d'électrons. Des observations ont alors été réalisées sur le microscope I2TEM au CEMES, dédié à l'holographie off-axis, en utilisant les bactériophages T4 et T5 comme échantillons test. À température ambiante, nous avons réussi à visualiser les différentes parties de ces phages. En mode cryogénique, la structure des bactériophages a été observée de façon plus détaillée, mais nous avons rencontré des limitations importantes, notamment l'augmentation du bruit à de faibles doses d'électrons et l'instabilité thermique du porte-échantillon. L'holographie « in-line » en mode cryogénique a en revanche permis d'obtenir des images contrastées et bien résolues des phages, et montré la possibilité d'accéder à la charge de l'échantillon, ici la charge de leurs capsides qui joue un rôle important dans leur assemblage. Pour compléter ces données, nous avons également exploré la combinaison des deux méthodes d'holographie, qui offrent des performances complémentaires dans les basses et hautes fréquences spatiales. Nous présentons aussi des résultats préliminaires sur la visualisation des phages par ptychographie électronique, une autre méthode d'imagerie de phase. Ce travail exploratoire et interdisciplinaire met en lumière les possibilités originales offertes par l'holographie électronique pour l'imagerie biologique, et identifie les barrières à lever pour rendre ces approches plus opérationnelles.

Abstract

The goal of this thesis was to assess the capabilities of phase imaging by electron holography for the observation of biological samples, by coupling the most advanced methodologies in this field with cryo-electron microscopy, which enables samples to be observed in a quasi-native state. We explored the capabilities of off-axis and in-line holography, at room temperature and in cryogenic conditions. Sample preparation and TEM experimental conditions were optimized, with particular emphasis on the implementation of a low-dose electron protocol. Observations were then made on the I2TEM microscope at CEMES, a microscope dedicated to off-axis holography, using T4 and T5 bacteriophages as test samples. At room temperature, we managed to visualize the different parts of these phages. In cryogenic mode, the structure of bacteriophages was observed in greater detail, but we encountered significant limitations, including increased noise at low electron doses and thermal instability of the sample holder. In-line holography in cryogenic mode, on the other hand, enabled us to obtain contrasted, well-resolved images of the phages, and showed the possibility of assessing the charge of the sample, in this case the charge of the phage capsid, which plays an important role in their assembly. To complement these data, we also explored the combination of the two holography methods, which offer complementary performance at high and low spatial frequencies, and we present preliminary results on phage visualization using electron ptychography, another phase imaging method. This exploratory and interdisciplinary thesis highlights the original possibilities offered by electron holography for biological imaging, and identifies the barriers to be overcome to make these approaches more operational.